UC Santa Cruz

UC Santa Cruz Electronic Theses and Dissertations

Title

Nanostructured Materials as Effective Catalysts for Oxygen Reduction Reactions (ORR)

Permalink

https://escholarship.org/uc/item/8pj4n36f

Author

Liu, Ke

Publication Date

2015

Peer reviewed|Thesis/dissertation

eScholarship.org Powered by the California Digital Library
University of California

UNIVERSITY OF CALIFORNIA
SANTA CRUZ

NANOSTRUCTURED MATERIALS AS EFFECTIVE CATALYSTS FOR OXYGEN REDUCTION REACTIONS (ORR)

A dissertation submitted in partial satisfaction
of the requirements for the degree of

DOCTOR OF PHILOSOPHY

in

CHEMISTRY

by

Ke Liu

September 2015

The Dissertation of Ke Liu
is approved:

_____

Professor Shaowei Chen, chair

_____

Professor Ilan Benjamin

_____

Professor Yat Li

_____

Tyrus Miller
Vice Provost and Dean of Graduate Studies

Copyright © by
Ke Liu
2015

TABLE OF CONTENTS

LIST OF FIGURES ..... **vi**
LIST OF TABLES ..... **xv**
ABSTRACT ..... **xvi**
DEDICATION ..... **xx**
Acknowledgements ..... **xxi**
Chapter 1 ..... **1**
1.1 Background **2**
1.2 Oxygen Reduction Reactions (ORR) **3**
1.3 Activity of Pt cathode catalysts **10**
1.3.1 facet-controlled Pt nanocrystals 10
1.3.2. Alloying Pt with transition metals 11
1.3.3 Modifying surfaces of Pt with foreign species 12
1.3.4 Strong metal-support interactions 14
1.4 Stability **14**
1.4.1 Platinum dissolution 15
1.4.2 Ostwald ripening 16
1.4.3 Agglomeration 17
1.4.4 Corrosion of carbon support 18
1.4.5 Particle detachment 19
1.5 Dissertation Outline **19**
1.6 Reference **22**
Chapter 2 ..... **36**
2.1 Chemicals Required **37**
2.2 Particles Synthesis **38**
2.2.1 Platinum nanoparticles functionalized with acetylene derivatives 38
2.2.2 Graphene Quantum Dots (GQD) 39
2.2.3 GQD-Supported Platinum Nanoparticles (Pt/G) 39
2.2.4 Alkyne-capped copper nanoparticles 40
2.2.5 GQD-Supported Copper Nanoparticles (Pt/G) 40

2.2.6 TiO_2 nanoparticles 41
2.2.7 TiO_2 supported Cu nanoparticles 41
2.3 Instruments 42
2.3.1 Microscopy 42
2.3.2 Spectroscopy 42
2.3.3 Electrochemistry 43
2.3.4 Electronic Conductivity Measurements 44
2.4 Reference 45
Chapter 3 46
3.1 Introduction 47
3.2. Results and Discussion 49
3.2.1. Structural characterizations 49
3.2.2. Electronic conductivity 58
3.2.3. Electrocatalytic activity 64
3.3. Conclusion 74
3.4. References 76
Chapter 4 79
4.1 Introduction 80
4.2 Results and Discussion 83
4.3 Conclusion 103
4.4 References 105
Chapter 5 109
5.1 Introduction 110
5.2 Results and discussion 112
5.3 Conclusion 132
5.4 References 134
Chapter 6 138
6.1 Introduction 139
6.2 Results and discussion 141
6.3 Conclusion 174
6.4 References 175
Chapter 7 179

7.1 Introduction..... 180
7.2 Results and discussion 182
7.3 Conclusion 204
7.4 References..... 206

LIST OF FIGURES

Chapter 3

Figure 3. 1. Representative TEM micrograph of PtHC10 nanoparticles prepared by thermolytic reduction of $PtCl_2$. Scale bar 5 nm. Inset shows the corresponding nanoparticle core size histogram. 49

Figure 3. 2. FTIR spectra of PtHC10, PtEPA, and PtBPA nanoparticles along with those of monomeric HC10, EPA and BPA ligands. 52

Figure 3. 3. UV-vis spectra of PtHC10, PtEBA, and PtBPA nanoparticles in $CHCl_3$. Note that the spectra have been normalized to their respective absorbance at 300 nm. The difference spectra between the PtEPA (PtBPA) and PtHC10 nanoparticles are also included in the figure (right axis). 55

Figure 3. 4. Excitation and emission spectra of PtHC10 (solid curves), PtEPA (dotted curve) and PtBPA (dashed curve) in $CHCl_3$. Note that the fluorescence intensity has been normalized to the optical density at the respective excitation wavelength position. 57

Figure 3. 5. Current-potential (I-V) curves of the nanoparticle solid ensembles at varied temperatures: (A) PtHC10, (B) PtEPA, and (C) PtBPA. Potential scan rate 20 mV/s. Arrows denote the increase of temperature from 80 K to 300 K. 59

Figure 3. 6. Variation of nanoparticle ensemble conductivity with temperature. Data are obtained from the slopes of the I-V curves in Fig.3.5. The left y axis is for both PtHC10 and PtEPA, and the right y axis for PtBPA alone. 62

Figure 3. 7. Cyclic voltammograms of a glassy-carbon disk electrode modified with

PtHC10, PtEPA, PtBPA and commercial Pt/C nanoparticles in a nitrogen-purged 0.1M NaOH solution. Pt loadings were 2.44 μg (PtHC10), 1.90 μg (PtEPA), 1.90 μg (PtBPA), and 2.00 μg (Pt/C). Potential scan rate 100 mV/s. 65

Figure 3. 8. RRDE voltammograms of a gold ring-glassy-carbon disk electrode modified with (A) PtHC10, (B) PtEPA, (C) PtBPA and (D) commercial Pt/C nanoparticles in an oxygen-saturated 0.1M NaOH solution. Electrode rotation rates are specified in the figure legends. Pt loadings were 2.44 μg (PtHC10), 1.90 μg (PtEPA), 1.90 μg (PtBPA), and 2.00 μg (Pt/C). Ring currents were collected by setting the ring potential at +0.4 V. 68

Figure 3. 9. Koutecky-Levich plots of (A) PtHC10, (B) PtEPA, (C) PtBPA and (D) commercial Pt/C nanoparticles in oxygen reduction in 0.1M NaOH solution. Symbols are experimental data acquired from Fig 3.8 and lines are the corresponding linear regressioins. 70

Figure 3. 10. Variation of the kinetic current density (J_k) with electrode potential at different nanoparticle catalysts in oxygen reduction. Symbols are experimental data obtained from the intercepts in Fig 3.9 and normalized to the effective electrochemical surface areas estimated from Fig 3.7. 72

Chapter 4

Figure 4. 1. Representative TEM micrographs of GQD-supported Pt nanoparticles. Scale bar is 20 nm in panel (A) and 5 nm in panel (B). Inset in panel (A) shows the nanoparticle core size histogram. Yellow lines in panel (B) highlight the lattice

fringes, and white arrays indicate the halos surrounding the Pt nanoparticles. 84

Figure 4. 2. XRD patterns of the Pt/G and Pt/C nanoparticles. 87

Figure 4. 3. XPS survey spectra of the (A) Pt4f and (B) C1s electrons of the Pt/G nanoparticles. Symbols are experimental data and lines are deconvolution fits. 89

Figure 4. 4. Cyclic voltammograms of a glassy carbon electrode (diameter 5.61 mm) loaded with Pt/G and Pt/C nanoparticle catalysts in a nitrogen-saturated 0.1 M $HClO_4$ solution. Metal loading was 12.1 μg for both nanoparticles. Potential sweep rate 20 mV/s. 91

Figure 4. 5. RRDE voltammograms of a glassy carbon electrode (diameter 5.61 mm) loaded with (A) Pt/C or (B) Pt/G nanoparticle catalysts in an oxygen-saturated 0.1 M $HClO_4$ solution. Metal loading was 12.1 μg for both nanoparticles. Potential sweep rate was 5 mV/s; electrode rotation rates were shown in the figure legends; ring potential was set at +1.5 V. 94

Figure 4. 6. Variation of the number of electron transfer (n) in oxygen reduction with electrode potential. Symbols are experimental data calculated from the RRDE voltammograms at 2500 rpm in Figure 4.5 by using eq 1. 95

Figure 4. 7. Koutecky−Levich plots of (A) Pt/C and (B) Pt/G nanoparticles in an oxygen-saturated 0.1 M $HClO_4$ solution. Symbols are experimental data acquired from Figure 4.5, and lines are the corresponding linear regressions. 97

Figure 4. 8. Variation of the kinetic current density (J_k, I_k normalized to the respective effective electrochemical surface area determined in Figure 4) with electrode potentials in oxygen reduction. Symbols are experimental data obtained

from the y-axis intercepts of the linear regressions in Figure 4.7..... 100

Figure 4. 9. Polarization curves for oxygen reduction catalyzed by Pt/C (solid curves) and Pt/G (dashed curves) before (red curves) and after (red curves) 2000 potential cycles with a potential scan rate of 200 mV/s from +0.05 to +1.10 V in O_2-saturated 0.1 M $HClO_4$. Electrode rotation rate: 1600 rpm. Other experimental conditions were the same as in Figure 4.5..... 102

Chapter 5

Figure 5. 1. Representative TEM micrographs of (A) CuHC10-IB and (B) CuHC10-RT nanoparticles. Scale bars 10 nm. Insets show the corresponding core size histograms. 114

Figure 5. 2. FTIR spectra of CuHC10 nanoaprticles (black curve) and monomeric 1-decyne ligands (red curve). 116

Figure 5. 3. Excitation and emission spectra of CuHC10-RT and CuHC10-IB nanoparticles in $CHCl_3$. 118

Figure 5. 4. (A) XPS survey spectra and (B) high-resolution scans of the Cu2p electrons of CuHC10-IB, CuHC10-RT and commercial CuO nanoparticles. In panel (B), black curves are the raw experimental data and color curves are the deconvolution fits..... 122

Figure 5. 5. Cyclic voltammograms of a glassy carbon-disk electrode modified with 15 μg of CuHC10-IB (black curve), CuHC10-RT (red curve) and commercial CuO (green curve) nanoparticles in a nitrogen-saturated 0.1M NaOH solution.

Nanoparticle loading is all 15 μg and potential scan rate is 0.01 V/s. 124

Figure 5. 6. RRDE voltammograms of a platinum ring-glassy-carbon disk electrode with the disk modified with (A) CuHC10-IB, (B) CuHC10-RT, and (C) commercial CuO nanoparticles in an oxygen-saturated 0.1 M NaOH solution. Nanoparticle loading is all 15 μg. Electrode rotation rates are specified in the figure legends. Ring currents are collected by setting the ring potential at +1.3 V vs RHE. 126

Figure 5. 7. Variation of the number of electron transfer (n, solid curves, left y axis) and percentage (xH_2O_2, dashed curves, right y axis) of peroxide formed in oxygen reduction with electrode potential for CuHC10-IB (black curves), CuHC10-RT (red curves) and commercial CuO (green curves) nanoparticles. Symbols were experimental data calculated from the RRDE voltammograms at 1600 rpm in Figure 5.6. 128

Figure 5. 8. Tafel plots of oxygen reduction catalyzed by CuHC10-IB (black circles), CuHC10-RT (red diamonds) and commercial CuO (green squares) nanoparticles. Data are acquired from linear regressions of the Koutecky-Levich plots based on the original data in Figure 5.6. 130

Chapter 6

Figure 6.1.(A) XPS survey spectra and high-resolution scans of (B) C1s and (C) Cu2p electrons of Cu/GQD nanocomposites at different Cu/C atomic ratios (x). In panels (B) and (C), black curves are experimental data and colored curves are deconvolution fits. 144

Figure 6. 2. TEM micrographs of Cu/GQD nanocomposites at different Cu/C atomic ratios (x): (A) x = 3.54%, (B) x = 3.32%, (C) x = 2.88%, and (D) x = 2.34%. Scale bars are all 20nm. 147

Figure 6. 3. Raman spectra of Cu/GQD nanocomposites at different Cu/C atomic ratios (x) which are specified in figure legends. 148

Figure 6. 4. Cyclic voltammograms of a glassy-carbon electrode (dia. 5.61 mm) modified with Cu/GQD nanocomposites in a nitrogen-purged 0.1 M NaOH solution. Potential scan rate: 10 mV/s. Catalyst loading: 15 μg. 151

Figure 6. 5. RRDE voltammograms of a platinum ring-glassy carbon disk electrode with the disk electrode modified with 15 μg of (A) Cu/GQD at different Cu/C atomic ratios (x), (A) 3.54%, (B) 3.32%, (C) 2.88%, and (D) 2.34% in an oxygen-saturated 0.1M NaOH solution. Electrode rotation rates are specified in the figure legends. Ring potential was set at +1.30 V vs RHE. 153

Figure 6. 6. Variation of the number of electron transfer (n) in oxygen reduction with electrode modified with 15 μg of Cu/GQD at different Cu/C atomic ratios (x), 3.54% (black curve), 3.32% (red curve), 2.88% (green curve), and 2.34% (blue curve). Symbols were experimental data calculated from the RRDE voltammograms of those three catalysts at 1600 rpm in Figure 6.5. 155

Figure 6. 7. Tafel plots of electrode modified with 15 μg of Cu/GQD at different Cu/C atomic ratios (x), 3.54% (black), 3.32% (red), 2.88% (green), and 2.34% (yellow). Symbols were experimental data obtained by linear regression of the Koutecky-Levich plots. 157

Figure 6. 8. Raman spectra of Cu/GQD-2.88% (black curve) and after hydrothermal treatment at 140°C (red curve), 160°C (green curve), 180°C (blue curve) and 200°C (pink curve). 160

Figure 6. 9. (A) XPS survey spectra and high-resolution scans of (B) C1s and (C) Cu2p electrons of Cu/GQD-2.88% nanocomposites and after hydrothermal treatments at different temperatures. In panels (B) and (C), black curves are experimental data and colored curves are deconvolution fits. 163

Figure 6. 10. Cyclic voltammograms of Pt-ring-glassy carbon-disk electrode modified with 15ug Cu-GQD-2.88% (black curve), and after hydrothermal treatments at 140°C (red curve), 160°C (green curve), 180°C (yellow curve) and 200°C (blue curve). 166

Figure 6. 11. RRDE voltammograms of a platinum ring-glassy-carbon disk electrode modified with 15ug Cu-GQD-2.88% hydrothermal treated at different temperatures, (A) 140°C, (B) 160°C, (C) 180°C and (D) 200°C in an oxygen-saturated 0.1M NaOH solution. Electrode rotation rates are specified in the figure legends. Ring potential was set at +1.30 V vs RHE. 168

Figure 6. 12. Variation of the number of electron transfer (n) in oxygen reduction with electrode modified with 15ug Cu-GQD-2.88% (black curve) and after hydrothermal treatments at different temperatures, 140°C (red curve), 160°C (green curve), 180°C (yellow curve) and 200°C (blue curve). Symbols were experimental data calculated from the RRDE voltammograms of those three catalysts at 1600 rpm in Figure 6.11. 170

Figure 6. 13. Tafel plots of electrode modified with 15ug Cu-GQD-2.88% (black curve), and after hydrothermal treatments at 140°C (red curve), 160°C (green curve), 180°C (yellow curve) and 200°C (blue curve). Symbols were experimental data obtained by linear regression of the Koutecky-Levich plots. 171

Chapter 7

Figure 7. 1. Representative TEM micrographs of (A and C) Cu/TiO_2 and (B and D) $CuHC10/TiO_2$ nanoparticles. Scale bars are 10 nm in panels (A) and (B), 5 nm in (C) and 2 nm in (D). Yellow lines highlight the Cu(111) lattice fringes whereas red lines are for anatase TiO_2 (101).. 184

Figure 7. 2. XRD patterns of TiO_2 (black curve), Cu/TiO_2 (red curve) and $CuHC10/TiO_2$ (green curve) nanoparticles. Legends "@" highlight the diffraction peaks of anatase TiO_2..... 186

Figure 7. 3. XPS full survey spectra (A) and high-resolution scans of the (B) Cu2p, (C) Ti2p and (D) O1s electrons of TiO_2, Cu/TiO_2 and $CuHC10/TiO_2$ nanoparticles. Black curves are experimental data and color curves are deconvolution fits. 191

Figure 7. 4. Cyclic voltammograms of a glassy carbon-disk electrode modified with 15 μg of TiO_2 (black curve), Cu/TiO_2 (red curve) or $CuHC10/TiO_2$ (green curve) nanoparticles in a nitrogen-saturated 0.1M NaOH solution. Potential scan rate 10 mV/s. 193

Figure 7. 5. RRDE voltammograms of a platinum ring-glassy-carbon disk electrode with the disk modified with (A) TiO_2, (B) Cu/TiO_2, and (C) $CuHC10/TiO_2$

nanoparticles in an oxygen-saturated 0.1 M NaOH solution. Nanoparticle loading is all 15 μg. Electrode rotation rates are specified in the figure legends. Ring currents are collected by setting the ring potential at +1.3 V vs RHE..... 195

Figure 7. 6. Variation of the number of electron transfer (n) in oxygen reduction with electrode potential for TiO_2 (black curves), Cu/TiO_2 (red curves) and $CuHC10/TiO_2$ (green curves) nanoparticles. Symbols were experimental data calculated from the RRDE voltammograms at 1600 rpm in Figure 7.5. Inset shows the corresponding Tafel plots. Data are acquired from linear regressions of the Koutecky-Levich plots in Figure S2. Electrode geometrical surface area was used to calculate the current density. 197

Figure 7. 7. Polarization curves for oxygen reduction catalyzed by TiO_2 (A), Cu/TiO_2 (B), and $CuHC10/TiO_2$ (C) before (solid curves) and after (dashed curves) 4000 potential cycles with a potential scan rate of 50 mV/s from +0.6 to 1.1V in O_2 saturated 0.1M NaOH solution. Electrode rotation rate: 1600 rpm. Other experimental conditions were the same as in Figure 7.5. 202

LIST OF TABLES

Chapter 5

Table 5. 1. Binding energies (eV) of the Cu2p electrons and the ratio (xCu(II)) of Cu(II) over Cu(I) and Cu(0) combined in CuHC10-IB, CuHC10-RT and commercial CuO nanoparticles..... 121

Chapter 6

Table 6. 1. Summary of XPS results of Cu/GQD nanocomposites..... 145

Table 6. 2. Summary of results from Raman spectroscopic measurements..... 149

Table 6. 3. Ratios of D peak over G peak and their corresponding positions on Raman spectrum for Cu/GQD-2.88% before and after hydrothermal treatment..... 160

Table 6. 4. Summary of XPS results of Cu/GQD-2.88% nanocomposites and after hydrothermal treatments. 164

ABSTRACT

NANOSTRUCTURED MATERIALS AS EFFECTIVE CATALYSTS FOR OXYGEN REDUCTION REACTIONS (ORR)

Ke Liu

Fuel cells are clean and efficient power sources which can convert chemical energy of hydrogen and oxygen into electricity. The Gibbs free energy of hydrogen fuel cells can be as high as -273.13 kJ mol^{-1}, and the theoretical energy conversion efficiency is high as well. However, the cathode oxygen reduction reaction (so-called ORR reaction) is kinetically slow and regarded as bottleneck of fuel cell technology. Thus extensive efforts have been spent on developing efficient catalysts where oxygen molecules can be reduced to water efficient and fast. In this thesis, the research efforts are focused on developing various nanostructured materials as efficient ORR catalysts. In detail, the research mainly focuses on two directions: first, develop Pt-based ORR catalysts with improved ORR activities compared to commercial Pt/C catalysts; second, develop non-precious but highly-efficient ORR catalysts.

Commercial Pt/C catalysts are one of the best ORR catalysts due to their good balance of activities and stabilities. However, the price of Pt is high and its reserve is limited, thus efforts should be spent in improving specific activity of Pt-based ORR catalysts aiming to decrease usage of Pt and the cost on catalysts. Recently it's reported that deliberate manipulation chemical functionalization of

metal nanoparticles can significantly increase their electrocatalytic activities. Inspired by those work, acetylene derivatives were adopted to functionalize surface of Pt nanoparticles in the first project, in order to explore different metal-ligand interfacial bonding interactions on the nanoparticle electrocatalytic activity. It's revealed that specific activity of Pt nanoparticles after ligand functionalization was all markedly better than that of commercial Pt/C catalysts, which was accounted for by the deliberate manipulation of the electronic structure of the Pt nanoparticles.

Besides organic ligand functionalization, graphene-based materials were reported capable of decreasing surface electron density of Pt, which is believed beneficial for the electrocatalytic activity. In the second project, Pt nanoparticles were deposited on graphene quantum dots, a relatively new member of graphene-based materials, producing Pt/GQD composite as evidenced by TEM and XRD measurements. In comparison with commercial Pt/C catalysts, the Pt/GQD composite showed markedly enhanced catalytic activity in oxygen reduction reaction, with an onset potential 70 mV more positive than that of Pt/C, a specific activity that was almost nine times higher, and excellent long-term stability.

Although it's proven effective to improve ORR activity of Pt-based materials by ligand functionalization and introducing interactions between graphene quantum dots, the high price of Pt still drives efforts spent in developing non-precious efficient ORR catalysts. Compared with Pt, copper is inexpensive candidate materials with good conductivity, and polycrystalline

copper electrode is reported to exhibit apparent electrocatalytic activity in oxygen reduction reaction. It's also suggested that partial oxidation of copper surfaces might be crucial for ORR activities, so alkyne-capped copper nanoparticles were prepared hoping to realize control oxidation on the surface and their catalytic activities were evaluated. Electrochemical studies showed that the as-prepared alkyne-capped copper nanoparticles exhibited much better activity in oxygen reduction than those poly- or single-crystalline copper electrodes, yet low-efficient 2e pathway is dominant for those copper-based materials.

To further improve ORR activity of copper-based material, graphene quantum dots, which contain both significant portion of sp^2 carbon and wealthy structural defects, were introduced to support copper nanoparticles. Cu/GQD nanocomposites with varied defect concentrations exhibited significantly electrocatalytic activities towards oxygen reduction reaction, where highly-efficient 4e pathway is dominant for those composite catalysts. It's also figured out that there is an optimal defect concentration where both metal-sp^2C interactions and surface defect mediations contribute most to the ORR activities.

For non-precious ORR catalysts, their long-term stabilities are more concerned than the catalytic activities. Although metal-sp^2C interactions are reported able to stabilize the overall structure, carbon-based supports can be oxidized at high potentials, hampering the stability under long-time cycle tests. TiO_2 is quite stable in extreme conditions (strong acidic or alkaline solutions) and can resist high oxidizing potentials. It's also reported that there are strong metal-

support interactions between TiO_2 and metal centers. Herein, copper nanoparticles were directly grown on surface of TiO_2 and selected organic ligands were also attached on surface of copper nanoparticles, producing both Cu/TiO_2 and $CuHC10/TiO_2$ nanoparticles. Electrochemical studies demonstrated that both Cu/TiO_2 and $CuHC10/TiO_2$ are able to catalyze oxygen reduction reactions following an almost four-electron reduction pathway. $CuHC10/TiO_2$ exhibited the best ORR activity with a high current density and long-term stability after 4000 cycles at high potentials.

DEDICATION

Dedicated

To

My Parents and Sister

Acknowledgements

I would like to express appreciation to my supervisor Prof. Shaowei Chen, for his patience and useful critiques, which help keep my progress on schedule. In the very beginning, I knew little on how to do research and he taught me almost hand by hand with great patience. He not only taught me a lot on research but also served as an example guiding my attitudes towards research work. Without his supervision on this work, I would not have been able to finish this thesis on time. Prof. Ilan Benjamin and Prof. Yat Li are appreciated for serving my dissertation committee and providing support throughout my graduate studies. They always hold a high standard for my second-year seminar, oral exam, fourth-year review and fifth year review. Numerous help from my supervisor and committee members for my job-seeking is also highly appreciated. Also I would like to thank Prof. David Belanger, for being the outside member in my Oral Qualifying Examination.

I would like to specially thank respected Prof. Jin Zhang, for his generous help and suggestions. He is always willing to give a hand for help and strongly supports students' career growth even though sometimes his weekend has to be sacrificed. Thanks to Prof. Zhiyou Zhou for leading me to the electrochemistry field, coaching my first research project, and giving quite valuable suggestions in research as well as life. Also thanks to Prof. Jie Huang, Prof. Shengyong Zhai, Prof. Yan Guo, for their warm friendship which makes me feel less stressful or lonely, and to Prof. Fanli Lu, Prof. Fen Ran and his wife.

I would like to convey my appreciation to my laboratory colleagues, Dr, Guoqiang He, Dr. Xiongwu Kang, Dr. Yang Song, Bruce Phebus, Christopher Deming, Peiguang Hu, Mauricio Rajas-Andrade, Limei Chen, Gabriella Jia Lu, Sam Sweeney, Yi Peng, John Diniz, and Rene Mercado for their support and friendship. Special thanks go to Dr. Xiongwu Kang, Dr. Yang Song, who helped me get started on the research work as well as life in Santa Cruz, and to Bruce Phebus and Gabriella Jia Lu, who made my days happy.

My thanks also go to the Li lab, Dr. Gongming Wang, Dr. Xihong Lu, Dr. Feng Luan, Dr. Yichuan Ling, Dr. Hanyu Wang, Yi Yang, Tianyu Liu and the Zhang lab, Dr. Jianying Shi, Dr. Bob Fitzmorris, Staci Adams, and to my friends Salina Long, Jeremy Tsang for their companionship. Warm thanks are extended to all my other friends who have been with me.

At last, I would like to thank my family and my boyfriend Chengcheng for their companionship, encouragements, and trust. I cherish everything they have done for me, and I am deeply indebted for their love.

The text of this dissertation includes reprints of the following previously published or subsequently published materials.

Chapter 3: Ke Liu, Xiongwu Kang, Zhi-you Zhou, Yang Song, Lyman Lee, Daniel Tian, Shaowei Chen, "Platinum Nanoparticles Functionalized with Acetylene Derivatives: Electronic Conductivity and Electrocatalytic Activity in Oxygen Reduction", *J. Electroanal. Chem.*, **2013**, *688*, 143.

Chapter 4: Guoqiang He†, Yang Song†, Ke Liu† (†co-1st

authors), Andrew Walter, Sophie Chen, Shaowei Chen, "Oxygen Reduction Catalyzed by Platinum Nanoparticles Supported on Graphene Quantum Dots", *ACS Catal.*, **2013**, *3*, 831.

Chapter 5: Ke Liu, Yang Song, Shaowei Chen, "Electrocatalytic activities of alkyne-functionalized copper nanoparticles in oxygen reduction in alkaline media", *J. Power Sources*, **2014**, *268*, 469.

Chapter 7: Ke Liu, Yang Song, Shaowei Chen, "Defective TiO_2-supported Cu nanoparticles as efficient and stable electrocatalysts for oxygen reduction in alkaline media", *Nanoscale*, **2015**, *7*, 1224.

Chapter 1

Introduction

1.1 Background

Fuel cells, particularly hydrogen fuel cells, are clean and efficient power sources which can convert chemical energy of hydrogen and oxygen into electricity producing only water as finally product. Driven by the high Gibbs free energy (-273.13 kJ mol^{-1}), the fuel cell reaction is thermodynamically favorable and the energy conversion efficiency of fuel cell is much higher than that of internal combustion engine. Combining its experimental-friendly process, high theoretical energy as well as energy conversion efficiency, fuel cells have the potential to alleviate a series of environmental problems associated with fossil foil based energy production, such as air pollution and green-house emission etc. As electrochemical power sources, fuel cells have wide applications in stationary power plant, automobiles, and portable electronics. For automobile applications, most efforts are focused on polymer electrolyte membrane fuel cells (PEMFC) due to their low operation-temperatures, short start-up and transient-response times[1].

However, PEMFCs face two main obstacles on the way to realize large-scale commercialization: cost and lifetime. One significant portion of cost on PEMFCs arises from expensive anode and cathode catalysts most of which are based on Pt nanoparticles dispersed on carbon black supports, which can contribute to 56% of the cost in fuel cell stack according to a United States Department of Energy's (DOE) study in 2007[2]. Actually for H_2-fed anode electrodes the Pt loading can be as low as 0.05 mg_{Pt}/cm^2 due to excellent activity

towards hydrogen oxidation reactions[3], however the real challenge lies in decreasing current Pt loading of ca. 0.4 mg_{Pt}/cm^2 for the cathode because of complex and sluggish oxygen reduction reactions (ORR) involved[4]. Actually the cathode loadings are desired to be < 0.1 mg_{Pt}/cm^2 and US DOE 2017[5] targets for catalysts aim for a total (anode plus cathode) loading of 0.125 mg_{Pt}/cm^2. If that goal can be realized, each vehicle only needs 8 g of platinum group metals[6] and the cost on catalysts can be significantly reduced.

For automotive applications, durability of fuel cell cathode electrocatalysts is an even more severe challenge. Serious degradation on cathode catalysts is possible during long-term operation considering platinum-particle dissolution and sintering, carbon-support corrosion and membrane thinning[7]. Even during the short times when H_2/air waves move through the flow fields during start-up or shut-down[8], there is still high tendency that the carbon supports are oxidized when the cathode reach high enough potentials. State-of-the-art catalysts can be durable for 2,500 h's operation, however DOE 2017 targets to extend that time to 5,000 h[9] including hundreds of thousands of load cycles and tens of thousands of start-up and shut-down events.

1.2 Oxygen Reduction Reactions (ORR)

Oxygen reduction reaction (ORR) plays a very important role in advanced electrochemical energy conversion devices, such as fuel cells and metal-air batteries[10]. With kinetics of the cathode ORR six or more orders of magnitude slower than that of anode hydrogen oxidation reactions, it is crucial to improve

activities of cathode catalysts based on the understanding of the ORR catalytic mechanism.

Although the understanding of the ORR mechanism at the atomic-level is in early stage, it is well known that each oxygen molecules require four net coupled proton and electron transfers to be reduced to water completely, among which several elementary steps are involved. The oxygen molecules can be directly reduced to water (in acidic solution) or to OH- (in alkaline solutions) via a favored four-electron pathway; another pathway is the low-efficient two-electron pathway which partially reduces oxygen molecules to hydrogen peroxide; more complex pathway is also possible when the two-electron and four-electron pathways proceed in series or parallel.

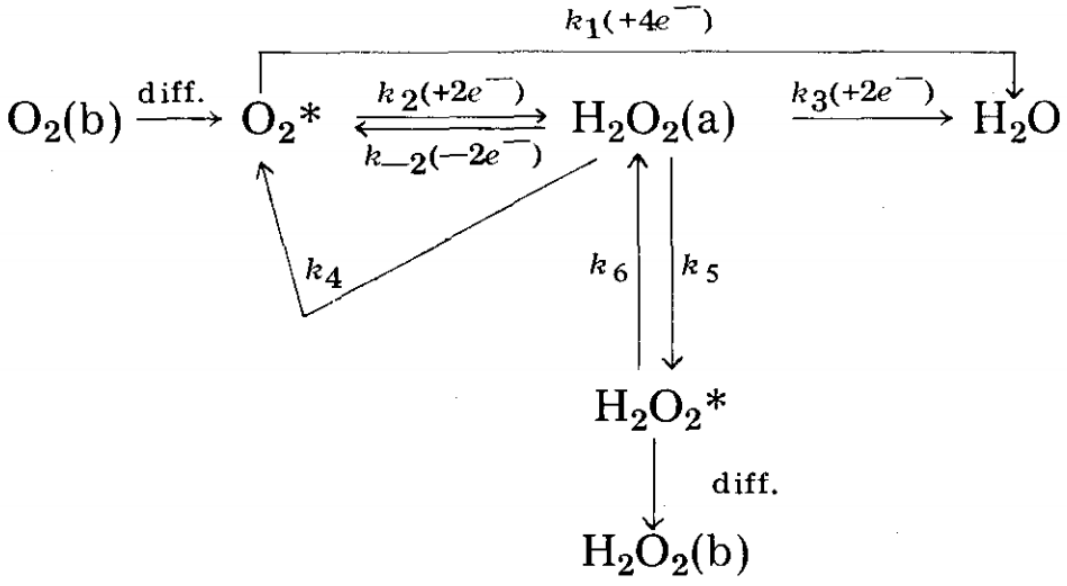


Figure 1.2.1 General scheme of possible oxygen reduction reaction pathways. Reprinted with permission from *J. Electroanal. Chem*.(1976, 69, 195-201). Copyright ©1976 Elsevier Sequoia S.A., Lausanne.

Following those branched ORR pathways above, several different intermediates can be formed, including O*, HO* and HOO* (where O*, HO* and HOO* are oxygen, hydroxyl, and superhydroxyl groups adsorbed on active sites)[11]. Those adsorbed oxygenated species are suggested to be the crucial step of ORR and decisive process for determining the catalyst performance[12]. Yet those intermediates make it challenging to elucidate the reaction mechanisms experimentally since they could not be easily probed in situ[13]. Some studies show that adsorption energies of the oxygenated species are proportional to each other[14], which stems from a more universal correlation between the adsorption energies of any adsorbates bound similarly to a surface[15]. Especially taking consideration that those oxygenated species bind to the surface via the oxygen atom[16], a surface that binds O* strongly is also expected to bind HO* and HOO* strongly.

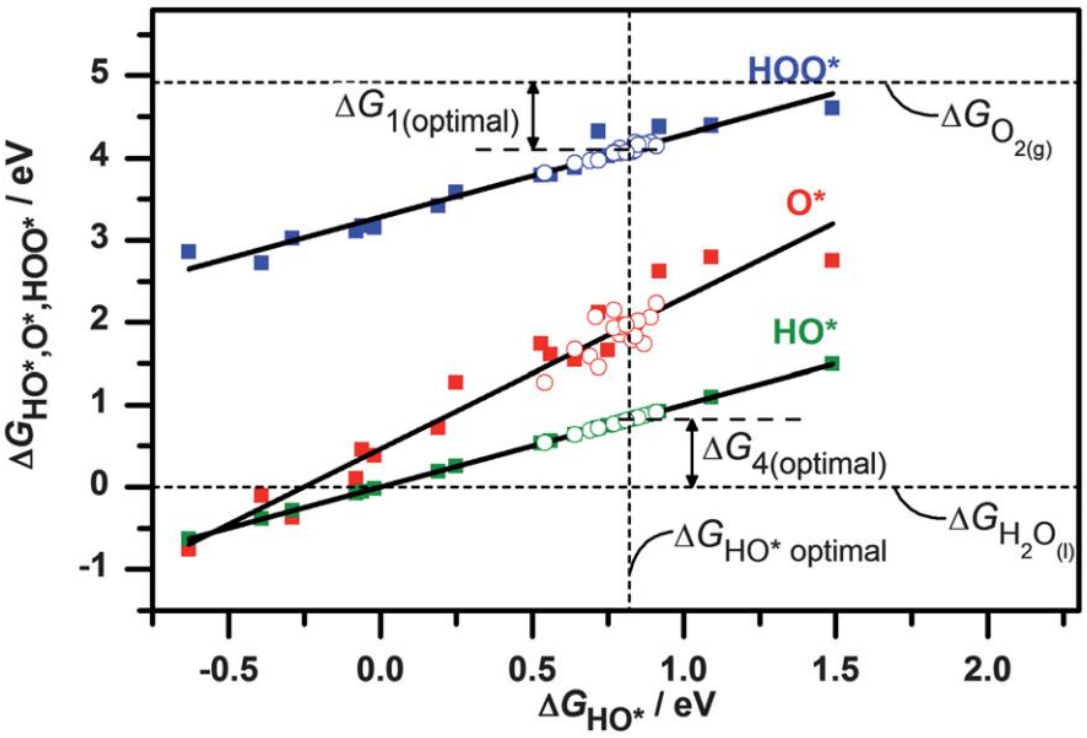


Figure 1.2.2 Theoretical plot of free energies of adsorption of OOH*, OH* and O*, ΔG_{OOH*}, ΔG_{OH*} and ΔG_{O*}, respectively, as a function of ΔG_{OH*} for (111), (100) and (211) pure metal surfaces (shown with filled squares),[14a, 16] as well as Pt overlayers on Pt-alloy surfaces (shown with open circles).[17] Reprinted with permission from *Energy. Environ. Sci*. (2012, 5, 6744-6762). Copyright © 2012 Royal Society of Chemistry.

Such scaling relationship makes it possible to consider only one oxygenated specie's adsorption energy to determine the catalytic trends. DFT calculations were conducted to obtain oxygen binding energy for a number of interesting metals and a volcano shape[12a] appeared which showed that Pt and Pd are the best catalysts for ORR, although the two metals fall on the left side of the volcano shape and there was some room for activity improvements. As shown by Figure 1.2.3, metals fall on the left side bind oxygen too strongly, the rate of which depends on the removal of adsorbed O and OH species; metals lying on the right side bind oxygen too weakly, and the transfer of electrons and proton to adsorbed O_2 is the rate-determining step[18]. The volcano plot indicates that there was some room for improvement on ORR activities of Pt-based catalysts, and the catalyst which binds oxygen more weakly than Pt by about 0.2 eV should behave better in oxygen reduction reactions. Furthermore, a microkinetic model was developed for ORR by calculating the activity on materials with a varying OH binding energy[19], and similar volcano shape was found which is consistent with the previous volcano plot and scaling relationship between different oxygenated species. Actually over 100 years ago Sabatier already proposed that the optimal catalyst for a given reaction is the one which exhibits intermediate binding to its intermediates[20], and the volcano plot is widely used in both gas-phase heterogeneous catalysis and electrocatalysis.[12a, 14b, 21]

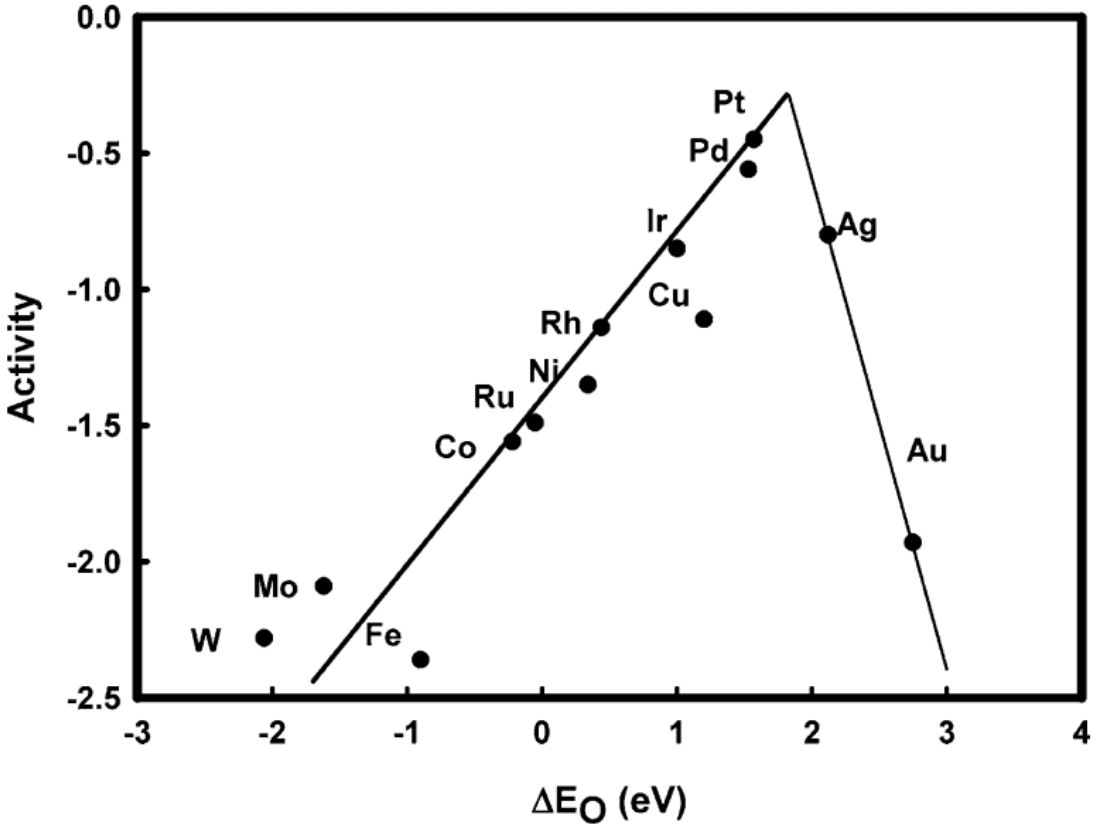


Figure 1.2.3 Trends in oxygen reduction activity plotted as a function of the oxygen binding energy. Reprinted with permission from *J. Phys. Chem. B* (2004, 108, 17886-17892). Copyright © 2004, American Chemical Society.

1.3 Activity of Pt cathode catalysts

As stated in previous section, platinum nanoparticles are mostly used cathode materials for sluggish oxygen reduction reactions[22]. However the high price and limited reserve of Pt hinder its extensive application, and lead efforts spent in developing Pt-based catalysts with improved mass activity which can result in decreased usage on Pt and lower cost. Manipulating surface electronic structure of Pt can induce changes in adsorption behavior of reaction intermediates, specifically a shift of surface-oxide formation to higher potentials[23], which is believed to be beneficial for the high ORR activity[24].

1.3.1 facet-controlled Pt nanocrystals

Ways to manipulate electronic structure of Pt are various and synthesizing facet-controlled Pt nanocrystals is one promising route, since studies of single-crystal Pt electrodes revealed dependence of ORR activities on different crystal facets[25]. For example, ORR activity of Pt (+0.9 V vs RHE) in 0.1 M $HClO_4$ decreases in this order: 110 > 111 > 100[26], while different trends in H_2SO_4 (110 > 100 > 111) and KOH (111 > 110 > 100)[27]. When extended to nanoparticulate form, improved activities over commercial Pt catalysts were observed, such as (100)-terminated Pt nanocubes by Sun[28] *et al*. Although there are both experimental and theoretical evidence that undercoordinated sites are inactive for ORR on Pt[10c, 29] because those open facets (steps, edges and kinks) are believed to bind adsorbates such as HO* more strongly, Pt nanocrystals with high-index facets, such as (730), (210), and (520) by applying a square-wave potential to

polycrystalline Pt microspheres[30] or Pt concave nanocubes with (510), (720), and (830) by simple reduction method[31], show enhanced ORR activity per unit surface area compared with those bounded by low-index planes such as (100) and (111). Currently mechanisms of such counter-intuitive observations are not clear, and the steps or other undercoordinated sites are found meaningless for ORR activity of Pt nanoparticles[16, 32].

1.3.2. Alloying Pt with transition metals

Alloying Pt with less noble *solute* metal, *e.g.* Co, Ni, Fe, Cu or Y, is an effective way to manipulate surface electronic properties of platinum and thus oxygen adsorption properties. Vast majority of research has focused on Pt and its alloys, due to very acidic and oxidizing operation conditions of PEM fuel cell under which conditions almost all other metals are unstable. For Pt-alloys based ORR catalysts, the surface layer is almost always composed of pure Pt[23, 33], which can provide kinetic stability against the dissolution of the solute metal. The Pt overlayer catalysts can be fabricated via UPD[34] (under potential deposition), (electro)chemical dealloying/leaching methods or thermal annealing methods. The leached structure was denoted as a "Pt-skeleton" surface[33d] which was first reported by Watanabe and co-workers and then by other following groups[23, 33b, 35]. The surface of the "Pt-skeleton" structure is atomically rough and composed of Pt atoms with low/no lateral coordination, and such structures maintain good ORR activities if the Pt shell is thin enough. On the other hand, the annealed structure was denoted as a "Pt-skin" surface. Driven by the lower surface energy

of Pt relative to the solute metal, an order surface can be formed with segregation of a pure Pt atomic layer on top of the solute metal in the second layer[36]. For both Pt-skin and Pt-skeleton surfaces two effects are involved, ligand effects and strain effects[37], which can modify the electronic structure of the Pt overlayer to weaken the binding strength of reaction intermediates[12b]. Ligand effects work as the electronic of the Pt surface atoms is modified by solute metal atoms of a different composition in the second atomic layer, while strain effects occur when Pt overlayer is compressed laterally. In most cases, it's difficult to distinguish relative contributions of the two effects because they usually occur in parallel. However it's clear that they both can modify the surface electronic properties of the platinum and corresponding different chemisorption properties.

1.3.3 Modifying surfaces of Pt with foreign species

Apart from controlling exposed facets of Pt nanocrystals or alloying Pt with transition metals, modify surfaces of Pt with selected foreign species[38], such as molecules, ions, organic or inorganic compounds can also benefit their ORR activities. Zhang[39] modified Pt nanoparticles with Au clusters where activity and surface area of Pt were well maintained under harsh fuel cell work environment possibly due to raised oxidation potential of Pt via Au clusters. Organic ligands are widely used in synthesis of metal nanoparticles to control particle size, structure and stability[40], although many approaches such as UV-ozone[41], plasma[42], potential cycling[43], calcination[44] and chemical treatment[45] have been applied to remove those surfactants so that the surface of catalysts is "clean".

However some studies showed that modifying surfaces of metal with selective ligands can tune the selectivity of electrocatalysts or block the adsorption of poisoning species or tune the bonding interactions with respective reactants. For example, Markovic[46] modified platinum with calix[4]arene molecules and such catalysts exhibited high selectivity towards hydrogen oxidation reaction while suppressed oxygen reduction reaction meantime. The same group also developed cyanide-modified Pt(111) as ORR catalysts[47], where the electrostatic repulsive interactions between electronegative CN_{ad} adlayer and the negative SO_4^{2-} or PO_4^{3-} lead to suppressed adsorption of existent anions, and thus showed a 25-/10-fold increase in H_2SO_4/H_3PO_4 electrolytes compared with unmodified surfaces. Modification of electrode surfaces with aryl groups via reduction of diazonium salts has been studied extensively[48] providing a unique structural framework for fundamental studies of catalysis, and recently this strategy has been extended to metal nanoparticles. Zhou[49] synthesized chlorophenyl-stabilized platinum nanoparticles by co-reduction of H_2PtCl_4 and 4-chlorophenyl diazonium, and the Pt-ArCl nanoparticles exhibited an ORR mass activity up to 2.8 times higher than that of "naked" commercial Pt/C catalysts. Such enhanced catalytic activity was suggested to be correlated with the impeded adsorption of oxygenate species on the Pt surfaces, although the exact fundamental mechanism is not clear. Studies of the impacts of the electron-withdrawing capability of substituents on ORR were also conducted[50] by stabilizing Pt nanoparticles with para-substituted (R= -CF_3, -F, -Cl, -OCF_3 and –CF_3) phenyl groups. It's demonstrated that the electron-

withdrawing capability of the substituents (manifested by the Hammet substituent constant σ) correlates with the ORR activity, and the higher σ usually means higher ORR activity. It's also suggested that the electronegative ligands can weaken the oxygen adsorption energy and thus improve the catalytic activity.

1.3.4 Strong metal-support interactions

Carbon black is most commonly used support for ORR catalysts[51], however carbon is easy to be oxidized at high electrode potentials and Pt particles can be de-attached from the carbon support leading to activity losses[52]. What's more, the interactions between carbon and metal nanoparticles are not sufficient to stabilize the overall structure, which may lead to migration and aggregation of supported metal particles during long-term operation[53]. Carbon materials with a higher graphitic character, such as carbon nanofibers, nanotubes, nanohorns, and graphenes, can better resist the high oxidizing potentials[54] and wealthy π sites on graphitized carbon surface can interact strongly with metal particles stabilizing the whole structure. On the other hand, research efforts have also been directed to support Pt nanoparticles with non-carbonaceous and more stable materials, such as TiO_2[55], TiC[56], ITO[57], RuO_2-SiO_2[58], WC[59], WO_x[60], and TaB_2[61], where the strong metal-support interactions (SMSI) can tune the electronic states of the Pt nanoparticles and hence affect the activity and stability[62].

1.4 Stability

Compared with the probably limited enhancements in ORR activity, the long-term stability of catalysts is equally important or even more urgent and their

degradation limits the useful lifetime of a PEMFC[63]. As to the nanostructured Pt-based catalysts, they can undergo dissolution of Pt following which Pt tends to redeposit on larger nanoparticles via the Ostwald ripening mechanism[64] or in the membrane, as well as the corrosion of the carbon support at high potentials which can lead to detachment of Pt nanoparticles or loss of electrical contact[65]. In summary, dissolution of platinum and carbon corrosion are two primary degradation processes, where the former is the precondition for secondary degradation phenomena such as Ostwald ripening or platinum deposition in the ionomer and the latter can be the cause for secondary processes such as platinum particle detachment or agglomeration[66].

1.4.1 Platinum dissolution

Platinum dissolution can occur on nanoparticulate or extended platinum surface, and it seems to be more significant on small nanoparticles[67]. The dissolution potential of bulk Pt is above ~1 V. Compared with bulk Pt, the average cohesive energy of a Pt atom in a nanoparticle is lower[68], and the dissolution potential of a nanoparticle will decrease following a shrinked size[69]. Moreover, the Pt dissolution is enhanced at high potentials[70] during potential cycling, such as during the start-up and shut down of a fuel cell[52b]. There are also debates on whether the dissolution of Pt occurs directly from the metallic phase[1] as shown below,

$$Pt \rightarrow Pt^{2+} + 2e^{-} \qquad (1.4.1)$$

or includes the formation of platinum oxides followed by its subsequent chemical

dissolution or reduction[71] like indicated below,

$$Pt + xH_2O \rightarrow PtO_x + 2xH^+ + 2xe^- \quad (1.4.2)$$

$$PtO_x + 2xH^+ \rightarrow Pt^{2x+} + xH_2O \quad (1.4.3)$$

$$PtO_2 + 4H^+ + 2e^- \rightarrow Pt^{2+} + 2H_2O \quad (1.4.4)$$

However, some recent studies shed light in distinguishing the corrosion of platinum during an anodic and a cathodic process and suggest that platinum dissolution is associated with formation of platinum oxides and subsequent reduction or the opposite direction[68b, 72]. First, surface roughening was observed where an initially ordered Pt terrace becomes corrugated after a few cycles between 0.05 V and 1.5 V[73], and it's further suggested that the first step in the roughening process occurs at anodic potentials where subsurface oxides form[74]. When it approaches to cathodic potentials, the Pt terraces become more corrugated where subsurface oxides are suggested to be reduced with Pt atoms destabilized, and the corrugation continues with roughening and growth of step edges upon repeated cycling between 0.1 and 1.3 V. Evidence for subsurface oxide formation on Pt was provided based on electrochemical measurements[75], and X-Ray absorption spectroscopy (XAS) also offer more direct evidence for it[76]. To sum up, surface roughening and subsurface oxide formation play significant roles in the dissolution of Pt, and corresponding efforts should be spent in alleviating those processes.

1.4.2 Ostwald ripening

Apart from re-deposition in the membrane of PEMFCs due to reduction

by permeated hydrogen[77], the dissolved platinum species are also readily deposited on larger particles driven by the tendency of reduced surface energy. That significant particle growth and according degradation mechanism is the Ostwald ripening, during which small particles shrink while large particles become even larger. There are two types of Ostwald ripening, including 3D Ostwald ripening[78] where the dissolved platinum species travel through the electrolyte prior to reduction and deposition and 2D Ostwald ripening if platinum atoms are believed to diffuse along the carbon support[79].

1.4.3 Agglomeration

Another possible reason for increased size of platinum nanoparticles in the catalyst layer is their strong tendency of agglomeration, which decrease utilization of platinum as regards to the mass. First, the original neighboring particles after synthesis may coalesce immediately driven by potential of reduced surface energy[80]. On the other hand, original separated particles may migrate over the support and come into contact with other particles, forming large agglomerated particles. In that case, the closer the interparticle distance is, the higher probability of the agglomeration is, which means higher particle density or higher platinum content[52c, 65, 81] increase the probability of agglomeration. What's more, the adjacent particles may coalesce with each other due to shrinkage of the carbon support during corrosion process of carbon and thus weakened interactions between platinum and carbon support[82].

1.4.4 Corrosion of carbon support

Apart from the dissolution of platinum, carbon corrosion is another primary degradation process which can result in detachment of platinum particles and agglomeration of adjacent particles. Thermodynamically carbon can be oxidized to CO_2 above +0.207 V vs RHE[83], while from the kinetics perspective that oxidation process can occur when higher than +1.2 V vs RHE[84]. At elevated temperatures it's suggested that the corrosion of carbon can be initiated by the corrosion of disordered carbon sites in the core of the carbon particles[85], and resulting shrinked structure has been recently observed in electrochemical studies[86]. At room temperature, harsh potential conditions can result in severe carbon corrosion and thus lead to shrinkage of the support structure similarly[87]. To alleviate that carbon corrosion issue, one possible approach is to strengthen the metal-carbon interactions via introducing carbon structures with higher sp^2 carbon content, such as graphene[88], multi-walled carbon nanotubes[89], ordered mesoporous or nanoporous carbons[90], activated carbon nanofibers[91], hollow graphitic spheres[92], and carbon aerogels[93], and superior stability was observed. Another possible solution is to utilize transition metal oxides as supports such as TiO_2, WO_3, NbO_2, and TaO_2[94], which is well known for stability under harsh conditions, low cost and abundance, yet their low electronic conductivity needs to be increased either via introducing oxygen vacancies or doping elements. Alternatively, some commercial catalyst manufactures, for example 3M, has developed nanostructured thin film catalysts where a Pt thin film is deposited on

nanostructured non-conducting whiskers[95]. Such platinum nanostructures have a mass activity comparable to the conventional commercial catalysts but much higher stability.

1.4.5 Particle detachment

As stated in previous section, carbon corrosion can lead to a weakening of the interactions between particles and support, and such weakening of the particle-support interaction can initiate particle detachment as well as agglomeration which usually occur in parallel after carbon corrosion[96]. The complete loss of platinum particles originating from the particle detachment has been visualized by electron microscopy[97]. Also severe carbon corrosion can impair the structural integrity of the catalyst layer, and reduce the porosity resulting in mass transport limitations for the reactants[98].

1.5 Dissertation Outline

The dissertation research described herein primarily focuses on developing efficient catalysts for oxygen reduction reactions (ORR), where one direction is to improve catalytic activities of Pt-based nanoparticles via ligand functionalization and the other direction is to develop inexpensive Cu-based nanomaterials as efficient ORR catalysts. As-prepared Pt nanoparticles or Cu-based nanomaterials will be characterized by microscopy techniques such as transmission electron microscopy (TEM), spectroscopic techniques like UV-Vis, photoluminescence, ^{1}H nuclear magnetic resonance (NMR), FT-infrared, Raman spectroscopy, and X-ray photoelectron spectroscopy (XPS) and electrochemical

techniques for instance cyclic voltammetry (CV), electrochemical impedance spectroscopy (EIS), and rotating ring-disk electrode (RRDE) technique.

Within the context of developing nanostructured materials as efficient ORR catalysts, the rest of the dissertation consists of the following chapters:

In chapter 2, experimental details such as the chemicals used, the methods of nanoparticle synthesis, and characterization of electrochemical properties will be included.

In chapter 3, synthesis of platinum nanoparticles functionalized with acetylene derivatives will be reported. FTIR measurements and photoluminescence spectroscopy will be conducted to investigate adsorption of the acetylene ligands onto the Pt nanoparticle surface and intraparticle charge delocalization between the acetylene moieties as well. Electrocatalytic activities of those nanoparticulate catalysts will be evaluated, and compared with that of commercial Pt/C catalysts to see the effects of ligand functionalization.

In chapter 4, nanosized graphene quantum dots were prepared by acid etching of carbon fibers and used to support platinum nanoparticles via thermolytic reduction of platinum chloride in ethylene glycol. ORR activity of the Pt/G nanocomposites will be evaluated and compared with that of commercial Pt/C.

In chapter 5, stable alkyne-capped copper nanoparticles were prepared by chemical reduction of copper acetate with sodium borohydride in the presence of alkyne ligands. FTIR and photoluminescence spectroscopic measurements will

be used to evaluate the successful attachment of the alkyne ligands onto the nanoparticle surface, and oxidation degree of alkyne-capped copper nanoparticle surfaces will be detected by XPS measurements. Electrochemical performance of the alkyne-capped copper nanoparticles will be studied also.

In chapter 6, graphene quantum dots were introduced to support copper nanoparticles and the surface defect concentrations of different Cu/GQD nanocomposites will be quantified by XPS measurements. Electrochemical techniques will be utilized to compare the catalytic activities of the Cu/GQD nanocomposites before and after careful tuning surface defect concentrations via hydrothermal treatments.

In chapter 7, TiO_2-supported copper nanoparticles were prepared by a hydrothermal method where copper nanoparticles with or without the passivation of 1-decyne were chemically grown onto TiO_2 surfaces (denoted as CuHC10/TiO_2 and Cu/TiO_2 respectively). XPS measurements will be conducted to confirm anticipated strong metal-support interactions, and electrochemical performance of both samples will be compared with that of TiO_2 nanocolloids and other non-Pt catalysts reported in the literature.

1.6 Reference

1. Borup, R.; Meyers, J.; Pivovar, B.; Kim, Y. S.; Mukundan, R.; Garland, N.; Myers, D.; Wilson, M.; Garzon, F.; Wood, D.; Zelenay, P.; More, K.; Stroh, K.; Zawodzinski, T.; Boncella, J.; McGrath, J. E.; Inaba, M.; Miyatake, K.; Hori, M.; Ota, K.; Ogumi, Z.; Miyata, S.; Nishikata, A.; Siroma, Z.; Uchimoto, Y.; Yasuda, K.; Kimijima, K. I.; Iwashita, N., Scientific aspects of polymer electrolyte fuel cell durability and degradation. *Chem Rev* **2007,** *107* (10), 3904-3951.

2. (a) James, B. K., J. DOE-EERE Fuel Cell Technologies Program-2009 DOE Hydrogen Program Review. www.hydrogen.energy.gov/pdfs/review09/fc_30_james.pdf ; (b) Sinha, J. L., S.; Yang, Y., DOE-EERE-Fuel Cell Technologies Program-2009 DOE Hydrogen Program Review.

3. (a) Gasteiger, H. A.; Panels, J. E.; Yan, S. G., Dependence of PEM fuel cell performance on catalyst loading. *J Power Sources* **2004,** *127* (1-2), 162-171; (b) Markovic, N. M., The hydrogen electrode reaction and the electrooxidation of CO and H_2/CO mixtures on well-characterized Pt and Pt-bimetallic surfaces. In *Handbook of Fuel Cells-Fundamentals, Technology and Applications*, Vielstich, W. G., H.; Lamm, A., Ed. Wiley: Chichester, UK, 2003; Vol. 2, p 368.

4. Gasteiger, H. A. G., W.; Makharia, R.; Mathias, M.F.; Sompalli, B., Begining-of-life MEA performance: efficiency loss contributions. In *Handbook of Fuel Cells-Fundamentals, Technology and Applications*, Vielstich, W. G., H.A.; Lamm, A., Ed. Wiley: Chichester, UK, 2003; Vol. 3, p 593.

5. (DOE), T. U. D. o. E. Energy Efficiency and Renewable Energy. http://www.eere.energy.gov/hydrogenandfuelcells/mypp/pdfs/fuel_cells.pdf

6. Debe, M. K., Electrocatalyst approaches and challenges for automotive fuel cells. *Nature* **2012,** *486* (7401), 43-51.

7. (a) Chalk, S. G.; Miller, J. E., Key challenges and recent progress in batteries, fuel cells, and hydrogen storage for clean energy systems. *J Power Sources* **2006,** *159* (1), 73-80; (b) Wilson, M. S.; Garzon, F. H.; Sickafus, K. E.; Gottesfeld, S., Surface-Area Loss of Supported Platinum in Polymer Electrolyte Fuel-Cells. *J Electrochem Soc* **1993,** *140* (10), 2872-2877; (c) Fowler, M. M., R.F.; Amphlett, J.C.; Peppley, B.A.; Roberge, P.R., In *Handbook of Fuel Cells: Fundamentals, Technology and Applications*, Vielstich, W. G., H.A.; Lamm, A., Ed. Wiley: Chichester, UK, 2003; Vol. 3, p 663.

8. Reiser, C. A.; Bregoli, L.; Patterson, T. W.; Yi, J. S.; Yang, J. D. L.; Perry, M. L.; Jarvi, T. D., A reverse-current decay mechanism for fuel cells. *Electrochem*

Solid St **2005,** *8* (6), A273-A276.

9. (a) Wipke, K. Controlled Hydrogen Fleet and Infrastructure Analysis: 2011 DOE Hydrogen Program Annual Merit Review and Peer Evaluation Meeting. http://www.hydrogen.energy.gov/pdfs/review11/tv001_wipke_2011_o.pdf; (b) (DOE), T. U. D. o. E. The US DRIVE Fuel Cell Technical Team Technology Roadmap. http://www.uscar.org/guest/teams/17/Fuel-Cell-Tech-Team.

10.(a) Bruce, P. G.; Freunberger, S. A.; Hardwick, L. J.; Tarascon, J. M., Li-O-2 and Li-S batteries with high energy storage (vol 11, pg 19, 2012). *Nat Mater* **2012,** *11* (2); (b) Wagner, F. T.; Lakshmanan, B.; Mathias, M. F., Electrochemistry and the Future of the Automobile. *J Phys Chem Lett* **2010,** *1* (14), 2204-2219; (c) Gasteiger, H. A.; Kocha, S. S.; Sompalli, B.; Wagner, F. T., Activity benchmarks and requirements for Pt, Pt-alloy, and non-Pt oxygen reduction catalysts for PEMFCs. *Appl Catal B-Environ* **2005,** *56* (1-2), 9-35; (d) Yu, W. T.; Porosoff, M. D.; Chen, J. G. G., Review of Pt-Based Bimetallic Catalysis: From Model Surfaces to Supported Catalysts. *Chem Rev* **2012,** *112* (11), 5780-5817.

11.(a) Katsounaros, I.; Cherevko, S.; Zeradjanin, A. R.; Mayrhofer, K. J. J., Oxygen Electrochemistry as a Cornerstone for Sustainable Energy Conversion. *Angew Chem Int Edit* **2014,** *53* (1), 102-121; (b) Stephens, I. E. L.; Bondarenko, A. S.; Gronbjerg, U.; Rossmeisl, J.; Chorkendorff, I., Understanding the electrocatalysis of oxygen reduction on platinum and its alloys. *Energ Environ Sci* **2012,** *5* (5), 6744-6762.

12.(a) Norskov, J. K.; Rossmeisl, J.; Logadottir, A.; Lindqvist, L.; Kitchin, J. R.; Bligaard, T.; Jonsson, H., Origin of the overpotential for oxygen reduction at a fuel-cell cathode. *J Phys Chem B* **2004,** *108* (46), 17886-17892; (b) Stamenkovic, V.; Mun, B. S.; Mayrhofer, K. J. J.; Ross, P. N.; Markovic, N. M.; Rossmeisl, J.; Greeley, J.; Norskov, J. K., Changing the activity of electrocatalysts for oxygen reduction by tuning the surface electronic structure. *Angew Chem Int Edit* **2006,** *45* (18), 2897-2901; (c) Tripkovic, V.; Skulason, E.; Siahrostami, S.; Norskov, J. K.; Rossmeisl, J., The oxygen reduction reaction mechanism on Pt(111) from density functional theory calculations. *Electrochim Acta* **2010,** *55* (27), 7975-7981.

13.(a) Gewirth, A. A.; Thorum, M. S., Electroreduction of Dioxygen for Fuel-Cell Applications: Materials and Challenges. *Inorg Chem* **2010,** *49* (8), 3557-3566; (b) Bondarenko, A. S.; Stephens, I. E. L.; Hansen, H. A.; Perez-Alonso, F. J.; Tripkovic, V.; Johansson, T. P.; Rossmeisl, J.; Norskov, J. K.; Chorkendorff, I., The Pt(111)/Electrolyte Interface under Oxygen Reduction Reaction Conditions: An Electrochemical Impedance Spectroscopy Study. *Langmuir* **2011,** *27* (5), 2058-2066.

14.(a) Rossmeisl, J.; Logadottir, A.; Norskov, J. K., Electrolysis of water on (oxidized) metal surfaces. *Chem Phys* **2005,** *319* (1-3), 178-184; (b) Man, I. C.; Su, H. Y.; Calle-Vallejo, F.; Hansen, H. A.; Martinez, J. I.; Inoglu, N. G.; Kitchin, J.; Jaramillo, T. F.; Norskov, J. K.; Rossmeisl, J., Universality in Oxygen Evolution Electrocatalysis on Oxide Surfaces. *Chemcatchem* **2011,** *3* (7), 1159-1165.

15.(a) Calle-Vallejo, F.; Martinez, J. I.; Garcia-Lastra, J. M.; Rossmeisl, J.; Koper, M. T. M., Physical and Chemical Nature of the Scaling Relations between Adsorption Energies of Atoms on Metal Surfaces. *Phys Rev Lett* **2012,** *108* (11); (b) Fernandez, E. M.; Moses, P. G.; Toftelund, A.; Hansen, H. A.; Martinez, J. I.; Abild-Pedersen, F.; Kleis, J.; Hinnemann, B.; Rossmeisl, J.; Bligaard, T.; Norskov, J. K., Scaling relationships for adsorption energies on transition metal oxide, sulfide, and nitride surfaces. *Angew Chem Int Edit* **2008,** *47* (25), 4683-4686.

16.Greeley, J.; Rossmeisl, J.; Hellman, A.; Norskov, J. K., Theoretical trends in particle size effects for the oxygen reduction reaction. *Z Phys Chem* **2007,** *221* (9-10), 1209-1220.

17.Hansen, H. A. PhD thesis, Technical University of Denmark, 2009.

18.Nie, Y.; Li, L.; Wei, Z. D., Recent advancements in Pt and Pt-free catalysts for oxygen reduction reaction. *Chem Soc Rev* **2015,** *44* (8), 2168-2201.

19.(a) Viswanathan, V.; Hansen, H. A.; Rossmeisl, J.; Norskov, J. K., Unifying the 2e(-) and 4e(-) Reduction of Oxygen on Metal Surfaces. *J Phys Chem Lett* **2012,** *3* (20), 2948-2951; (b) Hansen, H. A.; Viswanathan, V.; Norskov, J. K., Unifying Kinetic and Thermodynamic Analysis of 2 e(-) and 4 e(-) Reduction of Oxygen on Metal Surfaces. *J Phys Chem C* **2014,** *118* (13), 6706-6718.

20.Sabatier, P., Announcement. Hydrogenation and dehydrogenation for catalysis. *Ber Dtsch Chem Ges* **1911,** *44*, 1984-2001.

21.(a) Grabow, L. C.; Mavrikakis, M., Nanocatalysis beyond the Gold-Rush Era. *Angew Chem Int Edit* **2008,** *47* (39), 7390-7392; (b) Norskov, J. K.; Bligaard, T.; Rossmeisl, J.; Christensen, C. H., Towards the computational design of solid catalysts. *Nat Chem* **2009,** *1* (1), 37-46; (c) Hansgen, D. A.; Vlachos, D. G.; Chen, J. G. G., Using first principles to predict bimetallic catalysts for the ammonia decomposition reaction. *Nat Chem* **2010,** *2* (6), 484-489; (d) Neurock, M., Engineering Molecular Transformations for Sustainable Energy Conversion. *Ind Eng Chem Res* **2010,** *49* (21), 10183-10199; (e) Parsons, R., The Rate of Electrolytic Hydrogen Evolution and the Heat of Adsorption of Hydrogen. *T Faraday Soc* **1958,** *54* (7), 1053-1063; (f) Trasatti, S., Work Function, Electronegativity, and Electrochemical Behavior of Metals .3. Electrolytic

Hydrogen Evolution in Acid Solutions. *J Electroanal Chem* **1972,** *39* (1), 163-&; (g) Greeley, J.; Stephens, I. E. L.; Bondarenko, A. S.; Johansson, T. P.; Hansen, H. A.; Jaramillo, T. F.; Rossmeisl, J.; Chorkendorff, I.; Norskov, J. K., Alloys of platinum and early transition metals as oxygen reduction electrocatalysts. *Nat Chem* **2009,** *1* (7), 552-556; (h) Norskov, J. K.; Bligaard, T.; Logadottir, A.; Kitchin, J. R.; Chen, J. G.; Pandelov, S.; Norskov, J. K., Trends in the exchange current for hydrogen evolution. *J Electrochem Soc* **2005,** *152* (3), J23-J26; (i) Logadottir, A.; Rod, T. H.; Norskov, J. K.; Hammer, B.; Dahl, S.; Jacobsen, C. J. H., The Bronsted-Evans-Polanyi relation and the volcano plot for ammonia synthesis over transition metal catalysts. *J Catal* **2001,** *197* (2), 229-231; (j) Bligaard, T.; Norskov, J. K.; Dahl, S.; Matthiesen, J.; Christensen, C. H.; Sehested, J., The Bronsted-Evans-Polanyi relation and the volcano curve in heterogeneous catalysis. *J Catal* **2004,** *224* (1), 206-217; (k) Ferrin, P.; Nilekar, A. U.; Greeley, J.; Mavrikakis, M.; Rossmeisl, J., Reactivity descriptors for direct methanol fuel cell anode catalysts. *Surf Sci* **2008,** *602* (21), 3424-3431.

22.Markovic, N. M.; Ross, P. N., Surface science studies of model fuel cell electrocatalysts. *Surf Sci Rep* **2002,** *45* (4-6), 121-229.

23.Strasser, P.; Koh, S.; Anniyev, T.; Greeley, J.; More, K.; Yu, C. F.; Liu, Z. C.; Kaya, S.; Nordlund, D.; Ogasawara, H.; Toney, M. F.; Nilsson, A., Lattice-strain control of the activity in dealloyed core-shell fuel cell catalysts. *Nat Chem* **2010,** *2* (6), 454-460.

24.Kitchin, J. R.; Norskov, J. K.; Barteau, M. A.; Chen, J. G., Modification of the surface electronic and chemical properties of Pt(111) by subsurface 3d transition metals. *J Chem Phys* **2004,** *120* (21), 10240-10246.

25.(a) Markovic, N. M.; Adzic, R. R.; Cahan, B. D.; Yeager, E. B., Structural Effects in Electrocatalysis - Oxygen Reduction on Platinum Low-Index Single-Crystal Surfaces in Perchloric-Acid Solutions. *J Electroanal Chem* **1994,** *377* (1-2), 249-259; (b) Macia, M. D.; Campina, J. M.; Herrero, E.; Feliu, J. M., On the kinetics of oxygen reduction on platinum stepped surfaces in acidic media. *J Electroanal Chem* **2004,** *564* (1-2), 141-150; (c) Kuzume, A.; Herrero, E.; Feliu, J. M., Oxygen reduction on stepped platinum surfaces in acidic media. *J Electroanal Chem* **2007,** *599* (2), 333-343; (d) Cahan, B. D.; Villullas, H. M., The Hanging Meniscus Rotating-Disk (Hmrd). *J Electroanal Chem* **1991,** *307* (1-2), 263-268; (e) Abe, T.; Swain, G. M.; Sashikata, K.; Itaya, K., Effect of Underpotential Deposition (Upd) of Copper on Oxygen Reduction at Pt(111) Surfaces. *J Electroanal Chem* **1995,** *382* (1-2), 73-83; (f) Hoshi, N.; Nakamura, M.; Hitotsuyanagi, A., Active sites for the oxygen reduction reaction on the high index planes of Pt. *Electrochim Acta* **2013,** *112*, 899-904; (g) Hitotsuyanagi, A.; Nakamura, M.; Hoshi, N., Structural effects on the activity for the oxygen reduction reaction on n(111)-(100) series of Pt: correlation with the oxide film

formation. *Electrochim Acta* **2012,** *82*, 512-516.

26.Strmcnik, D. Active sites for PEM fuel cell reactions in model and real systems. PhD dissertation, Univerza v Ljubljani, 2007.

27.(a) Markovic, N. M.; Gasteiger, H. A.; Ross, P. N., Oxygen Reduction on Platinum Low-Index Single-Crystal Surfaces in Sulfuric-Acid-Solution - Rotating Ring-Pt(Hkl) Disk Studies. *J Phys Chem-Us* **1995,** *99* (11), 3411-3415; (b) Markovic, N. M.; Gasteiger, H. A.; Philip, N., Oxygen reduction on platinum low-index single-crystal surfaces in alkaline solution: Rotating ring disk(Pt(hkl)) studies. *J Phys Chem-Us* **1996,** *100* (16), 6715-6721.

28.(a) Wang, C.; Daimon, H.; Onodera, T.; Koda, T.; Sun, S. H., A general approach to the size- and shape-controlled synthesis of platinum nanoparticles and their catalytic reduction of oxygen. *Angew Chem Int Edit* **2008,** *47* (19), 3588-3591; (b) Wang, C.; Daimon, H.; Lee, Y.; Kim, J.; Sun, S., Synthesis of monodisperse Pt nanocubes and their enhanced catalysis for oxygen reduction. *J Am Chem Soc* **2007,** *129* (22), 6974-+.

29.(a) Mayrhofer, K. J. J.; Strmcnik, D.; Blizanac, B. B.; Stamenkovic, V.; Arenz, M.; Markovic, N. M., Measurement of oxygen reduction activities via the rotating disc electrode method: From Pt model surfaces to carbon-supported high surface area catalysts. *Electrochim Acta* **2008,** *53* (7), 3181-3188; (b) Shao, M. H.; Peles, A.; Shoemaker, K., Electrocatalysis on Platinum Nanoparticles: Particle Size Effect on Oxygen Reduction Reaction Activity. *Nano Lett* **2011,** *11* (9), 3714-3719; (c) Nesselberger, M.; Ashton, S.; Meier, J. C.; Katsounaros, I.; Mayrhofer, K. J. J.; Arenz, M., The Particle Size Effect on the Oxygen Reduction Reaction Activity of Pt Catalysts: Influence of Electrolyte and Relation to Single Crystal Models. *J Am Chem Soc* **2011,** *133* (43), 17428-17433; (d) Yang, Z.; Ball, S.; Condit, D.; Gummalla, M., Systematic Study on the Impact of Pt Particle Size and Operating Conditions on PEMFC Cathode Catalyst Durability. *J Electrochem Soc* **2011,** *158* (11), B1439-B1445.

30.Tian, N.; Zhou, Z. Y.; Sun, S. G.; Ding, Y.; Wang, Z. L., Synthesis of tetrahexahedral platinum nanocrystals with high-index facets and high electro-oxidation activity. *Science* **2007,** *316* (5825), 732-735.

31.Yu, T.; Kim, D. Y.; Zhang, H.; Xia, Y. N., Platinum Concave Nanocubes with High-Index Facets and Their Enhanced Activity for Oxygen Reduction Reaction. *Angew Chem Int Edit* **2011,** *50* (12), 2773-2777.

32.(a) Perez-Alonso, F. J.; McCarthy, D. N.; Nierhoff, A.; Hernandez-Fernandez, P.; Strebel, C.; Stephens, I. E. L.; Nielsen, J. H.; Chorkendorff, I., The Effect of Size on the Oxygen Electroreduction Activity of Mass-Selected Platinum Nanoparticles. *Angew Chem Int Edit* **2012,** *51* (19), 4641-4643; (b) Tritsaris, G.

A.; Greeley, J.; Rossmeisl, J.; Norskov, J. K., Atomic-Scale Modeling of Particle Size Effects for the Oxygen Reduction Reaction on Pt. *Catal Lett* **2011,** *141* (7), 909-913.

33.(a) Stamenkovic, V. R.; Fowler, B.; Mun, B. S.; Wang, G. F.; Ross, P. N.; Lucas, C. A.; Markovic, N. M., Improved oxygen reduction activity on Pt3Ni(111) via increased surface site availability. *Science* **2007,** *315* (5811), 493-497; (b) Toda, T.; Igarashi, H.; Uchida, H.; Watanabe, M., Enhancement of the electroreduction of oxygen on Pt alloys with Fe, Ni, and Co. *J Electrochem Soc* **1999,** *146* (10), 3750-3756; (c) Stephens, I. E. L.; Bondarenko, A. S.; Perez-Alonso, F. J.; Calle-Vallejo, F.; Bech, L.; Johansson, T. P.; Jepsen, A. K.; Frydendal, R.; Knudsen, B. P.; Rossmeisl, J.; Chorkendorff, I., Tuning the Activity of Pt(111) for Oxygen Electroreduction by Subsurface Alloying. *J Am Chem Soc* **2011,** *133* (14), 5485-5491; (d) Stamenkovic, V. R.; Mun, B. S.; Mayrhofer, K. J. J.; Ross, P. N.; Markovic, N. M., Effect of surface composition on electronic structure, stability, and electrocatalytic properties of Pt-transition metal alloys: Pt-skin versus Pt-skeleton surfaces. *J Am Chem Soc* **2006,** *128* (27), 8813-8819.

34.Sasaki, K.; Naohara, H.; Cai, Y.; Choi, Y. M.; Liu, P.; Vukmirovic, M. B.; Wang, J. X.; Adzic, R. R., Core-Protected Platinum Monolayer Shell High-Stability Electrocatalysts for Fuel-Cell Cathodes. *Angew Chem Int Edit* **2010,** *49* (46), 8602-8607.

35.(a) Stephens, I. E. L.; Bondarenko, A. S.; Bech, L.; Chorkendorff, I., Oxygen Electroreduction Activity and X-Ray Photoelectron Spectroscopy of Platinum and Early Transition Metal Alloys. *Chemcatchem* **2012,** *4* (3), 341-349; (b) Chen, S.; Sheng, W. C.; Yabuuchi, N.; Ferreira, P. J.; Allard, L. F.; Shao-Horn, Y., Origin of Oxygen Reduction Reaction Activity on "Pt3Co" Nanoparticles: Atomically Resolved Chemical Compositions and Structures. *J Phys Chem C* **2009,** *113* (3), 1109-1125; (c) Wang, C.; Chi, M. F.; Wang, G. F.; van der Vliet, D.; Li, D. G.; More, K.; Wang, H. H.; Schlueter, J. A.; Markovic, N. M.; Stamenkovic, V. R., Correlation Between Surface Chemistry and Electrocatalytic Properties of Monodisperse PtxNi1-x Nanoparticles. *Adv Funct Mater* **2011,** *21* (1), 147-152.

36.Gauthier, Y.; Joly, Y.; Baudoing, R.; Rundgren, J., Surface-Sandwich Segregation on Nondilute Bimetallic Alloys - Pt50ni50 and Pt78ni22 Probed by Low-Energy Electron-Diffraction. *Phys Rev B* **1985,** *31* (10), 6216-6218.

37.(a) Mavrikakis, M.; Hammer, B.; Norskov, J. K., Effect of strain on the reactivity of metal surfaces. *Phys Rev Lett* **1998,** *81* (13), 2819-2822; (b) Lischka, M.; Mosch, C.; Gross, A., Tuning catalytic properties of bimetallic surfaces: Oxygen adsorption on pseudomorphic Pt/Ru overlayers. *Electrochim Acta* **2007,** *52* (6), 2219-2228; (c) Hoster, H. E.; Alves, O. B.; Koper, M. T. M., Tuning

Adsorption via Strain and Vertical Ligand Effects. *Chemphyschem* **2010,** *11* (7), 1518-1524.

38.(a) Ferrandez, A. C.; Baranton, S.; Bigarre, J.; Buvat, P.; Coutanceau, C., Chemical Functionalization of Carbon Supported Metal Nanoparticles by Ionic Conductive Polymer via the "Grafting From" Method. *Chem Mater* **2013,** *25* (19), 3797-3807; (b) Miyabayashi, K.; Nishihara, H.; Miyake, M., Platinum Nanoparticles Modified with Alkylamine Derivatives as an Active and Stable Catalyst for Oxygen Reduction Reaction. *Langmuir* **2014,** *30* (10), 2936-2942; (c) Snyder, J.; Livi, K.; Erlebacher, J., Oxygen Reduction Reaction Performance of [MTBD][beti]-Encapsulated Nanoporous NiPt Alloy Nanoparticles. *Adv Funct Mater* **2013,** *23* (44), 5494-5501; (d) Jiang, Z. Z.; Wang, Z. B.; Gu, D. M.; Smotkin, E. S., Carbon riveted Pt/C catalyst with high stability prepared by in situ carbonized glucose. *Chem Commun* **2010,** *46* (37), 6998-7000; (e) Takenaka, S.; Miyamoto, H.; Utsunomiya, Y.; Matsune, H.; Kishida, M., Catalytic Activity of Highly Durable Pt/CNT Catalysts Covered with Hydrophobic Silica Layers for the Oxygen Reduction Reaction in PEFCs. *J Phys Chem C* **2014,** *118* (2), 774-783; (f) Takenaka, S.; Matsumori, H.; Nakagawa, K.; Matsune, H.; Tanabe, E.; Kishida, M., Improvement in the durability of pt electrocatalysts by coverage with silica layers. *J Phys Chem C* **2007,** *111* (42), 15133-15136; (g) Chen, S. G.; Wei, Z. D.; Qi, X. Q.; Dong, L. C.; Guo, Y. G.; Wan, L. J.; Shao, Z. G.; Li, L., Nanostructured Polyaniline-Decorated Pt/C@PANI Core-Shell Catalyst with Enhanced Durability and Activity. *J Am Chem Soc* **2012,** *134* (32), 13252-13255.

39.Zhang, J.; Sasaki, K.; Sutter, E.; Adzic, R. R., Stabilization of platinum oxygen-reduction electrocatalysts using gold clusters. *Science* **2007,** *315* (5809), 220-222.

40.Xia, Y. N.; Xiong, Y. J.; Lim, B.; Skrabalak, S. E., Shape-Controlled Synthesis of Metal Nanocrystals: Simple Chemistry Meets Complex Physics? *Angew Chem Int Edit* **2009,** *48* (1), 60-103.

41.Kang, Y. J.; Murray, C. B., Synthesis and Electrocatalytic Properties of Cubic Mn-Pt Nanocrystals (Nanocubes). *J Am Chem Soc* **2010,** *132* (22), 7568-+.

42.Zhang, J.; Fang, J. Y., A General Strategy for Preparation of Pt 3d-Transition Metal (Co, Fe, Ni) Nanocubes. *J Am Chem Soc* **2009,** *131* (51), 18543-18547.

43.Solla-Gullon, J.; Montiel, V.; Aldaz, A.; Clavilier, J., Electrochemical characterisation of platinum nanoparticles prepared by microemulsion: how to clean them without loss of crystalline surface structure. *J Electroanal Chem* **2000,** *491* (1-2), 69-77.

44.Lee, I.; Morales, R.; Albiter, M. A.; Zaera, F., Synthesis of heterogeneous catalysts with well shaped platinum particles to control reaction selectivity. *P*

Natl Acad Sci USA **2008,** *105* (40), 15241-15246.

45.(a) Lee, Y. H.; Lee, G.; Shim, J. H.; Hwang, S.; Kwak, J.; Lee, K.; Song, H.; Park, J. T., Monodisperse PtRu nanoalloy on carbon as a high-performance DMFC catalyst. *Chem Mater* **2006,** *18* (18), 4209-4211; (b) Mazumder, V.; Sun, S. H., Oleylamine-Mediated Synthesis of Pd Nanoparticles for Catalytic Formic Acid Oxidation. *J Am Chem Soc* **2009,** *131* (13), 4588-+.

46.Genorio, B.; Strmcnik, D.; Subbaraman, R.; Tripkovic, D.; Karapetrov, G.; Stamenkovic, V. R.; Pejovnik, S.; Markovic, N. M., Selective catalysts for the hydrogen oxidation and oxygen reduction reactions by patterning of platinum with calix[4]arene molecules. *Nat Mater* **2010,** *9* (12), 998-1003.

47.Strmcnik, D.; Escudero-Escribano, M.; Kodama, K.; Stamenkovic, V. R.; Cuesta, A.; Markovic, N. M., Enhanced electrocatalysis of the oxygen reduction reaction based on patterning of platinum surfaces with cyanide. *Nat Chem* **2010,** *2* (10), 880-885.

48.Allongue, P.; Delamar, M.; Desbat, B.; Fagebaume, O.; Hitmi, R.; Pinson, J.; Saveant, J. M., Covalent modification of carbon surfaces by aryl radicals generated from the electrochemical reduction of diazonium salts. *J Am Chem Soc* **1997,** *119* (1), 201-207.

49.Zhou, Z. Y.; Kang, X. W.; Song, Y.; Chen, S. W., Enhancement of the electrocatalytic activity of Pt nanoparticles in oxygen reduction by chlorophenyl functionalization. *Chem Commun* **2012,** *48* (28), 3391-3393.

50.Zhou, Z. Y.; Kang, X. W.; Song, Y.; Chen, S. W., Ligand-Mediated Electrocatalytic Activity of Pt Nanoparticles for Oxygen Reduction Reactions. *J Phys Chem C* **2012,** *116* (19), 10592-10598.

51.(a) Wang, Z. B.; Zhao, C. R.; Shi, P. F.; Yang, Y. S.; Yu, Z. B.; Wang, W. K.; Yin, G. P., Effect of a Carbon Support Containing Large Mesopores on the Performance of a Pt-Ru-Ni/C Catalyst for Direct Methanol Fuel Cells. *J Phys Chem C* **2010,** *114* (1), 672-677; (b) Fang, B.; Chaudhari, N. K.; Kim, M. S.; Kim, J. H.; Yu, J. S., Homogeneous Deposition of Platinum Nanoparticles on Carbon Black for Proton Exchange Membrane Fuel Cell. *J Am Chem Soc* **2009,** *131* (42), 15330-15338.

52.(a) Hartnig, C.; Schmidt, T. J., Simulated start-stop as a rapid aging tool for polymer electrolyte fuel cell electrodes. *J Power Sources* **2011,** *196* (13), 5564-5572; (b) Kinoshit.K; Lundquis.Jt; Stonehar.P, Potential Cycling Effects on Platinum Electrocatalyst Surfaces. *J Electroanal Chem* **1973,** *48* (2), 157-166; (c) Meier, J. C.; Galeano, C.; Katsounaros, I.; Topalov, A. A.; Kostka, A.; Schuth, F.; Mayrhofer, K. J. J., Degradation Mechanisms of Pt/C Fuel Cell Catalysts under

Simulated Start-Stop Conditions. *Acs Catal* **2012,** *2* (5), 832-843; (d) Schmidt, T. J.; Baurmeister, J., Properties of high-temperature PEFC Celtec (R)-P 1000 MEAs in start/stop operation mode. *J Power Sources* **2008,** *176* (2), 428-434; (e) Tang, H.; Qi, Z. G.; Ramani, M.; Elter, J. F., PEM fuel cell cathode carbon corrosion due to the formation of air/fuel boundary at the anode. *J Power Sources* **2006,** *158* (2), 1306-1312.

53.(a) Donthu, S.; Cai, M.; Ruthkosky, M.; Halalay, I., Carbon-titania composite substrates for fuel cell catalyst applications. *Chem Commun* **2009,** (28), 4203-4205; (b) Liu, Y.; Mustain, W. E., Structural and Electrochemical Studies of Pt Clusters Supported on High-Surface-Area Tungsten Carbide for Oxygen Reduction. *Acs Catal* **2011,** *1* (3), 212-220.

54.(a) Yu, X. W.; Ye, S. Y., Recent advances in activity and durability enhancement of Pt/C catalytic cathode in PEMFC - Part II: Degradation mechanism and durability enhancement of carbon supported platinum catalyst. *J Power Sources* **2007,** *172* (1), 145-154; (b) Coloma, F.; Sepulvedaescribano, A.; Rodriguezreinoso, F., Heat-Treated Carbon-Blacks as Supports for Platinum Catalysts. *J Catal* **1995,** *154* (2), 299-305.

55.(a) Yao, C. H.; Li, F.; Li, X.; Xia, D. G., Fiber-like nanostructured Ti4O7 used as durable fuel cell catalyst support in oxygen reduction catalysis. *J Mater Chem* **2012,** *22* (32), 16560-16565; (b) Senevirathne, K.; Hui, R.; Campbell, S.; Ye, S. Y.; Zhang, J. J., Electrocatalytic activity and durability of Pt/NbO2 and Pt/Ti4O7 nanofibers for PEM fuel cell oxygen reduction reaction. *Electrochim Acta* **2012,** *59*, 538-547.

56.Liu, H. J.; Wang, F.; Zhao, Y.; Fong, H., Mechanically resilient electrospun TiC nanofibrous mats surface-decorated with Pt nanoparticles for oxygen reduction reaction with enhanced electrocatalytic activities. *Nanoscale* **2013,** *5* (9), 3643-3647.

57.(a) Chhina, H.; Campbell, S.; Kesler, O., An oxidation-resistant indium tin oxide catalyst support for proton exchange membrane fuel cells. *J Power Sources* **2006,** *161* (2), 893-900; (b) Liu, Y.; Mustain, W. E., High Stability, High Activity Pt/ITO Oxygen Reduction Electrocatalysts. *J Am Chem Soc* **2013,** *135* (2), 530-533.

58.Lo, C. P.; Ramani, V., SiO2-RuO2: A Stable Electrocatalyst Support. *Acs Appl Mater Inter* **2012,** *4* (11), 6109-6116.

59.(a) Shao, Y. Y.; Liu, J.; Wang, Y.; Lin, Y. H., Novel catalyst support materials for PEM fuel cells: current status and future prospects. *J Mater Chem* **2009,** *19* (1), 46-59; (b) Sharma, S.; Pollet, B. G., Support materials for PEMFC and DMFC electrocatalysts-A review. *J Power Sources* **2012,** *208*, 96-119; (c)

Liu, Y.; Shrestha, S.; Mustain, W. E., Synthesis of Nanosize Tungsten Oxide and Its Evaluation as an Electrocatalyst Support for Oxygen Reduction in Acid Media. *Acs Catal* **2012,** *2* (3), 456-463.

60.(a) Cui, X. Z.; Shi, J. L.; Chen, H. R.; Zhang, L. X.; Guo, L. M.; Gao, J. H.; Li, J. B., Platinum/mesoporous WO3 as a carbon-free electrocatalyst with enhanced electrochemical activity for methanol oxidation. *J Phys Chem B* **2008,** *112* (38), 12024-12031; (b) Rajeswari, J.; Viswanathan, B.; Varadarajan, T. K., Tungsten trioxide nanorods as supports for platinum in methanol oxidation. *Mater Chem Phys* **2007,** *106* (2-3), 168-174.

61.Toyoda, E.; Jinnouchi, R.; Ohsuna, T.; Hatanaka, T.; Aizawa, T.; Otani, S.; Kido, Y.; Morimoto, Y., Catalytic Activity of Pt/TaB2(0001) for the Oxygen Reduction Reaction. *Angew Chem Int Edit* **2013,** *52* (15), 4137-4140.

62.(a) Horsley, J. A., Molecular-Orbital Study of Strong Metal-Support Interaction between Platinum and Titanium-Dioxide. *J Am Chem Soc* **1979,** *101* (11), 2870-2874; (b) Van, T. T. H.; Pan, C. J.; Rick, J.; Su, W. N.; Hwang, B. J., Nanostructured Ti0.7Mo0.3O2 Support Enhances Electron Transfer to Pt: High-Performance Catalyst for Oxygen Reduction Reaction. *J Am Chem Soc* **2011,** *133* (30), 11716-11724.

63.(a) Shao-Horn, Y.; Sheng, W. C.; Chen, S.; Ferreira, P. J.; Holby, E. F.; Morgan, D., Instability of supported platinum nanoparticles in low-temperature fuel cells. *Top Catal* **2007,** *46* (3-4), 285-305; (b) Ferreira, P. J.; la O', G. J.; Shao-Horn, Y.; Morgan, D.; Makharia, R.; Kocha, S.; Gasteiger, H. A., Instability of Pt/C electrocatalysts in proton exchange membrane fuel cells - A mechanistic investigation. *J Electrochem Soc* **2005,** *152* (11), A2256-A2271.

64.Bett, J. A. S.; Kinoshita, K.; Stonehart, P., Crystallite Growth of Platinum Dispersed on Graphitized Carbon-Black .2. Effect of Liquid Environment. *J Catal* **1976,** *41* (1), 124-133.

65.Hartl, K.; Hanzlik, M.; Arenz, M., IL-TEM investigations on the degradation mechanism of Pt/C electrocatalysts with different carbon supports. *Energ Environ Sci* **2011,** *4* (1), 234-238.

66.Meier, J. C.; Galeano, C.; Katsounaros, I.; Witte, J.; Bongard, H. J.; Topalov, A. A.; Baldizzone, C.; Mezzavilla, S.; Schuth, F.; Mayrhofer, K. J. J., Design criteria for stable Pt/C fuel cell catalysts. *Beilstein J Nanotech* **2014,** *5*, 44-67.

67.(a) Tang, L.; Han, B.; Persson, K.; Friesen, C.; He, T.; Sieradzki, K.; Ceder, G., Electrochemical Stability of Nanometer-Scale Pt Particles in Acidic Environments. *J Am Chem Soc* **2010,** *132* (2), 596-600; (b) Tang, L.; Li, X.; Cammarata, R. C.; Friesen, C.; Sieradzki, K., Electrochemical Stability of

Elemental Metal Nanoparticles. *J Am Chem Soc* **2010,** *132* (33), 11722-11726; (c) Holby, E. F.; Sheng, W. C.; Shao-Horn, Y.; Morgan, D., Pt nanoparticle stability in PEM fuel cells: influence of particle size distribution and crossover hydrogen. *Energ Environ Sci* **2009,** *2* (8), 865-871; (d) Perez-Alonso, F. J.; Elkjaer, C. F.; Shim, S. S.; Abrams, B. L.; Stephens, I. E. L.; Chorkendorff, I., Identical locations transmission electron microscopy study of Pt/C electrocatalyst degradation during oxygen reduction reaction. *J Power Sources* **2011,** *196* (15), 6085-6091.

68.(a) Rinaldo, S. G.; Stumper, J.; Eikerling, M., Physical Theory of Platinum Nanoparticle Dissolution in Polymer Electrolyte Fuel Cells. *J Phys Chem C* **2010,** *114* (13), 5773-5785; (b) Darling, R. M.; Meyers, J. P., Mathematical model of platinum movement in PEM fuel cells. *J Electrochem Soc* **2005,** *152* (1), A242-A247.

69.Jinnouchi, R.; Toyoda, E.; Hatanaka, T.; Morimoto, Y., First Principles Calculations on Site-Dependent Dissolution Potentials of Supported and Unsupported Pt Particles. *J Phys Chem C* **2010,** *114* (41), 17557-17568.

70.Darling, R. M.; Meyers, J. P., Kinetic model of platinum dissolution in PEMFCs. *J Electrochem Soc* **2003,** *150* (11), A1523-A1527.

71.Johnson, D. C.; Napp, D. T.; Buckenst.S, A Ring-Disk Electrode Study of Current/Potential Behaviour of Platinum in 1.0 M Sulphuric and 0.1 M Perchloric Acids. *Electrochim Acta* **1970,** *15* (9), 1493-&.

72.Inzelt, G.; Berkes, B.; Kriston, A., Temperature dependence of two types of dissolution of platinum in acid media. An electrochemical nanogravimetric study. *Electrochim Acta* **2010,** *55* (16), 4742-4749.

73.Itaya, K. S., S.; Sashikata, K.; Furuya, N., *J. Vac. Sci.Technol., A* **1990,** *8*, 515-519.

74.Wakisaka, M.; Asizawa, S.; Uchida, H.; Watanabe, M., In situ STM observation of morphological changes of the Pt(111) electrode surface during potential cycling in 10 mM HF solution. *Phys Chem Chem Phys* **2010,** *12* (16), 4184-4190.

75.Angerstein-Kozlowska, H. C., B.E.; Sharp, W.B.A., *J. Electroanal. Chem.* **1973,** *43*, 9-36.

76.(a) Mukerjee, S.; McBreen, J., Effect of particle size on the electrocatalysis by carbon-supported Pt electrocatalysts: an in situ XAS investigation. *J Electroanal Chem* **1998,** *448* (2), 163-171; (b) Zhang, J.; Mo, Y.; Vukmirovic, M. B.; Klie, R.; Sasaki, K.; Adzic, R. R., Platinum monolayer electrocatalysts for O-2 reduction:

Pt monolayer on Pd(111) and on carbon-supported Pd nanoparticles. *J Phys Chem B* **2004,** *108* (30), 10955-10964; (c) Teliska, A.; O'Grady, W. E.; Ramaker, D. E., Determination of O and OH adsorption sites and coverage in situ on pt electrodes from Pt L-23 X-ray absorption spectroscopy. *J Phys Chem B* **2005,** *109* (16), 8076-8084; (d) Tada, M.; Murata, S.; Asakoka, T.; Hiroshima, K.; Okumura, K.; Tanida, H.; Uruga, T.; Nakanishi, H.; Matsumoto, S.; Inada, Y.; Nomura, M.; Iwasawa, Y., In situ time-resolved dynamic surface events on the Pt/C cathode in a fuel cell under operando conditions. *Angew Chem Int Edit* **2007,** *46* (23), 4310-4315; (e) Imai, H.; Izumi, K.; Matsumoto, M.; Kubo, Y.; Kato, K.; Imai, Y., In Situ and Real-Time Monitoring of Oxide Growth in a Few Monolayers at Surfaces of Platinum Nanoparticles in Aqueous Media. *J Am Chem Soc* **2009,** *131* (17), 6293-6300.

77.Aragane, J.; Urushibata, H.; Murahashi, T., Effect of operational potential on performance decay rate in a phosphoric acid fuel cell. *J Appl Electrochem* **1996,** *26* (2), 147-152.

78.Ross, P. N., In *Catalyst deactivation*, Petersen, E. E. B., A.T., Ed. Marcel Dekker: New York, 1987; p 165.

79.Bett, J.; Lundquis.J, Platinum Crystallite Size Considerations for Electrocatalytic Oxygen Reduction .1. *Electrochim Acta* **1973,** *18* (5), 343-348.

80.Schlogl, K.; Mayrhofer, K. J. J.; Hanzlik, M.; Arenz, M., Identical-location TEM investigations of Pt/C electrocatalyst degradation at elevated temperatures. *J Electroanal Chem* **2011,** *662* (2), 355-360.

81.Ruckenstein, E. P., B., *J. Catal* **1973,** *29*, 224-245.

82.Yaguchi, T.; Kanemura, T.; Shimizu, T.; Imamura, D.; Watabe, A.; Kamino, T., Development of a technique for in situ high temperature TEM observation of catalysts in a highly moisturized air atmosphere. *J Electron Microsc* **2012,** *61* (4), 199-206.

83.Pourbaix, M., *Atlas of Electrochemical Equilibria in Aqueous Solutions*. Pergamon: Brussels, 1966.

84.Kinoshita, K., *Carbon-Electrochemical and Physicochemical Properties* Wiley: New York, 1988.

85.Gruver, G. A., *J. Electrochem. Soc.* **1978,** *125*, 1719-1720.

86.Schlogl, K. M., J.J.; Hanzlik, M.; Arenz, M., *J. Electroanal. Chem.* **2011,** *662*, 355-360.

87.Liu, Z. Y.; Zhang, J. L.; Yu, P. T.; Zhang, J. X.; Makharia, R.; More, K. L.; Stach, E. A., Transmission Electron Microscopy Observation of Corrosion Behaviors of Platinized Carbon Blacks under Thermal and Electrochemical Conditions. *J Electrochem Soc* **2010,** *157* (6), B906-B913.

88.Seger, B.; Kamat, P. V., Electrocatalytically Active Graphene-Platinum Nanocomposites. Role of 2-D Carbon Support in PEM Fuel Cells. *J Phys Chem C* **2009,** *113* (19), 7990-7995.

89.(a) Kim, J.; Lee, S. W.; Carlton, C.; Shao-Horn, Y., Pt-Covered Multiwall Carbon Nanotubes for Oxygen Reduction in Fuel Cell Applications. *J Phys Chem Lett* **2011,** *2* (11), 1332-1336; (b) Hasche, F.; Oezaslan, M.; Strasser, P., Activity, stability and degradation of multi walled carbon nanotube (MWCNT) supported Pt fuel cell electrocatalysts. *Phys Chem Chem Phys* **2010,** *12* (46), 15251-15258.

90.(a) Banham, D.; Feng, F. X.; Pei, K.; Ye, S. Y.; Birss, V., Effect of carbon support nanostructure on the oxygen reduction activity of Pt/C catalysts. *J Mater Chem A* **2013,** *1* (8), 2812-2820; (b) Joo, S. H.; Choi, S. J.; Oh, I.; Kwak, J.; Liu, Z.; Terasaki, O.; Ryoo, R., Ordered nanoporous arrays of carbon supporting high dispersions of platinum nanoparticles (vol 412, pg 169, 2001). *Nature* **2001,** *414* (6862), 470-470.

91.Alcaide, F.; Alvarez, G.; Miguel, O.; Lazaro, M. J.; Moliner, R.; Lopez-Cudero, A.; Solla-Gullon, J.; Herrero, E.; Aldaz, A., Pt supported on carbon nanofibers as electrocatalyst for low temperature polymer electrolyte membrane fuel cells. *Electrochem Commun* **2009,** *11* (5), 1081-1084.

92.Galeano, C.; Meier, J. C.; Peinecke, V.; Bongard, H.; Katsounaros, I.; Topalov, A. A.; Lu, A. H.; Mayrhofer, K. J. J.; Schuth, F., Toward Highly Stable Electrocatalysts via Nanoparticle Pore Confinement. *J Am Chem Soc* **2012,** *134* (50), 20457-20465.

93.Marie, J.; Berthon-Fabry, S.; Achard, P.; Chatenet, M.; Pradourat, A.; Chainet, E., Highly dispersed platinum on carbon aerogels as supported catalysts for PEM fuel cell-electrodes: comparison of two different synthesis paths. *J Non-Cryst Solids* **2004,** *350*, 88-96.

94.(a) Jaksic, J. M.; Labou, D.; Papakonstantinou, G. D.; Siokou, A.; Jaksic, M. M., Novel Spillover Interrelating Reversible Electrocatalysts for Oxygen and Hydrogen Electrode Reactions. *J Phys Chem C* **2010,** *114* (43), 18298-18312; (b) Neophytides, S. G.; Murase, K.; Zafeiratos, S.; Papakonstantinou, G.; Paloukis, F. E.; Krstajic, N. V.; Jaksic, M. M., Composite hypo-hyper-d-intermetallic and interionic phases as supported interactive electrocatalysts. *J Phys Chem B* **2006,** *110* (7), 3030-3042.

95.Debe, M. K.; Schmoeckel, A. K.; Vernstrorn, G. D.; Atanasoski, R., High voltage stability of nanostructured thin film catalysts for PEM fuel cells. *J Power Sources* **2006,** *161* (2), 1002-1011.

96.(a) Schneider, W. B.; Benedikt, U.; Auer, A. A., Interaction of Platinum Nanoparticles with Graphitic Carbon Structures: A Computational Study. *Chemphyschem* **2013,** *14* (13), 2984-2989; (b) Schlogl, K.; Hanzlik, M.; Arenz, M., Comparative IL-TEM Study Concerning the Degradation of Carbon Supported Pt-Based Electrocatalysts. *J Electrochem Soc* **2012,** *159* (6), B677-B682.

97.(a) Mayrhofer, K. J. J.; Meier, J. C.; Ashton, S. J.; Wiberg, G. K. H.; Kraus, F.; Hanzlik, M.; Arenz, M., Fuel cell catalyst degradation on the nanoscale. *Electrochem Commun* **2008,** *10* (8), 1144-1147; (b) Mayrhofer, K. J. J.; Ashton, S. J.; Meier, J. C.; Wiberg, G. K. H.; Hanzlik, M.; Arenz, M., Non-destructive transmission electron microscopy study of catalyst degradation under electrochemical treatment. *J Power Sources* **2008,** *185* (2), 734-739.

98.Schulenburg, H.; Schwanitz, B.; Linse, N.; Scherer, G. G.; Wokaun, A.; Krbanjevic, J.; Grothausmann, R.; Manke, I., 3D Imaging of Catalyst Support Corrosion in Polymer Electrolyte Fuel Cells. *J Phys Chem C* **2011,** *115* (29), 14236-14243.

Chapter 2

Experimental Section

2.1 Chemicals Required

Platinum chloride ($PtCl_2$, 98% Alfa Aesar), 1-decyne (HC10,TCI America), 1-dodecyne (HC12, AROS, 98%), 1-tetradecyne (HC14, Wako), 1-hexadecyne (HC16, Alfa Aesar, 90%), 4-ethylphenylacetylene (EPA, 99%, Fisher Scientific), 4-tert-butylphenylacetylene (BPA, 90+%, Fisher Scientific), 1,2-propanediol (ACROS), sodium acetate trihydrate ($NaOAc \cdot 3H_2O$, MC&B), commercial Pt/C catalyst was purchased from Alfa Aesar (20 wt.%, HiSPEC^{TM}3000, Johnson Matthey), pitch carbon fibers (Fiber Glast Development Corporation), sodium carbonate (Na_2CO_3, ≥99.5%, Sigma Aldrich), ammonia (28 wt.% in water, ACROS), perchloric acid ($HClO_4$, 70 wt.%, ACROS), sulfuric acid (H_2SO_4, Fisher Scientific), nitric acid (HNO_3, Fisher Scientific), high-purity O_2 (99.993%, Airgas), copper acetate ($Cu(OAc)_2 \cdot H_2O$, 99.9%, Alfa Aesar), sodium borohydride ($NaBH_4$, ≥98%, ACROS), copper oxide nanopowders (CuO, 99%, dia. ~40 nm, SkySpring Nanomaterials), cupric sulfate pentahydrate ($CuSO_4 \cdot 5H_2O$, ≥98.0%, Fisher Scientific), 3-Chloroaniline (99%, ACROS), titanium(IV) n-butoxide (99%, ACROS), oleic acid (Fisher Scientific), and Nafion® 117 solution (Fluka) were all used as received. Solvents were purchased at the highest purity available from typical commercial sources and also used without further treatment. Water was deionized with a Barnstead Nanopure water system (18.3 MΩ•cm). Ultrapure N_2 and O_2 were used for the deaeration of the electrolyte solutions and oxygen reduction reactions, respectively.

2.2 Particles Synthesis

2.2.1 Platinum nanoparticles functionalized with acetylene derivatives

Pt nanoparticles stabilized by acetylene derivatives were prepared by adopting a previous procedure for the synthesis of alkyne-capped ruthenium nanoparticles[1]. Briefly, in a typical reaction, 0.28 mmol of $PtCl_2$ was dissolved in 2 mL of concentrated HCl and heated at 60 °C for 30 min, into which $NaHCO_3$ was added until no bubbling was observed. The resulting Na_2PtCl_4 and 2 mmol of NaOAc were then mixed in 200 mL of 1,2-propanediol and the solution was heated to 165 °C for 1 h under vigorous stirring. The solution turned dark brown signifying the formation of nanometer-sized platinum colloids. Upon cooling to room temperature, the solution was split equally into six round-bottom flasks into which a calculated amount of an acetylene derivative dissolved in toluene was added. The self-assembly of the ligands onto the platinum surface led to the effective extraction of the nanoparticles into the toluene phase, as manifested by the color appearance. The toluene part was collected, dried with a rotary evaporator and rinsed extensively with ethanol to remove excessive ligands. For alkyne-capped nanoparticles, they were denoted as $PtHC_x$ with x being the number of carbon atoms in the corresponding monomeric alkyne ligands; and for those stabilized by 4-ethylphenylacetylene and 4-tert-butylphenylacetylene, they were referred to as PtEPA and PtBPA, respectively.

2.2.2 Graphene Quantum Dots (GQD)

The GQDs were prepared by following a literature procedure[2]. In brief, 0.30 g of carbon fibers was added into a mixture of concentrated H_2SO_4 (60 mL) and HNO_3 (20 mL). The solution was sonicated for 2 h and stirred for 24 h at 120 °C. The mixture was then cooled and diluted with Nanopure water (800 mL) with the pH adjusted to about 8 by Na_2CO_3. The solution was then dialyzed in a dialysis bag (cutoff molecular weight 2000 Da) for 3 d, affording purified GQDs. These GQDs were then used as supporting substrates for platinum nanoparticles, as detailed below.

2.2.3 GQD-Supported Platinum Nanoparticles (Pt/G)

In a typical reaction, $PtCl_2$ (26.6 mg, 0.1 mmol) was dissolved in 2 mL of hydrochloric acid under heating. The solution was then condensed to about 1 mL and added into 100 mL of ethylene glycol, along with 80 mg of GQDs prepared above under magnetic stirring. The pH was adjusted to 10 by concentrated ammonia, and the mixture was heated at 165 °C for 30 min, where black precipitates appeared in the flask as a result of thermolytic reduction of Pt(II) by ethylene glycol to form GQDs-supported platinum (Pt/G) nanoparticles. The precipitates were collected, washed extensively with Nanopure water, and dried in a vacuum oven at 80 °C for 12 h. The product contained 20 wt% of Pt, similar to that of commercial Pt/C catalysts.

2.2.4 Alkyne-capped copper nanoparticles

In a typical synthesis, 0.1 mmol of copper acetate was dissolved in 2 mL of water, into which was added a 10-fold molar excess of 1-decyne dissolved in 10 mL of ethanol and 50 mL of dichloromethane. This solution was kept either in an ice-water bath or at ambient temperature, into which was added dropwise 1 mmol of $NaBH_4$ (37.8 mg) dissolved in 2 mL of water under vigorous stirring and N_2 protection. In both syntheses, the original blue solutions were found to turn green, light yellow, brown and finally black during the course of $NaBH_4$ addition. After three hours of magnetic stirring, the solutions were dried under rotary evaporation and the solids were washed with methanol five times to remove excessive ligands and reaction byproducts, affording purified 1-decyne-protected copper nanoparticles that were denoted as CuHC10-IB and CuHC10-RT, respectively. The nanoparticles were found to be readily dispersible in apolar solvents such as CH_2Cl_2, $CHCl_3$, THF, toluene, etc, but insoluble in polar solvents like alcohols, acetone, and acetonitrile.

2.2.5 GQD-Supported Copper Nanoparticles (Pt/G)

The GQDs were prepared by following a literature procedure[2-3] like in section 2.2.3 and as-prepared GQDs were used for the preparation of Cu/GQD nanocomposites. In a typical reaction, a calculated amount of $CuSO_4$ and NaOAc (at a 6:1 molar feed ratio of sodium acetate to Cu) were dissolved in 50 mL of 1,2-propanediol together with a certain amount of the GQDs prepared above. The mixture was first subject to nitrogen bubbling for 30 min and then thermal

refluxing at 140 °C under continuous stirring for 1 h before the solution was cooled down. The black precipitates were collected and purified with a copious amount of acetonitrile and Nanopure water. Four samples were prepared at varied Cu/C atomic ratio (*x*) of 3.54%, 3.32%, 2.88% and 2.34%, as determined by the integrated peak areas of the Cu2p and C1s electrons in XPS measurements.

2.2.6 TiO_2 nanoparticles

TiO_2 nanoparticles were prepared by following a literature procedure.[4] In a typical reaction, 0.05 mL of 3-chloroaniline was added into 5 mL of Nanopure water and then transferred to a Teflon-lined stainless-steel autoclave. Meanwhile, 0.085 g of titanium(IV) n-butoxide and 0.5 mL of oleic acid were dissolved in 5 mL of toluene and also transferred to the autoclave. The mixed solution was subject to hydrothermal treatments at 180 °C for 12 h, and the as-obtained white precipitates (TiO_2) were collected and rinsed extensively with methanol.

2.2.7 TiO_2 supported Cu nanoparticles

The TiO_2 nanoparticles prepared above were then used for the preparation of Cu-TiO_2 nanocomposites. In a typical reaction, a calculated amount of copper acetate and TiO_2 nanoparticles (at a TiO_2:Cu molar ratio of 4:1) was dispersed in THF. $NaBH_4$ dissolved in a small amount of water was added dropwise under vigorous stirring and N_2 protection, where the color of the solution was found to change quickly from blue to dark brown, signifying the formation of copper nanoparticles. After one hour of magnetic stirring, the solution was dried and the

solids were washed with a copious amount of methanol to remove reaction byproducts or excess ligands, affording purified nanocomposites that were denoted as Cu/TiO_2.

$CuHC10/TiO_2$ was prepared in a similar fashion except that a 10-fold molar excess of 1-decyne was added to the solution prior to the addition of $NaBH_4$.

2.3 Instruments

2.3.1 Microscopy

The morphology and size of the nanomaterials were characterized by transmission electron microscopic (TEM, Philips CM300 at 300kV). The samples were prepared by casting a drop of particles solution (cone. ~1 mg/mL) onto a 400 mesh carbon-only grid. The particle core diameter was estimated by counting at least 200 nanoparticles and then analyzed via Image J analysis of the TEM graphs.

2.3.2 Spectroscopy

UV-Vis spectroscopic studies were performed with a UNICAM ATI UV4 spectrometer using a 1 cm quartz cuvette with a resolution of 2 nm. Photoluminescence measurements were conducted with a PTI fluorospectrometer. Raman spectroscopic measurements were carried out with a Delta NU 532 nm Raman spectrometer. FTIR measurements were carried out with a Perkin-Elmer FTIR spectrometer (Spectrum One, spectral resolution 4 cm^{-1}), where the

samples were prepared by casting the particle solutions onto a ZnSe disk. X-ray photoelectron spectra (XPS) were recorded with a PHI 5400/XPS instrument equipped with an Al Kα source operated at 350 W and 10^{-9} Torr. Silicon wafers were sputtered by argon ions to remove carbon from the background and used as substrates. The Si 2p peak (99.15 eV)[5] was used as the reference, and deconvolution of the XPS spectra was carried out by using XPSPEAK 4.1.

2.3.3 Electrochemistry

Electrochemical tests were carried out in a standard three-electrode cell connected to a CHI 710C electrochemical work station, with a Pt foil counter electrode and a Hg/HgO (0.1M NaOH aq.) reference electrode. The working electrode is a rotating ring-disk electrode (RRDE, AFE7R9GCAU from Pine Instrument Co.) with a glassy carbon disk (GC, diameter 5.61 mm) and a platinum ring. The collection efficiency (N) was determined to be 37.3% by RRDE measurements in 5 mM $K_4Fe(CN)_6^+$ 0.1 M $Sr(NO_3)_2$, which is consistent with the manufacture's value of 37%[6]. To prepare catalyst solutions for oxygen reduction tests, typically 0.4 mg of the nanoparticle catalysts and 1.6 mg of carbon black with 4 μL of Nafion were ultrasonically mixed in 0.4 mL of ethanol. Then 15 μL of the catalyst inks was slowly dropcast onto the glassy-carbon disk electrode of the RRDE and dried under gentle N_2 (corresponding to a loading of 15 μg in total). When the electrode was dried, a dilute Nafion solution (0.1 wt.%, 3 μL) was added onto it, prior to being immersed into electrolyte solutions for electrochemical measurements.

Prior to electrochemical tests of oxygen reduction, the catalyst films on the glassy-carbon electrode surface were electrochemically pretreated in a nitrogen-saturated electrolyte (0.1 M NaOH) by rapid potential cycling at 100 mV/s in a desired potential window until a steady voltammogram was observed. The electrocatalytic activity for oxygen reduction was then evaluated in an oxygen-saturated electrolyte solution. The solution ohmic drop (i.e., IR drop) was electronically compensated.

2.3.4 Electronic Conductivity Measurements

Electronic conductivity of solid films of the nanoparticles was evaluated by using a procedure detailed previously[1]. A particle films was formed by dropcasting 1 μL of a concentrated particle solution in toluene (60 mg/mL) onto an interdigitated array (IDA) electrode (25 pairs of gold fingers of 3 mm × 5 μm × 5 μm, from ABTECH)[7]. At least 30 min was allowed for solvent evaporation, and the film thickness was found to be greater than the height of the IDA fingers. Conductivity measurements were then carried out in vacuum (Cryogenic Equipment, JANIS CO) with a CHI710 Electrochemical Workstation at different temperatures (Lakeshore 331 Temperature Controller). The conductivity (σ) was evaluated by the equation $\sigma = (1/(49R))(L/S)$, where R is the ensemble resistance calculated from the slope of the I-V curves, L is the IDA electrode interfinger gap (5 μm); and S is the film cross-section area approximated by (finger height, 5 μm) × (finger length, 3 mm). The constant (49) reflects that there are totally 49 junctions which are in parallel within the IDA chip.

2.4 Reference

1. Kang, X. W.; Zuckerman, N. B.; Konopelski, J. P.; Chen, S. W., Alkyne-Functionalized Ruthenium Nanoparticles: Ruthenium-Vinylidene Bonds at the Metal-Ligand Interface. *J Am Chem Soc* **2012,** *134* (3), 1412-1415.

2. Peng, J.; Gao, W.; Gupta, B. K.; Liu, Z.; Romero-Aburto, R.; Ge, L. H.; Song, L.; Alemany, L. B.; Zhan, X. B.; Gao, G. H.; Vithayathil, S. A.; Kaipparettu, B. A.; Marti, A. A.; Hayashi, T.; Zhu, J. J.; Ajayan, P. M., Graphene Quantum Dots Derived from Carbon Fibers. *Nano Lett* **2012,** *12* (2), 844-849.

3. (a) Song, Y.; Chen, S. W., Graphene Quantum-Dot-Supported Platinum Nanoparticles: Defect-Mediated Electrocatalytic Activity in Oxygen Reduction. *Acs Appl Mater Inter* **2014,** *6* (16), 14050-14060; (b) He, G. Q.; Song, Y.; Liu, K.; Walter, A.; Chen, S.; Chen, S. W., Oxygen Reduction Catalyzed by Platinum Nanoparticles Supported on Graphene Quantum Dots. *Acs Catal* **2013,** *3* (5), 831-838.

4. Pan, D. C.; Zhao, N. N.; Wang, Q.; Jiang, S. C.; Ji, X. L.; An, L. J., Facile synthesis and characterization of luminescent TiO2 nanocrystals. *Advanced Materials* **2005,** *17* (16), 1991-1995.

5. Krimmel, E. F., Proceedings of Symposium-B on Photon, Beam and Plasma Assisted Processing Fundamentals and Device Technology of the 1988 E-Mrs Spring Conference - Strasbourg, France, 31 May 2 June 1988 - Preface. *Appl Surf Sci* **1989,** *36* (1-4), R7-R8.

6. Zhou, Z. Y.; Kang, X. W.; Song, Y.; Chen, S. W., Enhancement of the electrocatalytic activity of Pt nanoparticles in oxygen reduction by chlorophenyl functionalization. *Chem Commun* **2012,** *48* (28), 3391-3393.

7. Pradhan, S.; Kang, X. W.; Mendoza, E.; Chen, S. W., Single electron transfer in thermally annealed nanoparticle dropcast thick films. *Appl Phys Lett* **2009,** *94* (4).

Chapter 3

Platinum Nanoparticles Functionalized with Acetylene Derivatives: Electronic Conductivity and Electrocatalytic Activity in Oxygen Reduction

Reproduced with permission from [Ke Liu, Xiongwu Kang, Zhi-You Zhou, Yang Song, Lyman J. Lee, Daniel Tian, Shaowei Chen*, ‘‘Platinum Nanoparticles Functionalized with Acetylene Derivatives: Electronic Conductivity and Electrocatalytic Activity in Oxygen Reduction”, *J. Electroanal. Chem.*, **2013**, 688, 143.] Copyright © 2013 Elsevier B.V.

3.1 Introduction

Recent studies have shown that the material properties of organically capped transition-metal nanoparticles can be readily manipulated not only by the chemical nature of the metal cores and protecting ligands but also by the metal–ligand interfacial bonding interactions[1]. For instance, when metal nanoparticles are stabilized by metal–carbon covalent bonds, the resulting nanoparticles exhibit much enhanced electronic conductivity of the solid ensembles as compared to the mercapto-stabilized counterparts, which is accounted for by the reduced metal–ligand interfacial contact resistance and hence the extensive spilling of core electrons into the organic capping matrix that facilitated interparticle charge transfer[2]. In addition, when the ligands are bound onto the nanoparticle surface by conjugated chemical linkages, effective intraparticle charge delocalization may occur for the particle-bound functional moieties, leading to the emergence of unprecedented optical and electronic properties that are analogous to those of their dimeric forms. This has been manifested in ruthenium nanoparticles functionalized with carbene fragments, alkynides, as well as acetylene derivatives using electroactive species such as ferrocene and fluorophores such as anthracene and pyrene as the molecular probes[3].

In more recent studies, we found that by deliberate chemical functionalization of Pd and Pt nanoparticles with selected aliphatic fragments using diazonium salts as the precursors (with the formation of M-C bonds), the resulting nanoparticles exhibited significant enhancement of their

electrocatalytic activities in formic acid oxidation as well as oxygen reduction[4]. The somewhat unexpected behaviors were accounted for by the unique tuning of the electronic structures of the metal cores that impacted the bonding interactions with the respective reactants. Yet, the effects of other metal-ligand interfacial bonding interactions on the nanoparticle electrocatalytic activity remain largely unexplored. This is the primary motivation of the present study.

In this study, we prepared a series of platinum nanoparticles that were capped by the self-assembly of acetylene derivatives, ranging from straight-chain 1-alkynes to aromatic acetylene derivatives. In our previous study with ruthenium nanoparticles, we demonstrated that terminal alkynes adsorbed onto the nanoparticle surface forming ruthenium-vinylidene (Ru=C=CH-) interfacial bonds by virtue of a tautomeric rearrangement process[3g]. Similar self-assembly was observed with Pt nanoparticles. The bonding interactions between the acetylene derivatives with Pt were then examined by FTIR, UV–vis and photoluminescence spectroscopic measurements. The results suggested effective breaking of the ≡ C-H bond and the formation of $Pt_{surface}$-H and $Pt_{surface}$-C≡ at the metal–ligand interface. With such conjugated metal–ligand bonding interactions, the resulting nanoparticles exhibited interesting electronic conductivity properties. For Pt nanoparticles functionalized with 1-alkynes or 4-ethylphenylacetylene, temperature dependence of the ensemble electronic conductivity was consistent with that of semiconducting materials, whereas for 4-tert-butylphenylacetylene-capped nanoparticles, metallic behaviors were

observed instead. This discrepancy of the ensemble conductivity properties also led to an apparent variation of the electrocatalytic activity in oxygen reduction. On the basis of onset potential and kinetic current density, the 4-ethylphenylacetylene-capped nanoparticles were found to exhibit the best performance among the series. This was accounted for by the combined contributions of (i) effective partial removal of nanoparticle surface ligands for ready accessibility of the nanoparticle surface by oxygen and electrolyte counter ions and (ii) tuning of the nanoparticle electronic structures that impacted the bonding interactions with oxygen. These results further demonstrate that surface chemical functionalization may represent a unique and effective tool in the manipulation and optimization of their electrocatalytic activity.

3.2. Results and Discussion

3.2.1. Structural characterizations

Fig. 1 depicts a representative TEM micrograph of the Pt nanoparticles. It can be seen that the nanoparticles were well dispersed without apparent aggregation, suggesting effective passivation of the nanoparticles by the self-assembly of acetylene derivatives onto the Pt surface, and the resulting nanoparticles exhibited well-defined crystalline structures. From the TEM image, one can see that the lattice fringes display a spacing of 0.230 nm corresponding to the separation between the Pt(1 1 1) planes. Furthermore, it can be seen that the size of the nanoparticles was rather uniform. In fact, the nanoparticle core size histogram based on a statistical analysis of more than 300 nanoparticles

(figure inset) shows that the nanoparticles exhibited an average core size of 2.85 ± 0.62 nm.

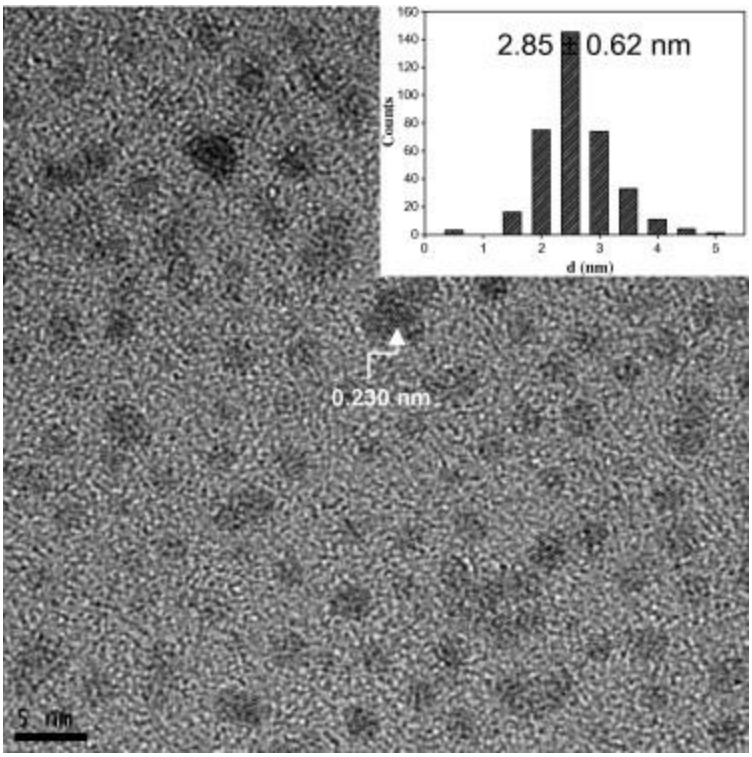


Figure 3.1. Representative TEM micrograph of PtHC10 nanoparticles prepared by thermolytic reduction of $PtCl_2$. Scale bar 5 nm. Inset shows the corresponding nanoparticle core size histogram.

The structures of the capping ligands were then examined by FTIR measurements, as depicted in Fig. 2 with PtHC10, PtEPA and PtBPA nanoparticles. The spectra of PtHC12, PtHC14, and PtHC16 nanoparticles were similar to that of PtHC10 and hence not shown. Whereas the monomeric ligands (dashed curves) all exhibited a well-defined ≡ C-H vibrational stretch (3314 cm^{-1} for HC10, and 3294 cm^{-1} for both EPA and BPA), such a feature vanished completely with the nanoparticle samples (solid curves), indicating facile breaking of the ≡ C-H bond when the ligands were adsorbed onto the nanoparticle surface. Previously Muetteries et al.[5] carried out an ultra-high vacuum study of the chemical reactivity of acetylene on Pt[6] and Pt{1 0 0} surfaces and found that at ambient temperature the carbon-hydrogen bond breaking was absent on the Pt{1 1 1} surface, whereas the process was detectable for Pt{1 0 0} even at 20°C with the formation of $Pt_{surface}$-H and $Pt_{surface}$-C≡ bonds. For the nanoparticles prepared above, the fact that the lattice fringes are well defined for the Pt(1 1 1) planes(Fig. 1) suggests that the {1 0 0} facets might constitute a substantial fraction of the metal core surface, which facilitated the breaking of the ≡C-H bond when the acetylene derivatives were adsorbed onto the Pt surfaces. Similar behaviors were observed with alkyne-capped ruthenium nanoparticles[3g], where the tautomeric rearrangement of the acetylene moieties adsorbed on the Ru nanoparticle surface led to a dynamic equilibrium between the η^2 configuration and a Ru–vinylidene interfacial linkage with the corresponding metal hydride as the intermediate species.

Notably, the disappearance of the ≡ C-H vibrational stretches also indicates that the platinum nanoparticles were free of excessive unbound ligands.

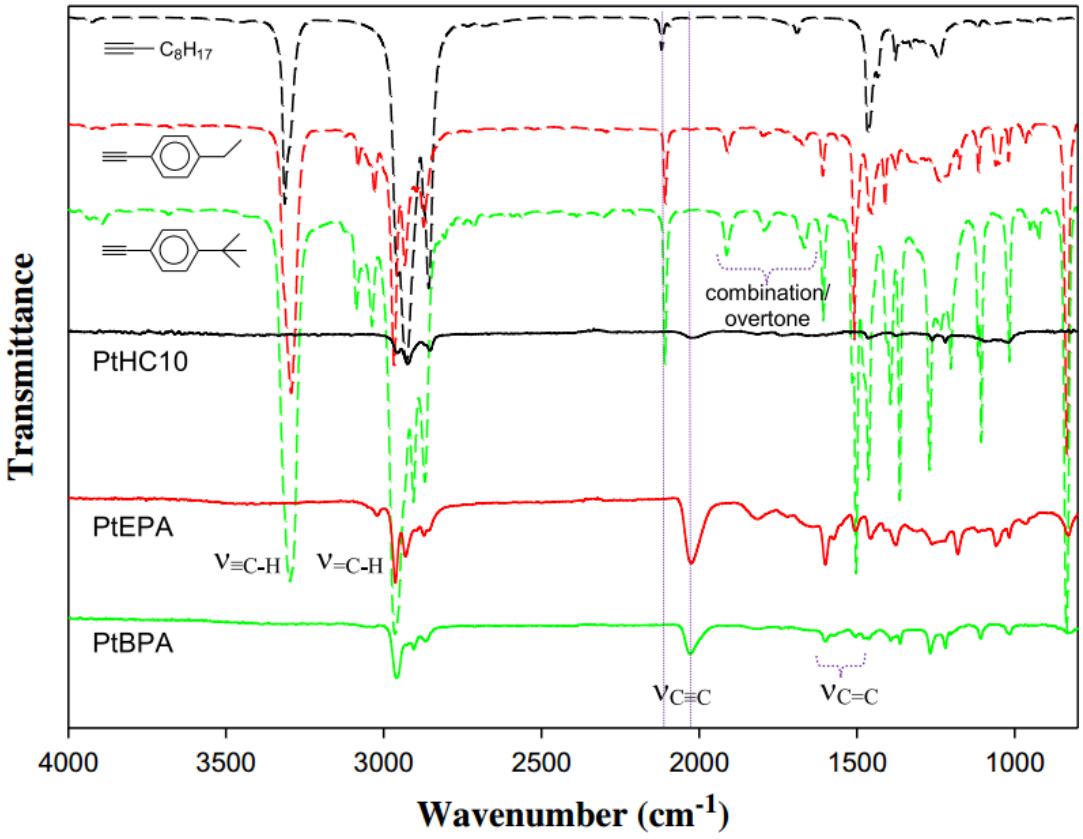


Figure 3.2. FTIR spectra of PtHC10, PtEPA, and PtBPA nanoparticles along with those of monomeric HC10, EPA and BPA ligands.

Additionally, for EPA and BPA monomers, the spectral features of the ring skeleton vibrations (C=C) at 1609 and 1460 cm^{-1} and C-H deformation at 841 cm^{-1} are also well-defined, along with the combination and/or overtone of the ring deformations that emerged between 1630 and 1970 cm^{-1} and the ring C-H vibrations at 3042 and 3089 cm^{-1}[17]. These characteristics are also very well-defined with the PtEPA and PtBPA nanoparticles.

The breaking of the ≡C-H bond and the formation of the Pt-C≡ linkage also led to a drastic variation of the C≡C vibrational stretch. From Fig.2, it can be seen that, for the monomeric ligands (dashed curves), the C≡C vibrational stretch can be identified at 2122 cm^{-1} for both EPA and BPA; whereas when the ligands were bound onto the nanoparticle surface, the C≡C vibrational stretch appears at a much lower wavenumber position, 2020 cm^{-1} for PtHC10, and 2030 cm^{-1} for PtEPA and PtBPA. This observation strongly indicates that the ligands were indeed chemically bonded onto the Pt surface, and the decreasing bonding order (lower peak wavenumber) might be attributed to the $\sigma\pi$ bonding interactions between the triple-bond moieties and the platinum metal cores, where effective intraparticle charge delocalization occurred between the particle-bound acetylene moieties. In fact, such a phenomenon has been observed extensively with other nanoparticles passivated by conjugated metal-ligand bonding interactions[3d, 3g, 8].

Notably, the fact that only one peak was observed for the C≡C vibrational stretch with the Pt nanoparticles prepared above is also consistent with the

formation of $Pt_{surface}$-H and $Pt_{surface}$-C≡ bonds at the metal–ligand interface. Note that for alknyide-capped Ru nanoparticles[3d], also one peak was observed for the particle bound C≡C bonds (i.e., with $Ru_{surface}$-C≡ interfacial bonds). However, the behaviors were sharply different with alkyne-capped ruthenium nanoparticles[3g] or with alkynes adsorbed onto Au and Ag surfaces by surface-enhanced Raman scattering (SERS) measurements[9], where three peaks emerged at ca. 2056 cm^{-1}, 1976 cm^{-1}, and 1950 cm^{-1} for the C≡C vibrational stretch, because of the formation of metal-vinylidene (Ru=C=CH-) linkages that display symmetric and asymmetric vibrational modes.

With the formation of $Pt_{surface}$-C≡ bonds at the metal–ligand interface, the Pt nanoparticles exhibited unique optical characteristics[3d]. Fig. 3 depicts the UV–vis absorption spectra of PtHC10 (black curve), PtEPA (red curve), and PtBPA (green curve) nanoparticles in $CHCl_3$. Note that the spectra have been normalized to their respective absorbance at 300 nm. It can be seen that all featured an exponential decay profile (the co-called Mie scattering), as anticipated for nanometer-sized transition-metal particles[10]. In comparison with PtHC10 nanoparticles, both PtEPA and PtBPA nanoparticles exhibited an additional broad absorption peak within the range of 300 and 550 nm (centered around 400 nm, brown and orange curves), as manifested in the difference spectra in the figure. This is likely due to intraparticle charge delocalization that was further extended by the participation of the phenyl π electrons[3g]. In fact, because of the extended conjugation, the particle-bound phenylacetylene

moieties in PtEPA and PtBPA nanoparticles now behaved analogously to diphenyldiacetylene (Ph-C≡C-C≡C-Ph)[11]. The resulting nanoparticles also exhibited interesting photoluminescence characteristics that are consistent with those of diphenyldiacetylene derivatives, as detailed below.

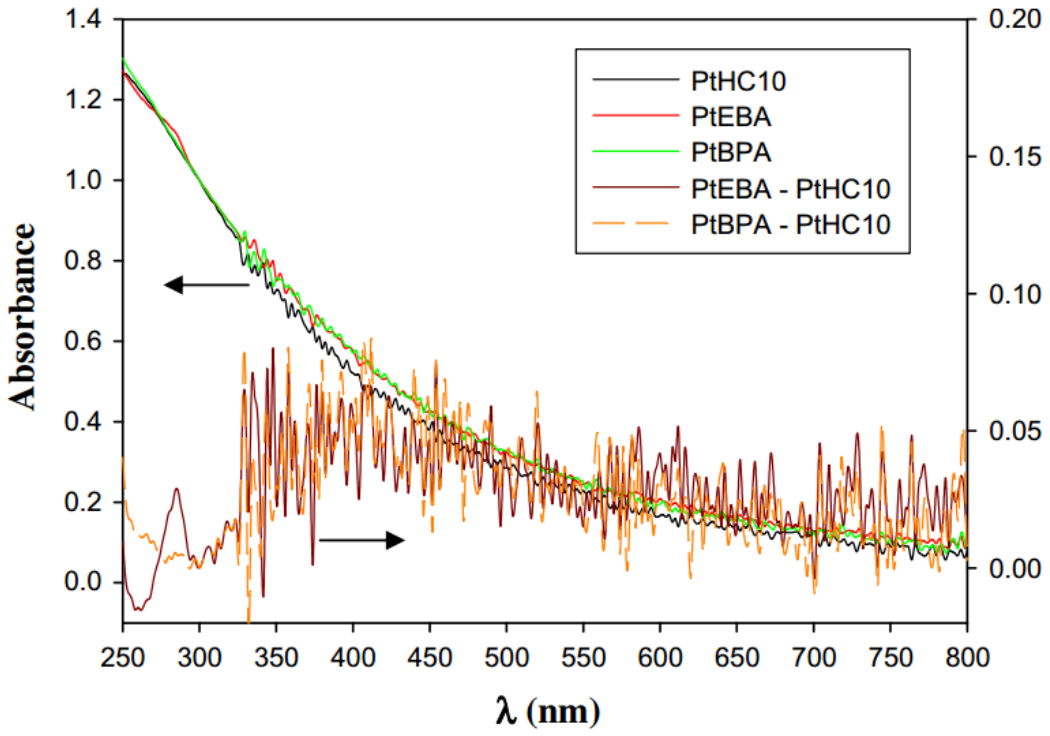


Figure 3.3. UV-vis spectra of PtHC10, PtEBA, and PtBPA nanoparticles in $CHCl_3$. Note that the spectra have been normalized to their respective absorbance at 300 nm. The difference spectra between the PtEPA (PtBPA) and PtHC10 nanoparticles are also included in the figure (right axis).

Fig. 4 depicts the excitation and emission spectra of the PtHC10 (solid curves), PtEPA (dotted curves), and PtBPA (dashed curves) nanoparticles in $CHCl_3$. Note that the fluorescence intensity has been normalized to the optical density at the respective excitation wavelength position. It can be seen that for Pt nanoparticles capped with 1-decyne (and other 1-alkynes), the excitation (λ_{ex}) and emission (λ_{em}) peak positions can be identified at 352 nm and 430 nm, respectively, consistent with the results of our previous studies with ruthenium nanoparticles capped with 1-alkynes[3g] or alkynide derivatives derivatives[3d]. Yet, for the nanoparticles functionalized with aromatic derivatives of acetylene, λ_{ex} and λ_{em} exhibit a significant redshift to 382 nm and 492 nm, respectively, for both PtEPA and PtBPA nanoparticles. This is most probably due to the additional contribution of the phenyl π electrons to the conjugation between the particle-bound acetylene moieties[11-12], which may also account for the (normalized) fluorescence intensity of both PtEPA and PtBPA nanoparticles that is over five times greater than that of PtHC10, as depicted in Fig. 4.

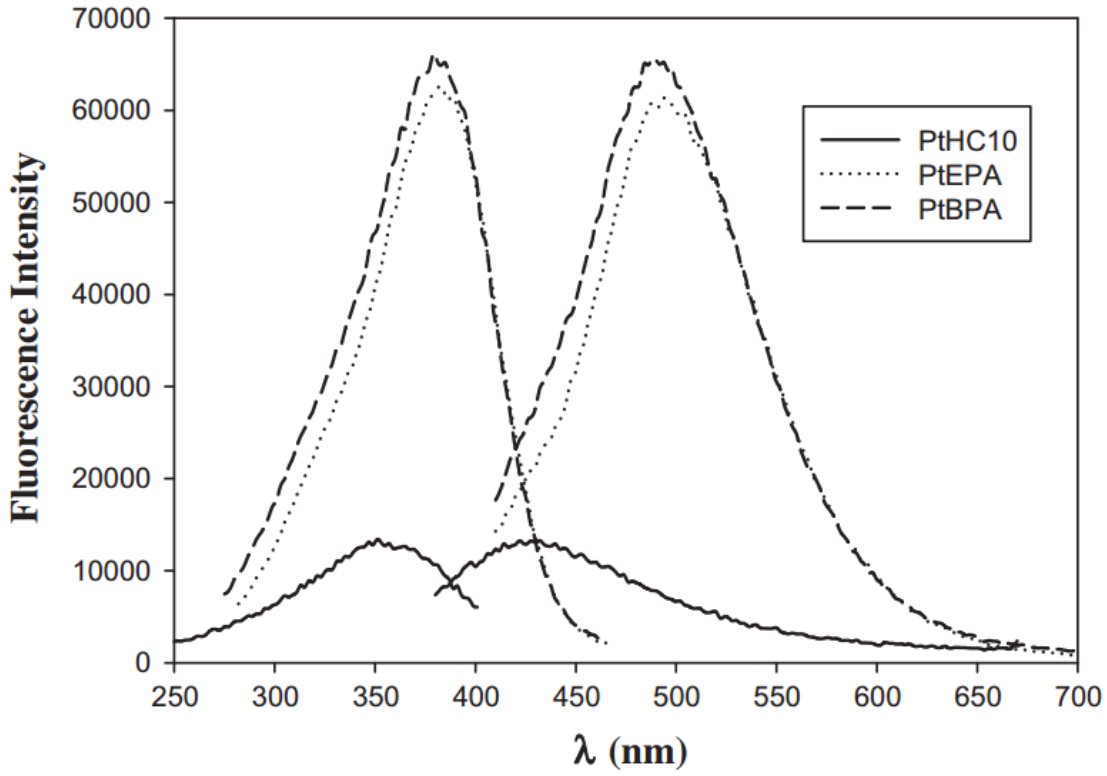


Figure 3.4. Excitation and emission spectra of PtHC10 (solid curves), PtEPA (dotted curve) and PtBPA (dashed curve) in $CHCl_3$. Note that the fluorescence intensity has been normalized to the optical density at the respective excitation wavelength position.

3.2.2. Electronic conductivity

The Pt nanoparticles obtained above also exhibited interesting electronic properties, as reflected in the electronic conductivity measurements of the nanoparticle solid films. Fig. 5 depicts the current–potential (I–V) curves of (A) PtHC10, (B) PtEPA and (C) PtBPA nanoparticle films prepared by dropcasting 1 μL of a 60 mg/mL particle solution in toluene onto an IDA surface. Within the bias voltage of -0.80 to +0.80 V, obvious ohmic behaviors (linear I–V responses) were observed throughout the entire temperature range of 80–300 K, signifying very efficient interparticle charge transfer, which might be, at least in part, attributed to the conjugated metal–ligand interfacial bonding interactions that allows extensive spilling of the metal core electrons into the organic ligand matrix[3g]. Furthermore, it can be seen that the conductivity of the nanoparticle solid films was markedly greater with PtBPA and PtEPA than that of PtHC10. For instance, at 300 K, the ensemble conductivity was 74.1 mS/m, 0.14 mS/m, and 0.051 mS/m for the PtBPA, PtEPA, and PtHC10 nanoparticles, respectively, consistentw ith the reduced charge transfer resistance of the aromatic spacers as compared with that of the saturated counterparts, which has been observed extensively in prior studies[13]. Note that the conductivity of these nanoparticles ensemble films is about 8–11 orders of magnitude lower than that of metallic platinum (9.52×10^6 S/m at 293 K)[14], as a result of the metal-organic hybrid nature of the nanoparticles.

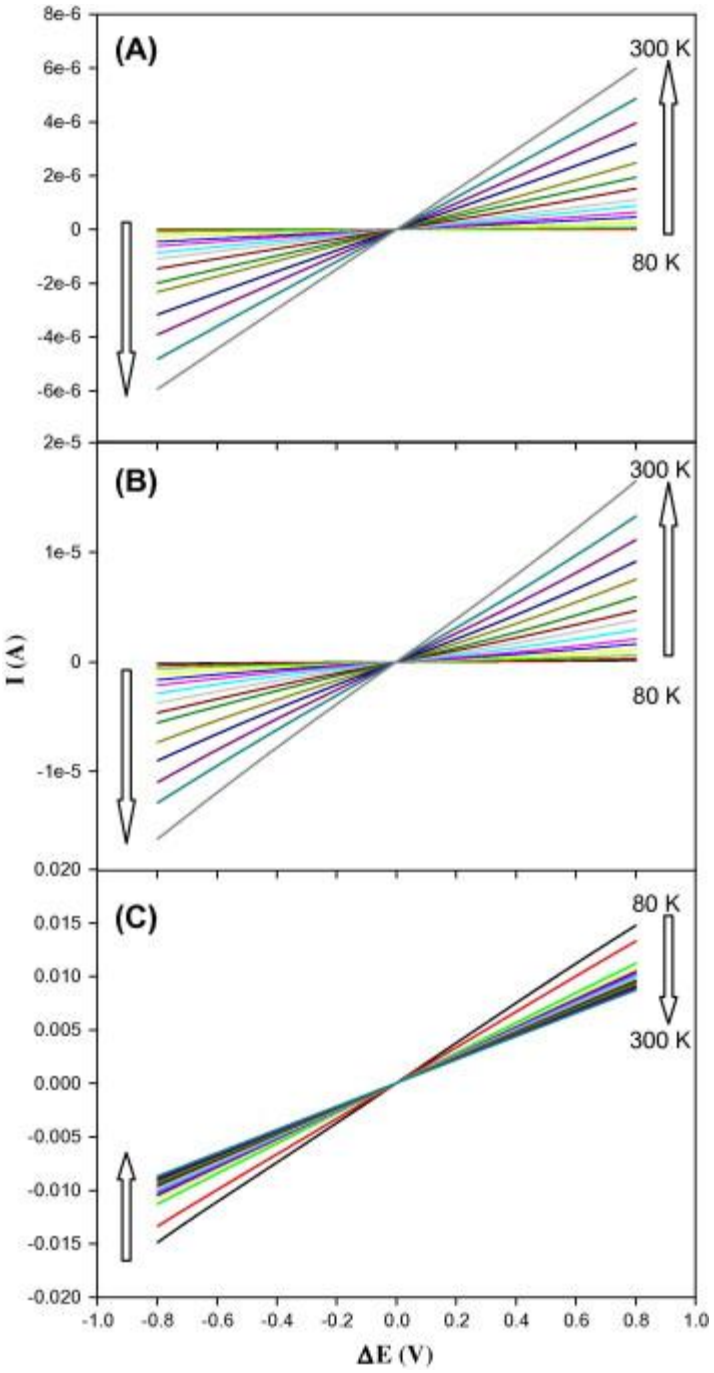


Figure 3.5. Current-potential (I-V) curves of the nanoparticle solid ensembles at varied temperatures: (A) PtHC10, (B) PtEPA, and (C) PtBPA. Potential scan rate 20 mV/s. Arrows denote the increase of temperature from 80 K to 300 K.

More interestingly, the three nanoparticles exhibited a significantly different variation of the ensemble conductivity with temperature. For (A) PtHC10 and (B) PtEPA nanoparticles, the ensemble conductivity increased monotonically with increasing temperature from 80 to 300 K, indicating semiconducting characteristics of the nanoparticle solid films which is consistent with the composite nature of the nanoparticle materials. Such a behavior has also been observed previously with a number of organically capped metal nanoparticles, where interparticle charge transfer was accounted for by a thermally activated hopping mechanism between adjacent nanoparticles[2]. From the temperature dependence of the ensemble conductivity (Fig. 6), the activation energy for interparticle charge transfer can be estimated, which is ca. 76.3 meV and 46.3 meV for the PtHC10 and PtEPA nanoparticles, respectively. Note that for ruthenium nanoparticles functionalized by 1-alkynes of varied chain lengths, the activation energy for interparticle charge transfer was also found to be around 70 meV[3g]. The reduced activation energy for PtEPA as compared to that of PtHC10, is most likely due to the lower charge transfer resistance of the aromatic moiety than with the saturated aliphatic chain.

However, for the PtBPA nanoparticles (Fig. 5C), the temperature dependence of the ensemble conductivity was totally different. As depicted in Fig. 6, the nanoparticle electronic conductivity actually decreased with increasing temperature, a behavior typically anticipated with metallic materials[14]. In a previous study with biphenyl-functionalized palladium and titanium

nanoparticles[2], we observed similar metallic characters in conductivity measurements, which was ascribed to the M-C covalent bonding interactions that reduced the contact resistance at the metal–ligand interface[15] as well as the π-π stacking between ligands of adjacent particles in the solid films, as a result of ligand intercalations that serves as an effective pathway for interparticle charge transfer[16]. Similar behaviors were also observed with ruthenium nanoparticles passivated by varied aliphatic fragments with Ru-C bonding interactions as a result of the strong metal–ligand interfacial bonding interactions[2b]. In the present study, with the conjugated Pt-C≡ interfacial linkage, the metal–ligand contact resistance is anticipated to be low, leading to extended conjugation between the particle-bound phenylacetylene moieties (e.g., as manifested in the photoluminescence measurements in Fig. 3 and 4) and hence a reduced energetic barrier for interparticle charge transfer.

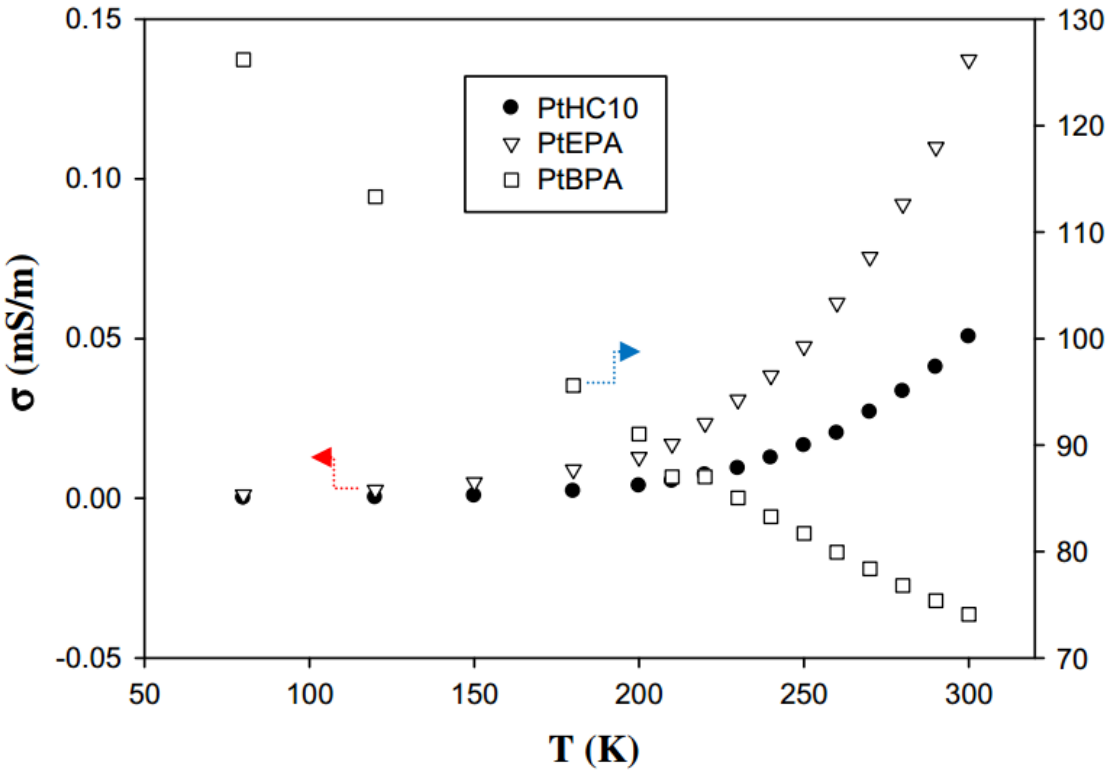


Figure 3.6. Variation of nanoparticle ensemble conductivity with temperature. Data are obtained from the slopes of the I-V curves in Fig.3.5. The left y axis is for both PtHC10 and PtEPA, and the right y axis for PtBPA alone.

Additional contributions may arise from the tert-butyl substituent group. Note that in nanoparticle solids, interparticle charge transfer takes place by a percolation pathway as the conducting metallic cores are embedded within an organic matrix. For straight-chain aliphatic capping ligands, because of the tight packing on the nanoparticle surface, charge transfer between neighboring nanoparticles most probably occurs by a hopping process through the molecular ligands, and the ensemble conductivity decreases exponentially with the ligand chain length because of intercalation between ligands of neighboring particles. In fact, this was manifested in further studies with the same Pt nanoparticles but capped with 1-alkynes of different chain lengths (i.e., 1-dodecyne, 1-tetradecyne, and 1-hexadecyne; results not shown), similar to that observed with alkyne-capped ruthenium nanoparticles[3g]. In contrast, for aromatic ligands, the packing is generally less tight because of steric hindrance, in particular with branched substituents such as the tert-butyl group. Thus, in these nanoparticle solid films, interparticle charge transfer is not necessarily through the surface ligands, but rather, via surface defects. Such a process is likely facilitated by the tert-butyl moiety, as tert-butyl group is known to exhibit higher electron-donating capability than the ethyl one[17]. This may explain why the PtEPA nanoparticles did not display the metallic characters like PtBPA, despite a similar ligand structure and extended chain length. Such tert-butyl effects have also been observed with molecular systems. For instance, recently Hankache and Wenger[18] examined the photoinduced electron transfer of covalent ruthenium(bipyridine)-

anthraquinone dyads and observed that the introduction of electron-donating tert-butyl substituents into the bipyridine ligands led to an order of magnitude enhancement of the electron transfer rate.

3.2.3. Electrocatalytic activity

In addition to an apparent difference of the ensemble conductivity, the above Pt nanoparticles also showed a marked variation of their electrocatalytic behaviors in oxygen reduction. Fig. 7 shows the steady-state cyclic voltammograms of a glassy-carbon disk electrode modified with a same amount (~ 2 μg) of PtHC10 (solid curve), PtEPA (dotted curve), PtBPA (dashed curve) and commercial Pt/C (dashed-double dotted curve) nanoparticles in 0.1 M NaOH at a potential sweep rate of 100 mV/s, after the electrodes were subject to about 30 potential cycles within the potential range of 0.80 V and +0.20 V (vs Hg/HgO). It can be seen that at all electrodes, the platinum butterfly features are quite well-defined. That is, in the anodic scan, a voltammetric peak emerged at ca. 0.11 V which can be attributed to the oxidation of the Pt surface. This was then reduced in the cathodic scan with a peak at 0.19 V. In addition, there appear a pair of voltammetric waves within the potential range of 0.50 V and 0.80 V, which may be ascribed to hydrogen adsorption/desorption on (naked) Pt surfaces, and from the integrated peak areas, the effective electrochemical surface area of the electrode was estimated to be 22.8 m^2/g_{Pt} (PtHC10), 21.0 m^2/g_{Pt} (PtEPA), and 8.1 m^2/g_{Pt} (PtBPA). In comparison to the physical surface area based on the nanoparticle average core size (98.1 m^2/g_{Pt} from Fig. 1), this represents 23.2%,

21.4%, and 8.3% of the Pt nanoparticle surface that was made accessible to electrolyte ions by the electrochemical treatments. Note that for ‘‘bare’’ commercial Pt/C, the effective electrochemical surface area was markedly higher at 61.5 m^2/g_{Pt}, signifying that about 72.5% of the Pt nanoparticle surface was electrochemically accessible[4c].

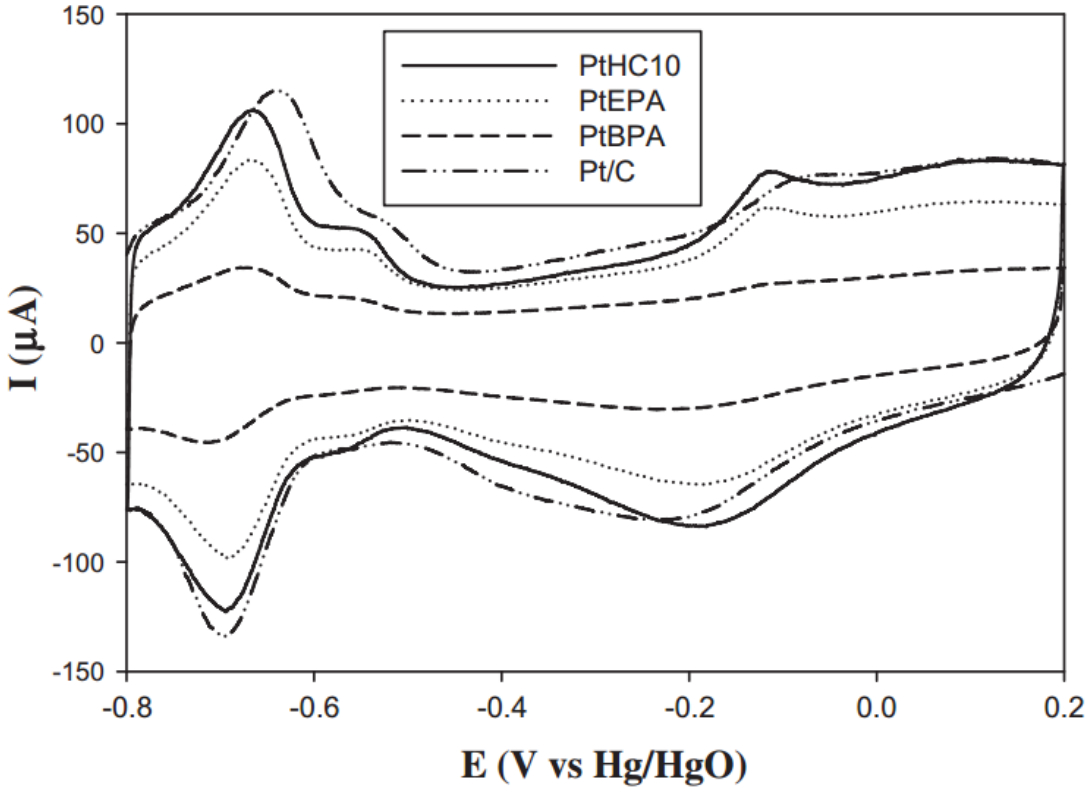


Figure 3.7. Cyclic voltammograms of a glassy-carbon disk electrode modified with PtHC10, PtEPA, PtBPA and commercial Pt/C nanoparticles in a nitrogen-purged 0.1M NaOH solution. Pt loadings were 2.44 μg (PtHC10), 1.90 μg (PtEPA), 1.90 μg (PtBPA), and 2.00 μg (Pt/C). Potential scan rate 100 mV/s.

Interestingly, the effective desorption of the capping ligands from the Pt nanoparticle surface happened to follow a trend opposite of the nanoparticle ensemble conductivity (vide ante). For the PtHC10 and PtEPA nanoparticles, both showed that more than 20% of the Pt surface area became accessible after the electrochemical treatments, whereas only 8.3% of the PtBPA nanoparticle surface was exposed. Note that the PtBPA nanoparticles exhibited metallic characters in interparticle charge transfer (Fig. 6), and thus the high electronic conductivity dictates that the potential drop within the nanoparticle layer would be significantly smaller than that in the semiconducting PtHC10 and PtEPA nanoparticles. Thus, the electrochemical desorption of the capping ligands from the PtBPA nanoparticle surface was less effective.

This discrepancy of the electrochemical reactivity also led to an apparent difference in the electrocatalytic reduction of oxygen, an important reaction process in fuel cell electrochemistry. Fig. 8 shows the ring and disk voltammograms of a gold ring-glassy-carbon disk electrode with the disk modified with (A) PtHC10, (B) PtEPA, (C) PtBPA, and (D) commercial Pt/C nanoparticles in an oxygen-saturated 0.1 M NaOH solution at varied rotation rates (the electrodes were the same as those in Fig. 7). It can be seen that on the disk electrode the cathodic currents of oxygen reduction start to emerge at +0.0 67 V (PtHC10), +0.077 V (PtEPA), +0.046 V (PtBPA), and +0.026 V (Pt/C), respectively. That is, the on- set potentials of the three acetylene-capped Pt nanoparticles were all somewhat more positive than that at the commercial Pt/C

catalysts, implying that oxygen reduction was facilitated at the acetylene-functionalized Pt nanoparticles as compared to the naked ones. Additionally, the voltammetric currents for oxygen reduction reach a plateau at potentials more negative than 0.40 V, and increase with increasing electrode rotation rate (from 100 to 2500 rpm). Notably, the corresponding ring currents collected at +0.40 V are all at least one order of magnitude smaller, indicating that the amounts of hydrogen peroxide (H_2O_2) produced during oxygen reduction were minimal. Importantly, from the ratio between the ring (I_R) and disk (I_D) currents, the number of electron transfer (n) in oxygen electroreduction can be estimated, n = $\frac{4I_D}{I_D+\frac{I_R}{N}}$ with N being the collection efficiency (37%)[4c]: PtHC10, 3.98; PtEPA, 3.92; PtBPA, 3.91; and Pt/C, 3.81[4c], suggesting that with the four nanoparticle catalysts, oxygen underwent efficient four-electron reduction to water, $O_2 + 2H_2O + 4e \leftrightarrow 4OH^-$.

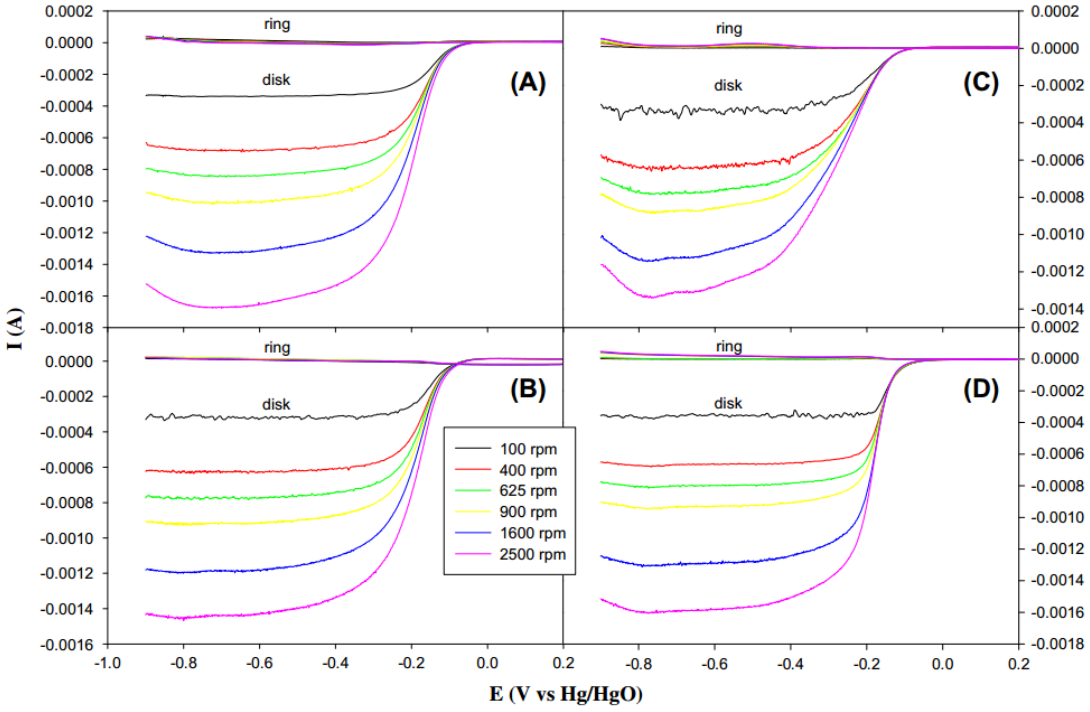


Figure 3.8. RRDE voltammograms of a gold ring-glassy-carbon disk electrode modified with (A) PtHC10, (B) PtEPA, (C) PtBPA and (D) commercial Pt/C nanoparticles in an oxygen-saturated 0.1M NaOH solution. Electrode rotation rates are specified in the figure legends. Pt loadings were 2.44 µg (PtHC10), 1.90 µg (PtEPA), 1.90 µg (PtBPA), and 2.00 µg (Pt/C). Ring currents were collected by setting the ring potential at +0.4 V.

Further insights into the electron transfer dynamics of oxygen reduction were obtained from the analysis of the Koutecky–Levich plots (I^{-1} vs $\omega^{-1/2}$). Note that in rotating disk voltammetric measurements, the measured currents (I) may involve both kinetic(I_K) and diffusion (I_D) controlled contributions[19],

$$\frac{1}{I} = \frac{1}{I_K} + \frac{1}{I_D} = \frac{1}{I_K} + \frac{1}{B\omega^{1/2}} \tag{3.1a}$$

$$B = 0.62nAFC_oD_o^{2/3}\nu^{-1/6} \tag{3.1b}$$

$$I_K = nFAkC_o \tag{3.1c}$$

where ω is the electrode rotation rate, n is the overall number of electron transfer, F is the Faraday constant, C_O is the bulk concentration of O_2 dissolved in the electrolyte, D_O is the diffusion coefficient for O_2, and ν is the kinematic viscosity of the electrolyte[20]. Thus, the plots of I^{-1} versus $\omega^{-1/2}$ are anticipated to yield straight lines with the intercept corresponding to I_K (Eq. (3.1c)) and the slopes reflecting the so-called B factors (Eq. (3.1b)). Fig. 9 displays the Koutecky–Levich plots of oxygen electroreduction at the four nanoparticle catalysts. One can see that within the potential range of 0.10 V to 0.30 V, the experimental data can all be fitted very well with linear regressions, and the slopes of each nanoparticle catalyst remained approximately constant. The linearity and parallelism of the plots are usually taken as a strong indication of a first-order reaction with respect to dissolved oxygen.

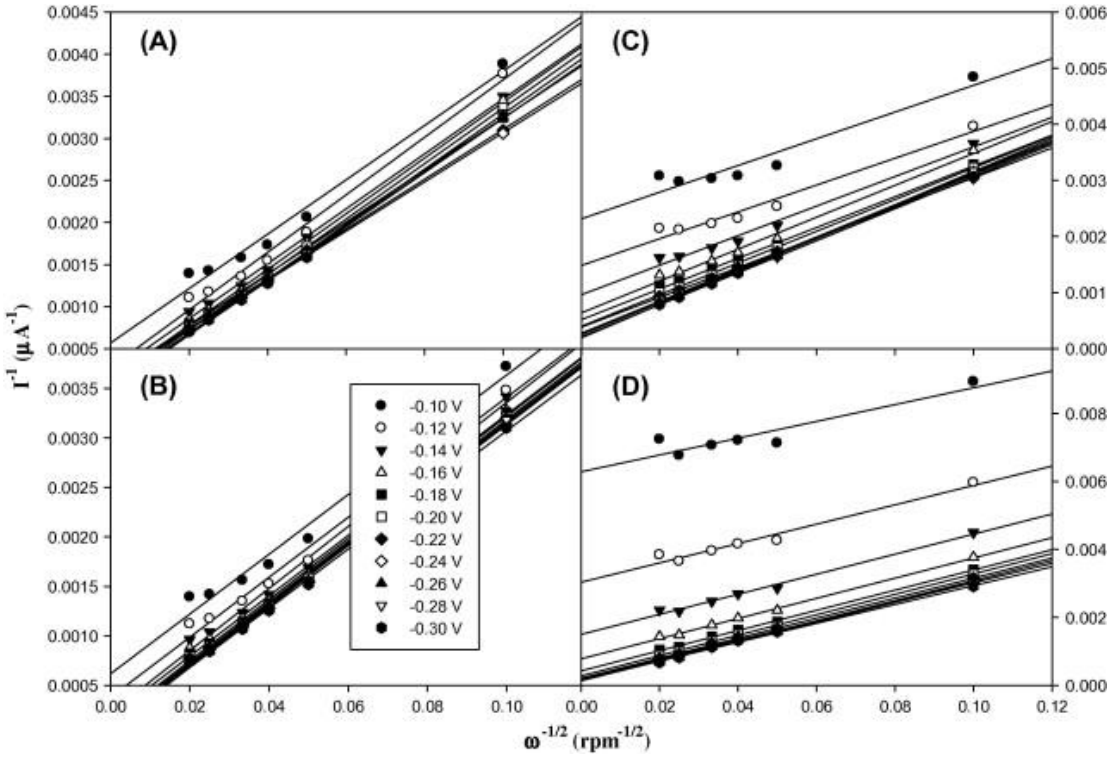


Figure 3.9. Koutecky-Levich plots of (A) PtHC10, (B) PtEPA, (C) PtBPA and (D) commercial Pt/C nanoparticles in oxygen reduction in 0.1M NaOH solution. Symbols are experimental data acquired from Fig 3.8 and lines are the corresponding linear regressioins.

In addition, from the y-axis intercepts of the linear regressions, the kinetic currents in oxygen reduction can also be quantitatively evaluated (Eq. (1a)). Interestingly, when normalized to the effective electrochemical surface area as estimated from Fig. 3.7, the kinetic current density (J_K) of the three acetylene-functionalized Pt nanoparticles was all markedly higher than that of the commercial "bare" Pt/C catalysts (Fig. 10), again, suggesting that surface functionalization by acetylene derivatives on the Pt surface facilitated the electroreduction of oxygen. Additionally, one may notice that whereas the experimental data for PtHC10 were somewhat scattered, the kinetic current density of PtEPA was consistently greater than that of PtBPA within the entire potential range of 0.10 V to 0.30 V. For instance, at 0.18 V, the kinetic current densitie ((J_K) at the four nanoparticle catalysts are 12.6 mA/cm^2 (PtBPA), 19.1 mA/cm^2 (PtEPA), 12.3 mA/cm^2 (PtHC10), and 4.1 mA/cm^2 (Pt/C), respectively.

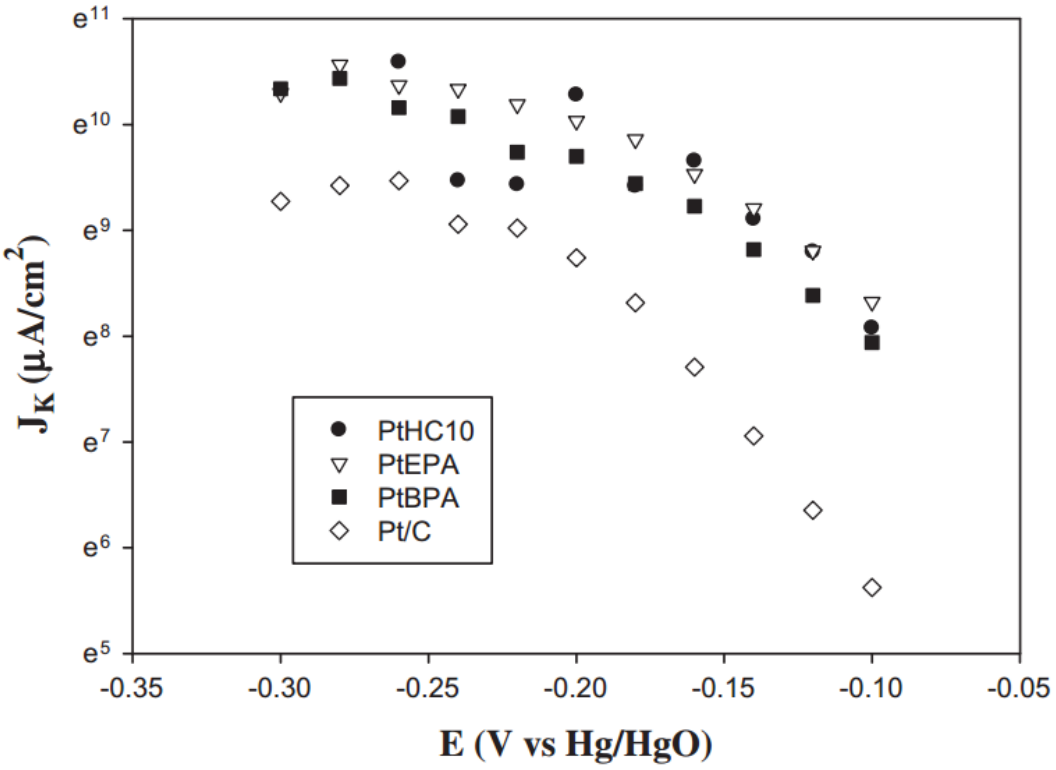


Figure 3.10. Variation of the kinetic current density (J_k) with electrode potential at different nanoparticle catalysts in oxygen reduction. Symbols are experimental data obtained from the intercepts in Fig 3.9 and normalized to the effective electrochemical surface areas estimated from Fig 3.7.

Therefore, it can be seen that on the basis of the onset potential and kinetic current density, of the three nanoparticle catalysts, the PtEPA nanoparticles exhibited the best electrocatalytic activity for oxygen reduction. This may be accounted for by the reaction mechanism of oxygen reduction on Pt surfaces. It has been known that the first electron-transfer process for the adsorbed oxygen molecules represents the rate-determining step[21],

$$Pt(O_{2,ad}) + e^- \rightarrow Pt(O^-_{2,ad}) \quad (3.2)$$

where oxygen is adsorbed onto the Pt surface in a linear or bridge-bonded configuration, involving both electron donation from the filled O_2 orbitals to the empty orbitals of Pt surface atoms by σ overlap, as well as back bonding interactions from the Pt filled d orbitals to the empty O_2 antibonding orbitals (π^*). Thus, it can be seen that an increase of the Pt d vacancy would facilitate electron donation from O_2 to Pt, leading to enhanced bonding interactions between Pt and O_2 and concurrently decreasing bonding order of O-O. Consequently, oxygen reduction is enhanced. Of the three nanoparticles under study above, extensive spilling of the Pt core electrons to the ligand shells is anticipated to occur because of the conjugated metal–ligand interfacial bonding interactions, and this intraparticle charge delocalization is more effective for the PtEPA and PtBPA nanoparticles than for the PtHC10 nanoparticles, as manifested in spectroscopic measurements presented above. Therefore, the effective electron density within the PtEPA and PtBPA nanoparticles is anticipated to be even somewhat lower than that of PtHC10, leading to enhanced

bonding adsorption between O_2 and Pt and eventual oxygen reduction activity. However, the less effective desorption of BPA ligands from the Pt nanoparticles rendered it difficult for O_2 and electrolyte counter ions to access the Pt surface and hence compromised the electrocatalytic activity. Consequently, within the present experimental context, PtEPA represented the optimal conditions for oxygen electroreduction by virtue of the extensive intraparticle charge delocalization and relative ease of partial ligand desorption from the nanoparticle surface.

3.3. Conclusion

Stable platinum nanoparticles were prepared by thermolytic reduction of H_2PtCl_4 followed by the self-assembly of acetylene derivatives onto the bare Pt colloid surface. TEM measurements showed the average core diameter of the nanoparticles was 2.85 ± 0.62 nm. FTIR measurements confirmed the bonding interactions of the acetylene ligands onto the Pt surface with the breaking of the ≡C-H bond and the formation of $Pt_{surface}$-H and $Pt_{surface}$-C≡ at the metal-ligand interface, as manifested by the disappearance of the ≡C-H vibrational stretches and the marked redshift of the C≡C vibrational band. With the conjugated metal-ligand interfacial bonding interactions, extended conjugation occurred between the particle-bound triple bonds, leading to the emergence of unique photoluminescence properties of the nanoparticles. Additionally, electronic conductivity measurements showed that for the nanoparticles stabilized by 1-alkynes or 4-ethylphenylacetylene, the temperature dependence of the ensemble

conductivity exhibited semiconducting characters whereas for the 4-tert-butylphenylacetylene-capped nanoparticles, metallic behaviors were observed instead. This discrepancy was accounted for by the reduced metal–ligand contact resistance and extensive spilling of core electrons into the organic protecting matrix. Furthermore, the acetylene-capped nanoparticles showed interesting electrocatalytic activity in oxygen reduction. On the basis of the onset potential and kinetic current density, all three nanoparticles exhibited improved performance as compared to naked commercial Pt/C catalysts; and among the series, 4-ethylphenylacetylene-capped nanoparticles exhibited the best electrocatalytic performance. This was accounted for by the deliberate manipulation of the Pt core electronic structure that impacted the bonding interactions with adsorbed oxygen and accessibility of the Pt surface by electrolyte counterions. The results presented herein further demonstrate the effectiveness of surface chemical functionalization in the manipulation and optimization of nanoparticle electrocatalytic activity in fuel cell electrochemistry.

3.4. References

1. Chen, S. W., Impact of Metal-Ligand Bonding Interactions on the Electron-Transfer Chemistry of Transition-Metal Nanoparticles. *Electroanal Chem* **2010,** *23*, 171-210.

2. (a) Ghosh, D.; Chen, S. W., Palladium nanoparticles passivated by metal-carbon covalent linkages. *J Mater Chem* **2008,** *18* (7), 755-762; (b) Ghosh, D.; Pradhan, S.; Chen, W.; Chen, S. W., Titanium nanoparticles stabilized by Ti-C covalent bonds. *Chem Mater* **2008,** *20* (4), 1248-1250.

3. (a) Chen, W.; Chen, S. W.; Ding, F. Z.; Wang, H. B.; Brown, L. E.; Konopelski, J. P., Nanoparticle-mediated intervalence transfer. *J Am Chem Soc* **2008,** *130* (36), 12156-12162; (b) Chen, W.; Brown, L. E.; Konopelski, J. P.; Chen, S. W., Intervalence transfer of ferrocene moieties adsorbed on electrode surfaces by a conjugated linkage. *Chem Phys Lett* **2009,** *471* (4-6), 283-285; (c) Chen, W.; Zuckerman, N. B.; Lewis, J. W.; Konopelski, J. P.; Chen, S. W., Pyrene-Functionalized Ruthenium Nanoparticles: Novel Fluorescence Characteristics from Intraparticle Extended Conjugation. *J Phys Chem C* **2009,** *113* (39), 16988-16995; (d) Chen, W.; Zuckerman, N. B.; Kang, X. W.; Ghosh, D.; Konopelski, J. P.; Chen, S. W., Alkyne-Protected Ruthenium Nanoparticles. *J Phys Chem C* **2010,** *114* (42), 18146-18152; (e) Chen, W.; Zuckerman, N. B.; Konopelski, J. P.; Chen, S. W., Pyrene-Functionalized Ruthenium Nanoparticles as Effective Chemosensors for Nitroaromatic Derivatives. *Anal Chem* **2010,** *82* (2), 461-465; (f) Chen, W.; Pradhan, S.; Chen, S. W., Photoluminescence and conductivity studies of anthracene-functionalized ruthenium nanoparticles. *Nanoscale* **2011,** *3* (5), 2294-2300; (g) Kang, X. W.; Zuckerman, N. B.; Konopelski, J. P.; Chen, S. W., Alkyne-Functionalized Ruthenium Nanoparticles: Ruthenium-Vinylidene Bonds at the Metal-Ligand Interface. *J Am Chem Soc* **2012,** *134* (3), 1412-1415.

4. (a) Zhou, Z. Y.; Kang, X. W.; Song, Y.; Chen, S. W., Butylphenyl-functionalized palladium nanoparticles as effective catalysts for the electrooxidation of formic acid. *Chem Commun* **2011,** *47* (21), 6075-6077; (b) Zhou, Z. Y.; Ren, J.; Kang, X. W.; Song, Y.; Sun, S. G.; Chen, S. W., Butylphenyl-functionalized Pt nanoparticles as CO-resistant electrocatalysts for formic acid oxidation. *Phys Chem Chem Phys* **2012,** *14* (4), 1412-1417; (c) Zhou, Z. Y.; Kang, X. W.; Song, Y.; Chen, S. W., Enhancement of the electrocatalytic activity of Pt nanoparticles in oxygen reduction by chlorophenyl functionalization. *Chem Commun* **2012,** *48* (28), 3391-3393.

5. Muetterties, E. L.; Tsai, M. C.; Kelemen, S. R., Chemistry of Acetylene on Platinum (111) and (100) Surfaces. *Proceedings of the National Academy of*

Sciences of the United States of America-Physical Sciences **1981,** *78* (11), 6571-6575.

6. Peuckert, M.; Yoneda, T.; Betta, R. A. D.; Boudart, M., Oxygen Reduction on Small Supported Platinum Particles. *J Electrochem Soc* **1986,** *133* (5), 944-947.

7. Whiffen, D. H., Infra-Red Summation Bands of the out-of-Plane C-H Bending Vibrations of Substituted Benzene Compounds. *Spectrochim Acta* **1955,** *7* (5), 253-263.

8. Kang, X. W.; Zuckerman, N. B.; Konopelski, J. P.; Chen, S. W., Alkyne-Stabilized Ruthenium Nanoparticles: Manipulation of Intraparticle Charge Delocalization by Nanoparticle Charge States. *Angew Chem Int Edit* **2010,** *49* (49), 9496-9499.

9. Feilchenfeld, H.; Weaver, M. J., Binding of Alkynes to Silver, Gold, and Underpotential-Deposited Silver Electrodes as Deduced by Surface-Enhanced Raman-Spectroscopy. *J Phys Chem-Us* **1989,** *93* (10), 4276-4282.

10.Creighton, J. A.; Eadon, D. G., Ultraviolet Visible Absorption-Spectra of the Colloidal Metallic Elements. *J Chem Soc Faraday T* **1991,** *87* (24), 3881-3891.

11.Black, H. K.; Horn, D. H. S.; Weedon, B. C. L., Studies with Acetylenes .1. Some Reactions of Grignard Reagents with Alk-1-Ynyl and Alk-1-Enyl Halides. *J Chem Soc* **1954,** (Jun), 1704-1709.

12.Glimsdal, E.; Carlsson, M.; Kindahl, T.; Lindgren, M.; Lopes, C.; Eliasson, B., Luminescence, Singlet Oxygen Production, and Optical Power Limiting of Some Diacetylide Platinum(II) Diphosphine Complexes. *J Phys Chem A* **2010,** *114* (10), 3431-3442.

13.Chen, S. J.; Yu, S. N.; Tzeng, J. E.; Chen, Y. T.; Chang, K. Y.; Cheng, K. S.; Hsiao, F. T.; Wei, C. K., Characterization of the Major Histopathological Components of Thyroid Nodules Using Sonographic Textural Features for Clinical Diagnosis and Management. *Ultrasound Med Biol* **2009,** *35* (2), 201-208.

14.D.R.Lide, *CRC Handbook of Chemistry and Physics: a Ready-Reference Book of Chemical and Physical Data*. CRC Press: Boca Raton, Fla, 2004.

15.(a) Mann, D.; Javey, A.; Kong, J.; Wang, Q.; Dai, H. J., Ballistic transport in metallic nanotubes with reliable Pd ohmic contacts. *Nano Lett* **2003,** *3* (11), 1541-1544; (b) Tarakeshwar, P.; Kim, D. M., Modulation of the electronic structure of semiconducting nanotubes resulting from different metal contacts. *J Phys Chem B* **2005,** *109* (16), 7601-7604; (c) Woo, Y.; Duesberg, G. S.; Roth, S., Reduced contact resistance between an individual single-walled carbon nanotube

and a metal electrode by a local point annealing. *Nanotechnology* **2007,** *18* (9).

16.Pradhan, S.; Ghosh, D.; Xu, L. P.; Chen, S. W., Interparticle charge transfer mediated by pi-pi stacking of aromatic moieties. *J Am Chem Soc* **2007,** *129* (35), 10622-+.

17.Raj, X. J.; Rajendran, N., Corrosion Inhibition Effect of Substituted Thiadiazoles on Brass. *Int J Electrochem Sc* **2011,** *6* (2), 348-366.

18.Hankache, J.; Wenger, O. S., Photoinduced electron transfer in covalent ruthenium-anthraquinone dyads: relative importance of driving-force, solvent polarity, and donor-bridge energy gap. *Phys Chem Chem Phys* **2012,** *14* (8), 2685-2692.

19.A.J.Bard, L. R. F., *Electrochemical Methods: Fundamentals and Applications*. John Wiley: New York 2001.

20.Chen, W.; Kim, J. M.; Sun, S. H.; Chen, S. W., Electrocatalytic reduction of oxygen by FePt alloy nanoparticles. *J Phys Chem C* **2008,** *112* (10), 3891-3898.

21.(a) Paulus, U. A.; Wokaun, A.; Scherer, G. G.; Schmidt, T. J.; Stamenkovic, V.; Markovic, N. M.; Ross, P. N., Oxygen reduction on high surface area Pt-based alloy catalysts in comparison to well defined smooth bulk alloy electrodes. *Electrochim Acta* **2002,** *47* (22-23), 3787-3798; (b) Toda, T.; Igarashi, H.; Uchida, H.; Watanabe, M., Enhancement of the electroreduction of oxygen on Pt alloys with Fe, Ni, and Co. *J Electrochem Soc* **1999,** *146* (10), 3750-3756.

Chapter 4

Oxygen Reduction Catalyzed by Platinum Nanoparticles Supported on Graphene Quantum Dots

Reproduced with permission from [Guoqiang He, Yang Song, Ke Liu, Andrew Walter, Sophie Chen, Shaowei Chen*, "Oxygen Reduction Catalyzed by Platinum Nanoparticles Supported on Graphene Quantum Dots", *ACS Catal.*, **2013**, *3*, 831.] Copyright © 2013 American Chemical Society.

4.1 Introduction

Precious metals have been used extensively as effective cathode catalysts for oxygen reduction in proton exchange membrane fuel cells. Typically these materials are dispersed as nanosized particles on supporting substrates of high surface areas to enhance accessibility and to reduce costs. In these, it has been found that the electronic interactions between the metal nanoparticles and the supporting substrates might also play a significant role in determining the electrocatalytic activity as a result of the manipulation of the electronic energy of the metalnanoparticles and hence the interactions with oxygen[1]. In both industrial and academic research, carbon-based materials are one of the most commonly used supporting substrates, such as carbon black, carbon nanotubes, and graphene sheets[2]. This is largely due to their low cost, high surface area, high conductivity, and high chemical inertness that may facilitate electron-transfer reactions at the electrode surface and hence improve catalyst stability and durability.

Among these, while a relatively new addition, graphene has attracted particular research interest in fuel cell electrocatalysis. In fact, a number of studies have been reported recently in the literature where graphene sheets are used as a support for the nanoparticle catalysts in oxygen reduction[3]. For instance, platinum nanoparticles (from 2.2 to 5.6 nm in dia.) supported on reduced graphene oxides (Pt/RGO) have been prepared by using perfluorosulfonic acid as the functionalization and anchoring reagent[4]. The catalytic performance in oxygen reduction was found to be enhanced by hydrogen heat treatment, which

was ascribed to the bifunctional effects of both improved graphitization and the oxygenated groups on the catalytic activity and stabilization of the metal nanoparticles. Inanother study[5], graphene-supported platinum nanoparticle composites were prepared by a chemical co-reduction method. The platinum nanoparticles were between 3.30 and 4.45 nm in diameter and exhibited apparent electrocatalytic activity in oxygen reduction. Furthermore, a composite catalyst has also been prepared by using graphene-supported platinum nanoparticles (average diameter 3.4 nm) impregnated with ionic liquid that exhibited enhanced electrocatalytic activity and excellent methanol tolerance for oxygen reduction because of increasing oxygen-philicity and methanol-phobicity[6].

In these early studies, the graphene sheets are generally produced from bulk graphite by the Hummers method through chemical oxidation and exfoliation with strong acids and oxidizing reagents[7]. The obtained graphene sheets mostly exhibit irregular shapes and a large size dispersity (ranging from nanoscale to micrometer-scale), and are prone to folding and wrinkling because of the strong π–π interactions, thus compromising the even dispersion and ready accessibility of the metal nanoparticle catalysts[8]. To overcome such technical challenges, a recent study showed that by inserting carbon black particles between the RGO sheets, stacking of RGO might be minimized, hence promoting oxygen diffusion through the RGO sheets and enhancing the electrocatalytic performance of graphene-supported Pt nanoparticles (5 nm in dia.)[2a]. Such issues can also be resolved by using nanosized graphene sheets[9]. Recently, an effective

protocol was reported for the preparation of nanometer-sized graphene quantum dots (GQDs) where the stacked submicrometer domains of traditional pitch-based carbon fibers were broken down by acid treatments and chemical exfoliation[9c].The size of the resulting GQDs was found to be within the range of 1 to 4 nm with 1 to 3 layers in thickness. Because of their large surface-volume ratio, such GQDs are anticipated to exhibit abundant structural defects, which may be exploited to promote charge transfer from platinum to oxygen as well as to manipulate the binding of reaction intermediates on the Pt surface, as suggested in a recent theoretical study[10]. This is the primary motivation of the present study.

In this study, we adopted the literature procedure to prepare GQDs from carbon fibers[9c] and then used them as supporting substrates for platinum nanoparticles. The electrocatalytic activity of the resulting nanocomposites (Pt/G) in oxygen reduction was then examined in acid electrolyte solutions, using commercial Pt/C catalysts as a benchmark material for comparative study. Voltammetric measurements showed that while oxygen was effectively reduced to water at both nanoparticle catalysts, the Pt/G nanocomposites exhibited a markedly enhanced electrocatalytic performance with a more positive onset potential, higher specific activity as well as stability, as compared to commercial Pt/C. The results were accounted for by the intimate electronic interactions between the nanosized GQDs and the Pt nanoparticles that manipulated the dissociative adsorption of oxygen and the binding of reaction intermediates on

the Pt surface.

4.2 Results and Discussion

Note that from DLS measurements the average hydrodynamic diameter of the as-produced GQDs was estimated to be 14.5 ± 3.9 nm; and AFM topographic analysis indicated that the thickness of the graphene quantum dots ranged from 0.5 to 2.0 nm, corresponding to one to four graphene (oxide) layers in the samples, consistent with TEM measurements (Supporting Information, Figure S1). These GQDs were then used to prepare Pt/G hybrid nanoparticles. Figure 1 shows two representative TEM micrographs of the Pt/G nanoparticles. In panel (A), it can be seen that the nanoparticles were dispersed rather homogeneously on the TEM grid, with the majority of the nanoparticles in the narrow range of 2.5 to 3.0 nm in diameter, as manifested in the core size histogram in the figure inset. In addition, statistical analysis shows that the average nanoparticle core diameter was 2.79±0.38 nm, slightly smaller than that of commercial Pt/C (3.30 ± 0.42 nm)[11]. Furthermore, from high-resolution TEM studies in panel (B), clearly defined lattice fringes can be identified, as highlighted by yellow lines, with a spacing of 0.23 nm. These are consistent with the (111) crystalline planes of fcc Pt[11]. In addition, one may see that the Pt nanoparticles were surrounded by a low-contrast halo, as indicated by white arrows, which might be ascribed to the GQDs that exhibited low crystallinity and low electron-density contrast. These results suggest the formation of an intimate composite structure in the Pt/G nanoparticles.

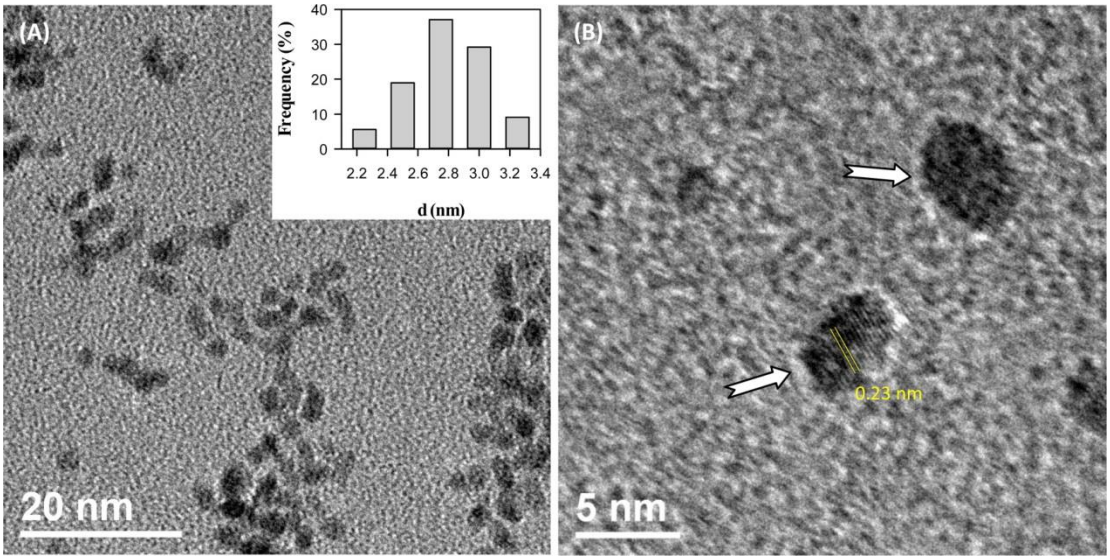


Figure 4.1. Representative TEM micrographs of GQD-supported Pt nanoparticles. Scale bar is 20 nm in panel (A) and 5 nm in panel (B). Inset in panel (A) shows the nanoparticle core size histogram. Yellow lines in panel (B) highlight the lattice fringes, and white arrows indicate the halos surrounding the Pt nanoparticles.

The composite nature of the Pt/G nanoparticles was further manifested in XRD measurements. From Figure 2, one can see that the nanoparticles (red curve) exhibited three well-defined diffraction peaks at $2\theta = 39.85°$, 46.23°, and 67.60° that may be assigned to the (111), (200), and (220) crystalline planes of fcc Pt, respectively. Additionally, the Pt/G nanoparticles also displayed two broad diffraction peaks centered at $2\theta \approx 25.80°$ and 22.67°, corresponding to a lattice spacing of 0.345 and 0.392 nm, respectively. Whereas both may be assigned to the graphite (002) planes, the somewhat larger value of the latter suggests lattice expansion as a result of the formation of oxygen-containing groups during the chemical oxidation and exfoliation of the carbon fibers[9c]. Additionally, the broad appearance of these peaks signifies the low crystallinity of the resulting GQDs, consistent with the results in TEM measurements presented in Figure 1 (B). Such diffraction features can also be clearly identified with the commercial Pt/C sample (black curve), except that the graphite diffraction peak was rather weak and ill-defined.

Furthermore, the average size (τ) of the crystalline domains of the Pt nanoparticles can be estimated by the Debye−Scherrer equation[12], $\tau = K\lambda/\beta \cos\theta$, where K is a dimensionless shape factor with a value of ~0.9, λ is the X-ray wavelength (1.54059 Å for Cu−Kα), and β is the full width at half-maximum (fwhm) of a selected diffraction peak. Therefore, based on the fwhm of the Pt(111) diffraction peaks, the average size of the nanoparticle crystalline domains was estimated to be 1.54 nm for Pt/C and 2.62 nm for Pt/G. The fact that the size

of the crystalline domains of the Pt/G nanoparticles was close to their geometrical diameter as determined by TEM measurements (Figure 1) signifies that the nanoparticles were likely of single crystal structures, in agreement with the clearly defined lattice fringes throughout the entire nanoparticles. In contrast, the size of the crystalline domains of the Pt/C nanoparticles was only half of the physical dimensions, suggesting a polycrystalline nature of the platinum nanoparticles in the commercial sample.

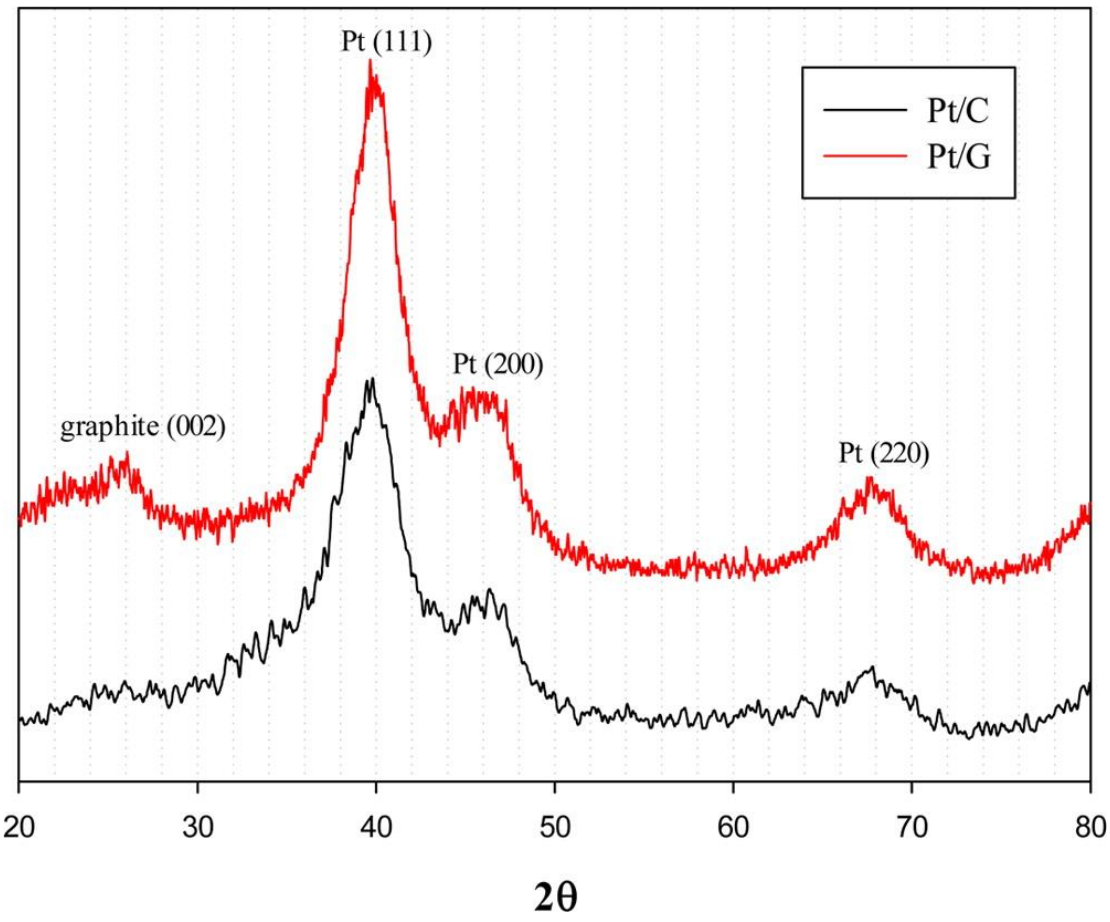


Figure 4.2. XRD patterns of the Pt/G and Pt/C nanoparticles.

The formation of a platinum-graphene nanocomposite in Pt/G particles was also evidenced in XPS measurements. Figure 3 depicts the survey spectra of the (A) Pt4f and (B) C1s electrons of the Pt/G nanoparticles. From panel (A), the binding energies of the Pt4f electrons can be found at 71.22 and 74.63 eV. Both the doublet energies and spin−orbit coupling are consistent with those of metallic platinum[13]. In panel (B), deconvolution revealed four major components of the carbon 1s electrons: sp^2 C at 284.53 eV (magenta curve)[14], sp^3 C at 285.46 eV (blue curve)[15], and carbon in C−OH (286.57 eV, yellow curve) and COOH (289.20 eV, green curve) bonds[9c, 16]. This suggests the formation of various oxygenated functional moieties on the GQD surfaces. Furthermore, one may notice that the concentration of sp^2 carbons is markedly lower than those of others, likely a result of the nanoscale dimensions of the graphene quantum dots and the formation of abundant oxygenated species on the graphene surface. Such structural defects within the GQD matrix might facilitate charge transfer between platinum and adsorbed oxygen and hence lead to improved electrocatalytic performance in oxygen reduction, as detailed below[10].

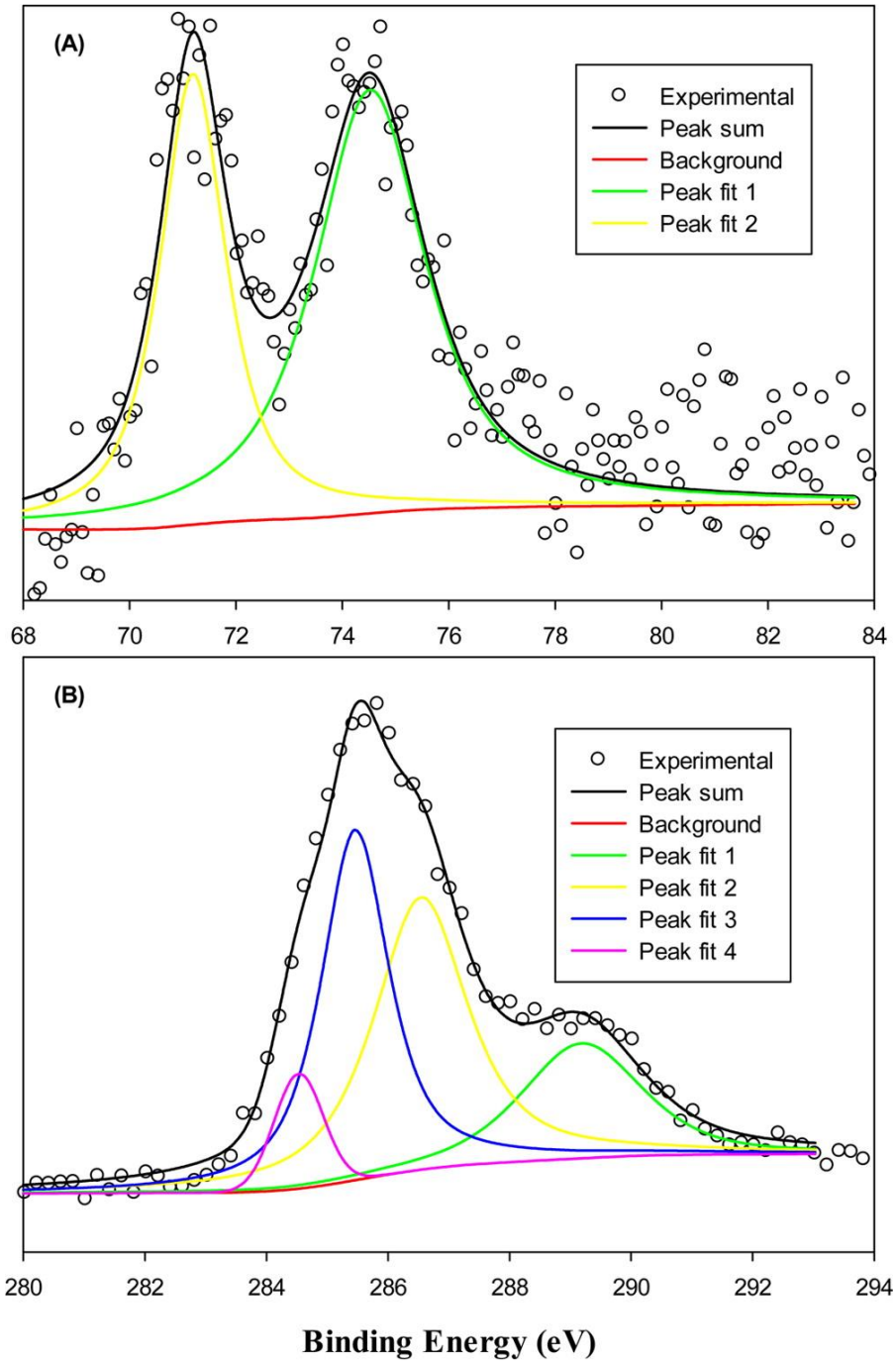


Figure4.3. XPS survey spectra of the (A) Pt4f and (B) C1s electrons of the Pt/G nanoparticles. Symbols are experimental data and lines are deconvolution fits.

The electrocatalytic activity of the resulting Pt/G nanoparticles was then examined for oxygen reduction reactions. Figure 4 shows the steady-state cyclic voltammograms of a glassy carbon electrode modified with a same amount of Pt/G or Pt/C in 0.1 M $HClO_4$ solution saturated with nitrogen. Both nanoparticles exhibited the well-defined butterfly voltammetric features of platinum in acid electrolytes. Of these, a pair of broad voltammetric peaks can be seen within the potential range of +0.6 and +1.0 V, which are ascribed to the formation of platinum oxide in the anodic scan and reduction of the oxide in the return sweep. Two additional pairs of voltammetric peaks appeared between 0 and +0.3 V. These are due to hydrogen adsorption/desorption on the platinum surface. Based on the integrated areas of these voltammetric features, the effective electrochemical surface area (ECSA) of the nanoparticle catalysts can be estimated to be 24.3 m^2/g for Pt/G and 20.1 m^2/g for Pt/C. In comparison to the geometric surface areas of the nanoparticles, this represents approximately 24.4% and 23.8% of the nanoparticle surface that was electrochemically accessible for the Pt/G and Pt/C nanoparticles, respectively.

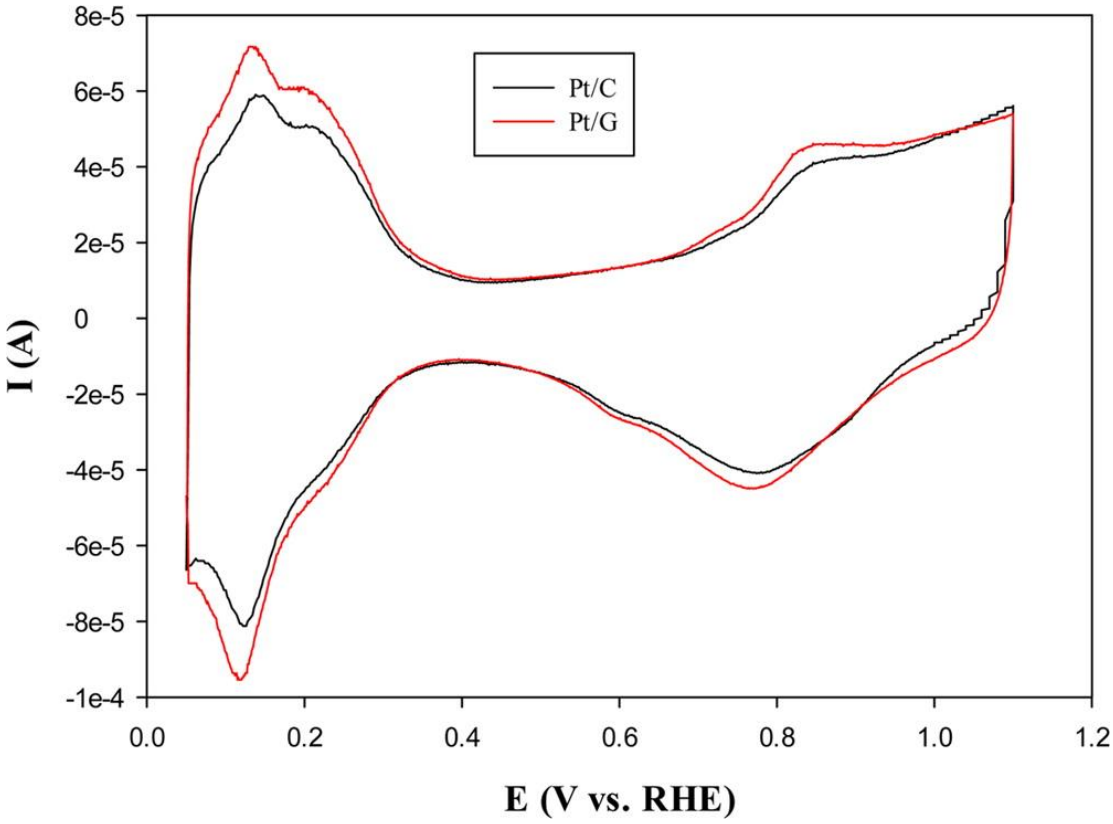


Figure 4.4. Cyclic voltammograms of a glassy carbon electrode (diameter 5.61 mm) loaded with Pt/G and Pt/C nanoparticle catalysts in a nitrogen-saturated 0.1 M HClO4 solution. Metal loading was 12.1 μg for both nanoparticles. Potential sweep rate 20 mV/s.

The electrocatalytic activity in oxygen reduction was then examined by voltammetric measurements in an oxygen-saturated 0.1 M $HClO_4$ solution. Figure 5 shows the RRDE voltammograms of the glassy carbon disk electrode modified with (A) Pt/C or (B) Pt/G nanoparticles with the electrode rotation rate varied from 100 rpm to 2500 rpm. There are at least two aspects that warrant attention here. First, at both electrodes nonzero cathodic currents at the disk electrode (I_D) became clearly identified as the electrode potential was swept in the negative direction, and the currents increased with increasing electrode rotation rates, signifying the apparent electrocatalytic activity of both nanoparticles in oxygen reduction. Second, the corresponding ring currents (I_R) at +1.5 V were about 3 orders of magnitude lower than those of the disk, suggesting that only minimal amounts of peroxide intermediates were produced during oxygen reduction and hence high efficiency of both nanoparticles in the electrocatalytic process. In fact, the number of electron transfer (n) during oxygen reduction can be estimated by the ratio between the disk and the ring currents[17],

$$n = \frac{4I_D}{I_D + (I_R/N)} \qquad (4.1)$$

where N is the collection efficiency (37%) of the RRDE electrode[11], as depicted in Figure 6. It can be seen that at sufficiently negative potentials, both electrodes exhibited $n \approx 4.00$, indicating that oxygen was fully reduced into water, $O_2 + 4H^+ + 4e \rightarrow 2H_2O$. Yet the onset potential for oxygen reduction was markedly

different. For Pt/C nanoparticles, the onset potential could be identified at +0.98 V, which was consistent with results observed previously[11]. In contrast, for Pt/G, the onset potential was substantially more positive at +1.05 V, which is among the best reported so far of oxygen reduction catalyzed by platinum nanoparticles[4-6]. Such a positive shift of about 70 mV signified the markedly improved performance of the Pt/G nanoparticles in oxygen reduction as compared to commercial Pt/C, likely a result of the electronic interactions between the platinum nanoparticles and the GQDs (more details below).

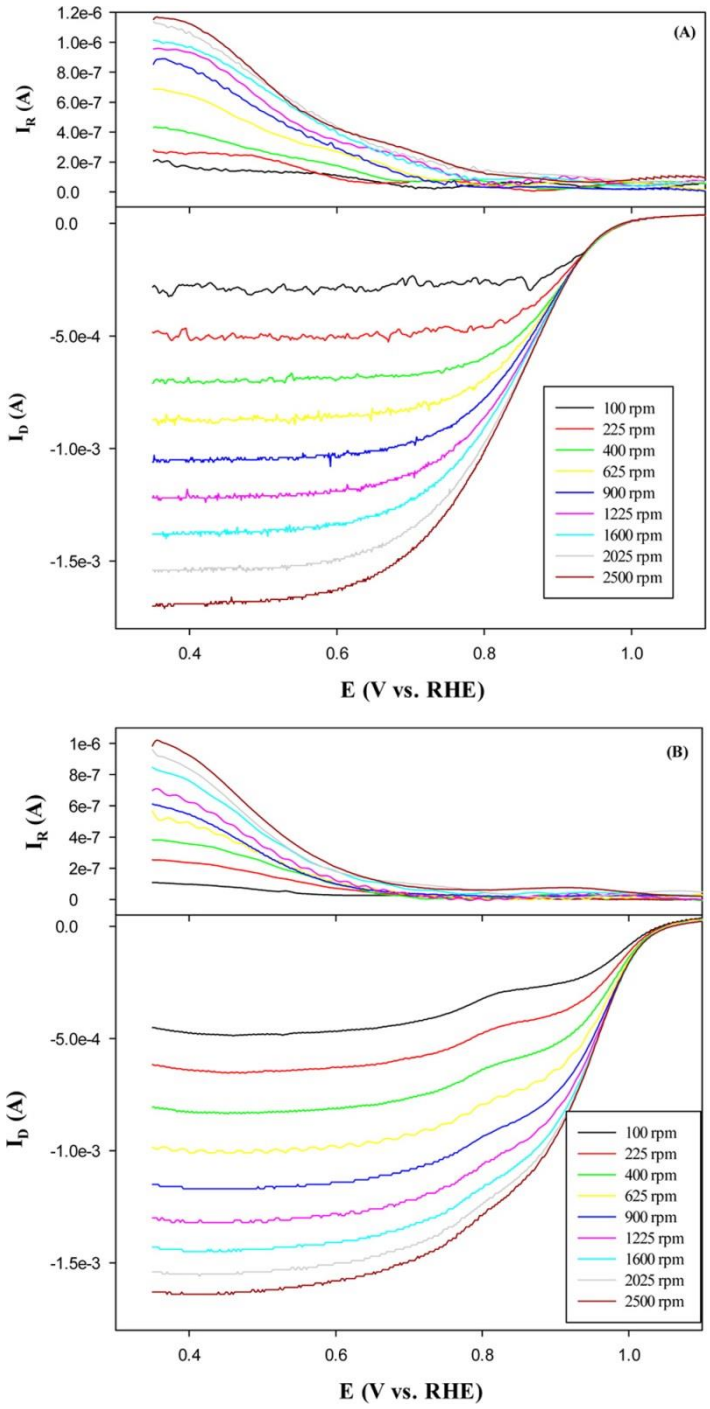


Figure 4.5. RRDE voltammograms of a glassy carbon electrode (diameter 5.61 mm) loaded with (A) Pt/C or (B) Pt/G nanoparticle catalysts in an oxygen-saturated 0.1 M HClO4 solution. Metal loading was 12.1 μg for both nanoparticles. Potential sweep rate was 5 mV/s; electrode rotation rates were shown in the figure legends; ring potential was set at +1.5 V.

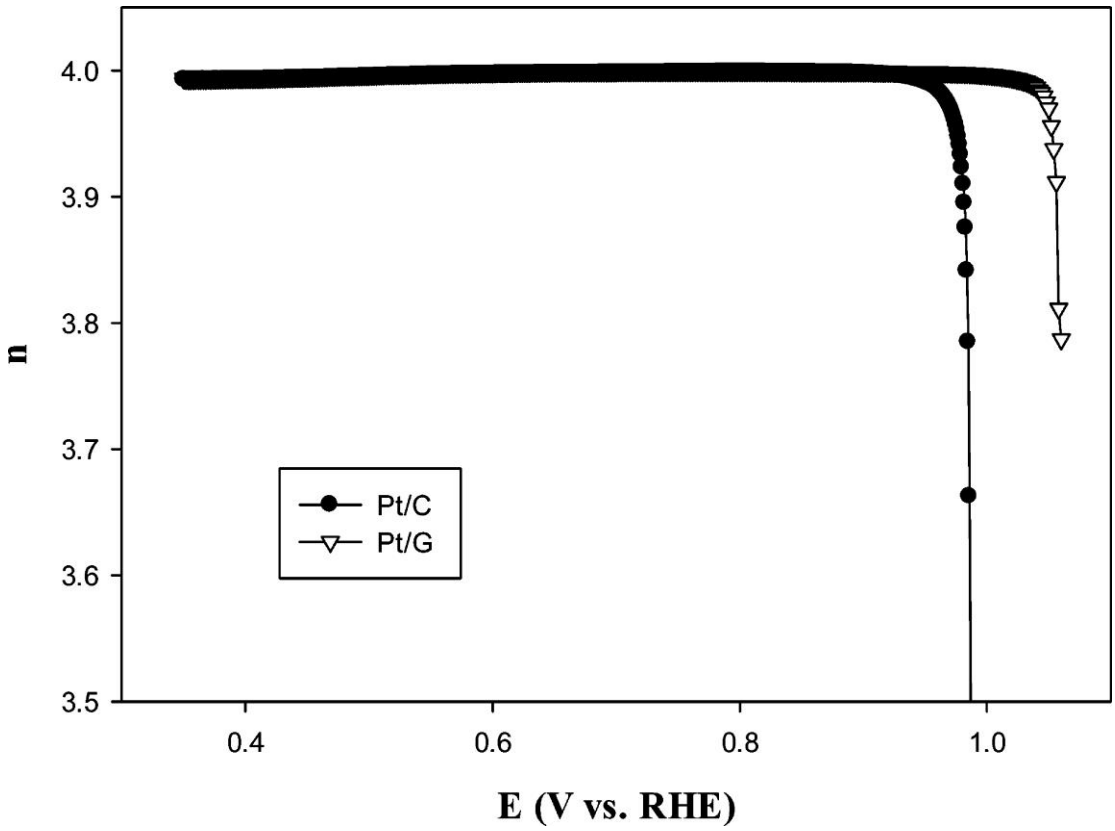


Figure 4.6. Variation of the number of electron transfer (n) in oxygen reduction with electrode potential. Symbols are experimental data calculated from the RRDE voltammograms at 2500 rpm in Figure 4.5 by using eq 1.

The electron-transfer kinetics involved were then quantified by the Koutecky−Levich analysis (eqs 4.2)[18], as the disk current (I_D) might include both kinetic- (I_k) and diffusion (I_d) controlled contributions,

$$\frac{1}{I_D} = \frac{1}{I_k} + \frac{1}{I_d} = \frac{1}{I_k} + \frac{1}{B\omega^{1/2}} \quad (4.2a)$$

$$B = 0.62nAFC_oD_o^{2/3}\nu^{-1/6} \quad (4.2b)$$

$$I_K = nFAkC_o \quad (4.2c)$$

where F is the Faradaic constant (96500 C/mol), D_O the diffusion coefficient of O_2 in 0.1 M $HClO_4$ aqueous solution (1.93×10^{-5} cm^2/s), ν the kinematic viscosity of the solution (9.87×10^{-3} cm^2/s), C_O the oxygen concentration in O_2-saturated solutions (1.18 mM), ω the electrode rotation rate, k the electron-transfer rate constant, and A the geometric surface area of the electrode[19]. Figure 7 depicts the Koutecky−Levich plots (I_D^{-1} vs $\omega^{-1/2}$) of both (A) Pt/C and (B) Pt/G nanoparticles within the potential range of +0.81 to +0.93 V and +0.84 to +0.99 V, respectively. First, one can see that all experimental data exhibited good linearity, and the slopes were rather consistent with each nanoparticle sample. This indicates that at both nanoparticle catalysts the oxygen reduction proceeded as a first-order reaction with respective to dissolved oxygen.

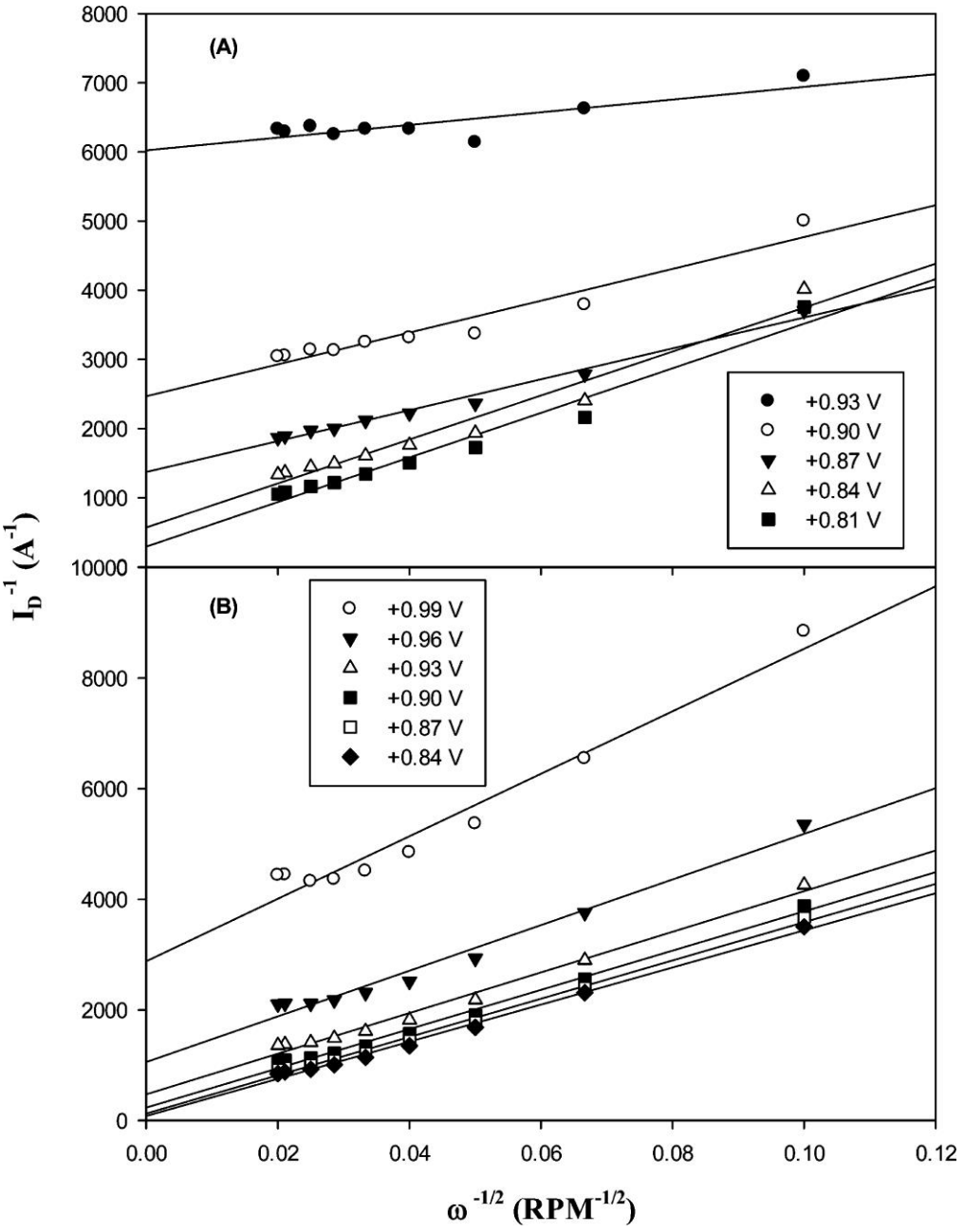


Figure 4.7. Koutecky−Levich plots of (A) Pt/C and (B) Pt/G nanoparticles in an oxygen-saturated 0.1 M HClO4 solution. Symbols are experimental data acquired from Figure 4.5, and lines are the corresponding linear regressions.

In addition, from the linear regressions in Figure 7, the kinetic currents (I_k) could also be quantified from the y-axis intercepts (eq 2c). This is manifested in the Tafel plot of Figure 8. It can be clearly seen that at both nanoparticle catalysts the kinetic currents increased with increasingly negative electrode potentials, and more importantly, within the electrode potential range of +0.80 V to +1.00 V, the kinetic currents were significantly higher with Pt/G than with Pt/C. For instance, the area-specific current density (J_k, I_k normalized by the respective effective electrochemical surface area as determined in Figure 4) at +0.90 V was 14.52 A/m^2 for Pt/G and only 1.66 A/m^2 for Pt/C. Whereas the latter is rather consistent with results obtained previously[11, 20], the former represents an almost 9 times improvement of the electrocatalytic activity, which is most likely attributable to the graphene substrate support (vide infra).

Further insights into the dynamics of oxygen reduction reactions may be obtained from the slope of the Tafel plot. Note that for oxygen electroreduction, the Tafel slopes are typically found at 60 mV/dec or 120 mV/dec, where the former corresponds to a pseudo two-electron reaction as the rate determining step, and in the latter the rate determining step is presumed to be the first-electron reduction of oxygen[21]. For the Pt/C nanoparticles it can be seen from Figure 8 that the Tafel slope was about 90.5 mV/dec within the potential rang of +0.80 V to +0.93 V, suggesting that both processes might play an important role in the oxygen reduction reactions. In contrast, at the Pt/G nanoparticles, the Tafel plot appears to exhibit two linear segments with different slopes. At low current

densities (E > +0.90 V), the Tafel slope was about 76.2 mV/dec, implying that the oxygen reduction reactions were largely limited by a pseudo two-electron process, whereas at high current densities (E < +0.90 V) the Tafel slope increased to 129.5 mV/dec, consistent with the first-electron reduction of oxygen as the rate-determining step. Such an observation of dual Tafel slopes has been observed previously[5], and accounted for by a double-trap kinetic model[21b], where the turning point (+0.90 V in the present study) reflects the equilibrium potential for the dynamic transition between the surface-adsorbed reaction intermediates of O* and HO*. In addition, in this model, the increase of reaction rate in the low overpotential region (with a low Tafel slope) is attributed both to the decrease of the highest activation energy barrier for the forward reactions and to the increase of the lowest barrier for the backward reactions. In contrast, at large overpotentials (with a high Tafel slope), the contributions of the backward reaction diminish. Such a transition was not apparent with the commercial Pt/C, possibly because of the hydrophobic carbon black that limited the access of protons to the nanoparticle surface, whereas for Pt/G, the GQD substrates were more hydrophilic with the surface oxygenated species.

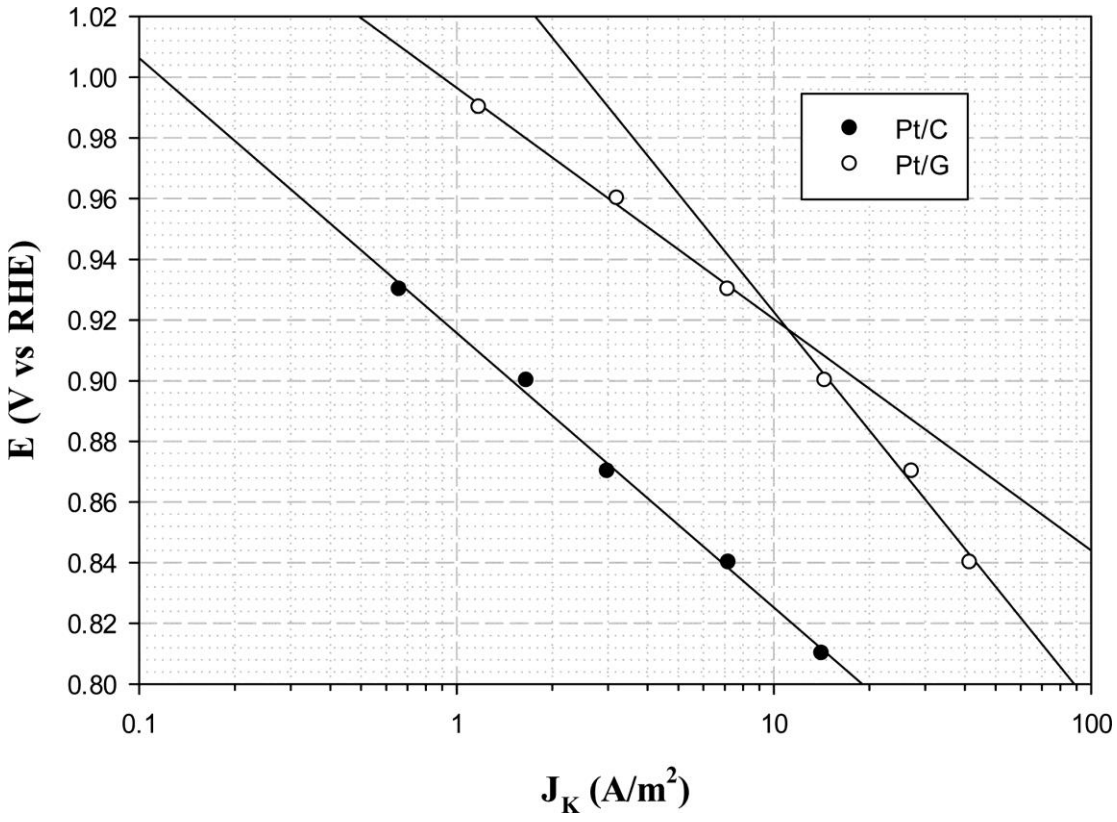


Figure 4.8. Variation of the kinetic current density (J_k, I_k normalized to the respective effective electrochemical surface area determined in Figure 4) with electrode potentials in oxygen reduction. Symbols are experimental data obtained from the y-axis intercepts of the linear regressions in Figure 4.7.

Durability is another important parameter in the quantification and comparison of nanoparticle catalytic performance. The durability test of the Pt/C and Pt/G nanoparticle catalysts was performed in oxygen-saturated 0.1 M $HClO_4$ at a potential sweep rate of 200 mV/s between +0.05 and +1.1 V for 2000 cycles. The RDE polarization curves before (black curves) and after (red curves) the tests were depicted in Figure 9. It can be seen that for the Pt/C nanoparticles (solid curves), whereas the limiting current only showed a 3% diminishment, the half-wave potential showed a cathodic shift of about 33 mV from +0.840 to +0.807 V. Markedly smaller variations were observed with the Pt/G nanoparticles (dashed curves), where the limiting current decreased by less than 2% and the shift of the half-wave potential was only 16 mV from +0.927 V to +0.911 V. These results indicate that the stability of the Pt/G nanoparticles was significantly better than that of commercial Pt/C. In fact, TEM measurements of the Pt/G nanoparticles after the durability test showed only a moderate increase (~10%) of the particle size to 3.10 ± 0.80 nm (Supporting Information, Figure S3); in contrast, in a previous study with organically capped Pt nanoparticles, the particle core size increased by almost 100% after a similar test[11]. This enhanced stability of the Pt/G nanoparticles may be ascribed to the GQD layers that wrapped around the Pt nanoparticles forming an intimate functional composite, as manifested in Figure 1.

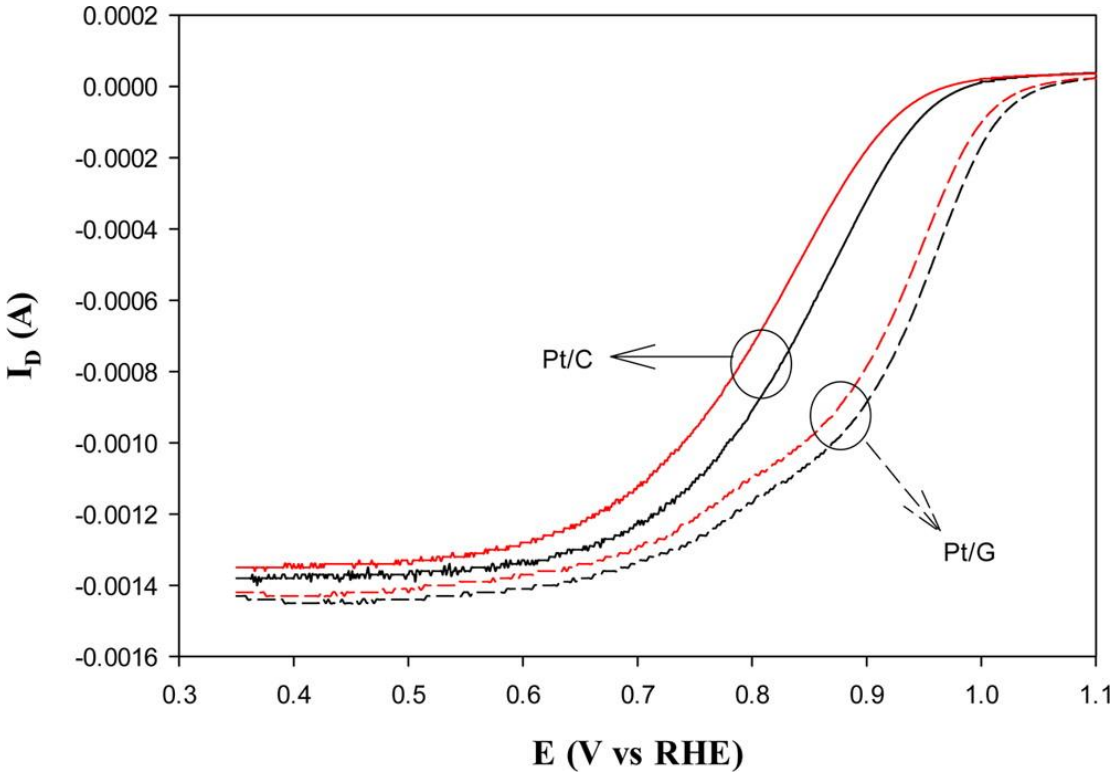


Figure 4.9. Polarization curves for oxygen reduction catalyzed by Pt/C (solid curves) and Pt/G (dashed curves) before (red curves) and after (red curves) 2000 potential cycles with a potential scan rate of 200 mV/s from +0.05 to +1.10 V in O_2-saturated 0.1 M $HClO_4$. Electrode rotation rate: 1600 rpm. Other experimental conditions were the same as in Figure 4.5.

The marked improvement of the Pt/G nanoparticles in oxygen reduction as observed above, in comparison with commercial Pt/C, might be rationalized by the impacts of the nanosized GQDs on the reaction dynamics. Note that when the O* and HO* intermediates bind strongly to the Pt surface, high overpotentials are needed in oxygen reduction. Thus, ideally a balance has to be struck between the strength of intermediate adsorption and reaction kinetics. In a recent study based on density functional theory calculation of a Pt_{13} nanoparticles supported on a monovacancy defective graphene[10], it was found that the defective graphene support not only lowered the activation energy for oxygen (O_2) dissociation by promoting charge transfer from Pt to O_2 but also decreased the energy barrier of the rate-limiting step by weakening the binding of the HO* species. In the present study, thanks to the large surface to volume ratio, the nanosized GQDs most likely carried abundant structural detects, as manifested in the XPS measurements (Figure 3) and the appearance of apparent photoluminescence emission of the GQDs (Supporting Information, Figure S2). The intimate interactions between the graphene support and platinum nanoparticles then led to deliberate manipulation of the platinum d-band center and hence the charge transfer dynamics of oxygen reduction[10].

4.3 Conclusion

Graphene quantum dots were prepared by chemical oxidation and exfoliation of carbon fibers and used as a unique substrate to support platinum nanoparticles by ethylene glycol thermolytic reduction of Pt(II) precursors. The

composite nature of the resulting Pt/G nanoparticles (diameter 2.79 ± 0.38 nm) was examined by XRD and XPS measurements where rather substantial structural defects within the graphene quantum dots were observed. Significantly, the Pt/G nanoparticles exhibited markedly enhanced electrocatalytic activity in oxygen reduction as compared to commercial Pt/C nanoparticles. Specifically, whereas both catalysts led to full reduction of oxygen to water (i.e., n = 4), the Pt/G nanoparticles exhibited an onset potential (+1.05 V) of oxygen reduction that was about 70 mV more positive than that (+0.98 V) of commercial Pt/C nanoparticles. Furthermore, the specific activity of the Pt/G nanoparticle was almost nine times that of Pt/C, along with much improved stability. These remarkable characteristics may be ascribed to the unique support of graphene quantum dots where the structural defects led to unique manipulation of the dissociative adsorption of O_2 and the binding of reaction intermediates O* and HO* on Pt surfaces.

4.4 References

1. (a) Liu, X.; Yao, K. X.; Meng, C. G.; Han, Y., Graphene substrate-mediated catalytic performance enhancement of Ru nanoparticles: a first-principles study. Dalton T 2012, 41 (4), 1289-1296; (b) Palaniselvam, T.; Irshad, A.; Unni, B.; Kurungot, S., Activity Modulated Low Platium Content Oxygen Reduction Electrocatalysts Prepared by Inducing Nano-Order Dislocations on Carbon Nanofiber through N-2-Doping. J Phys Chem C 2012, 116 (28), 14754-14763; (c) Timperman, L.; Feng, Y. J.; Vogel, W.; Alonso-Vante, N., Substrate effect on oxygen reduction electrocatalysis. Electrochim Acta 2010, 55 (26), 7558-7563; (d) Vogel, W.; Timperman, L.; Alonso-Vante, N., Probing metal substrate interaction of Pt nanoparticles: Structural XRD analysis and oxygen reduction reaction. Appl Catal a-Gen 2010, 377 (1-2), 167-173.

2. (a) Li, Y. J.; Li, Y. J.; Zhu, E. B.; McLouth, T.; Chiu, C. Y.; Huang, X. Q.; Huang, Y., Stabilization of High-Performance Oxygen Reduction Reaction Pt Electrocatalyst Supported on Reduced Graphene Oxide/Carbon Black Composite. J Am Chem Soc 2012, 134 (30), 12326-12329; (b) Zhang, K.; Yue, Q. L.; Chen, G. F.; Zhai, Y. L.; Wang, L.; Wang, H. S.; Zhao, J. S.; Liu, J. F.; Jia, J. B.; Li, H. B., Effects of Acid Treatment of Pt-Ni Alloy Nanoparticles@Graphene on the Kinetics of the Oxygen Reduction Reaction in Acidic and Alkaline Solutions. J Phys Chem C 2011, 115 (2), 379-389; (c) Seo, M. H.; Choi, S. M.; Kim, H. J.; Kim, W. B., The graphene-supported Pd and Pt catalysts for highly active oxygen reduction reaction in an alkaline condition. Electrochem Commun 2011, 13 (2), 182-185; (d) Rao, C. V.; Cabrera, C. R.; Ishikawa, Y., Graphene-Supported Pt-Au Alloy Nanoparticles: A Highly Efficient Anode for Direct Formic Acid Fuel Cells. J Phys Chem C 2011, 115 (44), 21963-21970; (e) Li, Y.; Hu, Y.; Zhao, Y.; Shi, G. Q.; Deng, L. E.; Hou, Y. B.; Qu, L. T., An Electrochemical Avenue to Green-Luminescent Graphene Quantum Dots as Potential Electron-Acceptors for Photovoltaics. Adv Mater 2011, 23 (6), 776-+.

3. (a) Li, Y.; Zhao, Y.; Cheng, H. H.; Hu, Y.; Shi, G. Q.; Dai, L. M.; Qu, L. T., Nitrogen-Doped Graphene Quantum Dots with Oxygen-Rich Functional Groups. J Am Chem Soc 2012, 134 (1), 15-18; (b) Zhang, Z. P.; Zhang, J.; Chen, N.; Qu, L. T., Graphene quantum dots: an emerging material for energy-related applications and beyond. Energ Environ Sci 2012, 5 (10), 8869-8890.

4. He, D. P.; Cheng, K.; Peng, T.; Sun, X. L.; Pan, M.; Mu, S. C., Bifunctional effect of reduced graphene oxides to support active metal nanoparticles for oxygen reduction reaction and stability. J Mater Chem 2012, 22 (39), 21298-21304.

5. Vinayan, B. P.; Nagar, R.; Ramaprabhu, S., Synthesis and investigation of mechanism of platinum-graphene electrocatalysts by novel co-reduction techniques for proton exchange membrane fuel cell applications. J Mater Chem 2012, 22 (48), 25325-25334.

6. Tan, Y. M.; Xu, C. F.; Chen, G. X.; Zheng, N. F.; Xie, Q. J., A graphene-platinum nanoparticles-ionic liquid composite catalyst for methanol-tolerant oxygen reduction reaction. Energ Environ Sci 2012, 5 (5), 6923-6927.

7. Park, S.; Ruoff, R. S., Chemical methods for the production of graphenes. Nat Nanotechnol 2009, 4 (4), 217-224.

8. (a) Huang, X.; Zeng, Z. Y.; Fan, Z. X.; Liu, J. Q.; Zhang, H., Graphene-Based Electrodes. Adv Mater 2012, 24 (45), 5979-6004; (b) Huang, C. C.; Li, C.; Shi, G. Q., Graphene based catalysts. Energ Environ Sci 2012, 5 (10), 8848-8868; (c) Cote, L. J.; Kim, J.; Tung, V. C.; Luo, J. Y.; Kim, F.; Huang, J. X., Graphene oxide as surfactant sheets. Pure Appl Chem 2011, 83 (1), 95-110.

9. (a) He, D. P.; Cheng, K.; Li, H. G.; Peng, T.; Xu, F.; Mu, S. C.; Pan, M., Highly Active Platinum Nanoparticles on Graphene Nanosheets with a Significant Improvement in Stability and CO Tolerance. Langmuir 2012, 28 (8), 3979-3986; (b) Shen, J. H.; Zhu, Y. H.; Yang, X. L.; Li, C. Z., Graphene quantum dots: emergent nanolights for bioimaging, sensors, catalysis and photovoltaic devices. Chem Commun 2012, 48 (31), 3686-3699; (c) Peng, J.; Gao, W.; Gupta, B. K.; Liu, Z.; Romero-Aburto, R.; Ge, L. H.; Song, L.; Alemany, L. B.; Zhan, X. B.; Gao, G. H.; Vithayathil, S. A.; Kaipparettu, B. A.; Marti, A. A.; Hayashi, T.; Zhu, J. J.; Ajayan, P. M., Graphene Quantum Dots Derived from Carbon Fibers. Nano Lett 2012, 12 (2), 844-849.

10.Lim, D. H.; Wilcox, J., Mechanisms of the Oxygen Reduction Reaction on Defective Graphene-Supported Pt Nanoparticles from First-Principles. J Phys Chem C 2012, 116 (5), 3653-3660.

11.Zhou, Z. Y.; Kang, X. W.; Song, Y.; Chen, S. W., Enhancement of the electrocatalytic activity of Pt nanoparticles in oxygen reduction by chlorophenyl functionalization. Chem Commun 2012, 48 (28), 3391-3393.

12.Kang, X. W.; Chen, S. W., Photocatalytic reduction of methylene blue by TiO2 nanotube arrays: effects of TiO2 crystalline phase. J Mater Sci 2010, 45 (10), 2696-2702.

13.(a) Wagner, C. D. M., G. E., Handbook of x-ray photoelectron spectroscopy: a reference book of standard data for use in x-ray photoelectron spectroscopy. Perkin-Elmer Corp.: Physical Electronics Division: Eden Prairie, MN, 1979; (b) Dablemont, C.; Lang, P.; Mangeney, C.; Piquemal, J. Y.; Petkov, V.; Herbst, F.;

Viau, G., FTIR and XPS study of Pt nanoparticle functionalization and interaction with alumina. Langmuir 2008, 24 (11), 5832-5841.

14.(a) Rybachuk, M.; Bell, J. M., Electronic states of trans-polyacetylene, poly(p-phenylene vinylene) and sp-hybridised carbon species in amorphous hydrogenated carbon probed by resonant Raman scattering. Carbon 2009, 47 (10), 2481-2490; (b) Turgeon, S.; Paynter, R. W., On the determination of carbon sp(2)/sp(3) ratios in polystyrene-polyethylene copolymers by photoelectron spectroscopy. Thin Solid Films 2001, 394 (1-2), 44-48; (c) Dettlaff-Weglikowska, U.; Benoit, J. M.; Chiu, P. W.; Graupner, R.; Lebedkin, S.; Roth, S., Chemical functionalization of single walled carbon nanotubes. Curr Appl Phys 2002, 2 (6), 497-501; (d) Iucci, G.; Carravetta, V.; Altamura, P.; Russo, M. V.; Paolucci, G.; Goldoni, A.; Polzonetti, G., XPS, NEXAFS and theoretical study of phenylacetylene adsorbed on Cu(100). Chem Phys 2004, 302 (1-3), 43-52; (e) Siegbahn, K., Electron Spectroscopy for Chemical Analysis (Esca). Philos Tr R Soc S-A 1970, 268 (1184), 33-&.

15.(a) Zhang, S.; Chandra, K. L.; Gorman, C. B., Self-assembled monolayers of terminal alkynes on gold. J Am Chem Soc 2007, 129 (16), 4876-+; (b) Okpalugo, T. I. T. P., P.; Murphy, H.; McLaughlin, J.; Brown, N. M. D., High resolution XPS characterization of chemical functionalized MWCNTs and SWCNTs. Carbon 2004, 43 (1), 153-161.

16.(a) Bajpai, R.; Roy, S.; Kulshrestha, N.; Rafiee, J.; Koratkar, N.; Misra, D. S., Graphene supported nickel nanoparticle as a viable replacement for platinum in dye sensitized solar cells. Nanoscale 2012, 4 (3), 926-930; (b) Moon, I. K.; Lee, J.; Ruoff, R. S.; Lee, H., Reduced graphene oxide by chemical graphitization. Nat Commun 2010, 1.

17.(a) Lefevre, M.; Dodelet, J. P., Fe-based catalysts for the reduction of oxygen in polymer electrolyte membrane fuel cell conditions: determination of the amount of peroxide released during electroreduction and its influence on the stability of the catalysts. Electrochim Acta 2003, 48 (19), 2749-2760; (b) Gojkovic, S. L.; Gupta, S.; Savinell, R. F., Heat-treated iron(III) tetramethoxyphenyl porphyrin chloride supported on high-area carbon as an electrocatalyst for oxygen reduction: Part III. Detection of hydrogen-peroxide during oxygen reduction. Electrochim Acta 1999, 45 (6), 889-897; (c) Meng, H.; Larouche, N.; Lefevre, M.; Jaouen, F.; Stansfield, B.; Dodelet, J. P., Iron porphyrin-based cathode catalysts for polymer electrolyte membrane fuel cells: Effect of NH3 and Ar mixtures as pyrolysis gases on catalytic activity and stability. Electrochim Acta 2010, 55 (22), 6450-6461.

18.Lim, B.; Jiang, M. J.; Camargo, P. H. C.; Cho, E. C.; Tao, J.; Lu, X. M.; Zhu, Y. M.; Xia, Y. N., Pd-Pt Bimetallic Nanodendrites with High Activity for Oxygen Reduction. Science 2009, 324 (5932), 1302-1305.

19.(a) Schumpe, A.; Adler, I.; Deckwer, W. D., Solubility of Oxygen in Electrolyte-Solutions. Biotechnol Bioeng 1978, 20 (1), 145-150; (b) Anastasijevic, N. A.; Dimitrijevic, Z. M.; Adzic, R. R., Oxygen Reduction on a Ruthenium Electrode in Acid Electrolytes. Electrochim Acta 1986, 31 (9), 1125-1130; (c) Markovic, N. M.; Gasteiger, H. A.; Grgur, B. N.; Ross, P. N., Oxygen reduction reaction on Pt(111): effects of bromide. J Electroanal Chem 1999, 467 (1-2), 157-163.

20.Zhou, Z. Y.; Kang, X. W.; Song, Y.; Chen, S. W., Ligand-Mediated Electrocatalytic Activity of Pt Nanoparticles for Oxygen Reduction Reactions. J Phys Chem C 2012, 116 (19), 10592-10598.

21.(a) Zhang, J., PEM fuel cell electrocatalysts and catalyst layers: fundamentals and applications. Springer: London, 2008; (b) Wang, J. X.; Uribe, F. A.; Springer, T. E.; Zhang, J. L.; Adzic, R. R., Intrinsic kinetic equation for oxygen reduction reaction in acidic media: the double Tafel slope and fuel cell applications. Faraday Discuss 2008, 140, 347-362.

Chapter 5

Electrocatalytic activities of alkyne-functionalized copper nanoparticles in oxygen reduction in alkaline media

Reproduced with permission from [Ke Liu, Yang Song, Shaowei Chen*, "Electrocatalytic activities of alkyne-functionalized copper nanoparticles in oxygen reduction in alkaline media", *J. Power Sources*, **2014**, *268*, 469.] Copyright © 2014 Elsevier B.V.

5.1 Introduction

Proton exchange membrane fuel cells are clean and environmental-friendly power sources[1]. For hydrogen fuel cells, with a large Gibbs free energy of −273.13 KJ/mol, the reaction of hydrogen and oxygen is thermodynamically favorable and expected to exhibit a high theoretical efficiency on energy conversion. However, as oxygen reduction reactions (ORR) on the cathode are kinetically sluggish, the reactions can proceed only at significantly large overpotentials and consequently compromise the overall efficiency[2]. Platinum-based nanoparticles have been used extensively as the catalysts of choice for ORR[3]; and a variety of strategies have been reported in the literature to further improve the ORR activities, such as rational design and preparation of Pt-based alloys[4] and surface engineering of Pt nanoparticles by selected organic ligands[5]. This is motivated by a deliberate balance between surface accessibility of active sites and control of electronic structures of the metal cores which may manipulate the adsorption and reduction of oxygen. Meanwhile, owing to the high price and scarcity of platinum, extensive efforts have also been focused on Pt-free catalysts such as transition metal oxides and chalcogenides[6], pyrolyzed metal macrocycle[7], N-doped carbon nanostructures[8], etc. Among these, studies on copper-based electrocatalysts for ORR have been relatively scarce. In fact, copper has been largely used as a supporting substrate or non-active component in the electrocatalytic reduction of oxygen[9]. Yet, using a polycrystalline copper electrode, Schiffrin and coworkers[10] have shown that the electrode exhibited

apparent electrocatalytic activity in oxygen reduction in a borax buffer solution, though at a large overpotential, and proposed that surface redox couples like Cu_2O/CuO played an important role in the reduction sequence with a CE mechanism whereas direct electron transfer to oxygen might occur from the oxide-free electrode surface. Brisard et al. [11]also observed electrocatalytic activity of Cu(100) and Cu(111) single-crystal electrodes in oxygen reduction in sulfuric acid where the reaction kinetics was impacted by the adsorption of (bi)sulfate ions on the electrode surface. In a more recent study[12], it was reported that cuprous oxide nanoparticles might serve as efficient catalyst for oxygen reduction; however, no detailed mechanism was included. Nevertheless, these earlier work suggests that partial oxidation of copper surfaces might be a key step in enhancing the adsorption and eventual electroreduction of oxygen on copper. This is the primary motivation of the present study.

Herein we prepared alkyne-capped copper nanoparticles by reducing copper acetate with sodium borohydride in the presence of alkyne ligands at two temperatures, 0 °C and room temperature. Transmission electron microscopic (TEM) studies showed that as-prepared copper nanoparticles were well separated, suggesting effective protection of the nanoparticles by the alkyne ligands; and the nanoparticle diameters were found to be in the range of 4 to 6 nm. FTIR and photoluminescence spectroscopic measurements confirmed the bonding attachment of the alkyne ligands onto the nanoparticle surface most likely forming Cu–C≡ interfacial bonds. XPS measurements revealed the formation of a

small amount of CuO in the nanoparticles with the concentration higher in the samples prepared at ambient temperature than that at 0 °C. Cu_2O was also identified in the nanoparticles, as well as in commercial CuO nanoparticles. Electrochemical studies indicated that the 0 °C samples exhibited the best electrocatalytic activity in oxygen reduction among the three in 0.1 M NaOH. This was accounted for by the low oxide concentration within the nanoparticles and the ready formation of Cu_2O that likely facilitated the further reduction of peroxide into hydroxide.

5.2 Results and discussion

Figure 1 depicts a representative TEM micrograph of the (A) CuHC10-IB and (B) CuHC10-RT nanoparticles. It can be seen that both Cu nanoparticles are roughly spherical and well separated, suggesting successful attachment of the alkyne ligands on the Cu nanoparticle surface forming stable nanoparticles. Additionally, statistical analysis based on more than 100 nanoparticles showed that the average diameter of the nanoparticles synthesized at room temperature (CuHC10-RT) was 4.28 ± 0.46 nm, whereas for the nanoparticles prepared at a lower temperature (CuHC10-IB), the size was somewhat larger at 6.29 ± 0.99 nm, as manifested in the respective figure insets. Note that for organically capped metal nanoparticles, the size of the nanoparticles is largely determined by two competing processes, nucleation of metal atoms to form the nanoparticle cores and passivation of the metal cores by organic capping ligands that impedes the core growth[13]. For mercapto-stabilized gold nanoparticles, typically the lower the

reaction temperature, the smaller the nanoparticle cores[14]. This is ascribed to the strong affinity of thiol moieties to gold surfaces and thus the reductive formation and nucleation of gold atoms plays a significant role in the determination of the eventual size of the nanoparticles. The behaviors are completely different with the decyne-stabilized copper nanoparticles in the present study. In the formation of CuHC10 nanoparticles, the adsorption of alkyne ligands onto the copper surface was relatively slow; thus the passivation of the growth of the copper nanoparticles was most likely to be enhanced at higher temperatures, leading to a smaller size of the nanoparticles, as observed above.

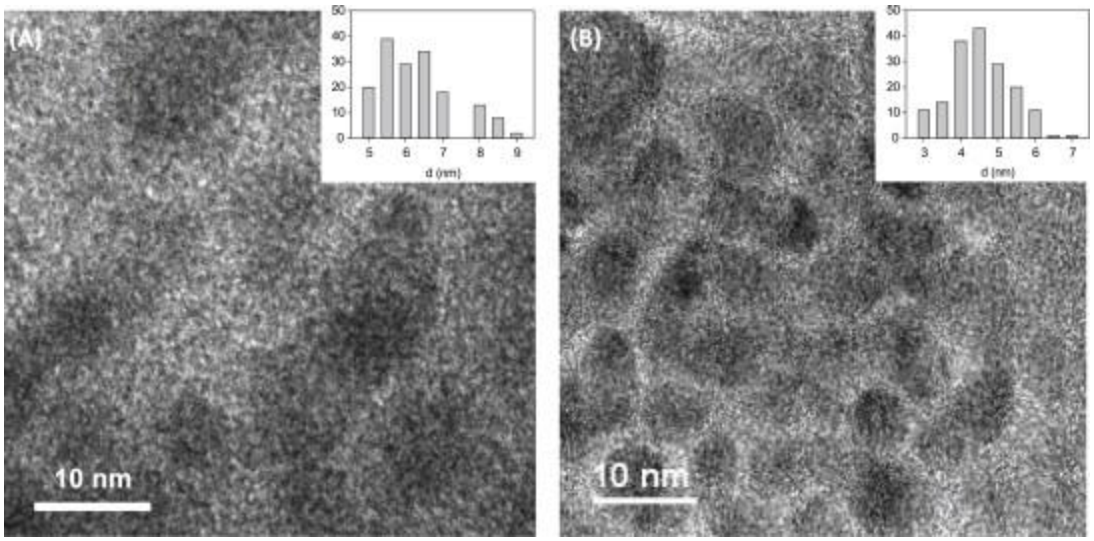


Figure 5.1. Representative TEM micrographs of (A) CuHC10-IB and (B) CuHC10-RT nanoparticles. Scale bars 10 nm. Insets show the corresponding core size histograms.

The successful passivation of the copper nanoparticles by the decyne ligands is further manifested in FTIR measurements, as shown in Figure 2. Note that the FTIR spectra were almost identical for both CuHC10-RT and CuHC10-IB nanoparticles, so only the one of CuHC10-RT was shown here (black curve), along with that of the 1-decyne monomers (red curve). From the figure it can be see that the ≡C–H vibrational stretch at 3312 cm^{-1} was well-defined for the monomeric ligands of 1-decyne; yet this feature vanished with the nanoparticle samples suggesting efficient breaking of the ≡C–H bond after the alkyne ligands were adsorbed onto the copper nanoparticle surface (the absence of this vibrational feature in the spectrum also indicates that the nanoparticles were free of excessive alkyne ligands). Additionally, for monomeric 1-decyne ligands, the C≡C vibrational stretch can be identified at 2120 cm^{-1}; yet for the CuHC10 nanoparticles, this band appears to red-shift to 1720 cm^{-1}, most likely as a result of the cleavage of the ≡C–H bond and the formation of Cu–C≡ interfacial linkages, where the conjugated metal-ligand bonds led to effective intraparticle charge delocalization between the particle-bound acetylene moieties and hence a decreasing bonding order of the C≡C moieties, as observed in previous studies[5c, 15]. Furthermore, with this interfacial configuration, the small shoulder at 1930 cm^{-1} may be assigned to Cu–H bonds, which is consistent with the Cu–H vibrational stretch that was identified at 1940 cm^{-1} in a previous study of crystalline metal hydrides[16]. Another discrepancy is the antisymmetric (d_-) and symmetric (d_+) CH_2 vibrational stretches which can be found at 2927 and 2856

cm^{-1}, respectively, for the monomeric ligands, but red-shifted somewhat to 2920 and 2850 cm^{-1}, as a result of increasing packing order of the molecules adsorbed on the nanoparticle surface.

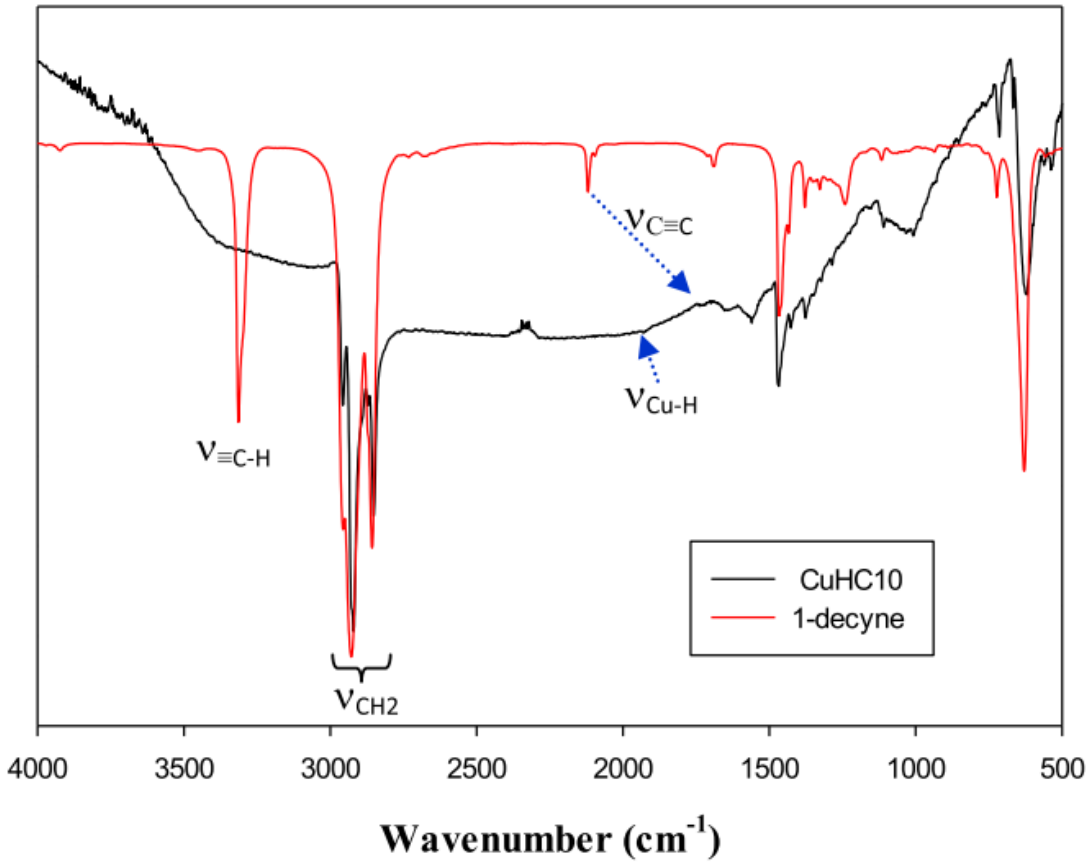


Figure 5.2. FTIR spectra of CuHC10 nanoaprticles (black curve) and monomeric 1-decyne ligands (red curve).

The formation of conjugated metal-ligand interfacial linkages is also evidenced in photoluminescence measurements. Figure 3 depicts the excitation and emission spectra of the CuHC10-RT (black curves) and CuHC10-IB (red curves) nanoparticles in $CHCl_3$. It can be seen that both nanoparticles exhibited a pair of rather well-defined excitation and emission peaks at almost identical positions of λ_{ex} = 416 nm and λ_{em} = 480 nm, respectively. Similar photoluminescence behaviors have also been observed with alkyne-functionalized Pt and Ru nanoparticles and ascribed to the formation of conjugated metal-ligand bonds that led to extensive intraparticle charge delocalization. Therefore, the particle-bound acetylene moieties behaved analogously to diacetylene (C≡C–C≡C) derivatives[5c, 17]. Yet one may notice that for decyne-functionalized Ru nanoparticles, the excitation and emission peak positions are typically found at 360 and 440 nm[17], and for the corresponding Pt nanoparticles, at 352 nm and 430nm[5c]. This discrepancy may be correlated with the electrical resistivity of the metals (at 0 °C)[18] that increases in the order of 1.543×10^{-8} Ωm for Cu < 7.1×10^{-8} Ωm for Ru < 9.6×10^{-8} Ωm for Pt, where the intraparticle charge delocalization is facilitated by the conducting metal cores, and a decreasing resistivity leads to a red-shift of the excitation and emission peak energies.

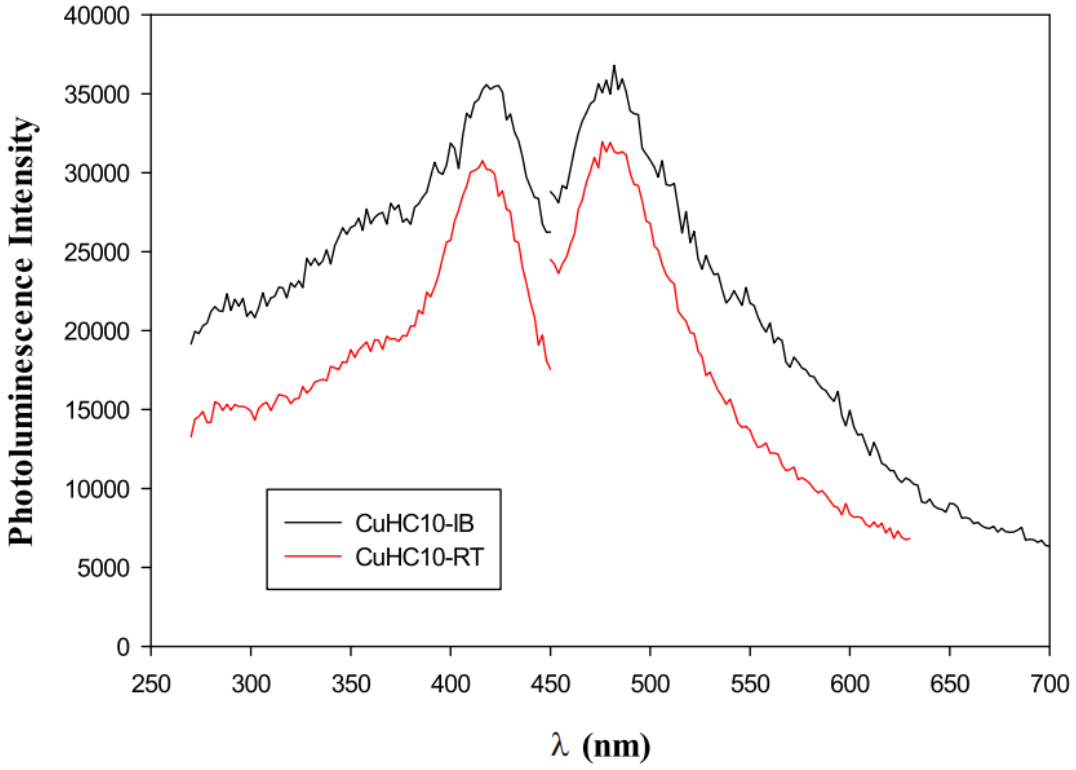


Figure 5.3. Excitation and emission spectra of CuHC10-RT and CuHC10-IB nanoparticles in $CHCl_3$.

The chemical nature of the resulting nanoparticles was then examined by XPS measurements. Figure 4 (A) shows the full survey spectra of the CuHC10-IB, CuHC10-RT, and commercial CuO nanoparticles. For all samples, the Cu2p electrons can be identified at the twin peaks of 933 eV and 953 eV and the C1s electrons at about 284 eV. Interesting, both decyne-capped copper nanoparticles exhibit a broad peak centered at around 570 eV, suggesting possible formation of cuprous oxide within the nanoparticles as the Cu LMM-2 auger transitions are typically found around 570 eV of metallic Cu and Cu_2O, respectively[19]. In fact, the O1s electrons can be readily found at around 530 eV.

High-resolution scans of the Cu2p electrons are depicted in panel (B), from which two main peaks may be identified at around 933 and 953 eV for all samples, as summarized in Table 1. These may be assigned to the Cu2p3/2 and Cu2p1/2 electrons, respectively, which are consistent with those of metallic copper and cuprous oxide, as the binding energies of the Cu2p electrons for Cu(0) and Cu(I) are only 0.1 eV apart[20]. This is also consistent with the appearance of the LMM-2 auger transitions at around 570 eV as observed above in panel (A). In addition, all samples exhibited a satellite peak between the two main peaks, yet at different positions: 946.91 eV for the CuHC10-IB nanoparticles, 943.50 eV for CuHC10-RT, and 941.59 eV for the commercial CuO nanoparticles. This is consistent with that of CuO, indicating the formation of a small fraction of cupric oxide in the nanoparticles, as the satellite peak is typically observed in ions with a partially filled 3d shell but absent in ions with a completely filled 3d shell[21].

Furthermore, the increasing intensity of the satellite peaks suggests the increasing concentration of the Cu(II) species, as depicted in Figure 4 (B). In fact, based on the integrated peak areas, the ratio of Cu(II) over Cu(I) and Cu(0) combined in the nanoparticles is estimated to be 7.1%, 26.2%, and 50.1% in CuHC10-IB, Cu-HC10-RT, and commercial CuO nanoparticles, respectively (Table 1).

Note that the appearance of the satellite peak has been largely ascribed to the shake-up effect where the outgoing electron interacts with a valence electron and excites it to a higher energy level[21]. Therefore, the observed red-shift of the satellite peaks, CuHC10-IB (946.91 eV) > CuHC10-RT (943.50 eV) > commercial CuO nanoparticles (941.59 eV), is consistent with the increasing content of the Cu(II) components that exhibit a vacant 3d orbital, in contrast to Cu(I) or Cu(0) that features a $3d^{10}$ electronic configuration with 4s being the lowest-energy empty orbital.

Table 5.1. Binding energies (eV) of the Cu2p electrons and the ratio ($x_{Cu(II)}$) of Cu(II) over Cu(I) and Cu(0) combined in CuHC10-IB, CuHC10-RT and commercial CuO nanoparticles.

	Cu2p3/2	**Cu2p1/2**	**Satellite**	$x_{\mathbf{Cu(II)}}$
CuHC10-IB	932.93	952.78	946.91	7.1%
CuHC10-RT	933.47	953.61	943.50	26.2%
Commercial CuO	932.99	953.13	941.13	50.1%

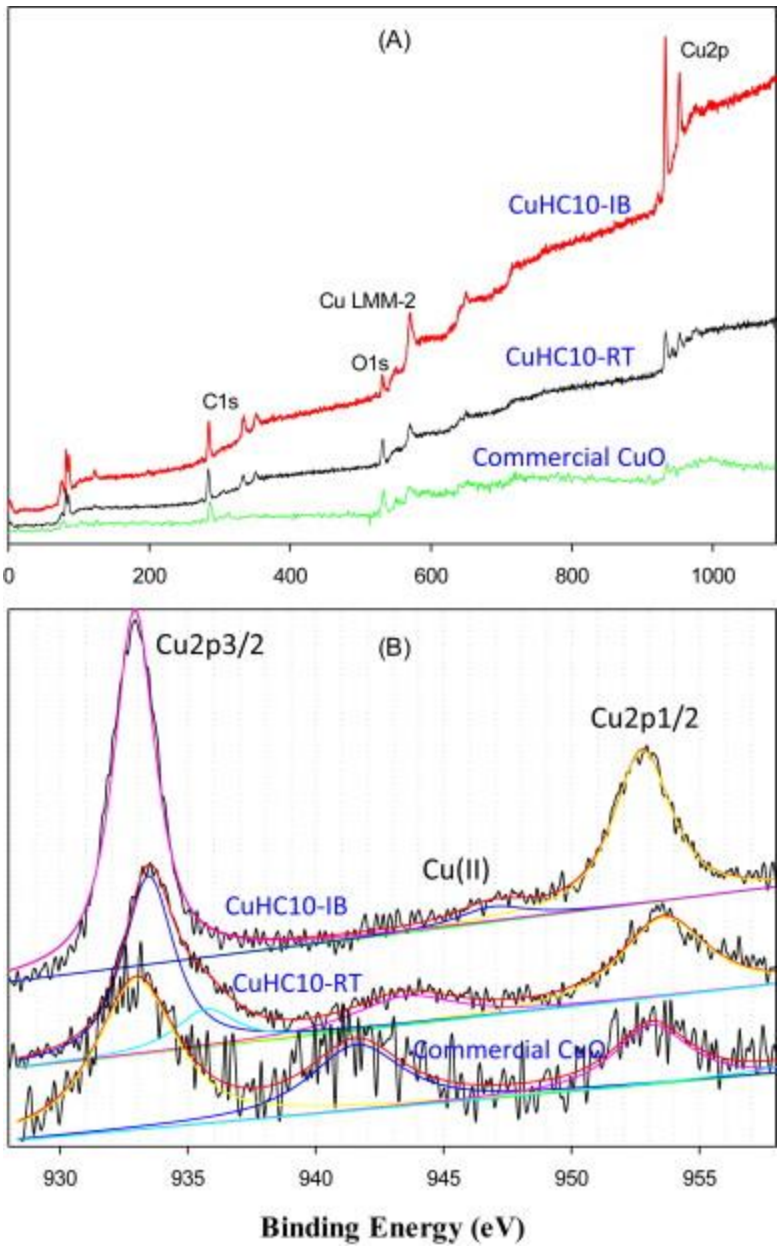


Figure 5.4. (A) XPS survey spectra and (B) high-resolution scans of the Cu2p electrons of CuHC10-IB, CuHC10-RT and commercial CuO nanoparticles. In panel (B), black curves are the raw experimental data and color curves are the deconvolution fits.

Interestingly, the nanoparticles synthesized above were found to exhibit apparent electrocatalytic activity in the reduction of oxygen. Note that prior to electrochemical measurements, the nanoparticles-modified electrodes were subject to about 100 potential cycles within the potential range of +0.5 V to +0.1 V (vs RHE) in order to desorb part of the protecting ligands and expose the nanoparticle cores. Figure 5 shows the steady-state cyclic voltammograms of the electrodes modified with the three nanoparticle catalysts in a N_2-saturated 0.1 M NaOH solution. From the figure, one can see that at the CuHC10-IB electrode (black curve), two anodic peaks are well-defined at around +0.55 V and +0.84 V (vs RHE). The former is believed to correspond to the formation of a monolayer of Cu_2O while the latter to the formation of a thick multilayer film of CuO, and the cathodic peak at around +0.60 V is likely to originate from the partial reduction of CuO to Cu_2O[22]. Similar features can also be seen with the CuHC10-RT electrode (red curve) and the commercial CuO nanoparticles (green curve) but at much lower current amplitudes. This seems to suggest more efficient electrochemical desorption of ligands from the CuHC10-IB nanoparticle surface than from CuHC10-RT, likely a result of somewhat stronger metal-ligand ($d\pi$–$p\pi$) interactions in the latter with the higher Cu(II) content.

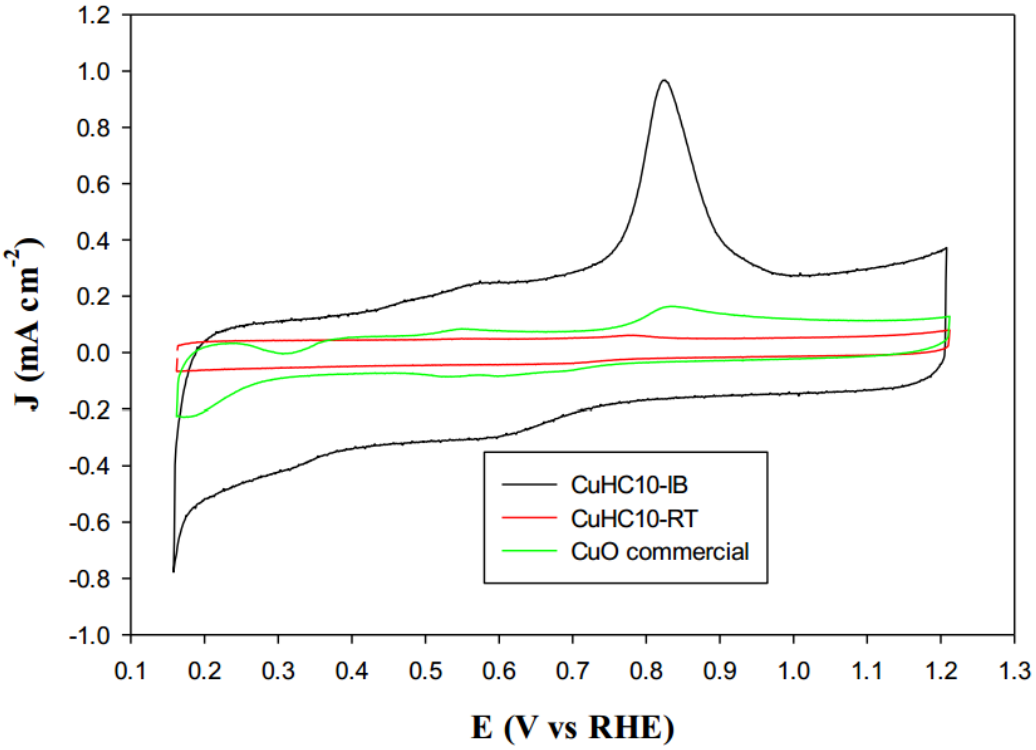


Figure 5.5. Cyclic voltammograms of a glassy carbon-disk electrode modified with 15 μg of CuHC10-IB (black curve), CuHC10-RT (red curve) and commercial CuO (green curve) nanoparticles in a nitrogen-saturated 0.1M NaOH solution. Nanoparticle loading is all 15 μg and potential scan rate is 0.01 V/s.

Figure 6 depicts the RRDE voltammagrams of a platinum ring-glassy-carbon disk electrode with the disk modified with a calculated amount of (A) CuHC10-IB, (B) CuHC10-RT, and (C) commercial CuO nanoparticles in an O_2-saturated 0.1 M NaOH solution at different rotation rates. It can be seen that on the disk electrode the cathodic currents start to increase at sufficiently negative potentials, indicating apparent electrocatalytic activity of the three nanoparticles in oxygen reduction. Yet it can be seen that the onset potential for oxygen reduction is different among the three nanoparticle catalysts, at +0.77 V for CuHC10-IB, +0.75 V for CuHC10-RT, and +0.74 V for commercial CuO nanoparticles, suggesting that CuHC10-IB nanoparticles was the best among the series. Note that at these potentials, (partial) reduction of CuO into Cu_2O occurred, indicating unlikely involvement of CuO in oxygen reduction[10].

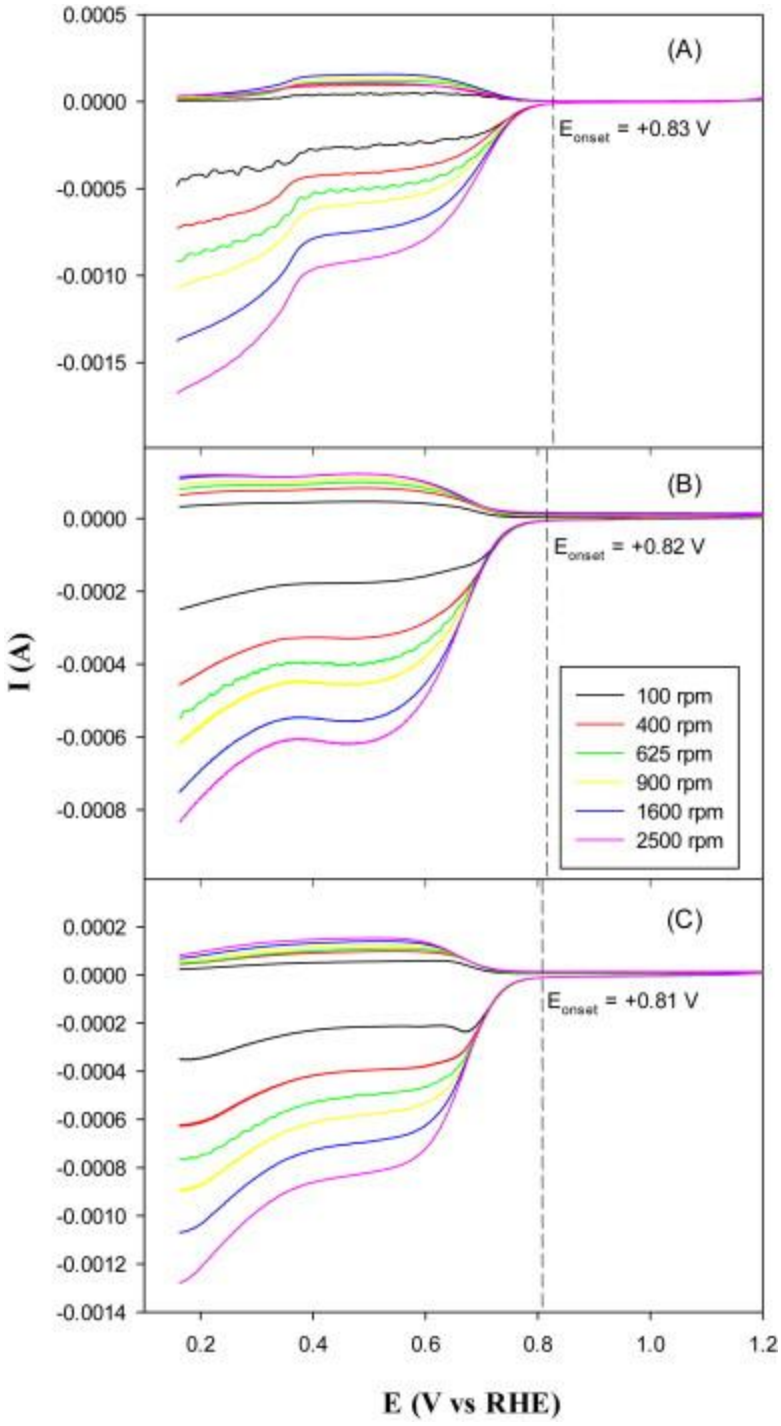


Figure 5.6. RRDE voltammograms of a platinum ring-glassy-carbon disk electrode with the disk modified with (A) CuHC10-IB, (B) CuHC10-RT, and (C) commercial CuO nanoparticles in an oxygen-saturated 0.1 M NaOH solution. Nanoparticle loading is all 15 μg. Electrode rotation rates are specified in the figure legends. Ring currents are collected by setting the ring potential at +1.3 V vs RHE.

Furthermore, the corresponding ring currents were all at least an order of magnitude lower. From the ratio of the ring current (I_R) and disk current (I_D), the number of electron transfer (n) during oxygen reduction can be estimated by $n = 4I_D/(I_D + I_R/N)$, and concurrently the percentage of peroxide formed in the reduction products by x_{H2O2} (%) = 200(1 – n/4), with N being collection efficiency (37%)[5a], which are depicted in Figure 7. It can be seen that the electrode potential at which n = 2 (corresponding to the 2-electron reduction of oxygen into peroxide species) is markedly different, +0.83 V for CuHC10-IB, +0.73 V for CuHC10-RT, and +0.75 V for commercial CuO nanoparticles, again signifying the best performance of the CuHC10-IB nanoparticles. At more negative potentials, the n values increases accordingly. For instance, within the potential range of +0.70 V to +0.40 V, the n values were rather consistent at 2.5 ~ 2.7 for the three nanoparticle catalysts, suggesting the formation of both peroxide and hydroxide as the final products of oxygen reduction. In fact, peroxides account for about 70% of the final products, indicating that oxygen reduction proceeded with a mixture of the 2- and 4-electron reduction pathways. Note that the reduction of Cu_2O to Cu occurred in this same potential range (Figure 5), and it has been proposed that Cu_2O might be involved in the reduction of peroxide intermediates with a CE mechanism[10]. At even more negative potentials (< +0.30 V) where reduction of Cu_2O to Cu is likely to take place, the n value reached 3.5 for CuHC10-IB nanoparticles (and x_{H2O2} exhibited an apparent diminishment down to <20%), markedly higher than those for CuHC10-RT and CuO

nanoparticles. This indicates that the formation of peroxides as the reduction products became minimal, with increasing metallic characters of the catalyst surface.

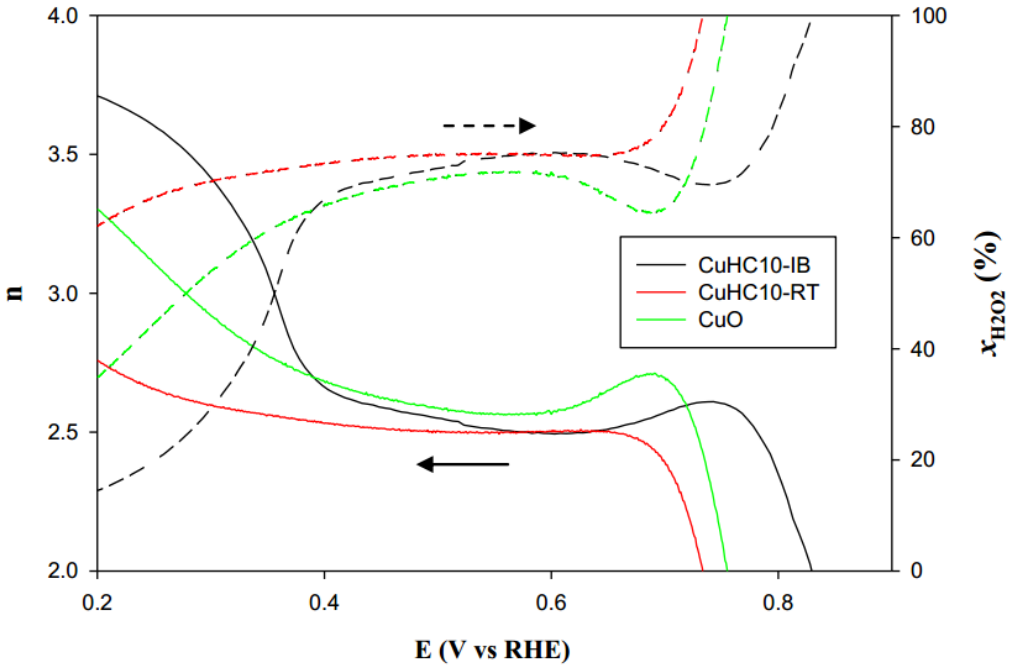


Figure 5.7. Variation of the number of electron transfer (n, solid curves, left y axis) and percentage (x_{H2O2}, dashed curves, right y axis) of peroxide formed in oxygen reduction with electrode potential for CuHC10-IB (black curves), CuHC10-RT (red curves) and commercial CuO (green curves) nanoparticles. Symbols were experimental data calculated from the RRDE voltammograms at 1600 rpm in Figure 5.6.

Further insights into the electron-transfer kinetics of oxygen reduction were revealed by Koutecky-Levich analysis, as the RRDE voltammetric currents include both kinetic current (I_k) and diffusion (I_d) controlled contributions[23],

$$\frac{1}{I_D} = \frac{1}{I_k} + \frac{1}{I_d} = \frac{1}{I_k} + \frac{1}{B\omega^{1/2}} \tag{5.1a}$$

$$B = 0.62nFAC_O D_O^{2/3} \nu^{-1/6} \tag{5.1b}$$

$$I_k = nAFkC_O \tag{5.1c}$$

where ω is the electrode rotation rate, n is the overall number of electron transfer, F is Faraday constant, C_O is the bulk concentration of O_2 dissolved in the electrolyte, D_O is the diffusion coefficient of O_2, and ν is the kinetic viscosity of the electrolyte. For all three nanoparticle catalysts, plots of I^{-1} vs $\omega^{-1/2}$ show good linearity and parallelism within the potential range of +0.80 to +0.60 V (not shown), indicating first order reaction with respect to dissolved oxygen. From the intercepts of the linear regression, the corresponding kinetic current densities (J_k, I_k normalized by the electrode surface area) can also be evaluated, as depicted in the Tafel plot of Figure 8. It can be seen that the kinetic currents within the potential range of +0.80 to +0.60 V increase in the order of commercial CuO < CuHC10-RT < CuHC10-IB, again, indicating the best electrocatalytic performance of the CuHC10-IB nanoparticles.

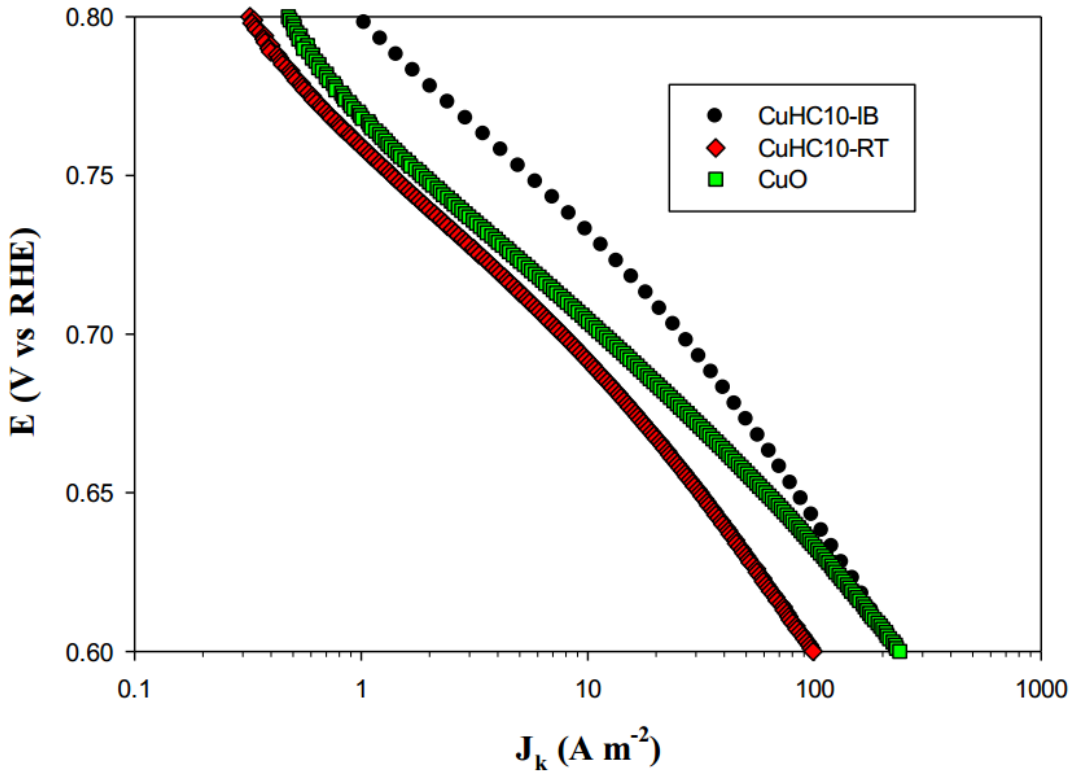


Figure 5.8. Tafel plots of oxygen reduction catalyzed by CuHC10-IB (black circles), CuHC10-RT (red diamonds) and commercial CuO (green squares) nanoparticles. Data are acquired from linear regressions of the Koutecky-Levich plots based on the original data in Figure 5.6.

In addition, linear regressions of the Tafel plots yield a slope of 82.7 mV/dec for CuHC10-IB, 76.2 mV for CuHC10-RT, and 69.3 mV/dec for commercial CuO nanoparticles. Note that for oxygen electroreduction at nanoparticle catalyst surfaces, the Tafel slopes are typically found at 60 mV/dec or 120 mV/dec, where the former corresponds to a pseudo two-electron reaction as the rate determining step, and in the latter the rate determining step is presumed to be the first-electron reduction of oxygen [24]. Therefore it is likely that oxygen reduction on the copper nanoparticle surface proceeded by the pseudo two-electron route. This is consistent with the above observation that peroxide derivatives constituted a rather large portion of the final products in the low overpotential regime (Figure 5.7). It is known that adsorption of O_2 on completely oxidized surfaces is energetically unfavorable and thus a high overpotential is required for oxygen reduction to proceed. Within this context, the higher the CuO component in the copper nanoparticles, the lower the catalytic activity in oxygen reduction. In addition, it has been suggested that Cu_2O may donate electrons to oxygen and serve as effective catalysts for ORR [25]; and from Figure 5, one can see the voltammetric peak currents for the formation of Cu_2O (at +0.55 V) was the highest with the CuHC10-IB nanoparticles and the lowest with the CuHC10-RT nanoparticles. This is in agreement with the ORR activity observed above.

It should be noted that whereas the electrocatalytic performance of these organically capped copper nanoparticles is not as good as those typically

observed with Pt-based nanoparticle catalysts [5a, 5c, 26], the activity does show marked enhancement as compared with those of oxygen reduction catalyzed by bulk copper electrodes [10-11, 27]. For instance, in the previous studies with a polycrystalline Cu or CuNi electrode [10], the onset potentials for oxygen reduction were found to be around +0.36 V (vs RHE) in a borax buffer solution; and even more negative onset potentials were observed with single-crystalline Cu(100) and Cu(111) electrodes in H_2SO_4 at about 0 V (vs RHE) [11a, 27]. These are far more negative than those observed above with the decyne-capped copper nanoparticles.

5.3 Conclusion

Stable alkyne-capped copper nanoparticles were prepared by a simple chemical reduction procedure. TEM measurements showed that the nanoparticles were of 4 to 6 nm in diameter when the nanoparticles were synthesized at ambient temperature or at 0 °C. The alkyne ligands were found to form Cu–C≡ interfacial bonds at the metal-ligand interface, as manifested in FTIR and photoluminescence measurements. XPS measurements suggested the formation of a small amount of CuO in the nanoparticles, along with Cu_2O. Electrochemical studies indicated that the nanoparticles exhibited apparent electrocatalytic activity in oxygen reduction in alkaline media, with the best performance observed with the samples prepared at 0 °C, in terms of onset potential, the number of electron transfer involved, as well as kinetic current density. Whereas the overall performance was not as good as that of platinum-based nanoparticle catalysts, the results showed that nanosized copper was much more active than

poly- or single-crystalline bulk copper in the electrocatalytic reduction of oxygen. Notably, the electrocatalytic activity might be further improved by deliberate interfacial engineering of the copper nanoparticles by other metals or chemical ligands. This is the focus of ongoing work and the results will be reported in due course.

5.4 References

1. (a) Zhang, J., *PEM fuel cell electrocatalysts and catalyst layers: fundamentals and applications*. Springer: London, 2008; (b) Koper, M. T. M., *Fuel Cell Catalysis : a Surface Science Approach*. Wiley: Hoboken, N.J 2009.

2. Stephens, I. E. L.; Bondarenko, A. S.; Gronbjerg, U.; Rossmeisl, J.; Chorkendorff, I., Understanding the electrocatalysis of oxygen reduction on platinum and its alloys. *Energ Environ Sci* **2012,** *5* (5), 6744-6762.

3. (a) Abruna, H. D.; Matsumoto, F.; Cohen, J. L.; Jin, J.; Roychowdhury, C.; Prochaska, M.; van Dover, R. B.; DiSalvo, F. J.; Kiya, Y.; Henderson, J. C.; Hutchison, G. R., Electrochemical energy generation and storage. Fuel cells and lithium-ion batteries. *B Chem Soc Jpn* **2007,** *80* (10), 1843-1855; (b) Wagner, F. T.; Lakshmanan, B.; Mathias, M. F., Electrochemistry and the Future of the Automobile. *J Phys Chem Lett* **2010,** *1* (14), 2204-2219; (c) Rizo, R.; Herrero, E.; Feliu, J. M., Oxygen reduction reaction on stepped platinum surfaces in alkaline media. *Phys Chem Chem Phys* **2013,** *15* (37), 15416-15425; (d) Wang, H. H.; Zhou, Z. Y.; Yuan, Q. A.; Tian, N.; Sun, S. G., Pt nanoparticle netlike-assembly as highly durable and highly active electrocatalyst for oxygen reduction reaction. *Chem Commun* **2011,** *47* (12), 3407-3409.

4. Zhang, J.; Sasaki, K.; Sutter, E.; Adzic, R. R., Stabilization of platinum oxygen-reduction electrocatalysts using gold clusters. *Science* **2007,** *315* (5809), 220-222.

5. (a) Zhou, Z. Y.; Kang, X. W.; Song, Y.; Chen, S. W., Enhancement of the electrocatalytic activity of Pt nanoparticles in oxygen reduction by chlorophenyl functionalization. *Chem Commun* **2012,** *48* (28), 3391-3393; (b) Zhou, Z. Y.; Kang, X. W.; Song, Y.; Chen, S. W., Ligand-Mediated Electrocatalytic Activity of Pt Nanoparticles for Oxygen Reduction Reactions. *J Phys Chem C* **2012,** *116* (19), 10592-10598; (c) Liu, K.; Kang, X. W.; Zhou, Z. Y.; Song, Y.; Lee, L. J.; Tian, D.; Chen, S. W., Platinum nanoparticles functionalized with acetylene derivatives: Electronic conductivity and electrocatalytic activity in oxygen reduction. *J Electroanal Chem* **2013,** *688*, 143-150.

6. (a) Suntivich, J.; Gasteiger, H. A.; Yabuuchi, N.; Nakanishi, H.; Goodenough, J. B.; Shao-Horn, Y., Design principles for oxygen-reduction activity on perovskite oxide catalysts for fuel cells and metal-air batteries. *Nat Chem* **2011,** *3* (7), 546-550; (b) Feng, Y. J.; Alonso-Vante, N., Carbon-supported cubic CoSe2 catalysts for oxygen reduction reaction in alkaline medium. *Electrochim Acta* **2012,** *72*, 129-133.

7. (a) Jahnke, H. G.; Schonbor.Mf; Zimmerma.Go, Transition-Metal Chelates as Catalysts for Fuel-Cell Reactions. *J Electrochem Soc* **1974,** *121* (3), C120-C120; (b) Jasinski, R., New Fuel Cell Cathode Catalyst. *Nature* **1964,** *201* (492), 1212-&.

8. Gong, K. P.; Du, F.; Xia, Z. H.; Durstock, M.; Dai, L. M., Nitrogen-Doped Carbon Nanotube Arrays with High Electrocatalytic Activity for Oxygen Reduction. *Science* **2009,** *323* (5915), 760-764.

9. (a) Koh, S.; Strasser, P., Electrocatalysis on bimetallic surfaces: Modifying catalytic reactivity for oxygen reduction by voltammetric surface dealloying. *J Am Chem Soc* **2007,** *129* (42), 12624-+; (b) Mani, P.; Srivastava, R.; Strasser, P., Dealloyed Pt-Cu core-shell nanoparticle electrocatalysts for use in PEM fuel cell cathodes. *J Phys Chem C* **2008,** *112* (7), 2770-2778; (c) Kariuki, N. N.; Wang, X. P.; Mawdsley, J. R.; Ferrandon, M. S.; Niyogi, S. G.; Vaughey, J. T.; Myers, D. J., Colloidal Synthesis and Characterization of Carbon-Supported Pd-Cu Nanoparticle Oxygen Reduction Electrocatalysts. *Chem Mater* **2010,** *22* (14), 4144-4152; (d) Li, H. H.; Cui, C. H.; Zhao, S.; Yao, H. B.; Gao, M. R.; Fan, F. J.; Yu, S. H., Mixed-PtPd-Shell PtPdCu Nanoparticle Nanotubes Templated from Copper Nanowires as Efficient and Highly Durable Electrocatalysts. *Adv Energy Mater* **2012,** *2* (10), 1182-1187; (e) Bakir, C. C.; Sahin, N.; Polat, R.; Dursun, Z., Electrocatalytic reduction of oxygen on bimetallic copper-gold nanoparticles-multiwalled carbon nanotube modified glassy carbon electrode in alkaline solution. *J Electroanal Chem* **2011,** *662* (2), 275-280.

10.(a) Vazquez, M. V.; Desanchez, S. R.; Calvo, E. J.; Schiffrin, D. J., The Electrochemical Reduction of Oxygen on Polycrystalline Copper in Borax Buffer. *J Electroanal Chem* **1994,** *374* (1-2), 189-197; (b) Cere, S.; Vazquez, M.; de Sanchez, S. R.; Schiffrin, D. J., Surface redox catalysis and reduction kinetics of oxygen on copper-nickel alloys. *J Electroanal Chem* **2001,** *505* (1-2), 118-124.

11.(a) Brisard, G.; Bertrand, N.; Ross, P. N.; Markovic, N. M., Oxygen reduction and hydrogen evolution-oxidation reactions on Cu(hkl) surfaces. *J Electroanal Chem* **2000,** *480* (1-2), 219-224; (b) Jiang, I.; Brisard, G. M., Determination of the kinetic parameters of oxygen reduction on copper using a rotating ring single crystal disk assembly (RRDCu(h k l)E). *Electrochim Acta* **2007,** *52* (13), 4487-4496.

12.Yan, X. Y.; Tong, X. L.; Zhang, Y. F.; Han, X. D.; Wang, Y. Y.; Jin, G. Q.; Qin, Y.; Guo, X. Y., Cuprous oxide nanoparticles dispersed on reduced graphene oxide as an efficient electrocatalyst for oxygen reduction reaction. *Chem Commun* **2012,** *48* (13), 1892-1894.

13.Chen, S. W.; Templeton, A. C.; Murray, R. W., Monolayer-protected cluster growth dynamics. *Langmuir* **2000,** *16* (7), 3543-3548.

14.Hostetler, M. J.; Wingate, J. E.; Zhong, C. J.; Harris, J. E.; Vachet, R. W.; Clark, M. R.; Londono, J. D.; Green, S. J.; Stokes, J. J.; Wignall, G. D.; Glish, G. L.; Porter, M. D.; Evans, N. D.; Murray, R. W., Alkanethiolate gold cluster molecules with core diameters from 1.5 to 5.2 nm: Core and monolayer properties as a function of core size. *Langmuir* **1998,** *14* (1), 17-30.

15.(a) Kang, X. W.; Chen, S. W., Electronic conductivity of alkyne-capped ruthenium nanoparticles. *Nanoscale* **2012,** *4* (14), 4183-4189; (b) Guo, Y. C., L.M.; Song, Y.; Hu, P.G.; Chen, S.W., Ruthenium Nanoparticles Stabilized by the Self-Assembly of Acetylene, Carboxylate, and Thiol Derivatives. *Sci. Adv. Mater.* **2014,** *6*, 1060-1067.

16.Mikheeva, V. I. M. t., N.N. , *J. Struct. Chem.* **1963,** *4*, 643-646.

17.Kang, X. W.; Zuckerman, N. B.; Konopelski, J. P.; Chen, S. W., Alkyne-Functionalized Ruthenium Nanoparticles: Ruthenium-Vinylidene Bonds at the Metal-Ligand Interface. *J Am Chem Soc* **2012,** *134* (3), 1412-1415.

18.Lide, D. R., *CRC Handbook of Chemistry and Physics : a Ready-reference Book of Chemical and Physical Data*. CRC Press: Boca Raton, Fla, 2004.

19.Ghodselahi, T.; Vesaghi, M. A.; Shafiekhani, A.; Baghizadeh, A.; Lameii, M., XPS study of the Cu@Cu2O core-shell nanoparticles. *Appl Surf Sci* **2008,** *255* (5), 2730-2734.

20.Wagner, C. D. R., W.M.; Davis, L.E. ; Moulder, J.F.; Muilenberg, G.E. , *Handbook of X-ray Photoelectron Spectroscopy: a Reference Book of Standard Data for Use in X-ray Photoelectron Spectroscopy*. Perkin-Elmer Corp.: Eden Prairie, Minn., 1979.

21.Kim, K. S., Charge-Transfer Transition Accompanying X-Ray Photoionization in Transition-Metal Compounds. *J Electron Spectrosc* **1974,** *3* (3), 217-226.

22.Elhaleem, S. M. A.; Ateya, B. G., Cyclic Voltammetry of Copper in Sodium-Hydroxide Solutions. *J Electroanal Chem* **1981,** *117* (2), 309-319.

23.Bard, A. J. F., L.R. , *Electrochemical Methods: Fundamentals and Applications*. John Wiley: New York 2001.

24.Zhang, J., *PEM fuel cell electrocatalysts and catalyst layers : fundamentals and applications*. Springer: London, 2008; p xxi, 1137 p.

25.Yan, X.-Y.; Tong, X.-L.; Zhang, Y.-F.; Han, X.-D.; Wang, Y.-Y.; Jin, G.-Q.; Qin, Y.; Guo, X.-Y., Cuprous oxide nanoparticles dispersed on reduced graphene oxide as an efficient electrocatalyst for oxygen reduction reaction. *Chem Commun* **2012,** *48* (13), 1892.

26.Zhou, Z.-Y.; Kang, X.; Song, Y.; Chen, S., Ligand-Mediated Electrocatalytic Activity of Pt Nanoparticles for Oxygen Reduction Reactions. *The Journal of Physical Chemistry C* **2012,** *116* (19), 10592-10598.

27.Jiang, T.; Brisard, G. M., Determination of the kinetic parameters of oxygen reduction on copper using a rotating ring single crystal disk assembly (RRDCu(hkl)E). *Electrochimica Acta* **2007,** *52* (13), 4487-4496.

Chapter 6

Graphene Quantum Dot Supported Copper Nanoparticles as Effective Catalysts for Oxygen Reduction in Alkaline Media

6.1 Introduction

Oxygen reduction reactions (ORR) have long been regarded as a major bottleneck of the overall fuel cell performance, due to the sluggish electron-transfer kinetics and complex reaction pathways. Therefore, extensive efforts have been devoted to the development of efficient catalysts so that sufficiently high current density can be achieved for practical applications. Towards this end, substrate-supported discrete nanoparticles have attracted particular attention. These typically include monometallic nanoparticles[1], alloy nanoparticles,[2] metal oxides nanoparticles,[3] or transition metal chalcogenides nanoparticles[4] that are supported on various substrates including metal structures,[5] metal oxides,[6] or carbon-based materials such as carbon black, standard carbon fibers, single- or multi-walled carbon nanotubes,[7] and graphene sheets.[8] These supporting materials play important roles in, for instance, preventing nanoparticle aggregation and hence increasing the corresponding surface areas;[9] manipulating electronic energy of the metal nanoparticles and hence interactions with O_2 molecules via intimate electronic interactions with the supporting substrates[5]; enhancing electronic conductivity and serving as current collectors; as well as improving structural stability of the catalysts in extreme acidic or basic environments.

Among these, Pt nanoparticles (diameter 2 to 4 nm) supported on high-surface-area carbon black have been used extensively.[10] However, the high costs and scarcity of platinum render it necessary to develop cost-effective non-Pt

substitutes for fuel cell electrocatalysis. Copper is inexpensive, abundant with excellent electronic conductivity. It has been reported that O_2 molecules can adsorb readily onto and migrate on copper surfaces[11] and the adsorbed oxygen may undergo a two-step hydrogenation process to form gaseous water.[12] ORR activities of bulk copper have also been observed in a borax buffer solution[13] or in sulfuric acid solution,[14] where the surface redox chemistry involving Cu_2O/CuO plays an important role in the reduction of oxygen molecules. In a more recent study reduced graphene oxide (rGO)-supported cuprous oxide nanoparticles were found to serve as efficient catalysts for oxygen reduction where electron transfer occurred from the rGO sheets to oxygen.[15] However, graphene sheets usually exhibit irregular shapes and are prone to folding and wrinkling because of strong π-π interactions leading to a loss of the surface area.[16] Such an issue may be minimized by using nanosized graphene quandum dots. For instance, platinum nanoparticles supported on graphene quantum dots (GQD) (in the range of 1 to 4 nm) have been reported to exhibit significantly enhanced catalytic activity towards oxygen reduction as compared to commercial Pt/C catalysts.[17] This was accounted for by the large surface-to-volume ratio and abundant structural defects of GQDs that manipulate the bonding interactions of oxygen on Pt and hence facilitate the corresponding charge transfer process. Such a fundamental principle may be exploited for the design and engineering of effective ORR catalysts based on GQD-supported metal nanocomposites. This is the primary motivation of the present study.

Herein, we prepared GQD-supported copper nanoparticle composites and examined the ORR activity in alkaline media. Experimentally, the submicrometer domains of traditional pitch-based carbon fibers were broken down by acid treatments and chemical exfoliation, yielding nanometer-sized GQDs.[18] The GQDs were then used to prepare a series of Cu/GQD nanocomposites at controlled copper loading by thermolytic reduction of copper salts in 1,2-propanediol, followed by hydrothermal treatments at various temperatures. The structural characteristics of the Cu/GQD nanocomposites were carefully examined by transmission electron microcscopic, Raman, and X-ray photoelectron measurements. Electrocatalytic activities of the nanocomposites were tested by using the rotating ring-disk electrode (RRDE) technique. The Cu/GQD nanocomposites with a copper loading of 2.88 at% and 3.32% show best performance among the series, within the context of onset potential, number of electron transfer as well as kinetic current density.

6.2 Results and discussion

The chemical compositions and valence states of the Cu/GQD nanocomposites were first evaluated by XPS measurements. Figure 1 (A) depicts the survey spectra of the series of samples where the elements of carbon (C1s 285 eV), oxygen (O1s 532 eV), and copper (Cu2p 979 eV) can be clearly identified (the Si2p peaks are from the Si substrate), suggesting the formation of Cu/GQD nanocomposites. High-resolution scans of the C1s and $Cu2p^{3/2}$ electrons are shown in panels (B) and (C), respectively. For all samples, deconvolution of

the C1s spectra in panel (B) yields three major components.[19] The first is sp^2 C (green curves) which exhibited a rather consistent binding energy among the samples within the narrow range of 284.7 – 285.0 eV. The second is carbons in C–OH (yellow curves) which might be identified with the peak energy between 285.5 and 286.2 eV. The third is C=O/COOH (blue curves) where the binding energy exhibited a rather apparent disparity among the samples, 287.11 eV for sample (1), 289.06 eV for sample (2), 287.67 eV for sample (3), and 288.22 eV for sample (4). This suggests that in samples (1), (3) and (4) the primary form was carbonyl carbons (C=O) whereas in sample (3) carboxylic carbons (COOH).[19] In addition, based on the integrated peak areas, the fraction of C=O/COOH among the total carbons was estimated to be (1) 24.78%, (2) 6.65%, (3) 15.54, and (4) 13.56%.

As for the $Cu2p^{3/2}$ electrons in panel (C), three major peaks were identified by spectral deconvolution with the binding energies very consistent among the four samples. Of these, the peaks at ca. 934.5 eV and 954.3 eV might be ascribed to the $Cu2p^{3/2}$ and $Cu2p^{1/2}$ electrons of metallic copper, respectively.[20] Yet, as the binding energy of Cu(I) and Cu(0) is only 0.1 eV apart, the presence of Cu(I) cannot be excluded. In fact, from panel (A), one can see a broad peak at around 570 eV that is consistent with the LMM-2 auger transitions of Cu(I), indicating at least partial oxidation of the nanoparticles into Cu_2O.[20] Additionally, the emergence of a satellite peak at ca. 944 eV between the $Cu2p^{3/2}$ and $Cu2p^{1/2}$ peaks suggested the formation of CuO. Such a satellite feature is typically

observed in ions with a partially filled 3d shell (e.g., Cu(II)) but absent in ions with a completely filled 3d shell (e.g., Cu(I) and Cu(0)), and has been largely ascribed to the shake-up effect where the outgoing electron interacts with a valence electron and excites it to a higher energy level.[21] Similar behaviors have been observed in previous studies with alkyne-capped copper nanoparticles.[22] Furthermore, based on the integrated peak areas, the fraction of Cu(II) among all copper species was all around 30%, whereas the atomic ratio of Cu/C in the nanocomposites was estimated to be (1) 2.34%, (2), 2.88%, (3) 3.32% and (4) 3.54%.

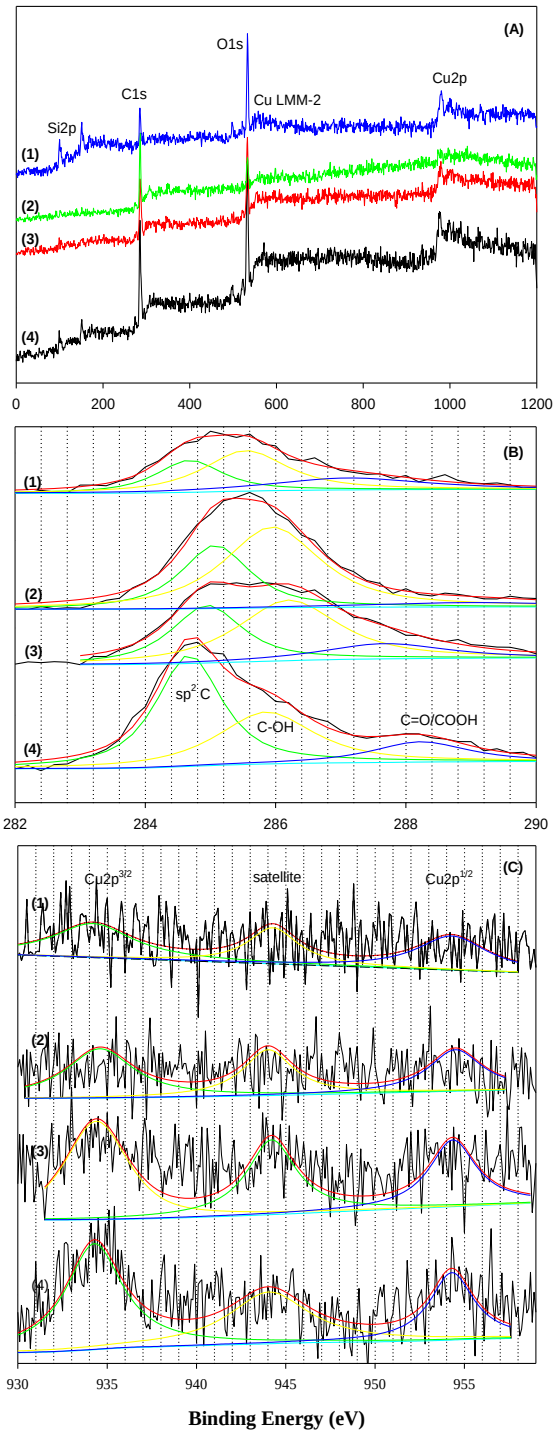


Figure 6.1.(A) XPS survey spectra and high-resolution scans of (B) C1s and (C) Cu2p electrons of Cu/GQD nanocomposites at different Cu/C atomic ratios (*x*). In panels (B) and (C), black curves are experimental data and colored curves are deconvolution fits.

Table 6.1. Summary of XPS results of Cu/GQD nanocomposites.

	Cu/GQD	**1**	**2**	**3**	**4**
C1s	Sp2 C (eV)	284.68	285.07	284.94	284.67
	C-OH (eV)	285.54	285.95	286.2	285.85
	C=O/COOH (eV)	287.11	289.06	287.67	288.22
	$x_{\text{non-sp2C}}$ (%)	71.13	66.63	66.04	48.49
	$x_{\text{C=O/COOH}}$ (%)	24.78	6.65	15.54	13.56
Cu2p	$Cu2p^{3/2}$ (eV)	934.20	934.60	934.40	934.28
	Satellite (eV)	944.28	944.01	944.21	944.06
	$Cu2p^{1/2}$ (eV)	954.30	954.50	954.35	954.30
	$x_{\text{Cu(II)}}$	26.19%	29.29%	30.07%	31.57%
Total copper loading (Cu:C) (at%)		2.34	2.88	3.32	3.54

The structures of the Cu/GQD nanocomposites were then examined by TEM measurements. Figure 2 shows representative TEM micrographs of Cu/GQD (*x*) nanocomposites at different Cu/C atomic ratios: (A) *x* = 3.54%, (B) *x* = 3.32%, (C) *x* = 2.88%, and (D) *x* = 2.34%. The formation of copper nanoparticles was evidenced by the dark-contrast objects (signified by the red arrows), which were embedded within the low-contrast GQDs that showed various degrees of agglomeration in all four samples. Furthermore, one can see that the size of the copper nanoparticles varied rather drastically with the copper loading: ca. 14 nm at x_{Cu} = 3.54% in panel (A), 12 nm at x_{Cu} = 3.32% in panel (B), 10 nm at x_{Cu} = 2.88% in panel (C), and 5 nm at x_{Cu} = 2.34% in panel (A). Such a variation of the nanoparticle dimensions might be accounted for by the nanoparticle growth dynamics where increasing concentration of capping ligands is known to lead to enhanced passivation of the nanoparticles and hence diminishing sizes.[23]

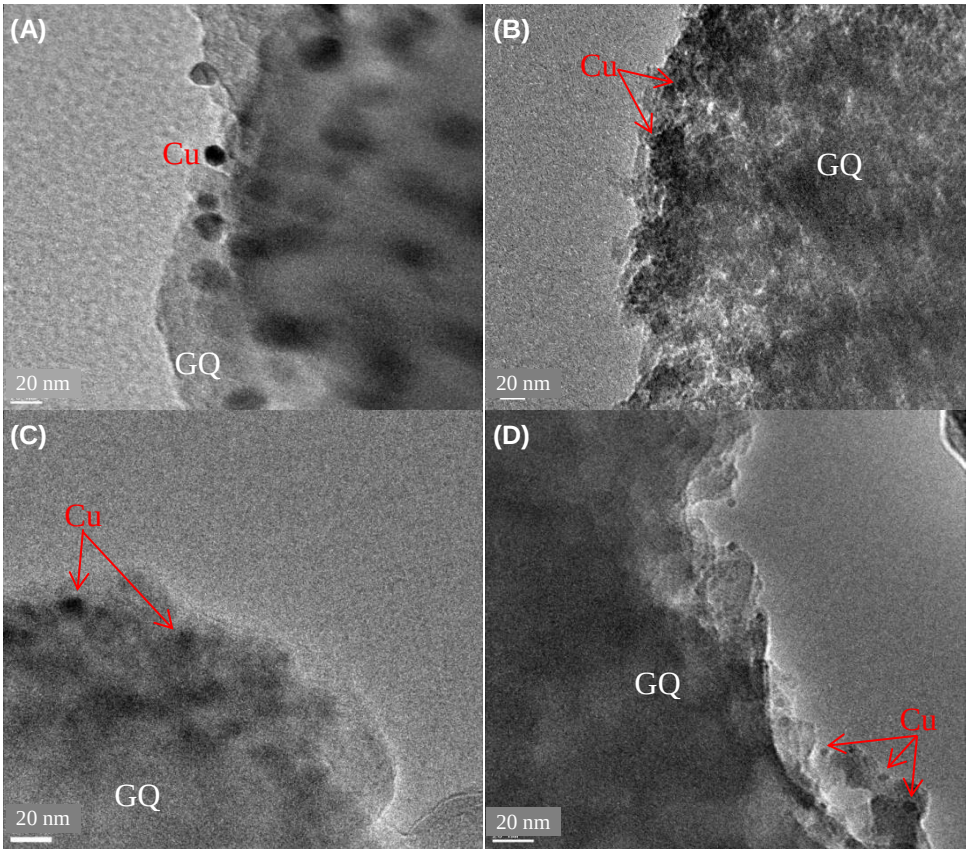


Figure 6.2. TEM micrographs of Cu/GQD nanocomposites at different Cu/C atomic ratios (x): (A) x = 3.54%, (B) x = 3.32%, (C) x = 2.88%, and (D) x = 2.34%. Scale bars are all 20nm.

Further structural insights were unraveled by Raman spectroscopic measurements. From Figure 3, one can see two prominent vibrational bands at *ca*. 1370 cm^{-1} and 1615 cm^{-1} for all samples, which might be assigned to the D and G bands of GQD, respectively. Additionally, the ratio of the D and G band intensity (I_D/I_G) increases in the order of 0.91 (x = 2.88%) <0.96 (x = 3.32%) < 0.97 (x = 3.54%) < 0.98 (x = 2.34%), suggesting that the Cu/GQD (2.88%) sample exhibited the least amount of structural defects among the series. This is consistent with results from the XPS measurements (Figure 1 and Table 1). Such a correlation has also been observed previously with Pt/GQD nanocomposites.[17a]

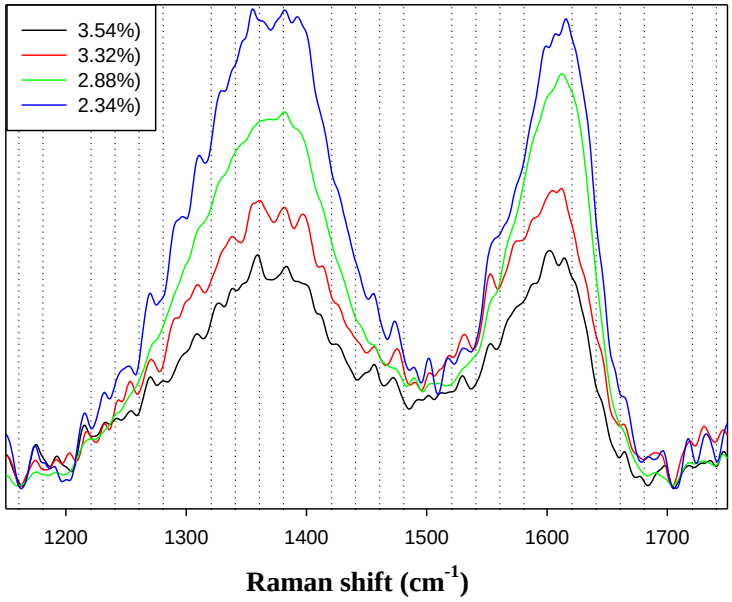


Figure 6.3. Raman spectra of Cu/GQD nanocomposites at different Cu/C atomic ratios (x) which are specified in figure legends.

Table 6.2. Summary of results from Raman spectroscopic measurements.

Cu/GQD (*x*)	I_D (cm^{-1})	I_G (cm^{-1})	I_D/I_G
3.54%	1361	1603	0.97
3.32%	1362	1612	0.96
2.88%	1381	1613	0.91
2.34%	1370	1616	0.99

The electrocatalytic activity of the nanocomposite catalysts for ORR was then tested by electrochemical measurements. Figure 4 shows the cyclic voltammograms of a glassy-carbon electrode modified with 15 μg of Cu/GQD in a nitrogen-purged NaOH solution. It can be seen that the Cu/GQD (3.32%, red curve) sample exhibited two rather prominent anodic peaks at around +0.55 V and +0.84 V (vs RHE), with the former due to the formation of a monolayer of Cu_2O while the latter to the formation of a thick multilayer film of CuO, and a cathodic peak at around +0.70 V that is likely to originate from the partial reduction of CuO to Cu_2O.[22, 24] Similar voltammetric featrures can be seen with the Cu/GQD (2.88%, green curve; 3.54%, black curve) samples. In contrast, for the Cu/GQD (2.34%, blue curve), the voltammogram was largely featureless, possibly because of the low loading of copper and encapsulation by the GQDs (Figure 2). Furthermore, one can see that despite the same catalyst loading, the double-layer charging currents, and hence the effective electrochemical surface area, exhibited an apparent variation among the series, increasing in the order of Cu/GQD (2.34%) < (3.54%) < (2.88%) < (3.32%).

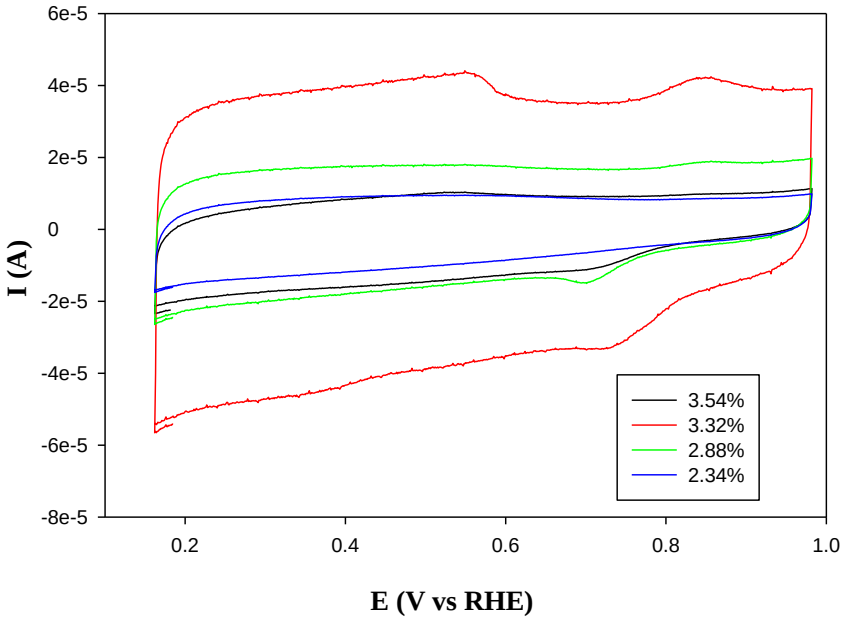


Fig 6.4. Cyclic voltammograms of a glassy-carbon electrode (dia. 5.61 mm) modified with Cu/GQD nanocomposites in a nitrogen-purged 0.1 M NaOH solution. Potential scan rate: 10 mV/s. Catalyst loading: 15 μg.

Figure 5 shows the RRDE voltammagrams of the same electrodes in an oxygen-saturated 0.1 M NaOH solution at the rotation rates of 100 to 2500 rpm. We can see that for all Cu/GQD nanocomposites, non-zero cathodic currents started to emerge at electrode potentials more negative than +0.80 V, and reached a plateau at sufficiently negative potentials (e.g., E < +0.60 V), indicating apparent ORR activity. Yet, marked discrepancy can be seen of the electrocatalytic performance. For instance, the onset potential varied with the copper concentration in the nanocomposites, +0.82 V for x = 3.54%, +0.83 V for x = 3.32%, +0.82 V for x = 2.88%, and +0.75 V for x = 2.34%. A similar variation can be seen with the disk limiting currents at +0.40 V at the rotation rate of 2500 rpm, 0.88 mA for x = 3.54%, 1.26 mA for x = 3.32%, 1.22 mA at x = 2.88%, and 0.94 mA for x = 2.34%.

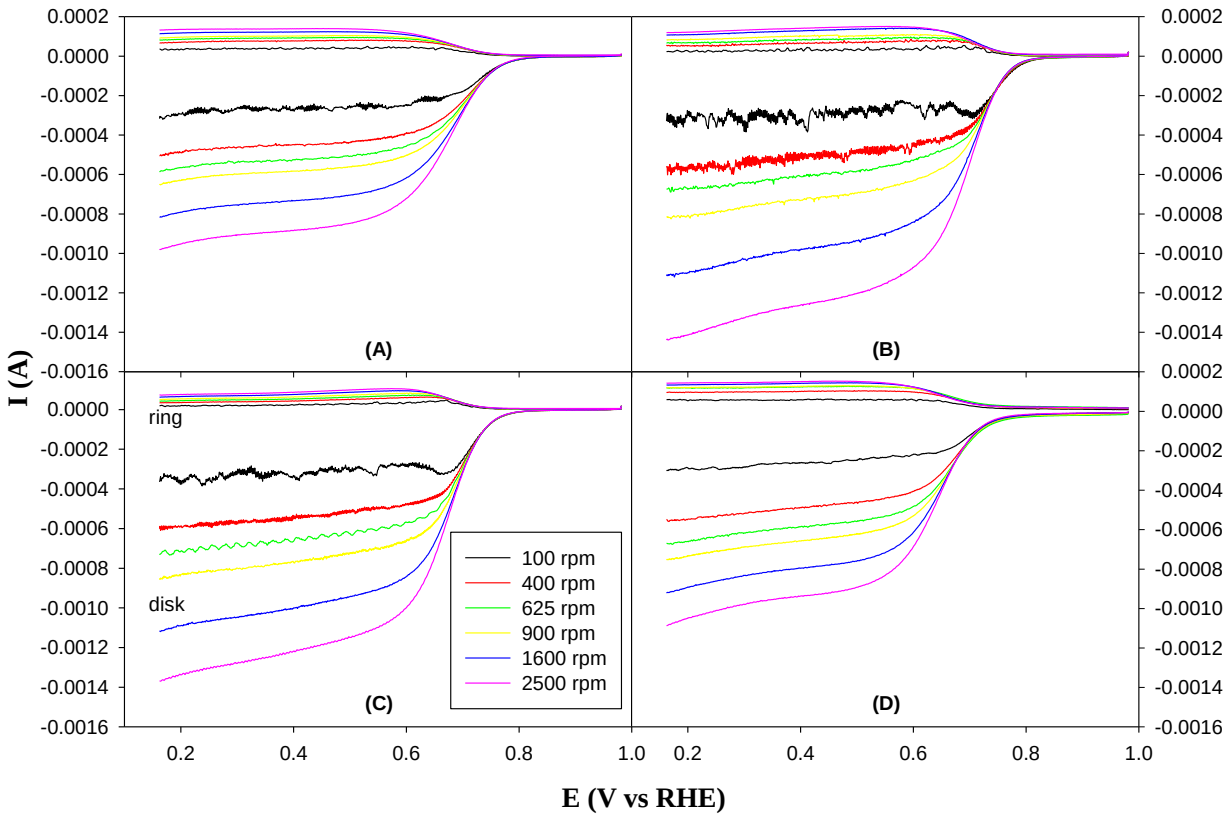


Figure 6.5. RRDE voltammograms of a platinum ring-glassy carbon disk electrode with the disk electrode modified with 15 μg of (A) Cu/GQD at different Cu/C atomic ratios (*x*), (A) 3.54%, (B) 3.32%, (C) 2.88%, and (D) 2.34% in an oxygen-saturated 0.1M NaOH solution. Electrode rotation rates are specified in the figure legends. Ring potential was set at +1.30 V vs RHE.

Furthermore, one can see that at the ring potential of +1.30 V, the ring currents were at least one order of magnitude smaller than the disk currents for all four nanocomposites catalysts, indicating a minimal amount of H_2O_2 as the oxygen reduction product. Based on the corresponding ring (I_{Ring}) and disk currents (I_{Disk}), the number (n) of electron transfer involved in ORR can be estimated by $n = 4I_{Disk}/(I_{Disk}+I_{Ring}/N)$ with N being the collection efficiency.[25] Figure 6 shows the variation of n with electrode potential. It can be seen that the n values increased rapidly with the electrode potential swept from ca. +0.80 V to +0.75 V in the so-called kinetic-controlled region, and at more negative potentials, the increment remained apparent but slow. Within the potential range of +0.60 to +0.10 V, the n values also exhibited a variation with the copper concentration (*x*) in the Cu/GQD composites, (3.54%) < (3.32%) ≈ (2.34%) < (2.88%). For instance, at +0.40 V, n = 2.76 for *x* = 3.54%, 3.17 for *x* = 3.32%, 3.20 for *x* = 2.34%, and 3.42 for *x* = 2.88%, corresponding to the fraction of peroxide species in the final products of 62%, 41%, 40%, and 31% respectively. This signifies that ORR took place predominantly by the two-electron pathway at Cu/GQD (3.54%) whereas complete reduction to hydroxide (OH^-) became favorable with other nanocomposites catalysts.

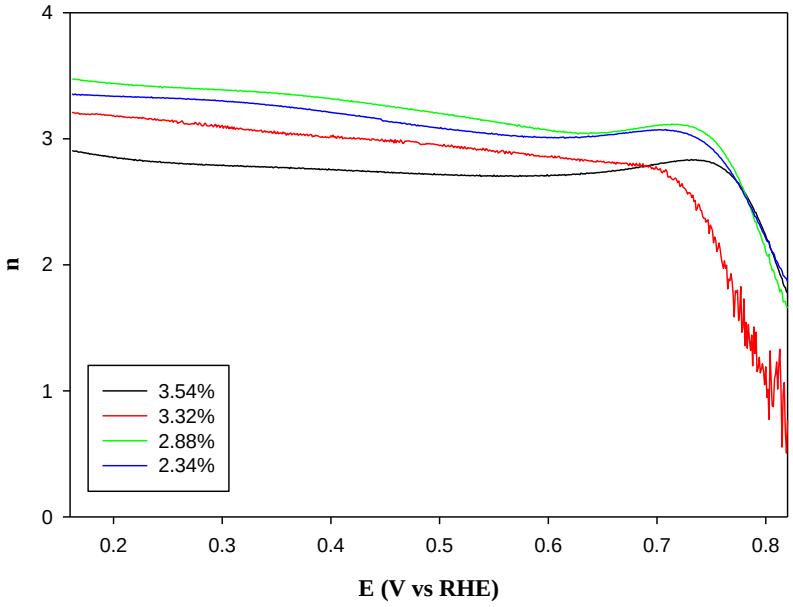


Figure 6.6. Variation of the number of electron transfer (n) in oxygen reduction with electrode modified with 15 μg of Cu/GQD at different Cu/C atomic ratios (*x*), 3.54% (black curve), 3.32% (red curve), 2.88% (green curve), and 2.34% (blue curve). Symbols were experimental data calculated from the RRDE voltammograms of those three catalysts at 1600 rpm in Figure 6.5.

Tafel plot was introduced as shown in Fig 7 to compare electron transfer kinetics of four electrodes. It's known that in rotating disk voltammetric measurement, measured currents include both kinetic current (I_k) and diffusion (I_d) controlled contributions[26].

$$\frac{1}{I_D} = \frac{1}{I_k} + \frac{1}{I_d} = \frac{1}{I_k} + \frac{1}{B\omega^{1/2}} \tag{6.1}$$

Plotting I_D^{-1} against $\omega^{-1/2}$ within respective kinetically-controlled region can yield linear regressions (so-called Koutecky-Levich plots), y-axis intercepts of which can be used to quantify the kinetic currents (I_K) as shown in Fig 7. Tafel plot enables us to see how much overpotential is required to obtain same kinetic current for four electrodes excluding mass-transport effects. Before reaching limiting currents smallest overpotential is required for Cu-GQD-3.32% to obtain same kinetic currents while largest overpotential is needed for Cu-GQD-2.34% in contrast. Difference in ORR kinetics of Cu-GQD-3.54% and Cu-GQD-2.88% is subtle although their Cu loadings are quite different.

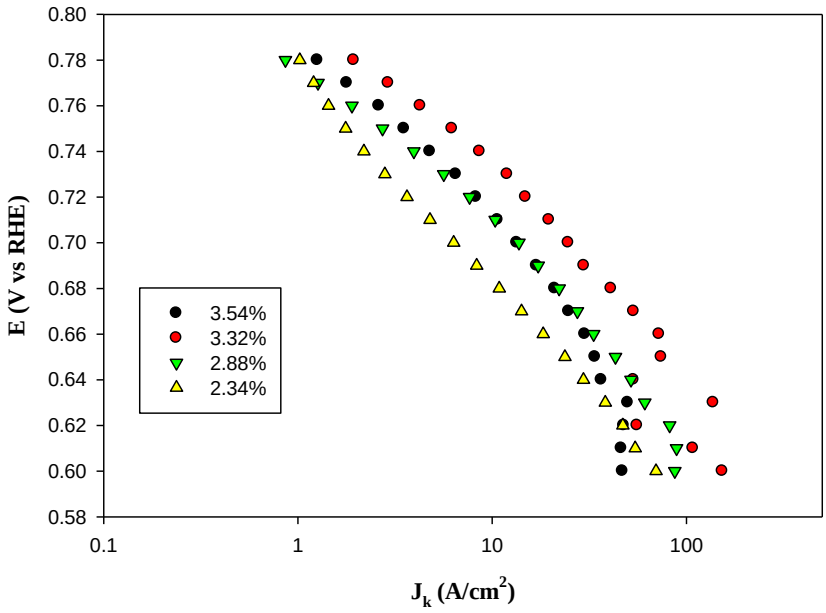


Fig 6.7. Tafel plots of electrode modified with 15 μg of Cu/GQD at different Cu/C atomic ratios (*x*), 3.54% (black), 3.32% (red), 2.88% (green), and 2.34% (yellow). Symbols were experimental data obtained by linear regression of the Koutecky-Levich plots.

In combination of ORR parameters such as limiting currents, onset potential, number of electrons transferred (n), and kinetic currents, we can find that Cu/C atomic ratio maters with ORR performance but it does not mean high Cu/C atomic ratio is always good. Among four electrodes, Cu-GQD-3.54% with most Cu contents show poorest performance and Cu-GQD-2.34% with least Cu contents show less-satisfying catalytic activity also. The composite catalysts with moderate Cu contents such as Cu-GQD-3.32% and Cu-GQD-2.88% exhibit best performances among the series. Coincidently, the two Cu/GQD nanocomposites contain moderate defect concentrations ($x_{\text{non-sp2C}}$) as shown by Table 1. This is reasonable since surface defects can help the nucleation of metal species and promote the intimate interactions between graphene support and metal nanoparticles, which can contribute to catalytic performance of those nanocomposites. Yet electronic conductivity of graphene quantum dots may also suffer a lot under high defect concentrations. Further enhanced performance may be obtained by deliberate manipulation of GQD structural defects, so Cu-GQD-2.88% was chosen for hydrothermal treatment at different temperatures aiming to remove some surface defects.

Sample of Cu/GQD (x=2.88%) was hydrothermal treated at different temperatures varying from 140°C, 160°C, 180°C to 200°C and as-obtained products were denoted as Cu/GQD-2.88%-140°C, Cu/GQD-2.88%-160°C, Cu/GQD-2.88%-180°C, and Cu/GQD-2.88%-200°C separately. Raman spectrum was also conducted to see if any differences in structures will be brought to those

hydrothermal-treated samples. Table 3 summarizes positions of D peak and G peak for samples above and corresponding ratio of D peak over G peak. One noteworthy fact is that after hydrothermal treatments at different temperatures positions of D peak went back to typical values in range of 1358 to 1361 cm^{-1}. This "self-healing" phenomenon was similarly observed on graphitic structures after heat treatments[27]. Significant differences on positions of G peaks were not found for hydrothermal-treated samples. What's more, hydrothermal treatments increase intensity of D peak and concentrations of defects while sample "Cu/GQD-2.88%-160°C" bear D peak with strongest intensity and most wealthy defects as indicated by fourth and fifth columns of table 3.

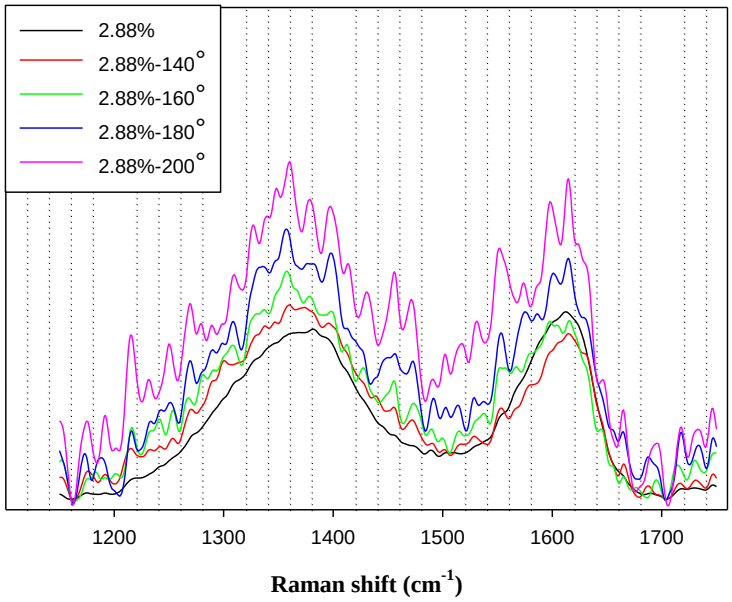


Fig 6.8. Raman spectra of Cu/GQD-2.88% (black curve) and after hydrothermal treatment at 140°C (red curve), 160°C (green curve), 180°C (blue curve) and 200°C (pink curve).

Table 6.3. Ratios of D peak over G peak and their corresponding positions on Raman spectrum for Cu/GQD-2.88% before and after hydrothermal treatment.

	$I_D(cm^{-1})$	$I_G(cm^{-1})$	I_D/I_G
2.88%	1381	1613	0.91
2.88%-140°C	1361	1616	1.17
2.88%-160°C	1358	1615	1.28
2.88%-180°C	1358	1613	1.14
2.88%-200°C	1360	1613	1.09

To investigate effects brought on surface defect concentrations via hydrothermal treatments, XPS measurements were also conducted for those hydrothermal-treated samples. Fig 9a shows the full survey spectra of Cu/GQD-2.88% sample and the sample after hydrothermal treatments with clearly-identified peaks of Si2p, C1s, O1s, and Cu2p seperately. High-resolution scans of C1s and Cu2p electrons of "Cu/GQD-2.88%" after hydrothermal treatments are shown in Fig 9b and 9c respectively. Binding positions of corresponding C1s and $Cu2p^{3/2}$ electrons were summarized in table 4. Similarly three major components, sp^2C, C-OH and C=O/C-OOH, were deconvoluted from the carbon 1s electrons as shown in Fig 9b. Compared with "Cu/GQD-2.88" sample, hydrothermal treatments indeed altered binding positions of C1s components and different hydrothermal annealing temperatures brought different effects. For carbon in COOH, binding positions of samples treated at different temperatures exhibit a volcano shape with the one annealed at 160°C at the top point. What's more, hydrothermal treatments also removed structural defects from surfaces of graphene quantum dots as indicated by decreased fractions of defective carbon in table 4 with increasing hydrothermal temperatures, and similar trend was observed in previous report[17a].

As for the $Cu2p^{3/2}$ electrons, both Cu_2O and CuO components were deconvoluted from four hydrothermal-treated samples as shown in Fig 9c and their corresponding positions and amount ratios were summarized in Table 4 also. After hydrothermal treatments, red-shifts on binding positions of $Cu2p^{3/2}$

electrons (including the Cu_2O and CuO components) were observed and the shifting degree varies following this order: Cu/GQD-2.88%-180°C < Cu/GQD-2.88%-200°C < Cu/GQD-2.88%-140°C < Cu/GQD-2.88%-160°C. In combination with observed shifts on C1s electrons, it's suspected that hydrothermal treatments altered electronic interactions between copper contents and GQDs. What's more, it's believed that more extensive electron-transfer occurred on "Cu/GQD-2.88%-160°C" sample from graphene support to copper species compared with original "Cu/GQD-2.88%" sample signified by blue-shift on C1s electrons and red-shifts on $Cu2p^{3/2}$ electrons. Hydrothermal treatments at other temperatures did not bring such promoting effect on electron interactions, but increased relative amounts of Cu(0) and Cu(I) species for all annealed samples as revealed in table 4. The increases on relative amounts of Cu(0) and Cu(I) species are consistent with blue-shits on binding positions of satellite peak.

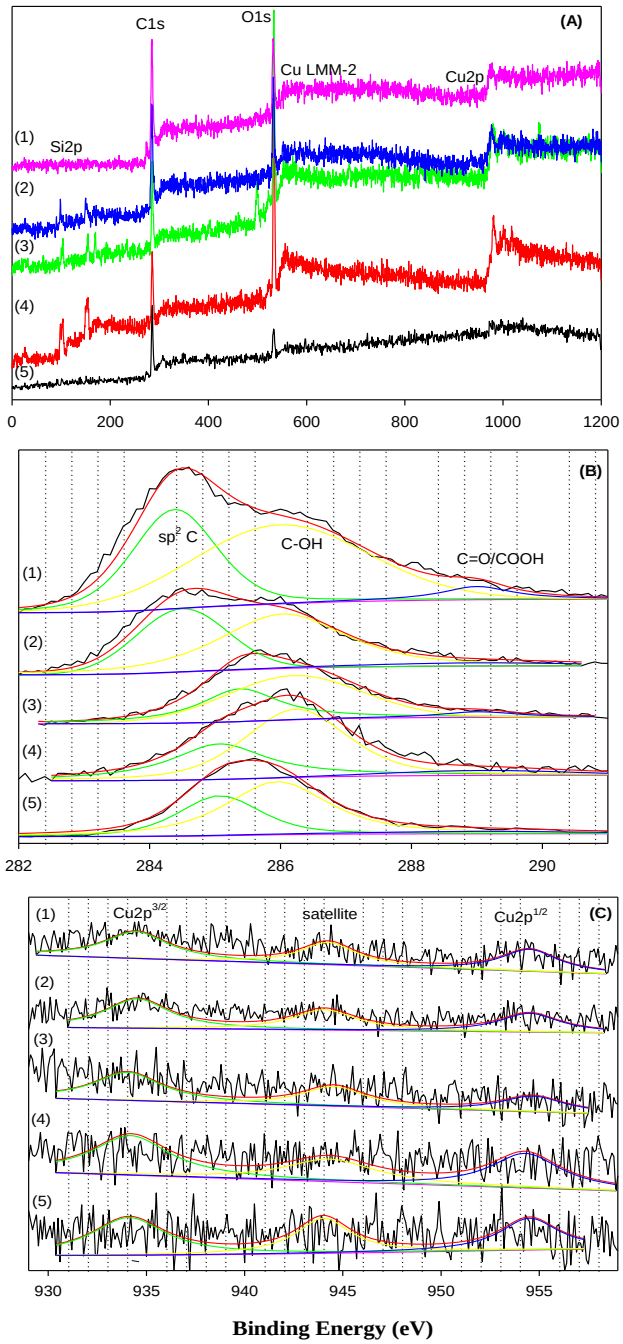


Fig 6.9. (A) XPS survey spectra and high-resolution scans of (B) C1s and (C) Cu2p electrons of Cu/GQD-2.88% nanocomposites and after hydrothermal treatments at different temperatures. In panels (B) and (C), black curves are experimental data and colored curves are deconvolution fits.

Table 6.4. Summary of XPS results of Cu/GQD-2.88% nanocomposites and after hydrothermal treatments.

	Cu/GQD-2.88%	**1**	**2**	**3**	**4**	**5**
C1s	Sp2 C (eV)	284.38	284.50	285.38	285.06	285.07
	C-OH (eV)	285.99	286.03	286.20	286.24	285.95
	C=O/COOH (eV)	289.00	288.99	289.15	289.10	289.06
	$x_{\text{non-sp2C}}$ (%)	61.65	62.39	63.42	64.38	66.63
	$x_{\text{C=O/COOH}}$ (%)	5.46	5.63	5.84	6.05	6.65
Cu2p	$Cu2p^{3/2}$ (eV)	934.48	934.53	934.03	934.20	934.60
	Satellite (eV)	944.25	944.06	944.53	944.33	944.01
	$Cu2p^{1/2}$ (eV)	954.50	954.50	954.68	954.30	954.50
	$x_{\text{Cu(II)}}$	29.52%	30.00%	30.03%	26.96%	29.29%
Hydrothermal treatment temperature (°C)		200	180	160	140	NA

Samples of Cu-GQD-2.88% hydrothermal treated at 140°C, 160°C, 180°C, and 200°C for 12 hours then underwent electrochemical characterizations such as cyclic voltammetry and RRDE measurement. Similarly CV graphs of Cu-GQD-2.88% before and after hydrothermal treatments show anodic peaks located at +0.55 V and +0.84 V indicating formation of Cu_2O and CuO correspondingly. And it seems that hydrothermal treatments have some effects on capacitive currents of samples above. Before hydrothermal treatment Cu-GQD-2.88% exhibit moderate capacitive currents and 140°C treatment reduced capacitive currents a bit while 160°C and 200°C treatments increase capacitive currents to different degrees. It seems that no apparent effect was brought on capacitive current as to 180°C treatments.

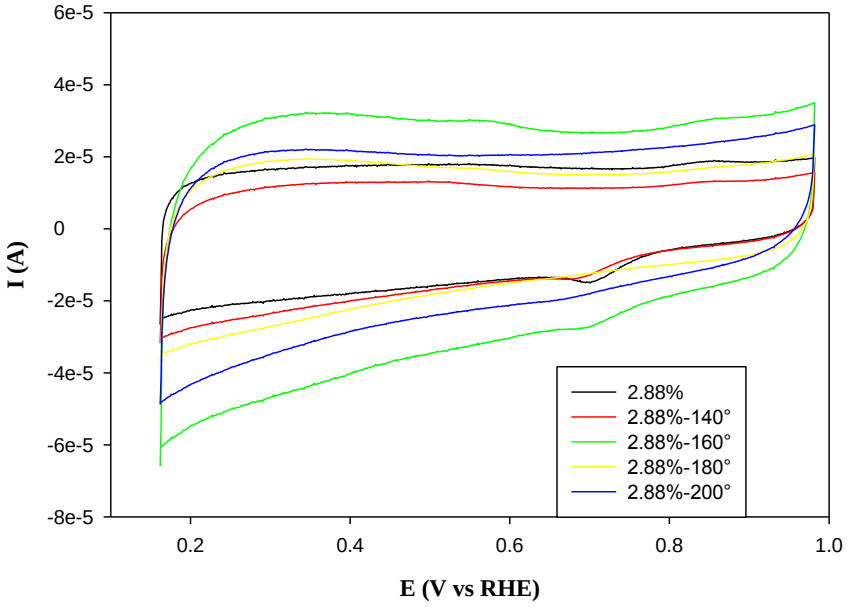


Fig 6.10. Cyclic voltammograms of Pt-ring-glassy carbon-disk electrode modified with 15ug Cu-GQD-2.88% (black curve), and after hydrothermal treatments at 140°C (red curve), 160°C (green curve), 180°C (yellow curve) and 200°C (blue curve).

Fig.11. shows RRDE graphs of Cu-GQD-2.88% after hydrothermal treatments. Different hydrothermal treating temperatures seem to bring different changes on onset potentials. For example, the 140°C, 180°C treatments negatively shifted the onset potential to different degrees although they increased diffusion limiting currents a bit when applied potential is more negative than +0.3 V. On the other hand, 160°C treatments significantly shifted onset potential more positively by approximately 25mV and increased diffusion limiting current from 1.36mA to 1.96mA. Also it's apparent that ring currents of Cu-GQD-2.88% treated at 160°C are significantly smaller than those treated at 140°C, 180°C, 200°C and those untreated samples.

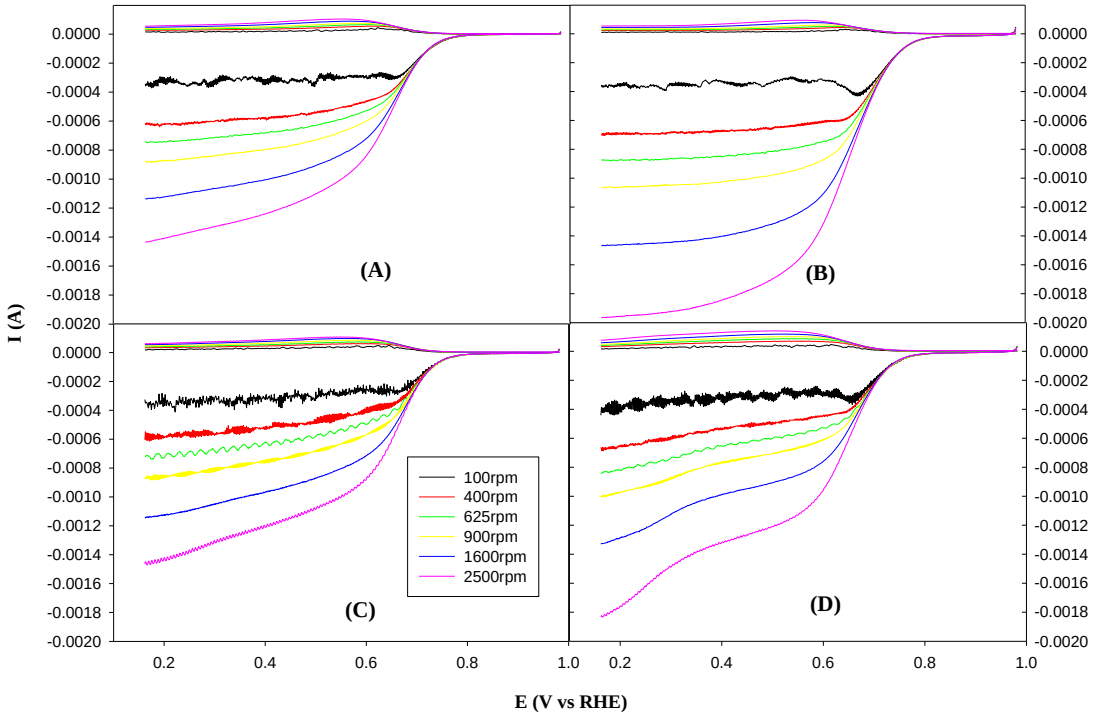


Fig 6.11. RRDE voltammograms of a platinum ring-glassy-carbon disk electrode modified with 15ug Cu-GQD-2.88% hydrothermal treated at different temperatures, (A) 140°C, (B) 160°C, (C) 180°C and (D) 200°C in an oxygen-saturated 0.1M NaOH solution. Electrode rotation rates are specified in the figure legends. Ring potential was set at +1.30 V vs RHE.

Plot of number of electrons transferred during whole potential range as shown on Fig.12. confirms that 160°C hydrothermal treatment shifted the onset potential by around 30mV in the positive direction, and 200°C treatment also positively shifted onset potential of untreated Cu-GQD-2.88% although the shift is subtle. What's more, after 160°C treatment number of electrons transferred was increased from 3.42 to 3.64 at +0.40 V, suggesting more favorable 4e pathway. Hydrothermal treatments at other temperatures seem to bring little effects on main pathway of oxygen reduction reaction as signified on number of electrons transferred.

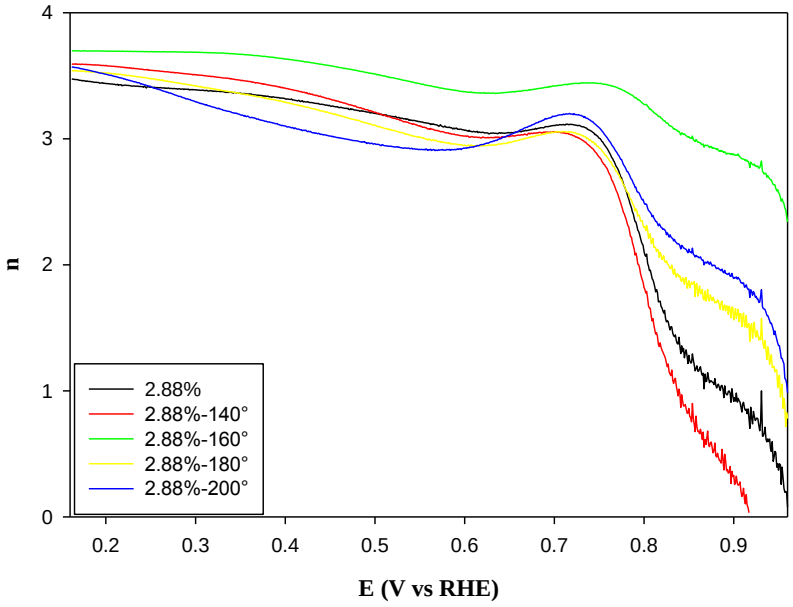


Fig 6.12. Variation of the number of electron transfer (n) in oxygen reduction with electrode modified with 15ug Cu-GQD-2.88% (black curve) and after hydrothermal treatments at different temperatures, 140°C (red curve), 160°C (green curve), 180°C (yellow curve) and 200°C (blue curve). Symbols were experimental data calculated from the RRDE voltammograms of those three catalysts at 1600 rpm in Figure 6.11.

We can easily see from Tafel plot as shown in Fig 13 that the sample hydrothermal treated at 160°C stood out in case of area-specific kinetic current density compared with untreated sample and sample hydrothermal treated at other temperatures. During the whole kinetic-controlled potential range, kinetic current densities were apparently increased when hydrothermal treated at 160°C while differences brought by the 180°C and 200°C treatments were subtle and the 140°C treatment decreased kinetic current densities compared with untreated sample.

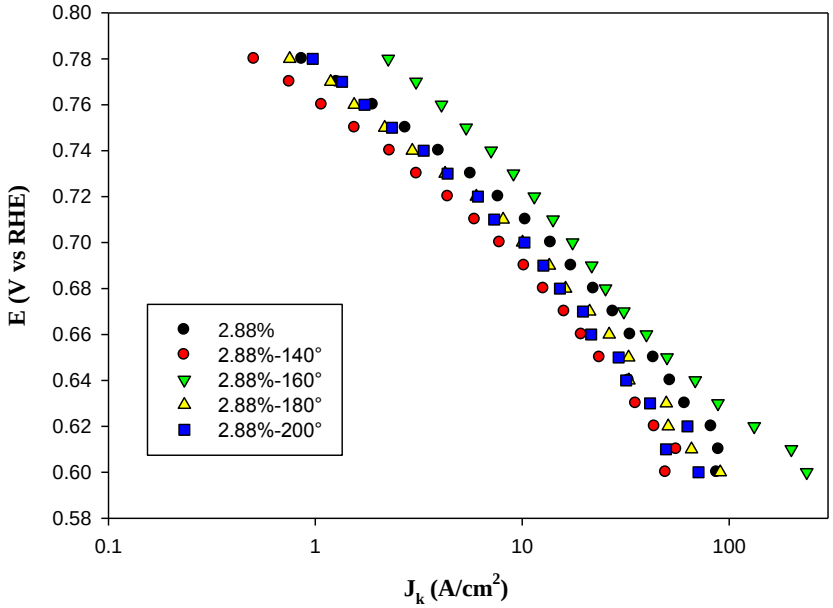


Fig 6.13. Tafel plots of electrode modified with 15ug Cu-GQD-2.88% (black curve), and after hydrothermal treatments at 140°C (red curve), 160°C (green curve), 180°C (yellow curve) and 200°C (blue curve). Symbols were experimental data obtained by linear regression of the Koutecky-Levich plots.

After deliberate manipulation of structural defects via hydrothermal treatments, it's obvious that the 160°C hydrothermal treatments actually enhanced catalytic performance as evidenced by positively-shifted onset potential, highest diffusion limiting current, increased number of electrons transferred and superior kinetics. This may be ascribed to the enhanced electronic interactions between graphene support and copper nanoparticles as discussed previously regarding to the XPS results, which led to deliberate manipulation of charge transfer dynamics of oxygen reduction.[28]

It's known that there is a volcano-shape relationship between ORR activity and d-band center of metals where Pt lies nearest to top of the volcano among pure metals[5, 29]. Yet the d-band center of Pt still needs to be further downshifted to weaken adsorption of intermediates and gain better ORR activity[30]. Copper has strong affinity for oxygen molecules and its d-band center lies on the right side of Pt[31], which means that decreased electron density and down-shifted d-band center are also favored for copper-based catalysts toward oxygen reduction. To address this issue, one possible solution is to deliberately manipulate electronic interactions between graphene support and copper nanoparticles. Those electronic interactions may promote charge transfer from support to metal center and adsorbed oxygen molecules, and tune the electron density and d-band center as well. Electronic interactions certainly vary a lot for the four Cu/GQD nanocomposites with varied defect concentrations, and samples with moderate defect concentrations exhibited best performance among the series

due to a balance between intimate electronic interactions and conductivity. After removing some structural defects via hydrothermal treatments, electronic interactions between graphene support and copper nanoparticles were further tuned by lower-concentrated defects. Under this defect-mediation strategy, the sample with strongest electronic interactions (signified by red-shift on B.E. of Cu2p and blue-shifts on B.E. of C1s) show optimal catalytic performance, which may be ascribed significantly alleviated adsorption strength of intermediates like O^- and OH^-.

It's noteworthy that electrocatalytic performance of Cu/GQD sample with optimized copper loadings and defects concentrations (Cu//GQD-2.88%-160°C) is subpar compared with Pt/GQD nanocomposites which exhibit onset potential more positive than +0.90 V and $n \approx 4.0$[17a, 32]. However the activity is better than that of Cu_2O/RGO composite (onset potential: ~+0.80 V and n in range of 3.2-3.6)[33], and significantly better than alkyne-capped copper nanoparticles supported on carbon black (n = 2.5-2.7 in potential window from +0.70 V to +0.40 V, I_{limit} was 0.8 mA at 2500rpm)[22], which confirms significance of replacing carbon black or bulk graphene sheets with graphene quantum dots that are excellent in conductivity and less prone to folding and wrinkling. What's more, the Cu/GQD nanocomposites all exhibit far more better catalytic activities than bulk polycrystalline Cu or CuNi electrode (onset potential: +0.36 V vs RHE in a borax buffer solution)[34] and singlecrystalline Cu(100) or Cu(111) electrodes (~0 V vs RHE in H_2SO4 solution)[35].

6.3 Conclusion

Copper nanoparticles supported on graphene quantum dots were prepared by thermal reflux reduction in polydiol. TEM measurements showed that Cu/GQD nanocomposites bear size of 14nm, 12nm, 10nm, and 5nm with decreasing Cu/C atomic ratios. All four nanocomposites exhibit roughly spherical shapes and typical D peak and G peak of carbon-based materials were also found on Raman spectrum. X-ray photoelectron spectra prove formation of Cu/GQD nanocomposites and different defect concentrations among series. Sample with moderate defect concentrations (Cu/GQD-3.32% and Cu/GQD-2.88%) show superior oxygen reduction performance among four nanocomposites signified by almost 4e reduction pathway. Further hydrothermal treatments on Cu/GQD-2.88% bring different effects on their ORR performance, and 160°C hydrothermal treatments realizes positive-shift on onset potential and increase on number of electrons transferred. That 160°C hydrothermal treated sample was proved to bear stronger electronic interactions between Cu_2O or CuO contents (red-shift on B.E. of Cu2p) and GQD support (blue-shift on B.E. of C1s) as indicated by XPS measurement.

6.4 References

1. Peuckert, M.; Yoneda, T.; Betta, R. A. D.; Boudart, M., Oxygen Reduction on Small Supported Platinum Particles. *J Electrochem Soc* **1986,** *133* (5), 944-947.

2. (a) U.A. Paulus, A. W., G.G. Scherer, T.J. Schmidt, V. Stamenkovic, N.M. Markovic, P.N. Ross, Oxygen reduction on high surface area Pt-based alloy catalysts in comparison to well defined smooth bulk alloy electrodes. *Electrochimica Acta* **2002,** *47*, 3787-3798; (b) H. Schulenburg, E. M. l., G. Khelashvili, Roser,Bo¨nnemann, A. Wokaun, and G. G. Scherer, Heat-Treated PtCo3 Nanoparticles as Oxygen Reduction Catalysts. *J. Phys. Chem. C* **2009,** *113*, 4069–4077.

3. (a) Wu, Z.-S.; Yang, S.; Sun, Y.; Parvez, K.; Feng, X.; Müllen, K., 3D Nitrogen-Doped Graphene Aerogel-Supported Fe3O4Nanoparticles as Efficient Electrocatalysts for the Oxygen Reduction Reaction. *J Am Chem Soc* **2012,** *134* (22), 9082-9085; (b) Y Liang, Y. L., H Wang, J Zhou, J Wang, T Regier, H Dai, Co3O4 nanocrystals on graphene as a synergistic catalyst for oxygen reduction reaction. *Nature Materials* **2011,** *10*, 780-786.

4. Alonso-Vante, N., Chaper 14 Transition Metal Chalcogenides for Oxygen Reduction. In *Electrocatalysis in Fuel Cells*, Springer-Verlag London: 2013.

5. Zhang, J.; Vukmirovic, M. B.; Xu, Y.; Mavrikakis, M.; Adzic, R. R., Controlling the Catalytic Activity of Platinum-Monolayer Electrocatalysts for Oxygen Reduction with Different Substrates. *Angewandte Chemie International Edition* **2005,** *44* (14), 2132-2135.

6. Elezovic, N. R.; Babic, B. M.; Radmilovic, V. R.; Vracar, L. M.; Krstajic, N. V., Synthesis and characterization of MoOx-Pt/C and TiOx-Pt/C nano-catalysts for oxygen reduction. *Electrochimica Acta* **2009,** *54* (9), 2404-2409.

7. Park, S.; Shao, Y.; Kou, R.; Viswanathan, V. V.; Towne, S. A.; Rieke, P. C.; Liu, J.; Lin, Y.; Wang, Y., Polarization Losses under Accelerated Stress Test Using Multiwalled Carbon Nanotube Supported Pt Catalyst in PEM Fuel Cells. *Journal of The Electrochemical Society* **2011,** *158* (3), B297.

8. (a) Li, Y.; Li, Y.; Zhu, E.; McLouth, T.; Chiu, C.-Y.; Huang, X.; Huang, Y., Stabilization of High-Performance Oxygen Reduction Reaction Pt Electrocatalyst Supported on Reduced Graphene Oxide/Carbon Black Composite. *J Am Chem Soc* **2012,** *134* (30), 12326-12329; (b) Seo, M. H.; Choi, S. M.; Kim, H. J.; Kim, W. B., The graphene-supported Pd and Pt catalysts for highly active oxygen reduction reaction in an alkaline condition. *Electrochemistry Communications* **2011,** *13* (2), 182-185; (c) K. Zhang , Q. Y., G. Chen , Y. Zhai, L. Wang , H.

Wang , J. Zhao , J. Liu , J. Jia , and H. Li, Effects of Acid Treatment of Pt-Ni Alloy Nanoparticles@Graphene on the Kinetics of the Oxygen Reduction Reaction in Acidic and Alkaline Solutions. *J. Phys. Chem. C* **2011,** *115*, 379–389.

9. Xing, Y., Synthesis and Electrochemical Characterization of Uniformly-Dispersed High Loading Pt Nanoparticles on Sonochemically-Treated Carbon Nanotubes. *J. Phys. Chem. B* **2004,** *108*, 19255–19259.

10.Debe, M. K., Electrocatalyst approaches and challenges for automotive fuel cells. *Nature* **2012,** *486* (7401), 43-51.

11.Ohno, S.-y.; Yagyuu, K.; Nakatsuji, K.; Komori, F., Dissociation preference of oxygen molecules on an inhomogeneously strained Cu(001) surface. *Surface Science* **2004,** *554* (2-3), 183-192.

12.(a) Küppers, T. K. a. J., The Kinetics of the Reaction of Gaseous Hydrogen Atoms with Oxygen on Cu(111) Surfaces toward Water. *J. Phys. Chem. B* **2001,** *105*, 8369–8374; (b) D. Kolovos-Vellianitis, T. K., J. Küppers, Interaction of gaseous hydrogen atoms with oxygen cover Cu(100) surfaces. *Surf. Sci.* **2001,** *482-485*, 166–170.

13.(a) M.V. Vazquez, S. R. d. S., E.J. Calvo, D.J. Schiffrin, The electrochemical reduction of hydrogen peroxide on polycrystalline copper in borax buffer. *J Electroanal Chem* **1994,** *374*, 189-197; (b) S. Cere, M. V., S.R. de Sanchez, D.J. Schiffrin, Surface redox catalysis and reduction kinetics of oxygen on copper–nickel alloys. *Journal of Electroanalytical Chemistry* **2001,** *505*, 118-124.

14.Jiang, T.; Brisard, G. M., Determination of the kinetic parameters of oxygen reduction on copper using a rotating ring single crystal disk assembly (RRDCu(hkl)E). *Electrochimica Acta* **2007,** *52* (13), 4487-4496.

15.Yan, X.-Y.; Tong, X.-L.; Zhang, Y.-F.; Han, X.-D.; Wang, Y.-Y.; Jin, G.-Q.; Qin, Y.; Guo, X.-Y., Cuprous oxide nanoparticles dispersed on reduced graphene oxide as an efficient electrocatalyst for oxygen reduction reaction. *Chem Commun* **2012,** *48* (13), 1892.

16.Samulski, Y. S. a. E., Exfoliated Graphene Separated by Platinum Nanoparticles. *Chem. Mater.* **2008,** *20*, 6792–6797.

17.(a) Song, Y.; Chen, S. W., Graphene Quantum-Dot-Supported Platinum Nanoparticles: Defect-Mediated Electrocatalytic Activity in Oxygen Reduction. *Acs Applied Materials & Interfaces* **2014,** *6* (16), 14050-14060; (b) He, G.; Song, Y.; Liu, K.; Walter, A.; Chen, S.; Chen, S., Oxygen Reduction Catalyzed by Platinum Nanoparticles Supported on Graphene Quantum Dots. *ACS Catalysis* **2013,** *3* (5), 831-838.

18.Peng, J.; Gao, W.; Gupta, B. K.; Liu, Z.; Romero-Aburto, R.; Ge, L. H.; Song, L.; Alemany, L. B.; Zhan, X. B.; Gao, G. H.; Vithayathil, S. A.; Kaipparettu, B. A.; Marti, A. A.; Hayashi, T.; Zhu, J. J.; Ajayan, P. M., Graphene Quantum Dots Derived from Carbon Fibers. *Nano Letters* **2012,** *12* (2), 844-849.

19.Rao, C. N. R.; Sood, A. K., *Graphene : synthesis, properties, and phenomena*. Wiley-VCH: Weinheim, 2013; p xviii, 416 pages.

20.Ghodselahi, T.; Vesaghi, M. A.; Shafiekhani, A.; Baghizadeh, A.; Lameii, M., XPS study of the Cu@Cu2O core-shell nanoparticles. *Applied Surface Science* **2008,** *255* (5), 2730-2734.

21.Kim, K. S., Charge transfer transition accompanying x-ray photoionization in transition-metal compounds. *J Elec Spec Rel Phen* **1974,** *3*, 217-226.

22.Liu, K.; Song, Y.; Chen, S. W., Electrocatalytic activities of alkyne-functionalized copper nanoparticles in oxygen reduction in alkaline media. *Journal of Power Sources* **2014,** *268*, 469-475.

23.Chen, S. W.; Templeton, A. C.; Murray, R. W., Monolayer-protected cluster growth dynamics. *Langmuir* **2000,** *16* (7), 3543-3548.

24.(a) Elhaleem, S. M. A.; Ateya, B. G., Cyclic Voltammetry of Copper in Sodium-Hydroxide Solutions. *J Electroanal Chem* **1981,** *117* (2), 309-319; (b) S.M.ABD EL HALEEM, B. G. A., Cyclic voltammetry of copper in sodium hydroxide solutions. *J. Electroanal. Chem* **1981,** *117*, 309-319.

25.Zhou, Z. Y.; Kang, X. W.; Song, Y.; Chen, S. W., Enhancement of the electrocatalytic activity of Pt nanoparticles in oxygen reduction by chlorophenyl functionalization. *Chemical Communications* **2012,** *48* (28), 3391-3393.

26.A.J.Bard, L. R. F., Electrochemical methods: Fundamentals and applications. **2001**.

27.Konstantin N.Kudin, B. O., Hannes C.Schniep, Robert K.Prud'homme, Ilhan A.Aksay, and Roberto Car, Raman Spectra of Graphite Oxide and Functionalized Graphene Sheets. *Nano Letters* **2008,** *8*, 36-41.

28.Lim, D. H.; Wilcox, J., Mechanisms of the Oxygen Reduction Reaction on Defective Graphene-Supported Pt Nanoparticles from First-Principles. *J Phys Chem C* **2012,** *116* (5), 3653-3660.

29.(a) Stamenkovic, V. R.; Mun, B. S.; Arenz, M.; Mayrhofer, K. J. J.; Lucas, C. A.; Wang, G.; Ross, P. N.; Markovic, N. M., Trends in electrocatalysis on extended and nanoscale Pt-bimetallic alloy surfaces. *Nature Materials* **2007,** *6*

(3), 241-247; (b) Lu, Y.; Jiang, Y.; Gao, X.; Wang, X.; Chen, W., Strongly Coupled Pd Nanotetrahedron/Tungsten Oxide Nanosheet Hybrids with Enhanced Catalytic Activity and Stability as Oxygen Reduction Electrocatalysts. *J Am Chem Soc* **2014,** *136* (33), 11687-11697.

30.Cai, Y.; Adzic, R. R., Platinum Monolayer Electrocatalysts for the Oxygen Reduction Reaction: Improvements Induced by Surface and Subsurface Modifications of Cores. *Advances in Physical Chemistry* **2011,** *2011*, 1-16.

31.Dahal, A.; Batzill, M., Graphene–nickel interfaces: a review. *Nanoscale* **2014,** *6* (5), 2548.

32.He, G. Q.; Song, Y.; Liu, K.; Walter, A.; Chen, S.; Chen, S. W., Oxygen Reduction Catalyzed by Platinum Nanoparticles Supported on Graphene Quantum Dots. *ACS Catalysis* **2013,** *3* (5), 831-838.

33.Yan, X. Y.; Tong, X. L.; Zhang, Y. F.; Han, X. D.; Wang, Y. Y.; Jin, G. Q.; Qin, Y.; Guo, X. Y., Cuprous oxide nanoparticles dispersed on reduced graphene oxide as an efficient electrocatalyst for oxygen reduction reaction. *Chemical Communications* **2012,** *48* (13), 1892-1894.

34.(a) Vazquez, M. V.; Desanchez, S. R.; Calvo, E. J.; Schiffrin, D. J., The Electrochemical Reduction of Oxygen on Polycrystalline Copper in Borax Buffer. *Journal of Electroanalytical Chemistry* **1994,** *374* (1-2), 189-197; (b) Cere, S.; Vazquez, M.; de Sanchez, S. R.; Schiffrin, D. J., Surface redox catalysis and reduction kinetics of oxygen on copper-nickel alloys. *Journal of Electroanalytical Chemistry* **2001,** *505* (1-2), 118-124.

35.(a) Jiang, I.; Brisard, G. M., Determination of the kinetic parameters of oxygen reduction on copper using a rotating ring single crystal disk assembly (RRDCu(h k l)E). *Electrochimica Acta* **2007,** *52* (13), 4487-4496; (b) Brisard, G.; Bertrand, N.; Ross, P. N.; Markovic, N. M., Oxygen reduction and hydrogen evolution-oxidation reactions on Cu(hkl) surfaces. *Journal of Electroanalytical Chemistry* **2000,** *480* (1-2), 219-224.

Chapter 7

Defective TiO_2-supported Cu nanoparticles as efficient and stable electrocatalysts for oxygen reduction in alkaline media

Reproduced with permission from [Ke Liu, Yang Song, Shaowei Chen*, "Defective TiO_2-supported Cu nanoparticles as efficient and stable electrocatalysts for oxygen reduction in alkaline media", *Nanoscale*, **2015**, *7*, 1224.] Copyright © 2015 The Royal Society of Chemistry

7.1 Introduction

Proton exchange membrane fuel cells (PEMFC) are clean, efficient and environmental-friendly electrochemical power generators[1]. However, the sluggish kinetics of oxygen reduction reaction (ORR) at the cathode represents one of the greatest challenges in the wide-spread commercialization of PEMFC. Carbon-supported platinum-based nanoparticle catalysts have been extensively used for fuel cell electrodes;[2] yet further improvement of their performance is urgently needed due to the scarcity and high costs of platinum. In fact, a variety of strategies have been developed to improve the ORR activities, such as preparation of Pt-based alloys[3] and surface functionalization of Pt nanoparticles with selected organic ligands.[4] An alternative approach is to replace Pt with earth-abundant non-precious materials.[5] Among these, little attention has been paid to copper-based electrocatalysts although copper is inexpensive and abundant with remarkable conductivity.[6] In fact, copper has been used extensively as supporting or non-active components in oxygen reduction reactions,[7] although ORR activities of poly- or single-crystalline bulk copper has been reported in the literature in a borax buffer solution[8] or in sulfuric acid solution.[9] More recently, it has been shown that the ORR activity might be markedly enhanced with alkyne- capped nanosized copper particles,[10] suggesting that copper, when properly engineered, might be a viable material for ORR electrocatalysis.

Note that metal nanoparticle catalysts are usually dispersed on substrates

of high surface areas and/or good conductivity. Of these, carbon black is one of the most commonly used catalyst supports in oxygen reduction reaction due to high surface area and good electronic conductivity.[11] However, oxidation of carbon supports at potentials higher than +0.9 V vs RHE causes degradation in catalyst performance during fuel cell operation.[12] Therefore, it is important to identify oxidation-resistant catalyst supports to meet the durability requirements of PEMFC catalysts. Titanium dioxide has been regarded as an attractive support for ORR catalysts due to its low costs, abundance, and long-term chemical stability in extreme conditions. In addition, the hypo-d-electron nature of titanium dioxide enables strong metal-support interactions,[13] leading to enhanced dispersion of catalyst nanoparticles and improved catalytic activities. In fact, it has been reported that platinum nanoparticles supported on TiO_2 nanoparticles possessed a greater surface area[14] and a higher ORR activity than commercial Pt/C,[15] and PtPd/TiO_2 nanocomposite electrocatalysts showed activity comparable to that of Pt/C with enhanced stability at high potentials.[16] Therefore, TiO_2 appears to be a promising alternative for ORR catalyst support.[17] This is the primary motivation of the present study where we examine the ORR activity of nanocomposites based on copper nanoparticles supported on TiO_2 nanocolloids.

Herein anatase TiO_2 nanocolloids were prepared by the hydrolysis of titanium(IV) n-butoxide with the assistance of chloroaniline and oleic acid via hydrothermal treatments. Then copper nanoparticles were chemically grown on TiO_2 nanocolloids by simple sodium borohydride reduction, as manifested in

TEM and XRD measurements. FTIR measurements confirmed successful attachment of the alkyne ligands onto the nanoparticle surface in CuHC10/TiO_2 possibly by the formation of Cu–C≡ interfacial bonds. XPS measurements revealed that CuO species were formed in the nanocomposites with the concentration higher in Cu/TiO_2 than in CuHC10/TiO_2. Interestingly, Ti(III) species were identified in CuHC10/TiO_2 but absent in Cu/TiO_2, which was believed to be beneficial to the electronic conductivity of the TiO_2 supports.[18] Electrochemical studies indicated that oxygen reduction reaction proceeded mainly via the 4e pathway on both Cu/TiO_2 and CuHC10/TiO_2 samples as compared to the 2e pathway at TiO_2 nanoparticles alone. Excellent long-term stability was also retained for the nanocomposite catalysts after 4000 cycles at high potentials, and CuHC10/TiO_2 samples stood out as the best catalysts among the series, likely the combined results of defective support and surface ligand engineering.

7.2 Results and discussion

Figure 1 depicts the representative TEM micrographs of the (A) Cu/TiO_2 and (B) CuHC10/TiO_2 nanoparticles. In both images, individual nanoparticles can be identified but with rather apparent agglomeration, especially with the Cu/TiO_2 samples in panel (A); and the size of the hybrid nanoparticles range from 5 to 15 nm in diameter. High-resolution imaging in panels (C) and (D) shows that indeed copper nanoparticles were grown on TiO_2 nanocolloid surfaces, forming nanocomposites, as manifested by the well-defined lattice fringes for

Cu(111) and anatase TiO_2 (101) that were in intimate contact and featured an interlayer spacing of 0.20 and 0.35 nm, respectively.[19] In addition, the Cu nanocrystals can be seen to be around 2 nm whereas TiO_2 was markedly larger at 5 nm and above.

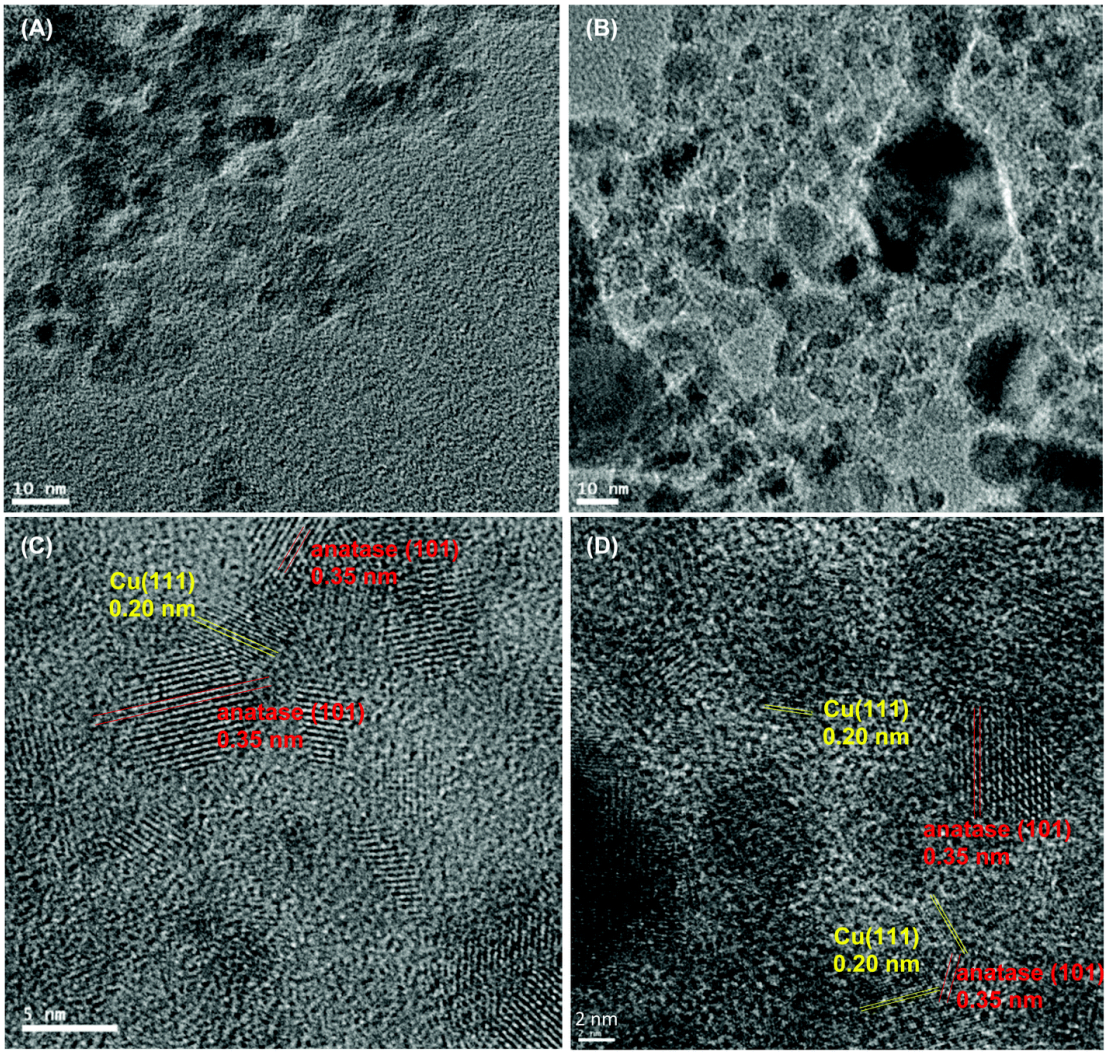


Figure 7.1. Representative TEM micrographs of (A and C) Cu/TiO_2 and (B and D) $CuHC10/TiO_2$ nanoparticles. Scale bars are 10 nm in panels (A) and (B), 5 nm in (C) and 2 nm in (D). Yellow lines highlight the Cu(111) lattice fringes whereas red lines are for anatase TiO_2 (101).

The structures of the nanocomposites were then characterized by XRD measurements. Figure 2 depicts the XRD patterns of the TiO_2 (black curve), Cu/TiO_2 (red curve) and $CuHC10/TiO_2$ (green curve) nanoparticles, which all exhibited a series of diffraction peaks (labelled by @) at 25.3°, 37.9°, 48.0°, 54.5° and 62.8°, corresponding to the (101), (004), (200), (213), and (116) crystalline planes of anatase TiO_2 (JCPDS 75-1537), respectively. Furthermore, based on the width of these difraction peaks, the average size (τ) of the TiO_2 nanocrystallites might be quantitatively estimated by using the Debye-Scherrer equation, $\tau = K\lambda/\beta\cos\theta$ where K is a dimentionless shape factor with a value of 0.9, λ is the X-ray wavelength (1.54059 Å for Cu Kα), and β is the full width at half-maximum (fwhm) of a selected diffraction peak. On the basis of the TiO_2 (101) peaks, the size (τ) was quantified and actually very consistent among the three samples, 5.1 nm for the as-prepared TiO_2, 4.1 nm for Cu/TiO_2, and 5.5 nm for $CuHC10/TiO_2$, in good agreement with the TEM results presented in Figure 1. Note that no Cu diffraction patterns can be identified in XRD measurements, probably because of the small size and low loading of the Cu nanocrystals† (Figure 1).

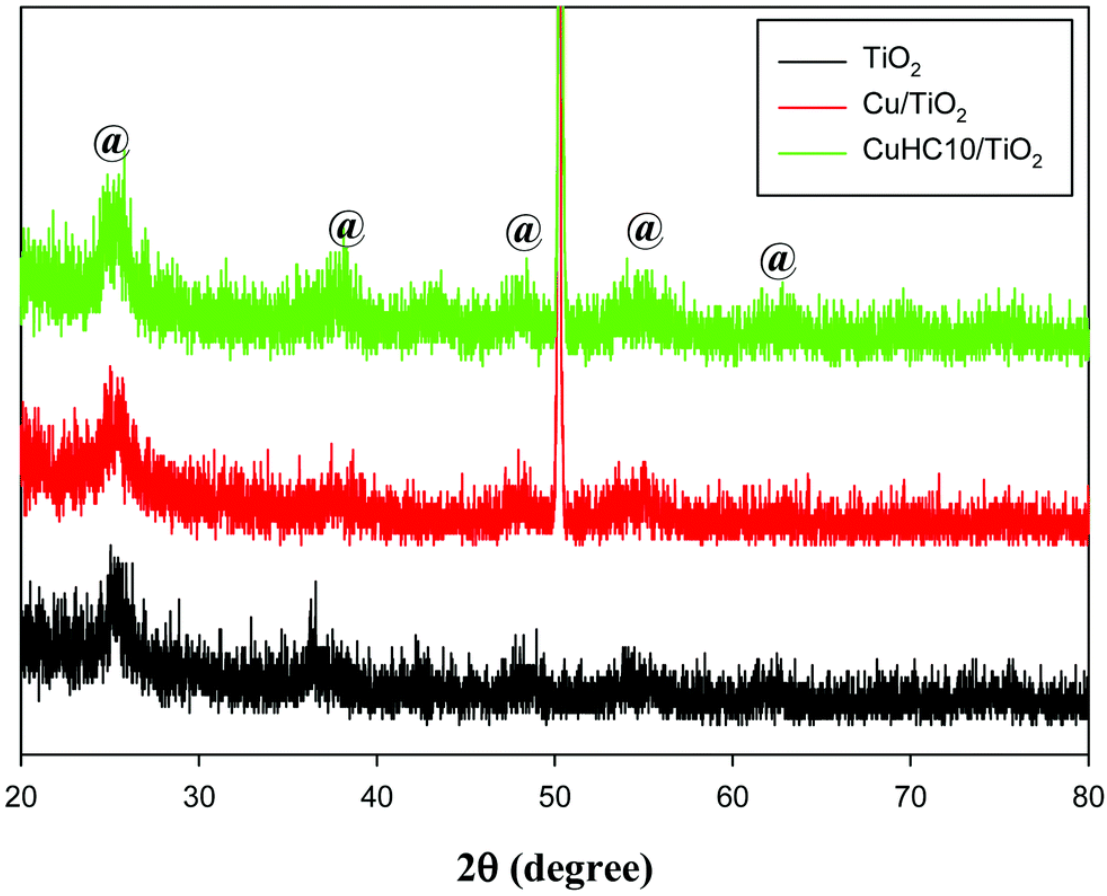


Figure 7.2. XRD patterns of TiO_2 (black curve), Cu/TiO_2 (red curve) and $CuHC10/TiO_2$ (green curve) nanoparticles. Legends "@" highlight the diffraction peaks of anatase TiO_2.

The successful passivation of the copper nanoparticles by the decyne ligands in CuHC10/TiO_2 is manifested in FTIR measurements, as shown in Figure S1. It can be seen that the ≡C–H vibrational stretch at 3312 cm^{-1} and bending vibration at 628 cm^{-1} were well-defined for the monomeric ligands of 1-decyne (red curve); yet both vanished with the nanoparticle samples (black curve, where the broad peak centered at 3300 cm^{-1} was likely due to residual water). This suggests efficient breaking of the ≡C–H bond after the alkyne ligands were adsorbed onto the copper nanoparticle surface. In addition, the absence of this vibration band also indicates that the CuHC10/TiO_2 nanocomposites were free of excessive alkyne ligands. Additionally the C≡C vibrational stretch can be identified at 2120 cm^{-1} for monomeric 1-decyne ligands; yet this band red-shifted to 1720 cm^{-1} for the CuHC10/TiO_2 nanoparticles. This phenomena may be explained by the cleavage of the ≡C–H bond and the formation of Cu–C≡ interfacial linkages, where the conjugated metal-ligand bonds led to effective intraparticle charge delocalization between the particle-bound acetylene moieties and hence a decreasing bonding order of the C≡C moieties, as observed in previous studies.[4c]

The chemical nature of the hybrid nanoparticles was then examined by XPS measurements. Figure 3 (A) shows the full survey spectra of TiO_2, Cu/TiO_2 and CuHC10/TiO_2 composite nanoparticles. In TiO_2 nanocolloids, four major peaks can be readily identified at 286 eV (C1s), 460 eV (Ti2p), 536 eV (O1s) and 976 eV (oxygen Auger). For Cu/TiO_2 and CuHC10/TiO_2 hybrid nanoparticles,

additional peaks emerged, and the peak at ca. 935 eV might be ascribed to Cu2p electrons, whereas the peak at around 570 eV most likely arose from the Cu LMM-2 auger transitions of Cu_2O.[20] This suggests the successful deposition of copper on the TiO_2 surfaces where cuprous oxide (Cu_2O) likely formed within the nanoparticles. Furthermore, based on the corresponding integrated peak areas, the Cu/Ti atomic ratio was found to be rather consistent between the two hybrid nanoparticles, 14.7% for Cu/TiO_2 and 12.6% for $CuHC10/TiO_2$.

High-resolution scans of the Cu2p electrons in Cu/TiO_2 and $CuHC10/TiO_2$ are depicted in panel (B), where the black curves are the experimental data and colored curves are deconvolution fits. Note that for all samples, the curve fittings were carried out based on reported values of full-width-half-maximum (FWHM) and mixed Lorentizan-Gaussian functions together with Shirley-type background. For both samples deconvolution yields two pairs of doublets for the Cu2p electrons. For Cu/TiO_2, the first doublet can be identified at 934.3 and 955.1 eV, which might be ascribed to metallic Cu2p electrons, and the second doublet at 936.8 and 957.5 eV most likely arising from CuO. Similar behaviors can be seen with the $CuHC10/TiO_2$ hybrids, where metallic Cu2p can be found at 934.6 and 954.5 eV and CuO at 937.1 and 956.4 eV (note that the binding energies of the Cu2p electrons for Cu(0) and Cu(I) are only 0.1 eV apart, thus the data likely reflected the combined contributions from both species).[21] One can see that the CuO concentration in Cu/TiO_2 was significantly greater than that in $CuHC10/TiO_2$. In fact, based on the integrated

peak areas, the ratio of Cu(II) over the entire copper species in the nanoparticles was estimated to be 48.2% for Cu/TiO_2 and 13.0% for $CuHC10/TiO_2$.

The formation of cupric oxide (CuO) in the nanoparticles is also manifested by the satellite between the twin peaks.[22] Note that the appearance of the satellite peak has been largely ascribed to the shake-up effect where the outgoing electron interacts with a valence electron and excites it to a higher energy level.[22] Cu(II) components exhibit a vacant 3d orbital while Cu(I) or Cu(0) features a $3d^{10}$ electronic configuration with 4s being the lowest-energy empty orbital. Therefore, one can see from panel (B) that the higher Cu(II) concentration in Cu/TiO_2 nanoparticles is consistent with the satellite peak (943.89 eV) that was somewhat red-shifted as compared to that (944.96 eV) of $CuHC10/TiO_2$ nanoparticles; and the peak intensity of the former is markedly greater than that of the latter, likely because of effective protection of the nanoparticle surface by the decyne ligands in $CuHC10/TiO_2$.

High-resolution scans of the Ti2p electrons of TiO_2, Cu/TiO_2 and $CuHC10/TiO_2$ are shown in panel (C). All three nanoparticle samples yield a doublet that was consistent with those of TiO_2 colloids reported previously,[23] 459.7 and 465.4 eV for TiO_2, 460.3 and 466.0 eV for Cu/TiO_2, and 460.5 and 466.0 eV for $CuHC10/TiO_2$, which is consistent with reported peak separation value of ~5.92 eV between $Ti2p^{1/2}$ and $Ti2p^{3/2}$. In addition, it is apparent that the $CuHC10/TiO_2$ nanoparticles show an extra peak at a somewhat lower energy (458.2 eV) than that of Ti(IV) (460.5 eV), which might be assigned to Ti(III),[24]

and from the integrated peak areas the relative ratio of Ti(III) over Ti(IV) was estimated to be 19.8%. In contrast, no Ti(III) was observed with Cu/TiO_2, which was likely due to the high concentration of CuO that impeded the reduction of Ti(IV) to Ti(III).

Panel (D) depicts the corresponding high-resolution scans of the O1s electrons. The O1s spectra of all three samples can be deconvoluted into a main peak at 531 eV and a shoulder at a higher binding energy of about 533 eV. The main peaks are consistent with those reported in the literature for bulk oxides, and the binding energy of the shoulders is in agreement with that of surface OH species.[25] The relative amounts of surface OH species can be quantified on the basis of the corresponding integrated peak areas: 29.6% for TiO_2, 30.2% for Cu/TiO_2, and 44.1% for $CuHC10/TiO_2$. It has been reported that hydroxyl groups are formed on TiO_2 surfaces during water dissociation with oxygen vacancies as the active sites.[26] In the present study, whereas the concentration of surface oxygen vacancies was rather comparable between TiO_2 and Cu/TiO_2, it was markedly higher in $CuHC10/TiO_2$. This is consistent with the formation of Ti(III) species in the $CuHC10/TiO_2$ nanoparticles as observed above that likely played an important role in enhancing the ORR activity, as detailed below.

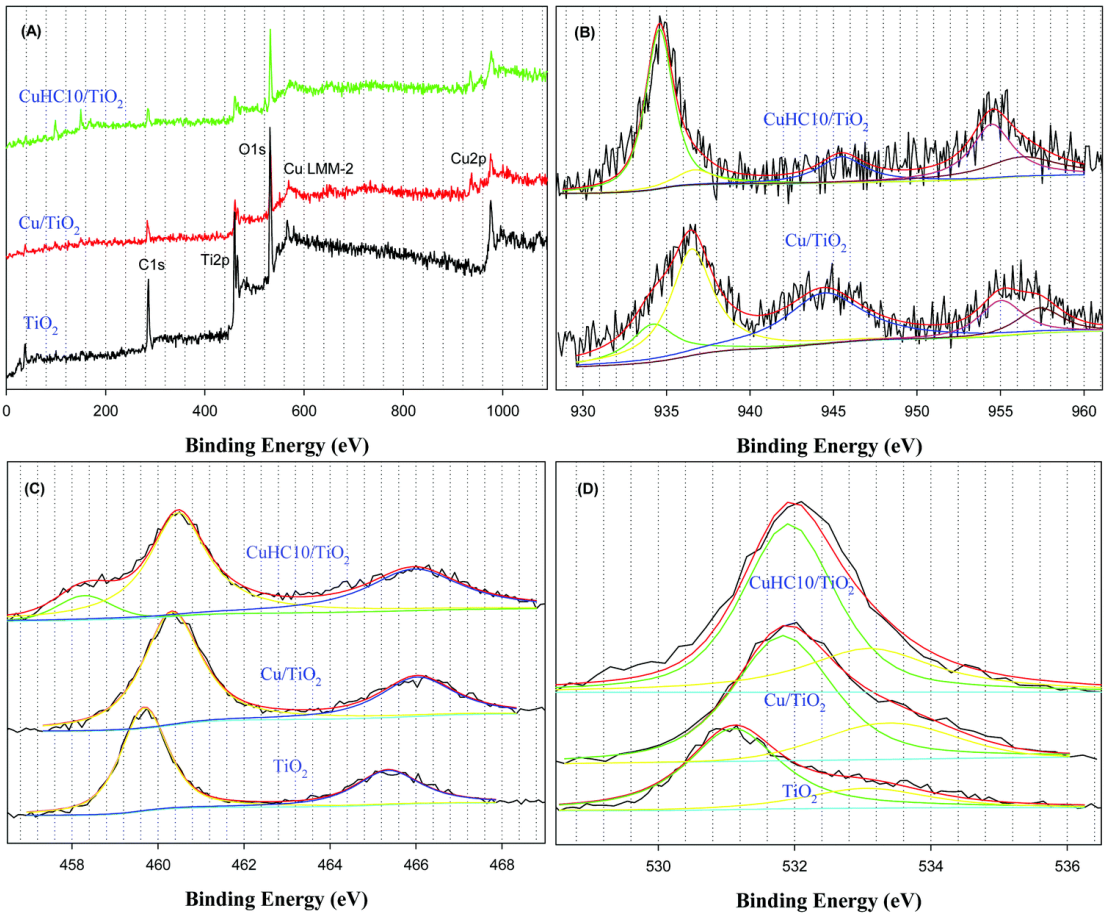


Figure 7.3. XPS full survey spectra (A) and high-resolution scans of the (B) Cu2p, (C) Ti2p and (D) O1s electrons of TiO_2, Cu/TiO_2 and $CuHC10/TiO_2$ nanoparticles. Black curves are experimental data and color curves are deconvolution fits.

Interestingly, both the Cu/TiO_2 and $CuHC10/TiO_2$ nanocomposites synthesized above exhibited apparent electrocatalytic activities towards oxygen reduction in alkaline media. Figure 4 shows the steady-state cyclic voltammograms of a glassy-carbon electrode (out of a platinum ring-glassy carbon disk electrode) modified with a calculated amount of Cu/TiO_2 and $CuHC10/TiO_2$ in a N_2-saturated 0.1 M NaOH solution. There are several aspects that warrant attention here. First, TiO_2 nanoparticles exhibited only featureless double-layer charging currents (black curve), primarily because of the large bandgap of TiO_2 and hence low electronic conductivity within the potential range of +0.1 to +1.1 V.[27] Second, the double-layer charging currents were markedly enhanced when the electrode was modified with Cu/TiO_2 (red curve) or $CuHC10/TiO_2$ (green curve) nanoparticles. For instance, the double-layer charging currents at +0.40 V increased in the order of $1(TiO_2):1.35(Cu/TiO_2):2.70(CuHC10/TiO_2)$, signifying enhanced dispersion of the hybrid nanoparticles on the electrode surface. Additional contributions might arise from the enhanced conductivity of $CuHC10/TiO_2$ by defective Ti(III) species (Figure 3).[18] Furthermore, two anodic peaks emerged at around +0.55 V and +0.84 V (vs RHE), where the former might be ascribed to the formation of a monolayer of Cu_2O while the latter to the formation of a thick multilayer film of CuO, and concurrently, a cathodic peak can be seen at around +0.66 V, likely arising from the partial reduction of CuO to Cu_2O.[28] Similar voltammetric features have also been observed in a previous study with decyne-capped copper

nanoparticles.[4c] Finally, the fact that these voltammetric peak currents were only slightly greater for CuHC10/TiO_2 than for Cu/TiO_2 suggests that electrochemically accessible surface areas of copper nanoparticles were rather comparable in both hybrid nanoparticles.

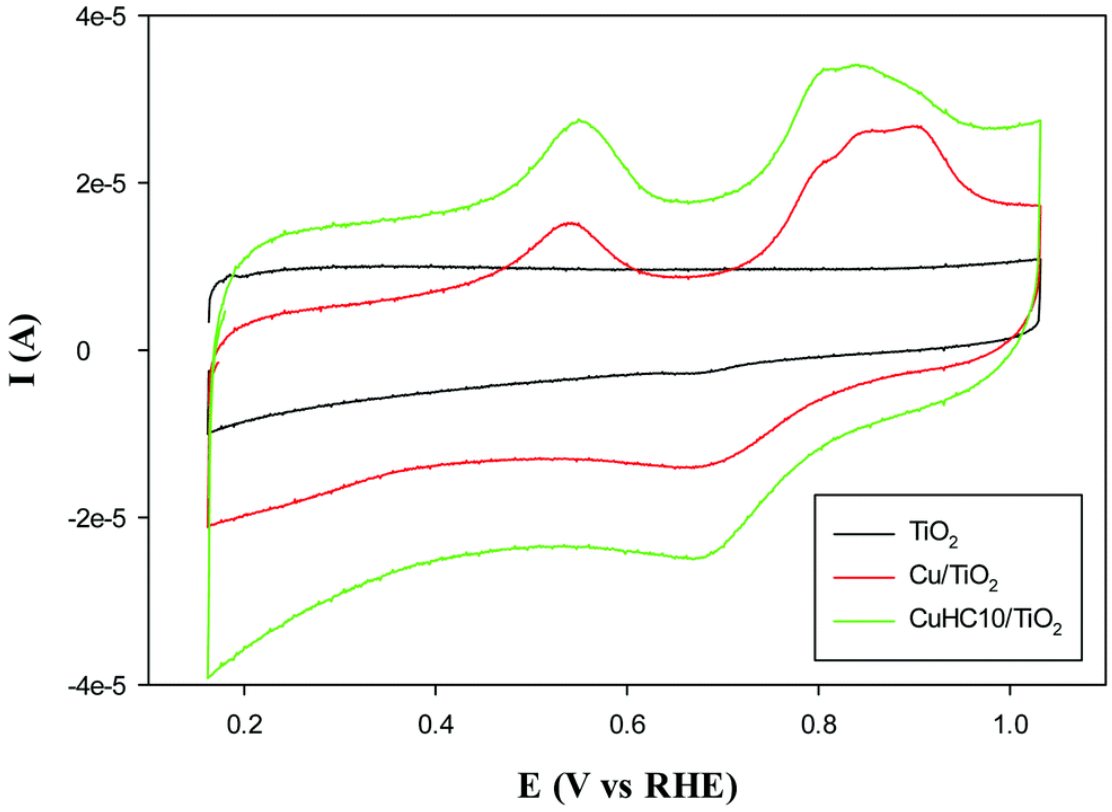


Figure 7.4. Cyclic voltammograms of a glassy carbon-disk electrode modified with 15 μg of TiO_2 (black curve), Cu/TiO_2 (red curve) or CuHC10/TiO_2 (green curve) nanoparticles in a nitrogen-saturated 0.1M NaOH solution. Potential scan rate 10 mV/s.

Figure 5 depicts the RRDE voltammagrams of the same electrodes in an O_2-saturated 0.1 M NaOH solution at different rotation rates. For all three electrodes, it can be seen that significant cathodic currents started to emerge at sufficiently negative potentials indicating apparent electrocatalytic activity towards oxygen reduction. For (A) TiO_2 and (B) Cu/TiO_2 catalysts, the onset potential was identified at around +0.74 V, and for (C) $CuHC10/TiO_2$ nanoparticles it was somewhat more positive at +0.75 V. In addition, with the $CuHC10/TiO_2$ and Cu/TiO_2 nanocomposites the limiting currents were significantly increased, as compared to that of TiO_2 alone. For instance, for TiO_2 nanoparticle catalysts alone, the limiting current at 2500 rpm was only about 0.87 mA, yet with Cu/TiO_2 catalyst the limiting current almost doubled to 1.54 mA, and with $CuHC10/TiO_2$ to 1.50 mA.

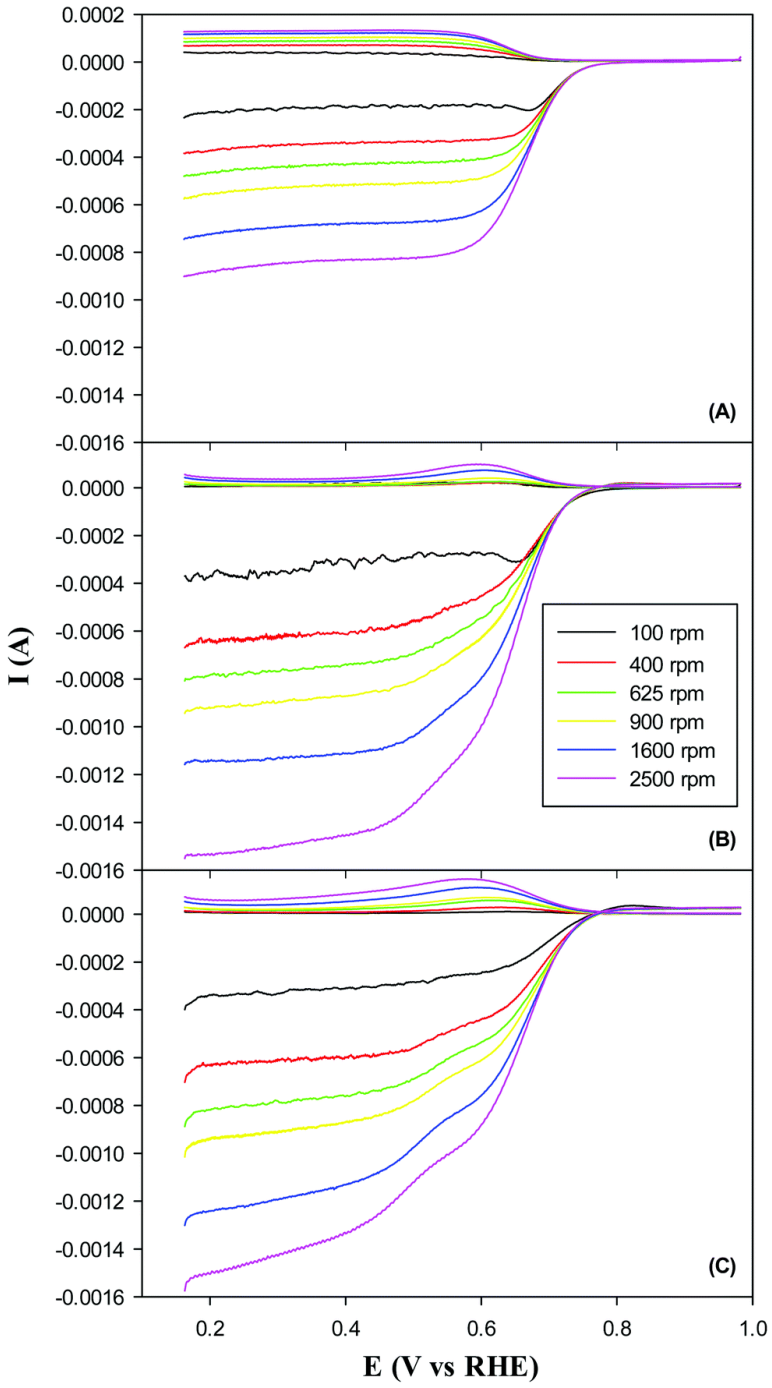


Figure 7.5. RRDE voltammograms of a platinum ring-glassy-carbon disk electrode with the disk modified with (A) TiO_2, (B) Cu/TiO_2, and (C) $CuHC10/TiO_2$ nanoparticles in an oxygen-saturated 0.1 M NaOH solution. Nanoparticle loading is all 15 μg. Electrode rotation rates are specified in the figure legends. Ring currents are collected by setting the ring potential at +1.3 V vs RHE

Furthermore, the voltammetric currents collected at the ring electrode, where the potential was set at +1.3 V, were about an order of magnitude lower than the corresponding disk currents, signifying that only a minimal amount of peroxide species were produced during oxygen reduction. From the ratio of the ring current (I_R) and disk current (I_D), the number of electron transfer (n) during oxygen reduction can be estimated by $n = 4I_D/(I_D + I_R/N)$, with N being the collection efficiency (37%), as depicted in Figure 6. It can be seen that for TiO_2, n increased from zero to 2 rapidly with the electrode potential swept from +0.76 V to +0.70 V, while for Cu/TiO_2 and $CuHC10/TiO_2$ the increase was much more drastic. At more negative potentials the n values increased accordingly and finally reached 2.69 for TiO_2, 3.74 for Cu/TiO_2 and 3.69 for $CuHC10/TiO_2$, and the corresponding fractions of peroxide species in the reaction products were estimated to be 65.5%, 13.0% and 15.5%, respectively. It is well known that oxygen reduction in aqueous solutions typically occurs through two major pathways: the direct four-electron reduction pathway from O_2 to OH^- (n = 4) and the two-electron reduction pathway from O_2 to H_2O_2 (n = 2). This means that at TiO_2 alone, the oxygen reduction was dominated by the 2-electron pathway, while the 4-electron reduction pathway was the dominant one for Cu/TiO_2 and $CuHC10/TiO_2$.

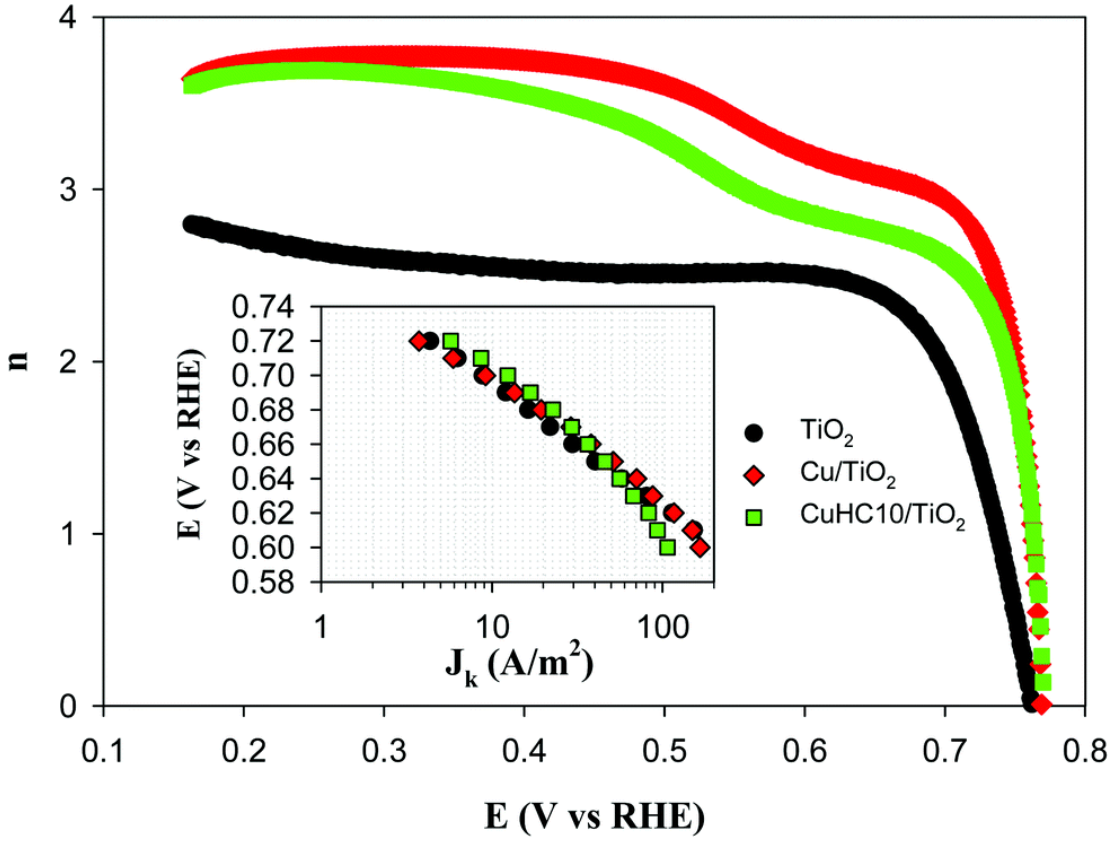


Figure 7.6. Variation of the number of electron transfer (n) in oxygen reduction with electrode potential for TiO_2 (black curves), Cu/TiO_2 (red curves) and $CuHC10/TiO_2$ (green curves) nanoparticles. Symbols were experimental data calculated from the RRDE voltammograms at 1600 rpm in Figure 5. Inset shows the corresponding Tafel plots. Data are acquired from linear regressions of the Koutecky-Levich plots in Figure S2. Electrode geometrical surface area was used to calculate the current density.

Further insights into the electron-transfer kinetics of oxygen reduction were revealed by Koutecky-Levich analysis, as the RRDE voltammetric currents include both kinetic (I_k) and diffusion (I_d) controlled contributions,[29]

$$\frac{1}{I_D} = \frac{1}{I_k} + \frac{1}{I_d} = \frac{1}{I_k} + \frac{1}{B\omega^{1/2}} \quad (7.1a)$$

$$B = 0.62nFAC_O D_O^{2/3} \nu^{-1/6} \quad (7.1b)$$

$$I_k = nAFkC_O \quad (7.1c)$$

where ω is the electrode rotation rate, n is the overall number of electron transfer, F is Faraday constant, C_O is the bulk concentration of O_2 dissolved in the electrolyte, D_O is the diffusion coefficient of O_2, and ν is the kinetic viscosity of the electrolyte.[30] Figure S2 depicts the Koutecky-Levich plots (I_D^{-1} vs $\omega^{-1/2}$) of (A) TiO_2, (B) Cu/TiO_2 and (C) $CuHC10/TiO_2$ nanoparticles within the potential range of +0.76 to +0.60 V. One can see that all experimental data exhibited good linearity and the slopes of each nanoparticle catalyst remained approximately constant. The linearity and parallelism of the plots are usually taken as a strong indication of a first-order reaction with respect to dissolved oxygen. From the linear regressions in Figure S2, the kinetic currents (I_k) could also be quantified from the y-axis intercepts. This is manifested in the Tafel plot (inset to Figure 6), where it can be seen that within the low overpotential region (E > +0.66 V), the kinetic currents increase in the order of TiO_2 < Cu/TiO_2 < $CuHC10/TiO_2$. For instance, at +0.70 V, the kinetic current density (J_k) was 8.83 A/m^2 for TiO_2, 9.18 A/m^2 for Cu/TiO_2 and 12.38 A/m^2 for $CuHC10/TiO_2$, indicating that

CuHC10/TiO_2 stood out as the best catalyst among the series (one may note that at high overpotentials (E < +0.66 V), the J_k values were actually higher for Cu/TiO_2 than for CuHC10/TiO_2. This may be ascribed to the much higher concentration of CuO in Cu/TiO_2 that was electrochemically reduced to Cu_2O at these potentials (Figure 4) as Cu_2O was known to be active in ORR, vide infra).

The slope of the Tafel plot can also be used to gain further insights into the dynamics of oxygen reduction reaction. For oxygen electroreduction at nanoparticle catalyst surfaces, the Tafel slopes are typically found at 60 mV/dec or 120 mV/dec, where the former corresponds to a pseudo two-electron reaction as the rate determining step, and in the latter, ORR is presumed to be limited by the first-electron reduction of oxygen.[31] In the present study, linear regressions of the Tafel plots yield a slope of 70.5 mV/dec for TiO_2, suggesting that oxygen reduction reaction was largely limited by a pseudo two-electron process (corresponding to a relatively large fraction of peroxide species in the reduction products). For CuHC10/TiO_2, the Tafel plot actually includes two linear segments with different slopes. At low current densities (E > +0.66 V), the Tafel slope was about 58.5 mV/dec, implying the pseudo two-electron reaction as the rate-determining step in the low overpotential region. At high current densities (E < +0.66 V) the Tafel slope increased to 118.5 mV/dec, consistent with the first-electron reduction of oxygen as the rate-determining step (implying a facile O–O bond breaking step at high overpotentials). Similar behaviors can be seen with the Cu/TiO_2 sample with the two slopes of 56.7 mV/dec and 90.2 mV/dec,

respectively. Dual Tafel slopes in ORR have been observed previously with Pt-based electrocatalysts,[32] and accounted for by a double-trap kinetic model,[33] where the turning point (+0.66 V in the present study) reflects the equilibrium potential for the dynamic transition between surface-adsorbed reaction intermediates like O* and HO*. Note that this potential coincided with the formation of Cu_2O for both CuHC10/TiO_2 and Cu/TiO_2, as manifested in Figure 4, and Cu_2O has been suggested to serve as effective active sites for ORR by donating electrons to oxygen.[4c, 33] Additional contributions may arise from the relatively hydrophilic surfaces of CuHC10/TiO_2 and Cu/TiO_2 hybrid nanoparticles that facilitated water dissociation and formation of surface-adsorbed hydroxyl speciesas evidenced in XPS measurements (Figure 3) following by fast interactive effusion of H-adatoms over the hydrated surfaces which is believed to impose advanced electrocatalytic effects[34]. Furthermore, the Ti^{3+} defects in CuHC10/TiO_2 (Figure 3) might also help enhance the adsorption and eventual reduction of oxygen on copper by interfacial charge transfer.[18] All these led to a much enhanced ORR activity of CuHC10/TiO_2 as compared to those of Cu/TiO_2 and TiO_2.

Durability is another important parameter in the evaluation of nanoparticle catalytic performance. In the present study, durability tests were performed in oxygen-saturated 0.1 M NaOH at a potential sweep rate of 50 mV/s between +0.6 V and +1.1 V for 4000 cycles.[35] The RDE polarization curves before (solid curves) and after (dashed curves) durability tests were depicted in

Figure 7. It can be seen that for TiO_2 nanoparticles alone (black curves), the polarization curve showed a cathodic shift of about 10 mV with virtually no change of the diffusion limiting current. For the Cu/TiO_2 nanoparticles (red curves), the polarization curve was negatively shifted by as much as 30 mV, along with about 9% diminishment of the limiting current. In sharp contrast, no apparent change was observed with $CuHC10/TiO_2$ (green curves), indicating markedly enhanced stability of the hybrid nanoparticles that was likely due to the decyne capping ligands.

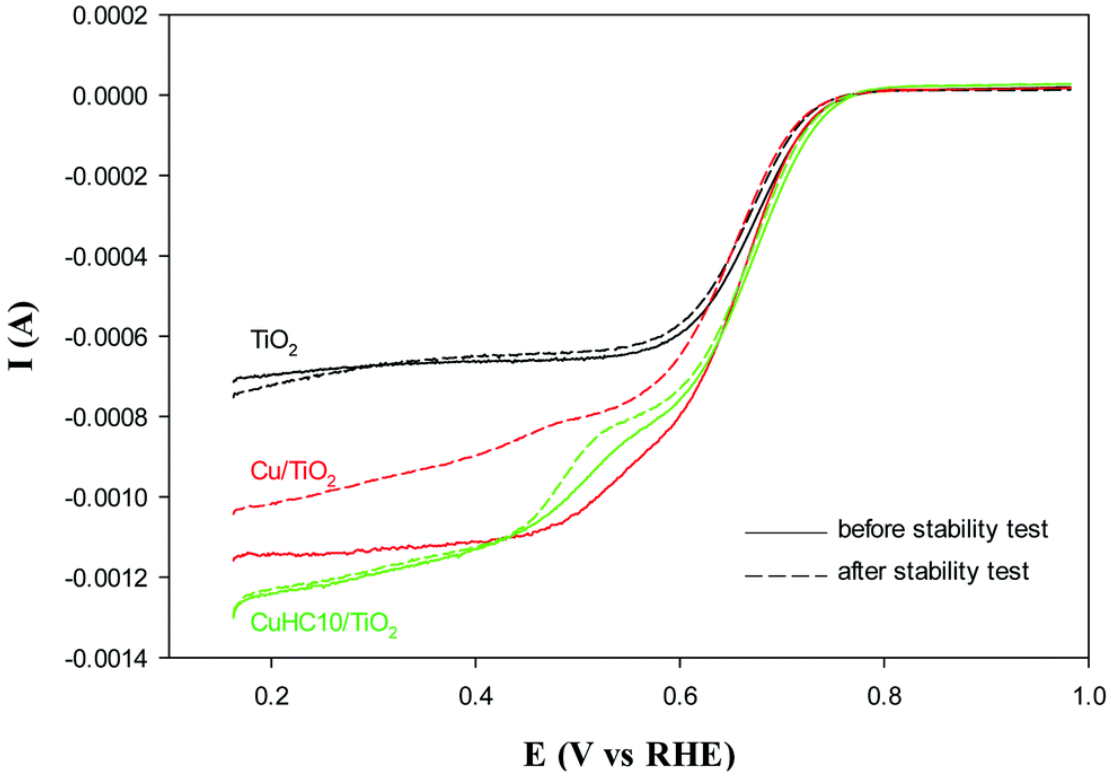


Figure 7.7. Polarization curves for oxygen reduction catalyzed by TiO_2 (A), Cu/TiO_2 (B), and $CuHC10/TiO_2$ (C) before (solid curves) and after (dashed curves) 4000 potential cycles with a potential scan rate of 50 mV/s from +0.6 to 1.1V in O_2 saturated 0.1M NaOH solution. Electrode rotation rate: 1600 rpm. Other experimental conditions were the same as in Figure 7.5.

One may note that the electrocatalytic performance of these Cu/TiO_2 and CuHC10/TiO_2 hybrid nanoparticles remains subpar as compared to that of Pt or Pd-based nanoparticle catalysts which typically exhibit an onset potentials more positive than +0.90 V and n ≈ 4.0.[4b, c, 36] Yet, the activity is actually rather comparable to that of Au-TiO_2 nanocomposites (10 – 50 nm in diameter, n = 3.7 at +0.60 V, onset potential +0.88 V),[37] and markedly better than that observed previously with alkyne-capped copper nanoparticles. Those alkyne-capped nanoparticles (4-6nm in diameter) bear same capping ligands (1-decyne) and were prepared in similar ways except for choosing carbon black rather than TiO_2 nanoparticles as supports. Without the strong metal-support interactions from TiO_2, peroxide species constituted a major portion of the oxygen reduction products of CuHC10/C (n = 2.5 – 2.7 within the potential range of +0.70 to +0.40 V)[4c] and corresponding limiting current at 2500rpm was only 0.8mA, signifying the importance of TiO_2 in the activation of water and formation of surface adsorbed hydroxyl species for oxygen reduction. It should be emphasized that the ORR activity of copper-based bulk electrodes is rather marginal.[8-9, 38] For instance, in the previous studies with a polycrystalline Cu or CuNi electrode,[8] the onset potentials for oxygen reduction were found to be around +0.36 V (vs RHE) in a borax buffer solution; and even more negative onset potentials were observed with single-crystalline Cu(100) and Cu(111) electrodes in H_2SO_4 at about 0 V (vs RHE).[9, 38] These are far more negative than those observed above with the hybrid nanoparticles.

7.3 Conclusion

In this study, copper nanoparticles with or without 1-decyne capping ligands were grown onto TiO_2 nanocolloid surfaces. The structures of the resulting nanocomposites were then subject to a wide range of characterizations. TEM measurements showed that the TiO_2 colloids were largely of anatase phase, and the close proximity of the TiO_2(101) and Cu(111) lattice fringes suggested intimate contacts between the two components. Further structural details were unravelled in XRD measurements where the diffraction features of anatase TiO_2 were clearly defined whereas those of copper were not resolved, likely because of the small size and low loading of copper in the composites. XPS measurements suggested the formation of CuO in both hybrid nanoparticles, with a much higher concentration in Cu/TiO_2 than in CuHC10/TiO_2, most probably because of the decyne capping ligands in the latter. Interestingly, Ti^{3+} species were identified in CuHC10/TiO_2 nanoparticles but not in Cu/TiO_2, which may, at least in part, account for the enhanced ORR activity of the former. Electrochemical studies indicated that electrocatalytic activity in oxygen reduction in alkaline media was significantly improved after copper species were chemically grown onto TiO_2 nanoparticles, as manifested in the increase in number of electrons transferred from about 2.69 up to 3.74, an apparent anodic shift of the onset potential, a rather drastic increase of the kinetic current density and remarkable long-term stability. Among the series, the best performance was observed with CuHC10 nanoparticles, which was ascribed to the activation of water by TiO_2 and the

formation of surface-adsorbed hydroxyl species facilitated by defective Ti^{3+} sites. Taken together, the results presented herein indicates that the synergistic interactions between non-precious metals and metal oxides might be exploited for the development of effective catalysts based on earth-abundant and cost-effective materials for fuel cell electrochemistry.

7.4 References

1. Proietti, E.; Jaouen, F.; Lefevre, M.; Larouche, N.; Tian, J.; Herranz, J.; Dodelet, J. P., Iron-based cathode catalyst with enhanced power density in polymer electrolyte membrane fuel cells. *Nat Commun* **2011,** *2*.

2. (a) Wagner, F. T.; Lakshmanan, B.; Mathias, M. F., Electrochemistry and the Future of the Automobile. *Journal of Physical Chemistry Letters* **2010,** *1* (14), 2204-2219; (b) Rizo, R.; Herrero, E.; Feliu, J. M., Oxygen reduction reaction on stepped platinum surfaces in alkaline media. *Phys Chem Chem Phys* **2013,** *15* (37), 15416-15425; (c) Wang, H. H.; Zhou, Z. Y.; Yuan, Q. A.; Tian, N.; Sun, S. G., Pt nanoparticle netlike-assembly as highly durable and highly active electrocatalyst for oxygen reduction reaction. *Chem Commun* **2011,** *47* (12), 3407-3409.

3. Zhang, J.; Sasaki, K.; Sutter, E.; Adzic, R. R., Stabilization of platinum oxygen-reduction electrocatalysts using gold clusters. *Science* **2007,** *315* (5809), 220-222.

4. (a) Zhou, Z. Y.; Kang, X. W.; Song, Y.; Chen, S. W., Enhancement of the electrocatalytic activity of Pt nanoparticles in oxygen reduction by chlorophenyl functionalization. *Chemical Communications* **2012,** *48* (28), 3391-3393; (b) Zhou, Z. Y.; Kang, X. W.; Song, Y.; Chen, S. W., Ligand-Mediated Electrocatalytic Activity of Pt Nanoparticles for Oxygen Reduction Reactions. *Journal of Physical Chemistry C* **2012,** *116* (19), 10592-10598; (c) Liu, K.; Kang, X. W.; Zhou, Z. Y.; Song, Y.; Lee, L. J.; Tian, D.; Chen, S. W., Platinum nanoparticles functionalized with acetylene derivatives: Electronic conductivity and electrocatalytic activity in oxygen reduction. *J Electroanal Chem* **2013,** *688*, 143-150.

5. Bashyam, R.; Zelenay, P., A class of non-precious metal composite catalysts for fuel cells. *Nature* **2006,** *443* (7107), 63-66.

6. (a) Lefevre, M.; Proietti, E.; Jaouen, F.; Dodelet, J. P., Iron-Based Catalysts with Improved Oxygen Reduction Activity in Polymer Electrolyte Fuel Cells. *Science* **2009,** *324* (5923), 71-74; (b) Wu, G.; More, K. L.; Johnston, C. M.; Zelenay, P., High-Performance Electrocatalysts for Oxygen Reduction Derived from Polyaniline, Iron, and Cobalt. *Science* **2011,** *332* (6028), 443-447; (c) Wang, S.; Yu, D.; Dai, L., Polyelectrolyte Functionalized Carbon Nanotubes as Efficient Metal-free Electrocatalysts for Oxygen Reduction. *J Am Chem Soc* **2011,** *133* (14), 5182-5185.

7. (a) Koh, S.; Strasser, P., Electrocatalysis on bimetallic surfaces: Modifying catalytic reactivity for oxygen reduction by voltammetric surface dealloying. *J*

Am Chem Soc **2007,** *129* (42), 12624-+; (b) Kariuki, N. N.; Wang, X.; Mawdsley, J. R.; Ferrandon, M. S.; Niyogi, S. G.; Vaughey, J. T.; Myers, D. J., Colloidal Synthesis and Characterization of Carbon-Supported Pd−Cu Nanoparticle Oxygen Reduction Electrocatalysts. *Chemistry of Materials* **2010,** *22* (14), 4144-4152; (c) Li, H. H.; Cui, C. H.; Zhao, S.; Yao, H. B.; Gao, M. R.; Fan, F. J.; Yu, S. H., Mixed-PtPd-Shell PtPdCu Nanoparticle Nanotubes Templated from Copper Nanowires as Efficient and Highly Durable Electrocatalysts. *Adv Energy Mater* **2012,** *2* (10), 1182-1187.

8. (a) Vazquez, M. V.; Desanchez, S. R.; Calvo, E. J.; Schiffrin, D. J., The Electrochemical Reduction of Oxygen on Polycrystalline Copper in Borax Buffer. *J Electroanal Chem* **1994,** *374* (1-2), 189-197; (b) Cere, S.; Vazquez, M.; de Sanchez, S. R.; Schiffrin, D. J., Surface redox catalysis and reduction kinetics of oxygen on copper-nickel alloys. *J Electroanal Chem* **2001,** *505* (1-2), 118-124.

9. Jiang, T.; Brisard, G. M., Determination of the kinetic parameters of oxygen reduction on copper using a rotating ring single crystal disk assembly (RRDCu(hkl)E). *Electrochimica Acta* **2007,** *52* (13), 4487-4496.

10.K. Liu, Y. S., S.Chen, Electrocatalytic activities of alkyne-functionalized copper nanoparticles in oxygen reduction in alkaline media. *J. Power. Sources* **2014,** *268*, 469-475.

11.(a) Schmidt, T. J.; Gasteiger, H. A.; Stab, G. D.; Urban, P. M.; Kolb, D. M.; Behm, R. J., Characterization of high-surface area electrocatalysts using a rotating disk electrode configuration. *Journal of the Electrochemical Society* **1998,** *145* (7), 2354-2358; (b) Min, M. K.; Cho, J. H.; Cho, K. W.; Kim, H., Particle size and alloying effects of Pt-based alloy catalysts for fuel cell applications. *Electrochimica Acta* **2000,** *45* (25-26), 4211-4217.

12.Rajalakshmi, N.; Lakshmi, N.; Dhathathreyan, K., Nano titanium oxide catalyst support for proton exchange membrane fuel cells. *International Journal of Hydrogen Energy* **2008,** *33* (24), 7521-7526.

13.(a) Hayden, B. E.; Malevich, D. V.; Pletcher, D., Platinum catalysed nanoporous titanium dioxide electrodes in H2SO4 solutions. *Electrochemistry Communications* **2001,** *3* (8), 395-399; (b) Wang, M.; Guo, D. J.; Li, H. L., High activity of novel Pd/TiO2 nanotube catalysts for methanol electro-oxidation. *Journal of Solid State Chemistry* **2005,** *178* (6), 1996-2000.

14.Shim, J. L., C. R.; Lee, H. K.; Lee, J. S.; Cairns, E. J. , Electrochemical characteristics of Pt–WO3-C and Pt–TiO2-C electrocatalysts in a polymer electrolyte fuel cell. *J. Power Sources* **2001,** *102*, 172.

15.Shanmugam, S.; Gedanken, A., Synthesis and Electrochemical Oxygen

Reduction of Platinum Nanoparticles Supported on Mesoporous TiO2. *Journal of Physical Chemistry C* **2009,** *113* (43), 18707-18712.

16.Huang, S.-Y.; Ganesan, P.; Popov, B. N., Electrocatalytic Activity and Stability of Titania-Supported Platinum–Palladium Electrocatalysts for Polymer Electrolyte Membrane Fuel Cell. *ACS Catalysis* **2012,** *2* (5), 825-831.

17.Jaksic, M. M.; Botton, G. A.; Papakonstantinou, G. D.; Nan, F. H.; Jaksic, J. M., Primary Oxide Latent Storage and Spillover Enabling Electrocatalysts with Reversible Oxygen Electrode Properties and the Alterpolar Revertible (PEMFC versus WE) Cell. *Journal of Physical Chemistry C* **2014,** *118* (17), 8723-8746.

18.Thompson, T. L.; Yates, J. T., Surface science studies of the photoactivation of TiO2-new photochemical processes. *Chemical Reviews* **2006,** *106* (10), 4428-4453.

19.(a) Ramanathan, R.; Field, M. R.; O'Mullane, A. P.; Smooker, P. M.; Bhargava, S. K.; Bansal, V., Aqueous phase synthesis of copper nanoparticles: a link between heavy metal resistance and nanoparticle synthesis ability in bacterial systems. *Nanoscale* **2013,** *5* (6), 2300-2306; (b) Zhu, Q.; Qian, J. S.; Pan, H.; Tu, L.; Zhou, X. F., Synergistic manipulation of micro-nanostructures and composition: anatase/rutile mixed-phase TiO2 hollow micro-nanospheres with hierarchical mesopores for photovoltaic and photocatalytic applications. *Nanotechnology* **2011,** *22* (39).

20.Ghodselahi, T.; Vesaghi, M. A.; Shafiekhani, A.; Baghizadeh, A.; Lameii, M., XPS study of the Cu@Cu2O core-shell nanoparticles. *Appl Surf Sci* **2008,** *255* (5), 2730-2734.

21.Wagner, C. D.; Riggs, W. M.; Davis, L. E.; Moulder, J. F.; Muilenberg, G. E., *Handbook of x-ray photoelectron spectroscopy : a reference book of standard data for use in x-ray photoelectron spectroscopy*. Perkin-Elmer Corp.: Eden Prairie, Minn., 1979; p 190.

22.Kim, K. S., Charge-Transfer Transition Accompanying X-Ray Photoionization in Transition-Metal Compounds. *J Electron Spectrosc* **1974,** *3* (3), 217-226.

23.Erdem, B.; Hunsicker, R. A.; Simmons, G. W.; Sudol, E. D.; Dimonie, V. L.; El-Aasser, M. S., XPS and FTIR surface characterization of TiO2 particles used in polymer encapsulation. *Langmuir* **2001,** *17* (9), 2664-2669.

24.Sodergren, S.; Siegbahn, H.; Rensmo, H.; Lindstrom, H.; Hagfeldt, A.; Lindquist, S. E., Lithium intercalation in nanoporous anatase TiO2 studied with XPS. *Journal of Physical Chemistry B* **1997,** *101* (16), 3087-3090.

25.Kunat, M.; Girol, S. G.; Burghaus, U.; Woll, C., The interaction of water with the oxygen-terminated, polar surface of ZnO. *Journal of Physical Chemistry B* **2003,** *107* (51), 14350-14356.

26.Schaub, R.; Thostrup, P.; Lopez, N.; Lægsgaard, E.; Stensgaard, I.; Nørskov, J.; Besenbacher, F., Oxygen Vacancies as Active Sites for Water Dissociation on Rutile TiO2(110). *Phys Rev Lett* **2001,** *87* (26).

27.Nozik, A. J.; Memming, R., Physical chemistry of semiconductor-liquid interfaces. *Journal of Physical Chemistry* **1996,** *100* (31), 13061-13078.

28.Elhaleem, S. M. A.; Ateya, B. G., Cyclic Voltammetry of Copper in Sodium-Hydroxide Solutions. *J Electroanal Chem* **1981,** *117* (2), 309-319.

29.Bard, A. J.; Faulkner, L. R., *Electrochemical methods : fundamentals and applications*. 2nd ed.; Wiley: New York, 2001; p xxi, 833 p.

30.Chen, W.; Kim, J. M.; Sun, S. H.; Chen, S. W., Electrocatalytic reduction of oxygen by FePt alloy nanoparticles. *J Phys Chem C* **2008,** *112* (10), 3891-3898.

31.Zhang, J. J., *PEM fuel cell electrocatalysts and catalyst layers : fundamentals and applications*. Springer: London, 2008; p xxi, 1137 p.

32.He, G.; Song, Y.; Liu, K.; Walter, A.; Chen, S.; Chen, S., Oxygen Reduction Catalyzed by Platinum Nanoparticles Supported on Graphene Quantum Dots. *ACS Catalysis* **2013,** *3* (5), 831-838.

33.Wang, J. X.; Uribe, F. A.; Springer, T. E.; Zhang, J. L.; Adzic, R. R., Intrinsic kinetic equation for oxygen reduction reaction in acidic media: the double Tafel slope and fuel cell applications. *Faraday Discuss* **2008,** *140*, 347-362.

34.(a) G. D. Papakonstantinou, J. M. J., D. Labou, A. Siokou and M. M. Jaksic, *Adv. Phys. Chem.* **2011,** *2011*, 1-22; (b) J. M. Jaksic, G. D. P., D. Labou, A. Siokou and M. M. Jaksic, In *New and future developments in catalysis: hybrid materials, composites, and organocatalysts*, Suib, S. L., Ed. Elsevier: Amsterdam, 2013; pp 175-212.

35.Lim, B.; Jiang, M.; Camargo, P. H. C.; Cho, E. C.; Tao, J.; Lu, X.; Zhu, Y.; Xia, Y., Pd-Pt Bimetallic Nanodendrites with High Activity for Oxygen Reduction. *Science* **2009,** *324* (5932), 1302-1305.

36.(a) Maheswari, S.; Sridhar, P.; Pitchumani, S., Pd-TiO2/C as a methanol tolerant catalyst for oxygen reduction reaction in alkaline medium. *Electrochemistry Communications* **2013,** *26*, 97-100; (b) Zhang, L.; Wang, L. Y.; Holt, C. M. B.; Navessin, T.; Malek, K.; Eikerling, M. H.; Mitlin, D., Oxygen

Reduction Reaction Activity and Electrochemical Stability of Thin-Film Bilayer Systems of Platinum on Niobium Oxide. *Journal of Physical Chemistry C* **2010,** *114* (39), 16463-16474.

37.Lin, C.; Song, Y.; Cao, L.; Chen, S., Oxygen Reduction Catalyzed by Au–TiO2Nanocomposites in Alkaline Media. *ACS Applied Materials & Interfaces* **2013,** *5* (24), 13305-13311.

38.Brisard, G.; Bertrand, N.; Ross, P. N.; Markovic, N. M., Oxygen reduction and hydrogen evolution-oxidation reactions on Cu(hkl) surfaces. *J Electroanal Chem* **2000,** *480* (1-2), 219-224.